

# On the Microstructural Stress and Strain Behavior Determination of Metallic Materials Based on Electromagnetic Phenomena



**Dissertation**

zur Erlangung des Grades des  
Doktors der Ingenieurwissenschaften  
der Naturwissenschaftlich-Technischen Fakultät III  
Chemie, Pharmazie, Bio- und Werkstoffwissenschaften  
der Universität des Saarlandes

von

**Meisam Sheikh Amiri**

Saarbrücken

2015

Tag des Kolloquiums: 02.11.2015

Dekan: Prof. Dr.-Ing. Dirk Bähre

Berichterstatter: Prof. Dr. -Ing. Christian Boller  
Prof. Dr. rer. nat. Siegfried Schmauder

Vorsitz: Prof. Dr.-Ing. Hans-Georg Herrmann

Akad. Mitarbeiter: Dr.-Ing. Mohammad Zamanzade

# Declaration of Originality

I, Meisam Sheikh Amiri, hereby declare that this thesis and the work reported herein was composed by and originated entirely from me. Information derived from the published and unpublished work of others has been acknowledged in the text and references are given in the list of sources.

Place and date

.....

Signature

.....

# Acknowledgements

Undertaking this PhD has been a truly life-changing experience for me and it would not have been possible to do without the support and guidance that I received from many people.

First of all, I would like to gratefully and sincerely thank my advisor, Prof. Dr. -Ing. Christian Boller, for his guidance, understanding and patience. Thank you for giving me the opportunity to work under your supervision, both in Fraunhofer IZFP and in Saarland University. I would also like to thank you for encouraging my research and for allowing me to grow as a research scientist. Your advice on both research as well as on my career have been priceless.

Furthermore, I would like to thank Prof. Dr. rer. nat. Siegfried Schmauder, Prof. Dr. -Ing. Hans-Georg Herrmann and Dr. -Ing. Mohammad Zamanzade for serving as my committee members. I also want to thank them for allowing my defence to be an enjoyable moment and for their brilliant comments and suggestions – many thanks!

I would like to thank specially Dr. -Ing. Klaus Szielasko, the team leader of the electromagnetic group at the Material Characterization Department of Fraunhofer IZFP. I greatly appreciate the support received through the collaborative work undertaken between Saarland University and Fraunhofer IZFP. Thank you for everything, especially for your friendship during my graduate studies - I learned a lot from you. I would also thank Dr. -Ing. Madalina Rabung for her endless support, very helpful discussions, brilliant advice and friendship.

I wish to thank Dipl. -Ing. Matthias Thielen for his wonderful collaboration, outstanding discussions and perfect understanding. Together, we designed and performed the tests, experiences and evaluations. Thank you for your memorable cooperation.

A good support system is important to surviving and staying sane during a PhD period. I was lucky to be a part of one of the best research groups. I would like to express my appreciation and thanks to Prof. e.h. Dr. rer. nat. Dr. -Ing. e.h. Gerd Dobmann, Dr. -Ing. Iris Altpeter, Dr. -Ing. Jochen Kurz, Dr. -Ing. Peter Starke, Dr. Yasmine Gabi, Dr. -Ing. Ralf Tschuncky, Dipl. -Ing. Melanie Kopp, Dipl. -Ing. Georg Seiler, M. Tech. Ramanan Sridaran Venkat, Dipl. -Ing. Sergey Pushkarev, Dipl. -Ing Sargon Yousef, Dr. -Ing Leonardo Batista, M.Sc. Alexander Surkov, Ms. Rosemarie Bettinger and Ms. Pardis Bayenat. Thank you greatly for your help and support.

I gratefully acknowledge the funding sources that made my PhD work possible. My project was funded by the German Research Foundation (DFG).

Most of all, my thanks go to my loving, supportive, encouraging and patient girlfriend, Vanessa, whose faithful support during this PhD is so appreciated. Her love and support without any claim or regret always gave me a positive energy and have enabled me to finish this thesis. Thank you so much.

Last, but not least, special thanks should also go to my family. Words cannot express how grateful I am to my mother, father, sister and brother for all of the sacrifices made on my behalf. Thank you all for your endless love, support and encouragement.

Meisam Sheikh Amiri  
Saarbrücken, November 2015

**In memory of my mom.  
You are always in my memory.**

## Abstract

The objective of this thesis has been to quantify residual stresses at the grain level of metallic materials determined as micro-residual stresses using magnetic Barkhausen noise, whereby a micro-residual stress mapping method based on magnetic Barkhausen noise (RESTMAB) is proposed. Compared to conventional electromagnetic testing, the process of referencing is significantly simplified when the RESTMAB is used. The RESTMAB is based on two characteristics: a) the fact that the behaviour of the magnetic Barkhausen noise under stress (called MBN( $\sigma$ )) curve shows an extremum which shifts when a stress is applied and which can be directly correlated to the MRS in the direction of stress, and b) that the MBN( $\sigma$ ) curve shows a linear range before the extremum that is constant. The interpretation of the results is discussed based on a micro-structural model of a single crystal to explain the physical reason for the MBN( $\sigma$ ) curves. To this end, magnetic hysteresis and magnetostriction curves were measured in situ. The results show that the activation of new magnetic easy axes due to stress anisotropy is the main reason for this behaviour. The change of the domain structures was measured in situ using magnetic force microscopy and the activation of new magnetic easy axes as a result of stress anisotropy could be confirmed. A Barkhausen noise and eddy current microscope was extended with the RESTMAB such that local MRS distributions could be determined for the crack tips of fatigued samples.

# Zusammenfassung

Ziel dieser Arbeit ist die Bestimmung der Eigenspannung von metallischen Werkstoffen auf der Ebene der Korngröße, ermittelt als MRS durch magnetisches Barkhausenrauschen, für das RESTMAB als Ermittlungsverfahren empfohlen wird. Verglichen mit herkömmlichen elektromagnetischen Prüfverfahren ist der Referenzierungsprozess durch die Benutzung von RESTMAB signifikant vereinfacht. RESTMAB basiert auf zwei Merkmalen: erstens auf der Tatsache, dass die MBN-( $\sigma$ )-Kurve einen Extrempunkt hat, der sich unter Spannung ändert und der direkt mit dem MRS in Richtung der Spannung korreliert und zweitens, dass die MBN-( $\sigma$ )-Kurve einen linearen Verlauf vor dem Extrempunkt aufweist, deren Steigung unabhängig von der Eigenspannung ist. Die Interpretation der Ergebnisse basiert auf einem Kristallstrukturmodell eines Monokristalls, mit dem der physikalische Hintergrund der MBN-( $\sigma$ )-Kurve erklärt wird. Zu diesem Zweck wurden die magnetische Hysterese und die Magnetostriktion in-situ bestimmt. Die Ergebnisse zeigen, dass die Aktivierung von neuen magnetischen leichten Richtungen bezüglich der Spannungsanisotropie der Hauptgrund für dieses Verhalten ist. Veränderungen in der Domänenstruktur wurden in-situ mit dem Magnetkraftmikroskop gemessen und die Aktivierung der neuen magnetisch leichteren Richtungen konnte aufgrund von Spannungsanisotropie bestätigt werden. Das BEMI wurde um die RESTMAB-Methode erweitert, so dass die MRS-Spannungen an der Risspitze einer ermüdeten Probe bestimmt werden konnten.

## Table of Abbreviations

$\alpha$	Cosines of the angles between the crystal axes and the magnetization direction
$\gamma$	Cosines of the angles between the crystal axes and the stress
$\varepsilon$	Strain
$\theta$	Bragg scattering angle
$\lambda$	Magnetostriction / wavelength (only in Bragg's law)
$\lambda_s$	Saturation magnetostriction
$\mu_0$	Permeability of vacuum
$\nu$	Poisson's ratio
$\rho$	Density / dislocation density
$\sigma$	Stress
$\sigma_R$	Residual stress
$u$	Velocity of sound
$\phi$	Angle between the spins of electrons
$\psi$	Angle between the normal of the surface and the incident and the reflected beam of X-rays
$\omega$	Angular frequency
A	Exchange stiffness or exchange constant
a	Position of crack
B	Magnetic flux density
$B_r$	Remanence
BEMI	Barkhausen noise and eddy current microscope
d	Inter-planar spacing
DIC	Digital image correlation
DW	Domain wall
E	Young's modulus
$E_{ex}$	Exchange energy
$E_{mc}$	Magnetocrystalline energy
$E_{me}$	Magnetoelastic energy
$E_{ms}$	Magnetostatic energy
$E_w$	Domain wall energy
EBSD	Electron backscatter diffraction
FFT	Fast Fourier transformation
GMR	Giant magnetoresistance
H	Magnetic field strength

$H_c$	Coercivity
$H_d$	Demagnetization field
$H_{\text{eff}}$	Effective magnetic field
$J_{\text{ex}}$	Exchange integral
$K$	Stress intensity factor
$K_0, K_1, K_2, \dots$	Crystal anisotropy constants
$K_\sigma$	Stress anisotropy
$L_1$	Total length of vertical grid lines in a TEM image
$L_2$	Total length of horizontal grid lines in a TEM image
$M$	Magnetization
$M_a$	An hysteretic magnetization
$M_{\text{irr}}$	Irreversible magnetization
$M_{\text{MAX}}$	Maximum amplitude of Barkhausen noise
$M_s$	Saturation magnetization
MBN	Magnetic Barkhausen noise
MRS	Micro-residual stresses
$N$	Number of cycles
$N_d$	Demagnetization coefficient
$n_1$	Number of intersection points between vertical lines and dislocation lines
$n_2$	Number of intersection points between horizontal lines and dislocation lines
$R^2$	Coefficient of determination (regression analysis)
$r_0$	Radius of an atom
$r_{3d}$	Radius of the third shell of an atom
RESTMAB	Micro-residual stress mapping method based on magnetic Barkhausen noise
$S$	Spin of an electron
SEM	Scanning electron microscope
$t$	Thickness

# Table of Contents

1. Motivation and objectives .....	1
1.1. Introduction .....	1
1.2. Objectives .....	2
2. Theoretical background .....	4
2.1. Magnetic Barkhausen noise .....	4
2.1.1. Formation of a stable domain structure .....	6
2.1.2. Types of domain walls.....	10
2.1.3. Domain wall motion .....	11
2.1.4. Hindrances against domain wall motion .....	12
2.1.4.1. Interaction between inclusions and domain walls .....	12
2.1.4.2. Interaction between stress anisotropy and domain walls.....	13
2.2. Residual stress and its measurement methods .....	14
2.2.1. Definition of residual stress and its classifications .....	14
2.2.2. Residual stress measurement methods.....	17
2.2.2.1. X-ray diffraction .....	17
2.2.2.2. The synchrotron method .....	19
2.2.2.3. Neutron diffraction.....	19
2.2.2.4. The ultrasonic method.....	20
2.2.2.5. Magnetic Barkhausen noise .....	20
2.2.2.6. Summary .....	20
3. State of the art .....	22
3.1. Effect of stress on magnetic Barkhausen noise.....	23
3.2. Effect of the micro-structure on magnetic Barkhausen noise.....	51
3.3. Summary .....	51
4. Statement and approach.....	53
5. Materials, experimental methods and devices .....	58
5.1. Sample preparation .....	58

5.2. Devices .....	60
5.2.1. The micro-magnetic, multi-parameter, micro-structure and stress analysis device ....	60
5.2.1.1. The standard sensor of the micro-magnetic, multi-parameter, micro-structure and stress analysis system .....	62
5.2.2. Barkhausen noise and eddy current microscopy .....	63
5.3. Micro-magnetic methods.....	66
5.3.1. Harmonic analysis of the tangential magnetic field strength .....	66
5.3.2. Magnetic Barkhausen noise.....	66
5.3.3. Multi-frequency eddy current .....	67
5.3.4. Incremental permeability .....	68
5.3.5. Hysteresis measurement.....	69
5.3.6. Magnetostriction measurement.....	70
5.4. Experimental setups .....	71
5.4.1. Micro-magnetic characterization of non-deformed samples.....	71
5.4.1.1. Investigation of the micro-magnetic properties of non-deformed samples in an unloaded state .....	71
5.4.1.2. Investigation of the micro-magnetic properties of non-deformed samples in an elastically loaded state.....	72
5.4.2. Micro-magnetic characterization of plastically pre-deformed samples .....	76
5.4.2.1. Investigation of the micro-magnetic properties of pre-deformed samples in an unloaded state .....	76
5.4.2.2. Investigation of the micro-magnetic properties of pre-deformed samples in an elastically loaded state.....	76
5.4.3. Study of the domain structure of non- and pre-deformed samples in un- and elastically loaded states.....	77
5.4.4. Analysis of magnetic Barkhausen noise behaviour to find a new stress measurement method .....	77
5.4.5. Simulation of the magnetization changes due to residual stresses for a soft magnetic material and a hard magnetic material .....	78
6. Results .....	80

6.1. Micro-magnetic characterization of non-deformed samples .....	80
6.1.1. Investigation of the micro-magnetic properties of non-deformed samples in an unloaded condition.....	80
6.1.2. Investigation of the micro-magnetic properties of non-deformed samples in an elastically loaded condition .....	81
6.1.3. Study of the domain structure of non-deformed samples in elastically loaded conditions .....	88
6.2. Micro-magnetic characterization of plastically pre-deformed samples.....	90
6.2.1. Investigation of the micro-magnetic properties of pre-deformed samples in an unloaded condition.....	90
6.2.2. Investigation of the micro-magnetic properties of pre-deformed samples in an elastically loaded condition .....	94
6.2.3. Study of the domain structure of plastically pre-deformed samples in elastically loaded conditions .....	97
6.3. Modelling of the magnetization process under the effect of stress .....	101
7. Discussion .....	106
7.1. Micro-magnetic characterization of non-deformed samples .....	106
7.1.1. Investigation of the micro-magnetic properties of non-deformed samples in an unloaded condition.....	106
7.1.2. Investigation of the micro-magnetic properties of non-deformed samples in an elastically loaded condition .....	107
7.1.3. Study of the domain structure of non-deformed samples in an elastically loaded condition.....	111
7.2. Micro-magnetic characterization of plastically pre-deformed samples.....	114
7.2.1. Investigation of the micro-magnetic properties of pre-deformed samples in an unloaded condition.....	114
7.2.2. Investigation of the micro-magnetic properties of pre-deformed samples in an elastically loaded condition .....	117
7.2.3. Analysis of the domain structure of plastically pre-deformed samples under elastically loaded conditions .....	118
7.3. Modelling of the magnetization process under the effect of stress .....	119

7.4. The micro-residual stress mapping method based on magnetic Barkhausen noise.....	120
7.4.1. The peak shift method .....	121
7.4.2. The slope method.....	124
7.4.3. The calibration process of the Barkhausen noise and eddy current microscope for measuring micro-residual stresses.....	128
7.5. Applications of the calibrated Barkhausen noise and eddy current microscope using the micro-residual stress mapping method based on magnetic Barkhausen noise .....	132
7.5.1. High-resolution determination of micro-residual stress distributions.....	132
7.5.2. Measurement of the residual stress and size of the plastic zone in front of a crack tip .....	135
8. Summary and future work .....	142
8.1. Summary .....	142
8.2. Future work .....	144
References.....	145

# 1. Motivation and objectives

## 1.1. Introduction

In the design process of engineering components, several factors need to be considered. Structural failure and the parameters characterizing these are of major importance and need specific attention. Residual stress is one of those parameters, which may lead to failure in such components specifically when being superimposed by applied stresses due to operational loads resulting in a change of the component's lifetime, becoming detrimental when the lifetime is shortened. In practice, many components are not free from residual stresses after manufacturing and specifically the machining process. Therefore, the analysis of the change in residual stresses becomes vital to determine and/or estimate their effect on a component's lifetime combined with specific failure mechanisms. In general, residual stresses of Type I arise from misfits between different regions (e.g., after shot peening) or different parts (such as stresses in two riveted plates) or different phases of material (e.g., composite or multiphase steels like TWIP). A very common classification categorizes residual stresses into three types based on their characteristic length, which is defined as the length over which residual stresses equilibrate [Hauk. 1997, With. 2001, Tott. 2002]. Type I, or macro-residual stresses, which equilibrate over a whole sample (e.g., compressive stresses in a shot peening surface), Type II, or micro-residual stresses, which equilibrate over a number of grains (e.g., local stresses between two different phases), and Type III, or micro-residual-stresses, which equilibrate over a grain (e.g., stresses around dislocation and precipitates).

By means of modern analytical and simulation techniques, which can nowadays estimate the stresses of components during service, a question arises: why are stress measurement methods essentially in need? To answer this question, it should be mentioned that computational methods are not sufficient to predict failure in components, especially in complicated situations where residual stresses cause failure in combination with applied stresses. On the other hand, a

simulation can always only be as good as its inputs are. Thus, experimental stress measurement techniques are an essential instrument of validation. Overall, there are three types of measurement relating to destructive, semi-destructive and non-destructive stress measurements methods respectively (a brief description is presented in Chapter 2), where each one has its advantages and disadvantages. Among many stress measurement techniques and methods, only a few are widely used. X-ray diffraction (XRD) and hole drilling are the two most popular. The hole drilling method has an easy principle; however, it is a destructive method and has huge sources of error. On the other hand, although the XRD technique is non-destructive, it is essentially complicated and may lead to large errors as well. Moreover, it might be necessary to prepare a sample for performing the measurements. When the time consumption factor is added to the above disadvantages, a new non-destructive stress measurement method that is reliable, quick, low-cost and easy to use is in need. This need is further underlined when a map of stress distributions is required (e.g., stress distributions in front of a crack tip to investigate a crack-opening procedure), which many conventional stress measurement methods either are not able to do or else are very time consuming. The magnetic Barkhausen noise (MBN) method is a valuable candidate to measure residual stresses non-destructively because of its capability to measure and its sensitivity to residual stresses in general.

## 1.2. Objectives

Since the German physicist Heinrich Barkhausen discovered the magnetic Barkhausen effect in 1919, further research has been performed to present the sensitivity and capability of MBN with respect to micro-structure and residual stress changes. Especially since the 1970s, researchers have presented the sensitivity of MBN to stresses. From this time up to the present, the effect of stress on MBN and the detection of residual stresses using MBN have become an important subject for researchers. Apart from the capability and sensitivity to stress of MBN, the use of MBN for stress measurement has a substantial disadvantage, namely the need for and the complexity of calibration. Although some researchers [Yelb. 2010] have tried to propose easier calibration methods using the linearity of the MBN( $\sigma$ ) curve, this problem still has no satisfactory solution. To find a method for measuring micro-residual stresses, the behaviour of MBN under elastic and plastic deformation in situ has been investigated.

The objective of this work is to propose a non-destructive approach called the “local micro-residual stress mapping method based on **m**agnetic **B**arkhausen noise” (RESTMAB), which requires minimal calibration effort. The RESTMAB is also proposed for a Barkhausen noise and eddy current microscope (BEMI), which has been used as equipment to develop and validate the

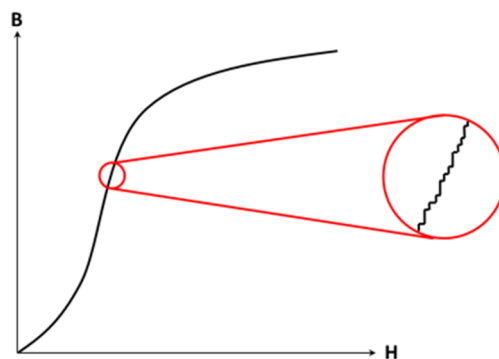
RESTMAB on the basis of the high-resolution measurement of local micro-residual stresses around a crack tip.

To achieve this objective, two steps need to be carried out: 1) to study the behaviour of the MBN under the elastic and plastic deformation of non- and pre-deformed ferromagnetic steels, and 2) to investigate the physical reason behind the MBN's behaviour under stress.

## 2. Theoretical background

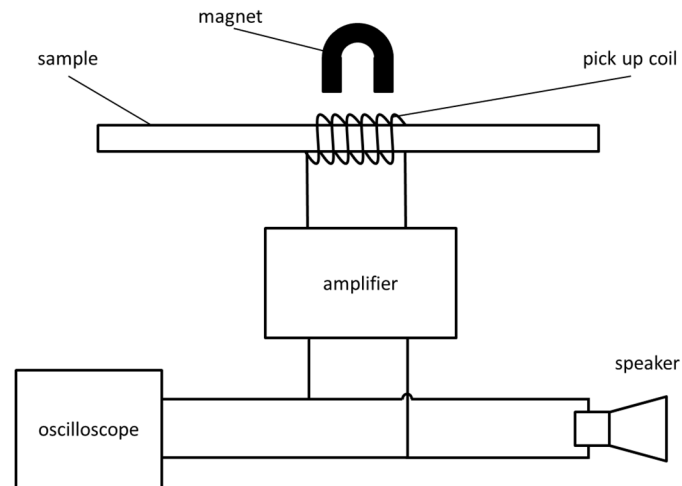
### 2.1. Magnetic Barkhausen noise

The magnetic structure of ferromagnetic materials consists of domains separated from each other by domain walls (DWs). When a magnetization process of a ferro- or paramagnetic material takes place, a hysteresis curve establishes while the DWs move. This movement is random, irreversible and discontinuous rather than smooth (Figure 2.1). Heinrich Barkhausen discovered this phenomenon in 1919 [Bark. 1919].



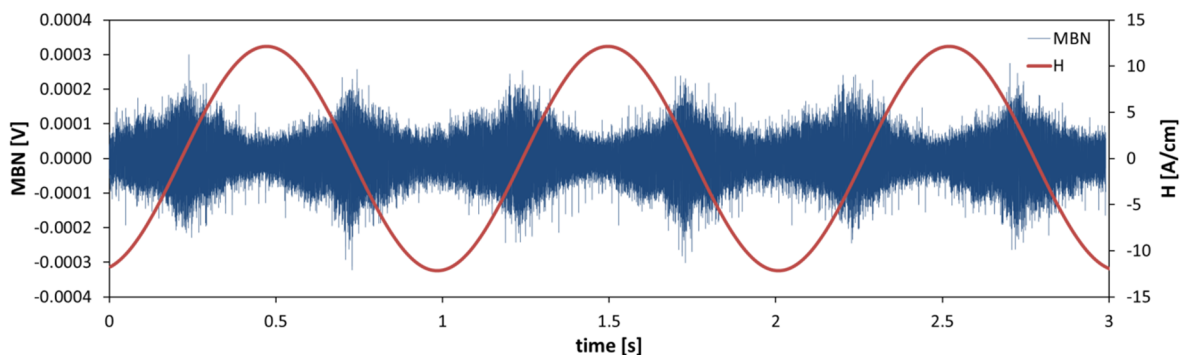
**Figure 2.1: The Barkhausen effect presented at the initial magnetization curve (maximized: discontinuous curve progression due to the discontinuous DW motion).**

Figure 2.2 shows the simple setup for detecting the MBN which Barkhausen originally used.



**Figure 2.2: Barkhausen's original setup to detect MBN.**

As can be seen in Figure 2.2, a pick-up coil is wound around a sample and connected to an amplifier and a speaker. The sample is then subjected to an increasing magnetic field. What can be heard through the speaker is an interrupted noise, regardless of whether the magnetic field is smoothly increased or reversed. If an oscilloscope is directly connected to a pick-up coil, irregular noise is observed as a voltage-time function (Figure 2.3). This voltage noise is known as Barkhausen noise.



**Figure 2.3: MBN (blue signal) and magnetic field input (red signal).**

The voltage induced in the pick-up coil is proportional to the first derivative of the flux density  $dB/dt$ , such that it is higher when the magnetization curve becomes steeper (Figure 2.3). A demagnetized sample consists of several magnetic regions (called magnetic domains) in which the magnetization is in a uniform direction. This means that the magnetic moments of the atoms within a domain are aligned in the same direction. This direction is called the magnetization direction ( $M_s$ ) of the domain. The rotation of the magnetization vector ( $M_s$ ) from one direction to another has been proposed as a reason for MBN, but recently it has become known that a sudden jump of the DW from one position to another is the source of MBN [Will. 1949]. In other words, a ferromagnetic material - which is not magnetized - has a large number

of domains in which the magnetization directions are randomly oriented. Therefore, the magnetic fields of the different domains mainly compensate each other, and the resulting magnetic force of the bulk can be considered as demagnetized (Figure 2.4a). When the bulk is subjected to an external magnetic field, domains - which are closely aligned to the direction of the external magnetic field - increase their volume (Figure 2.4b) while they vanish.

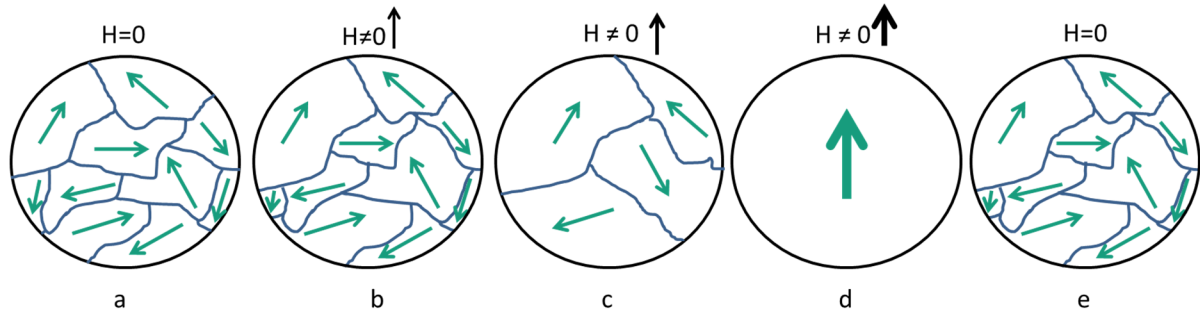


**Figure 2.4: Schematic domain structure of a ferromagnetic material and its variation during the magnetization process: a) demagnetized state, b) domain structure at a low magnetic field, c) domain structure at a high magnetic field strength, d) domain structure in a saturated state, e) domain structure in a remanence state.**

The process of domain growth happens gradually with DW motion (Figure 2.4c) until a saturation point, where all the domain magnetization directions turn into the direction of an external magnetic field (Figure 2.4d) [Cull. 2009].

When an external magnetic field is removed, the DWs do not necessarily return to their original position (Figure 2.4e). This is because the DWs interact with pinning sites. This phenomenon can be described with an energy equation based on the energy equilibrium of a DW, which is described in Section 2.1.1.

### 2.1.1. Formation of a stable domain structure

The formation of a DW occurs when the five basic energies involved in ferromagnetism are minimized (Equation 2.1) [Cull. 2009, Stef. 2008],

$$E = E_{ex} + E_{ms} + E_{mc} + E_{me} + E_w$$

**Equation 2.1**

where  $E_{ex}$ ,  $E_{ms}$ ,  $E_{mc}$ ,  $E_{me}$  and  $E_w$  are the exchange, magnetostatic, magnetocrystalline, magnetoelastic and wall energies, respectively, which are explained in more detail below.

The exchange energy  $E_{ex}$  depends on the relative orientation of the spins of two electrons. The term exchange comes from the position of the electrons where they turn around the protons. When two atoms are adjacent, the electrons of each atom may exchange their positions. The exchange energy  $E_{ex}$  is calculated by Equation 2.2 [Cull. 2009],

$$E_{ex} = -2J_{ex}S_iS_j = -2JS_iS_j \cos \varphi$$

**Equation 2.2**

where  $J_{ex}$  is the exchange integral,  $\varphi$  is the angle between the electrons and  $S$  is the spin of the different electrons. When  $J_{ex}$  is positive, like in ferromagnetic materials, then the minimum of  $E_{ex}$  occurs when all the spins are parallel. Figure 2.5 shows the Bethe-Slater curve, which presents the variations of the exchange integral  $J_{ex}$  with the ratio of  $r_a/r_{3d}$  where  $r_a$  is the radius of an atom and  $r_{3d}$  is the radius of the third shell of electrons.

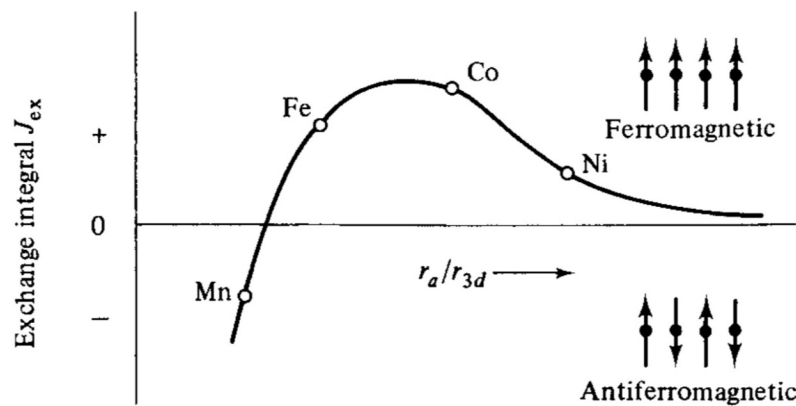


**Figure 2.5: Bethe-Slater curve (schematic) [Cull. 2009].**

The behaviour of the magnetostatic energy  $E_{ms}$  is described in Figure 2.6. When a ferromagnetic material is magnetized through a magnetic field to Level A and then the applied field is removed, the magnetization will be in Level C because of the demagnetizing field  $H_d$  which comes from the remanence of the magnetic field (Figure 2.6). In this situation, the sample contains magnetostatic energy  $E_{ms}$ , which is equal to the shaded area in Figure 2.6. Equation 2.3 [Cull. 2009] shows that  $E_{ms}$  is related to the magnetization  $M$  and the demagnetizing field strength  $H_d$ . Since  $H_d$  is directly related to the shape of the sample,  $E_{ms}$  reaches a minimum when the magnetization direction of a domain is parallel to the external magnetic field [Cull. 2009, Stef. 2008, Bozo. 1993],

$$E_{ms} = -\frac{1}{2}\vec{H}_d \cdot \vec{M} = \frac{1}{2}\mu_0 N_d M^2$$

Equation 2.3

where  $N_d$  is the demagnetization coefficient,  $\mu_0$  is the permeability of the vacuum and  $M$  is the magnetization.

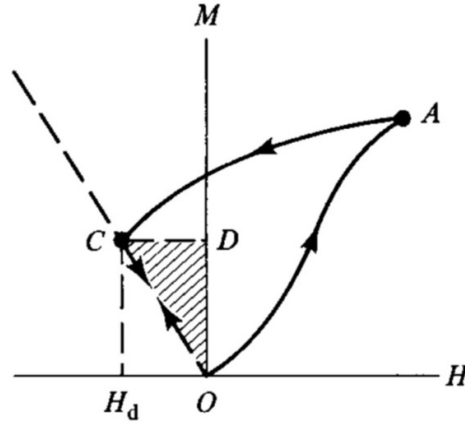


Figure 2.6: Magnetostatic energy ( $E_{me}$ ) of a magnetized sample when the applied field is zero [Cull. 2009].

The anisotropy of a crystal is mainly caused by spin-orbit coupling. When the spin of an electron is forced to reorient because of an external magnetic field, the orbit of that electron needs to reorient as well. Since the orbit is strongly coupled with lattice, the energy required to turn the electron spin depends on the lattice directions. In fact, the magnetocrystalline energy  $E_{mc}$  (Equation 2.4) is the energy required to overcome spin-orbit coupling [Cull. 2009]. Therefore, the magnetization in different crystallographic directions is different because of magnetocrystalline anisotropy (Figure 2.7).  $E_{mc}$  reaches a minimum when the magnetization direction of a domain aligns with the direction of the magnetic easy axis.  $E_{mc}$  is formulated as below,

$$E_{mc} = K_0 + K_1(\alpha_1^2\alpha_2^2 + \alpha_2^2\alpha_3^2 + \alpha_3^2\alpha_1^2) + K_2(\alpha_1^2\alpha_2^2\alpha_3^2) + \dots$$

Equation 2.4

where  $K_0$ ,  $K_1$  and  $K_2$  are material constants at particular temperatures (room temperature), and  $\alpha_1$ ,  $\alpha_2$  and  $\alpha_3$  are the cosines of the angles between the crystal axes and the magnetization direction  $M_s$ .

When a specimen is subjected to an external magnetic field, its dimensions change due to the rearrangement of the domains. This is called magnetostriction. The amount of magnetostrictive

strain in a certain direction depends on the magnetization direction. When a sample is exposed to an external stress, new strains apply to the crystal which are expected to change the magnetization direction. Therefore, in this case, the direction of magnetization is controlled by crystal anisotropy and the stress  $\sigma$ . The magnetoelastic energy  $E_{me}$  involves the magnetostrictive strains and stress given by Equation 2.5 [Cull. 2009],

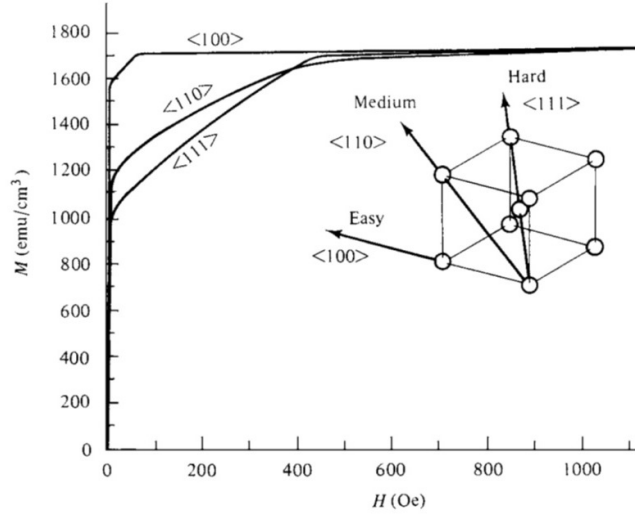


**Figure 2.7: Magnetization curves for single crystals of iron in different directions [Cull. 2009].**

$$E_{me} = -\frac{3}{2}\lambda_{100}\sigma(\alpha_1^2\gamma_1^2 + \alpha_2^2\gamma_2^2 + \alpha_3^2\gamma_3^2) - 3\lambda_{111}\sigma(\alpha_1\alpha_2\gamma_1\gamma_2 + \alpha_2\alpha_3\gamma_2\gamma_3 + \alpha_3\alpha_1\gamma_3\gamma_1)$$

**Equation 2.5**

where  $\gamma_1$ ,  $\gamma_2$  and  $\gamma_3$  are the cosines of the angles between the crystal axes and the stress  $\sigma$ , and  $\lambda_{100}$  and  $\lambda_{111}$  denote saturation magnetostriction in the  $\langle 100 \rangle$  and  $\langle 111 \rangle$  directions, respectively. Therefore, the deformation of the lattice, which causes the domain to elongate in the magnetization direction, makes  $E_{me}$  a minimum.

The wall energy  $E_{wall}$  is related to the energy per unit area of the surface and the thickness of the DW due to the different atomic moments in the DW, the latter of which is not parallel to the easy axis. The magnetic easy direction is the crystal direction, which is energetically favourable for the magnetic moment to align. Figure 2.8 shows a schematic structure of the DW. Since spins within a DW align in a non-easy direction, the crystal anisotropy of the wall is higher than the domain around the wall. Therefore, the crystal anisotropy tries to make the DW as small as possible to reduce the spins so as to align with the non-easy axis. On the other hand, exchange energy tends to make the DW as thick as possible to reduce the angle between the spins in the

DW and the adjacent domain. Finally,  $E_{wall}$  is obtained from the equivalent between the effect of the crystal anisotropy and the exchange energy on the DW.

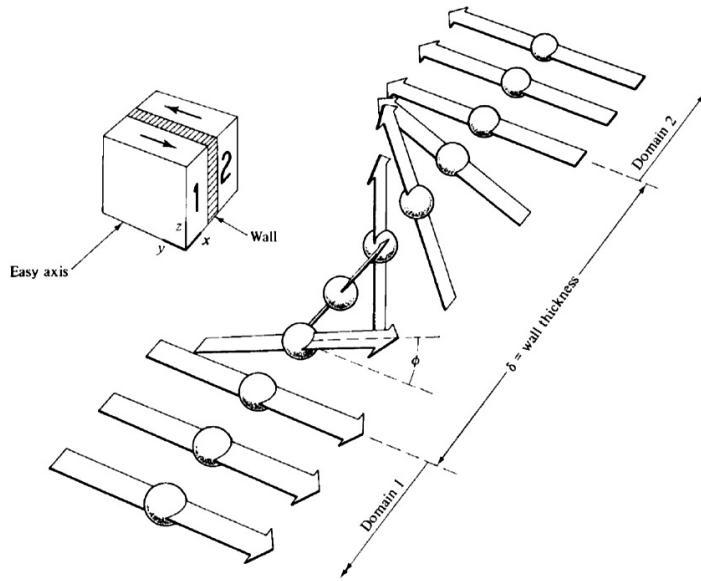


**Figure 2.8: Schematic structure of a 180° DW [Cull. 2009].**

In summary, a certain domain formation happens when the sum of those five energies (Equation 2.1) is minimized [Cull. 2009, Stef. 2008]. The DW motion can also be described with the energy equilibrium. Prior to explaining the DW motion, it is necessary to know the types of DWs.

### 2.1.2. Types of domain walls

In general, there are two types of DWs which are defined by the angle between the magnetization vectors  $M_s$  in two adjacent domains: these are 180° and non-180° (or 90°) DWs. In a 180° DW, the magnetization directions of the domains are parallel in two adjacent domains which  $M_s$  points out through opposite directions (Figure 2.9). In a non-180° DW, which may be called 90° DWs, the angle between the magnetization directions in two adjacent domains is generally 90°. 90° DWs have two typical configurations. In the first configuration, the magnetization directions  $M$  of adjacent domains are parallel to the wall (Figure 2.9a), while in the second configuration the magnetization directions build a 45° angle with the DW line (Figure 2.9b and c). The surface energies of 180° and 90° DWs are given in Equation 2.6 for cubic crystal structures,

$$E_{cubic}^{180} = 2 \times E_{cubic}^{90} = 4\sqrt{AK_1}$$

**Equation 2.6**

where  $E$  is the surface energy of the DW,  $A$  is the exchange stiffness or exchange constant and  $K_1$  is the crystal anisotropy constant, respectively. Since the surface energy of  $180^\circ$  DWs is higher than for  $90^\circ$  DWs,  $90^\circ$  DWs are energetically more stable than  $180^\circ$  DWs and more energy is therefore asked to move them [Cull. 2009].

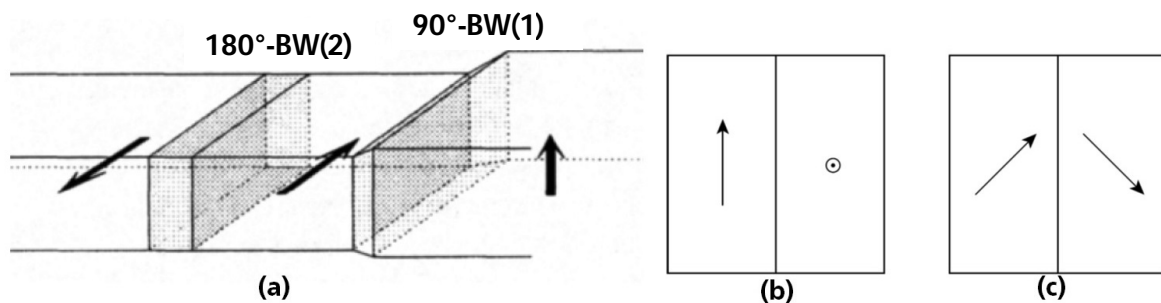


Figure 2.9:  $180^\circ$  (a) and  $90^\circ$  (b and c) types of DWs [Cull. 2009, Hauk. 1997].

### 2.1.3. Domain wall motion

As previously described, the magnetization process originates from discontinuous and irreversible movements of the DWs. DW motion can simply be described by means of the energy of the system. Figure 2.10 shows the variation of the single energy  $E$  with a changing wall position  $x$ . Assume that there is no external magnetic field. In this situation, the DW maintains itself at Position 1 which has minimum energy (Figure 2.10). When the magnetic field increases, the wall moves to Position 2, which has a maximum gradient energy (maximum restoring energy). If the applied magnetic field is removed, the DW goes back to Position 1 again, but if the applied field further increases, DW jumps to Position 3. This is what is considered to be the basis of Barkhausen noise. Now, if the applied field is removed, the DW moves to the nearest minimum energy position, which is Position 4 instead of Position 1. Therefore, the Barkhausen jump is an irreversible movement. Several micro-structural features influence the movement of the DW, or in other words there are some hindrances against DW movements, which are explained below in Section 2.1.4.

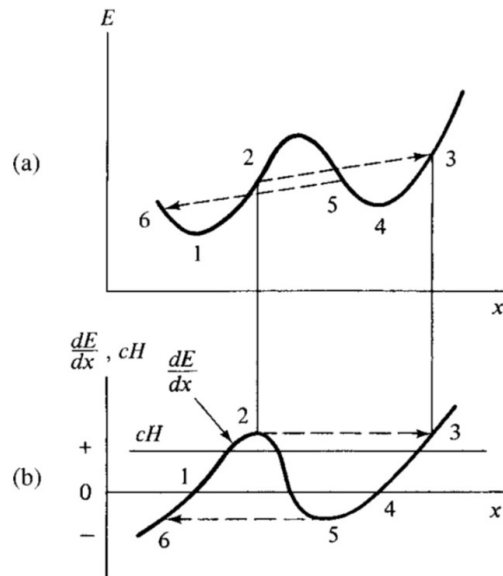


Figure 2.10: Changes of the energy of a system  $E$  with a wall motion  $x$  [Cull. 2009].

## 2.1.4. Hindrances against domain wall motion

In general, a DW is restricted by two different types of hindrances: 1) inclusions, and 2) stress anisotropy. Hindrances of DW motion result from interaction with inclusions and stress anisotropy, which are described in the following sections.

### 2.1.4.1. Interaction between inclusions and domain walls

The hindrance of DWs by inclusions is due to the change of the wall energy and the magnetostatic energy of a DW attached to an inclusion. The attachment of the DW to an inclusion causes magnetostatic energy to drastically decrease, although it increases the DW energy by the creation of two small domains (Figure 2.11a). This situation is the favourable position for the DW. When an external magnetic field is applied, the DW moves to the right in Figure 2.11 b, which results in spike domains. The magnetostatic energy still controls the position of the DW despite the DW energy being increased by an increase of the DW area. If the magnetic field is removed, the wall goes back to the previous situation (reversible motion), but if the magnetic field increases the extra energy applied to the system resulting from the DW area will be too big, which leads to a decrease of this energy when the DW jumps to the nearest minimum energy position (Figure 2.11c and d). This jump is a Barkhausen jump and is irreversible.

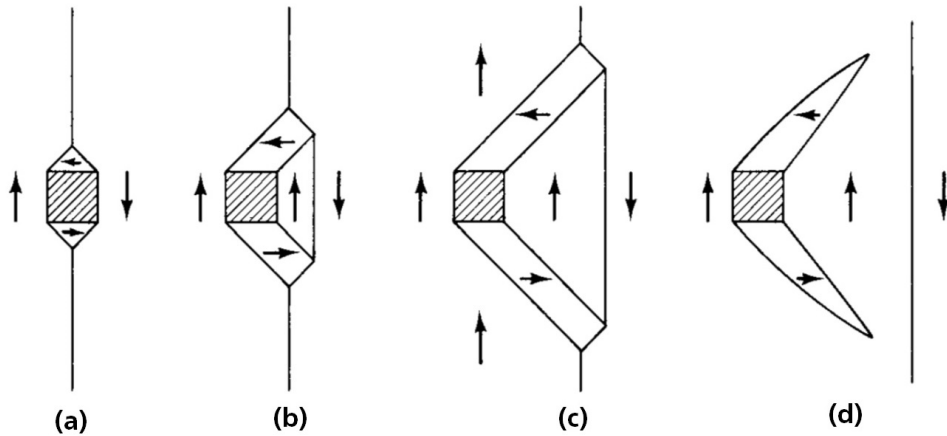


Figure 2.11: Passage of a DW through an inclusion [Cull. 2009].

It should be noted that the size of an inclusion is important for the hindrance mechanism of DWs. Inclusions with dimensions smaller than the DW thickness cause the DW energy to decrease and have a minor effect on DW motion, while inclusions with dimensions bigger than the DW thickness tend to stick to the DW while additionally creating side domains and decreasing the magnetostatic energy.

#### 2.1.4.2. Interaction between stress anisotropy and domain walls

Stress can change the energy equilibrium of a system similarly to the applied magnetic field. Two energy terms - a magnetocrystalline one and a magnetoelastic one - compete to control the energy equilibrium in the system by determining the easy axis of magnetization. Since relatively high applied stresses are required to change the magnetic easy axis, the minimum energy of the system is reached when the domain structure is rearranged through DW motion. DW motion in the presence of stress (residual or external) depends on the type of DW.  $90^\circ$  DWs dominate because of their tendency to impose an elastic distortion (magnetostrictive strain) in the volume. Furthermore, the motion of a  $90^\circ$  DW causes a change in the magnetization direction  $M$  of the domain, since the magnetization direction of two adjacent domains with  $90^\circ$  DWs is different. On the other hand, applied stress also imposes a stress distortion on the material. Therefore, the interaction of these two kinds of distortions makes the motion of  $90^\circ$  DWs difficult. The motion of  $180^\circ$  DWs is easier in the presence of stress when compared with the  $90^\circ$  DWs. Although the magnetization direction  $M$  changes when a  $180^\circ$  DW moves, there is no magnetostrictive strain in the volume because of the  $180^\circ$  DW. Thus, the effect of stress on the motion of the  $180^\circ$  DW is just sufficient to increase the energy of the DW by adding magnetoelastic energy.

As previously discussed, there are generally two types of hindrances of DW motions, namely inclusions and stresses. In fact, there are some other parameters too that can affect DW motion, which can be categorized in terms of one of the two hindrance types described below.

Dislocation is one of these parameters for which the effect on DWs and any resulting domains should be discussed in particular. Dislocations can be created even at elastic stresses that are lower than the yield point. This is because of non-uniform deformations of different grains which align in different directions relative to the applied stress. Most dislocations created below the yield point are concentrated on grain boundaries, which imposes elastic strain fields. These fields cause the energy equilibrium of DWs to change in such a way that more domains arise in the grain boundaries. Therefore, the MBN increases with an increase in dislocations. It should be taken into account that the grain size and the number of dislocations in a sample also affect the MBN. When stress is increased and the sample is yielded, a massive number of dislocations are created inside the grain whereby at high strains dislocation tangles will form. Such dislocation and dislocation tangles have an elastic strain field which works as a hindrance point for the DW motion.

Grain boundaries also directly affect DW motion. These work as a pinning site of the DW. A smaller grain size results in more grain boundaries, which on the one hand act as pinning sites while on the other hand they cause the formation of more domains per area. It is reported that, normally, samples with smaller grains exhibit higher MBN signals [Cull. 2009].

The micro-structure is another factor which directly affects DW motion. It is obvious that precipitations with different shapes and compositions interact differently with DWs. In general, bigger precipitates - being big in size - are the stronger pinning sites for DW motion. In other words, the ratio of the precipitation thickness to the DW thickness has a direct effect on DW motion.

## **2.2. Residual stress and its measurement methods**

### **2.2.1. Definition of residual stress and its classifications**

Residual stresses are those stresses remaining inside a material when the material is not subjected to external stresses. The origin of a residual stress can be elastic-plastic deformation, thermal gradient and phase transformation. There are two different common definitions for residual stress classification. One categorizes residual stresses into two groups: macro- and micro-residual stresses [With. 2001a]. Figure 2.12 presents how each of the two different situations is generated. In other publications, residual stresses are divided into the following

three types: Type I ( $\sigma^I$ ), Type II ( $\sigma^{II}$ ) and Type III ( $\sigma^{III}$ ) [Hauk. 1997, With. 2001, Tott. 2002]. The first type - or macro-residual stress - is the volume average which is affected by a large number of grains. Type II - or micro-residual stress - comes from the heterogeneity of grains in polycrystalline materials and is defined as the mean stress value inside a grain. Type III - or micro-residual stress - contains all those stress distributions inside a grain caused by crystalline defects such as vacancies, dislocations, twinning and grain boundaries. Figure 2.13 shows a schematic summary of the three types of stress.

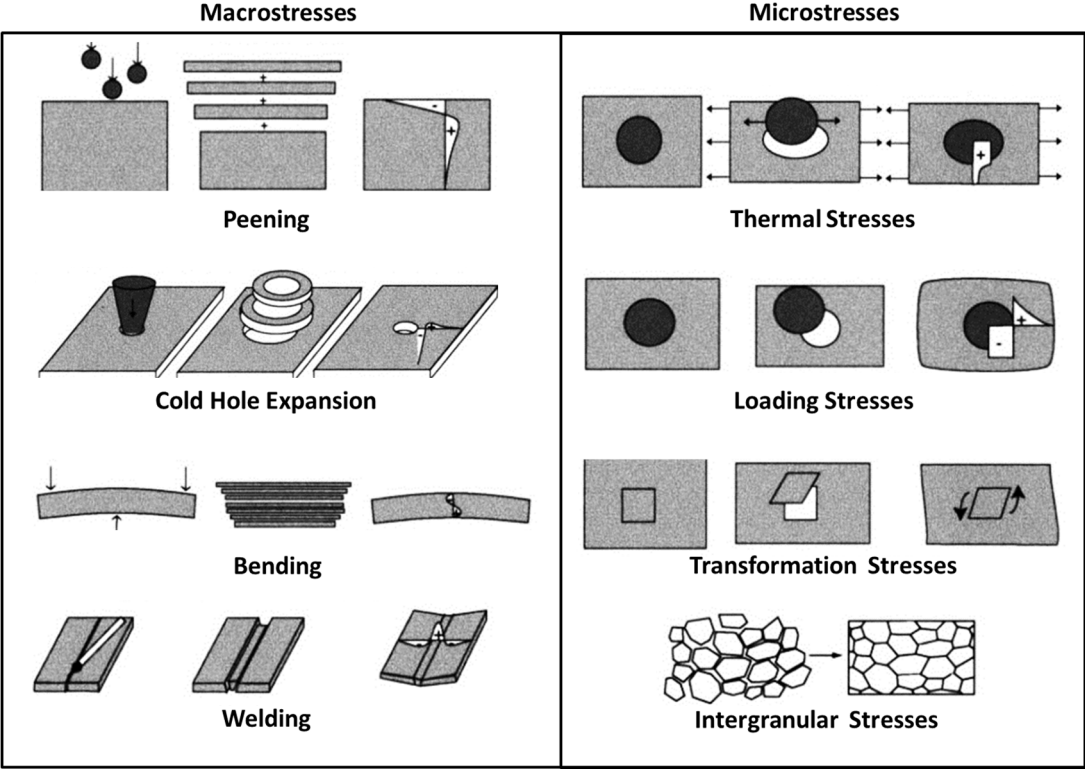


Figure 2.12: Different types of macro- and micro-residual stresses and their origins [With. 2001a].

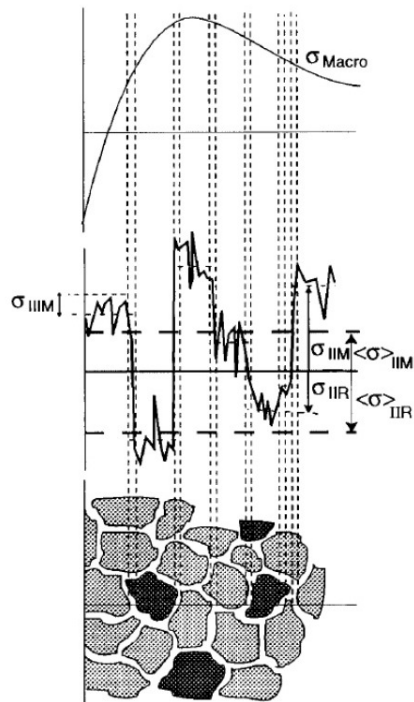


Figure 2.13: Different types of residual stresses. Residual stress Type I is comparable to the fraction of the material. Type II is comparable to the grain size and Type III is comparable to less than the grain size [With. 2001a].

Residual stresses can affect the performance of a material in different situations. Figure 2.14 shows areas which residual stresses affect directly. Therefore, the measuring and monitoring of residual stresses helps the material's behaviour under service conditions to be estimated.

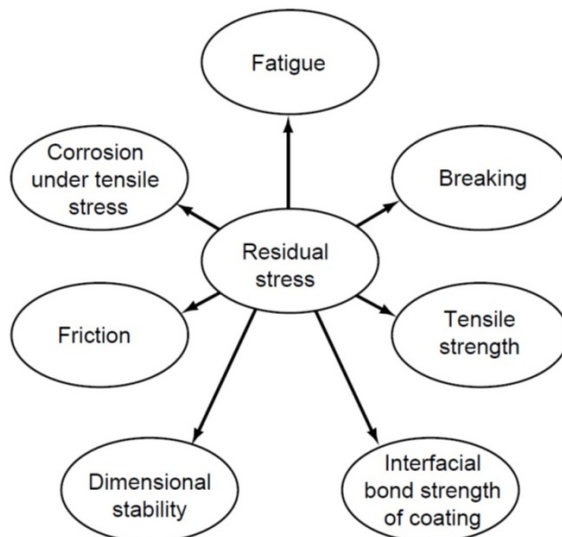


Figure 2.14: Material performance characteristics directly affected by residual stresses [Tott. 2002].

### 2.2.2. Residual stress measurement methods

There are several methods for measuring residual stresses which are broadly divided into the three categories, namely destructive, semi-destructive and non-destructive methods. Destructive methods are based on the sectioning of a sample to redistribute the residual stress. The residual stress is measured via a strain gauge. Semi-destructive methods are similar to the destructive ones, but just a small portion of the sample will be destroyed in which components may be repaired after the residual stress measurements. Non-destructive methods in no way affect any condition of the sample. Non-destructive methods are based on the measurement of the atomic lattice strain. Figure 2.15 shows residual stress measurement methods and their relevant spatial resolutions and penetration depths. A detailed discussion of all these methods is beyond the scope of this thesis and reference is, therefore, made to the relevant literature [Hauk, 1997, Tott. 2002, With. 2001a, With. 2001b]. However, the non-destructive testing methods of residual stress measurements will be addressed here.

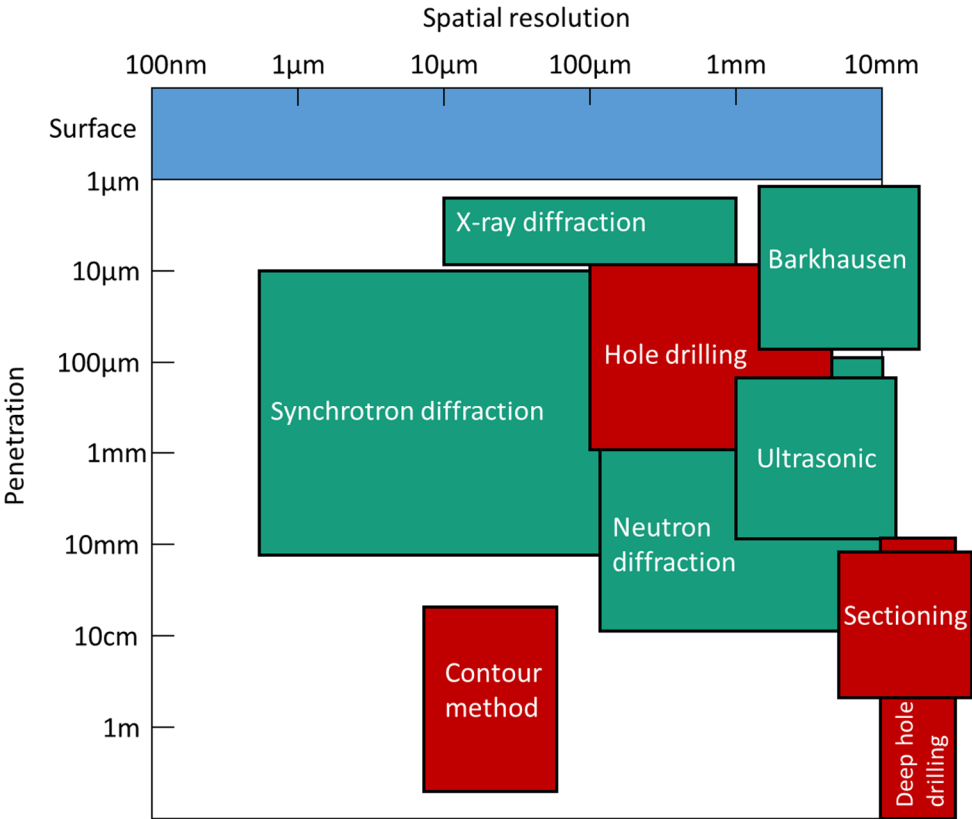


Figure 2.15: Different residual stress measurement methods with their measurement depths and spatial resolutions. Destructive methods are red and non-destructive ones are green [Ross. 2012].

#### 2.2.2.1. X-ray diffraction

The XRD method is a widely used technique for residual stress measurement. The basis of this technique can be simply described by Bragg’s law (Equation 2.7) [Hauk. 1997, Tott. 2002]. A

change in the inter-planar spacing  $d$  can be calculated when the incident wavelength  $\lambda$  and the Bragg scattering angle  $\theta$  are known. By use of the inter-planar spacing  $d$ , the elastic strain can be detected (Equation 2.8) [Hauk. 1997, Tott. 2002, Prev. 1986]. The strain  $\varepsilon$  can be converted to stress when Young's modulus is known:

$$\lambda = 2d \sin \theta$$

**Equation 2.7**

$$\varepsilon = \frac{\Delta d}{d} = -\cot \theta \Delta \theta$$

**Equation 2.8**

Figure 2.16 shows the diffraction of an X-ray beam at a diffraction angle of  $2\theta$  from the surface of the sample for two orientations of the sample relative to the X-ray beam.  $\psi$  is the angle between the normal of the surface and the incident and the reflected beam. The wavelength of the X-ray beam produced by metallic targets is known (depends on the X-ray target in the XRD device). Therefore, a  $2\theta$  angle for stress-free samples is also known. Any changes in the inter-planar spacing  $d$  which come from stress cause  $2\theta$  to change. The easiest model for measuring stress using XRD is the plane-stress elastic model. In this model, it is assumed that there are two principal stresses in the plane and no stress perpendicular to it. Based on the definitions in Figure 2.17 [Prev. 1986], the stress in the plane at any  $\varphi$  ( $\sigma_\varphi$ ) is given by

$$\sigma_\varphi = \left( \frac{E}{1 + \nu} \right)_{(hkl)} \frac{1}{d_0} \left( \frac{\partial d_{\varphi\psi}}{\partial \sin^2 \psi} \right)$$

**Equation 2.9**

where  $E$  and  $\nu$  are Young's modulus and Poisson's ratio, respectively. The stress of the sample can be calculated using Equation 2.9 by means of drawing the inter-planar spacing  $d$  versus  $\sin^2 \psi$  and determining the slope of the line.

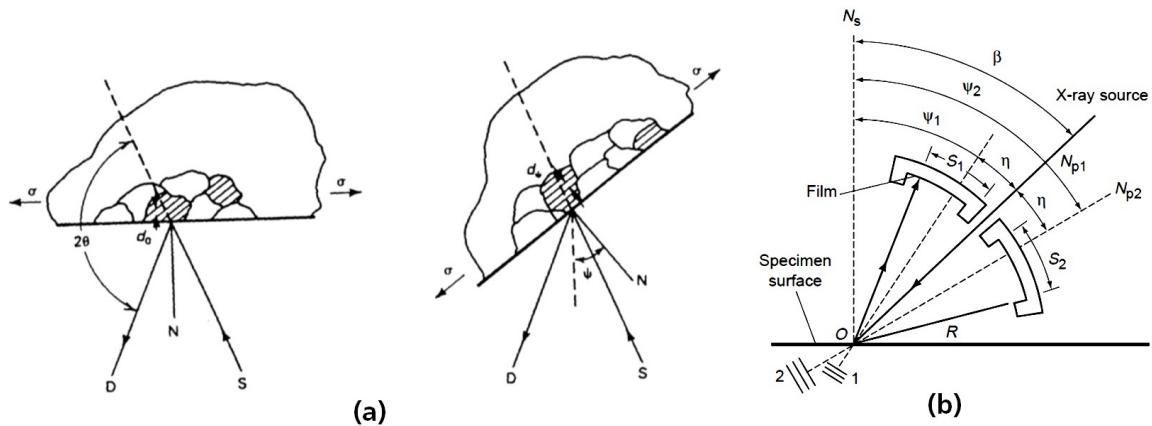


Figure 2.16: a) XRD of a grain from a different rotation sample angle ( $\psi$ ). b) Simple arrangement of an XRD measurement [Prev. 1986].

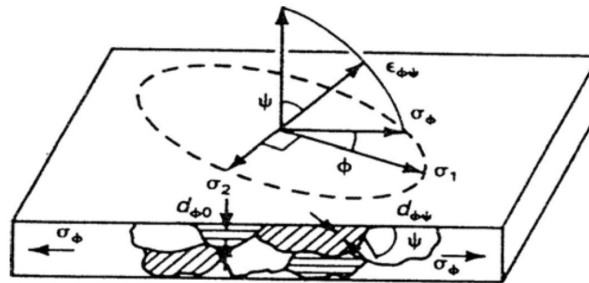


Figure 2.17: XRD measurements based on the plane stress elastic model [Prev. 1986].

### 2.2.2.2. The synchrotron method

Synchrotron - or hard X-ray - is essentially an XRD method which uses much higher energy X-ray beams (20-300 keV) and can, therefore, penetrate thousands of times further into the sample. In summary, it is faster and has a higher resolution than any conventional X-ray technique [With. 2001a].

### 2.2.2.3. Neutron diffraction

The neutron diffraction method is also very similar to the X-ray method, only that neutrons are used instead of X-ray beams [With. 2001a]. The scattering properties of neutrons are different from X-rays; therefore, neutrons and XRDs have complementary information. The advantage of neutrons in comparison to X-rays is the high penetration depth of neutrons. This allows a broader range of materials to be tested, such as higher atomic number materials where X-ray penetration is very slight.

#### 2.2.2.4. The ultrasonic method

The ultrasonic method is based on the acoustic elasticity effect where the velocity of the elastic wave propagation in solids depends on the stresses in the sample [Tott. 2002, With. 2001]. Equation 2.10 [With. 2001a] shows the relation between the velocity of sound in a material  $v$  and a strain  $\varepsilon$ .

$$v = \sqrt{\frac{E}{\rho} \left[ 1 + \frac{c}{2E} \varepsilon \right]}$$

Equation 2.10

where  $E$  is the elastic modulus,  $\rho$  is the density and  $c$  is the third-order of an anharmonic constant in a simplified anharmonic stress-strain law, written as  $\sigma = E\varepsilon + C\varepsilon^2$ . This is valid for longitudinal as well as transversal waves, even though longitudinal waves are commonly used. High penetration of depth, low cost, speed and portability are the main advantages of the ultrasonic method. Nevertheless, its disadvantages are its sensitivity to the micro-structure, which makes it difficult to separate the effect of stress and the micro-structure. Moreover, the measurement of the macro-stresses of a sample over the material volume makes measurement of micro-stresses nearly impossible.

#### 2.2.2.5. Magnetic Barkhausen noise

MBN is another non-destructive method for measuring stress so far as the micro-structure is known, and which is the subject of this thesis. As mentioned before, MBN is based on DW jumps which are affected by stress. In general, a calibration process is required for estimating stresses quantitatively. In Section 2.1, the basics of MBN are explained. Furthermore, the effect of stress on MBN will be elaborated in further detail in Chapter 3.

#### 2.2.2.6. Summary

In conclusion, Table 2.1 presents a summary of the advantages and disadvantages of non-destructive stress measurement methods.

**Table 2.1: Brief comparison of the residual stress measurement methods and their advantages and disadvantages [Ross. 2012].**

Technique	Advantage	Disadvantage
X-ray diffraction	Ductile Generally available Wide range of materials Hand-held systems Macro and Micro RS	Lab-based systems Small components Only basic measurements
Hole Drilling	Fast Easy use Generally available Hand-held Wide range of materials Macro and Micro RS	Interpretation of data Semi destructive Limited strain sensitivity and resolution
Neutron Diffraction	Optimal penetration and resolution 3D maps	Only specialist facility Lab-based system
Barkhausen Noise	Very quick Wide sensitive to Microstructure effects especially in welds Hand-held	Only ferromagnetic materials Need to divide the microstructure signal from that due to stress
Ultrasonic	Generally available Very quick Low cost Hand-held	Limited resolution Bulk measurements over whole volume
Sectioning	Wide range of material Economy and speed Hand-held	Destructive Interpretation of data Limited strain resolution
Contour	High-resolution maps of the stress normal to the cut surface Hand-held Wide range of material Larger components	Destructive Interpretation of data Impossible to make successive slices close together
Deep hole drilling	Deep interior stresses measurement Thick section components Wide range of material	Interpretation of data Semi destructive Limited strain sensitivity and resolution
Synchrotron	Improved penetration and resolution of X-rays	Only specialist facility Lab-based systems
	Depth profiling Fast Macro and micro RS	

### 3. State of the art

MBN is sensitive to several and varied parameters which affect the domain structure and DW motion. Seeger classified the factors affecting MBN into three categories, namely [Seeg. 1966]:

- Geometry and magnetization parameters;
- Micro-structure;
- Stresses.

Geometry parameters, such as thickness, sharp edges, the demagnetization effect and the surface condition, affect the magnetization process of samples [Bert. 1998, Cull. 2009, Jile. 1998]. Besides these, the magnetization amplitude, magnetization frequency and magnetization waveform also influence the magnetization process [Bozo. 1993]. It should be noted that the temperature and the magnetization direction [Cull. 2009] play a further role in the magnetization of a ferromagnetic material.

The effect of micro-structural parameters has been also investigated in many publications. Micro-structural parameters, such as different phases and precipitates [Altp. 2009], dislocation densities and dislocation tangles [Kas. 2013], grain boundaries and grain sizes [Moor 1997b], chemical composition [Moor. 1997a,b], the magnetic history of the material [Bozo. 1993] and crystal anisotropy [Cull. 2009, Jile. 1998, Stef. 2000], affect the domain structure and DW motion directly.

Stress is another factor which affects the magnetization process of the sample. The effect of applied stresses [Lind. 2001, Lind. 2003a], residual stresses [Altp. 2009, Rabu. 2014, Lind. 2003b] and stress anisotropy on the magnetization process have been reported in several of the publications referenced.

As mentioned above, plenty of publications have investigated the parameters affecting the magnetization process, and consequently MBN. A list of these parameters is presented in

Table 3.1. In other words, the MBN signal is a function of several parameters (MBN = f(geometry and magnetization parameters, micro-structure, stresses)) which makes it significantly difficult to simultaneously investigate all the parameters affecting MBN. Therefore, one should always choose one parameter to investigate solely while the others are kept constant and hence under control. Since this thesis focuses on measuring stresses by means of MBN, this section presents a literature review with respect to the effect of stresses on MBN. The first part presents the work published with respect to the effect of strain (elastic and plastic) and stress (applied and residual) on MBN. In the second part, the effects of the micro-structure as well as dislocation and grain size are presented. The aim of this chapter is firstly to review the published articles in which the effect of stress on MBN is presented, and secondly to summarize the results presented and the reasons for MBN behaviour under applied and residual stresses.

**Table 3.1: List of parameters which influence MBN.**

Parameters affecting MBN		
Geometry and magnetization parameters	Microstructural parameters	Stresses
thickness sharp edges demagnetization effect surface condition magnetization amplitude magnetization frequency magnetization waveform temperature magnetization direction	different phases and precipitates dislocations densities dislocation tangles grain boundaries and grain sizes chemical composition magnetic history of material crystal anisotropy	applied stresses residual stresses stress anisotropy

**3.1. Effect of stress on magnetic Barkhausen noise**

Kneller has reported that Kersten began to investigate the relationship between magnetic properties and micro-residual stresses in ferromagnetic materials in the 1930s [Knel. 1962]. The theory of micro-magnetism suggests that magnetic hysteresis is generated by microscopic DW motion and its interaction with the micro-structure and stress fields.

Cullity was one of the pioneering researchers who proposed a simple model of the interaction between DWs and stresses inside materials [Cull. 2009]. When trying to determine a unit to which the effect of stress on DW behaviour can be reduced best such that the resulting electromagnetic principle can be generalized, the smallest common “denominator” turns out to be a material’s single crystal. Figure 3.1a shows symbolically a single crystal comprising four domains in an unstressed state. A small tensile stress will lead the DWs to move in such a way that the size of the domains magnetized perpendicular to the stress directions will be reduced

because these domains have high magnetoelastic energy (Figure 3.1b). These domains will even vanish when the applied tensile stress has reached a certain level and the remaining magnetoelastic energy becomes a minimum (Figure 3.1c). Only a small additional applied electromagnetic field is now required to fully saturate the specimen because the transition can be achieved by a simple 180° wall motion (Figure 3.1d). When compressive stress is applied to the crystal (Figure 3.2a), the domains in the direction of the stress will gradually vanish (Figure 3.2b and c) and a much higher magnetic field has to be applied in case a fully saturated crystal is intended (Figure 3.2d).

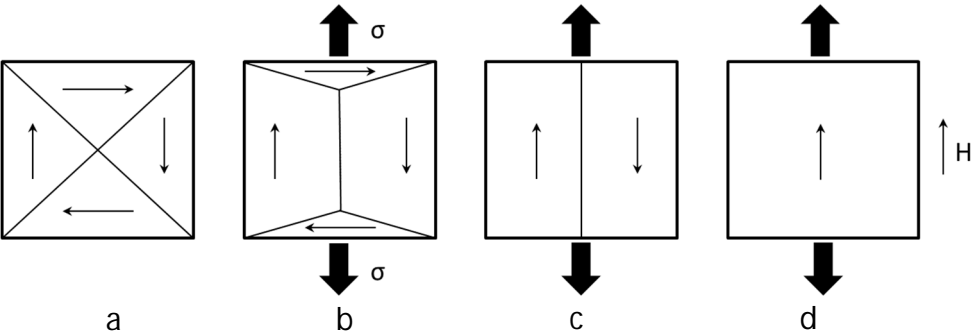


Figure 3.1: Schematic magnetization of a material with positive magnetostriction under tensile stress.

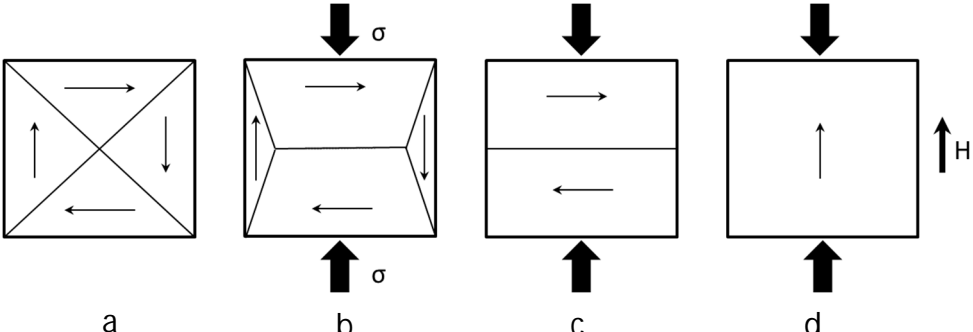


Figure 3.2: Schematic magnetization of a material with positive magnetostriction under compressive stress.

The type of crystal and its orientation can, therefore, become the building block for how to understand a structural material's and a component's stress behaviour based on MBN measurements, as well as for how to interpret MBN measurement results when stresses in a material and/or structure are known.

Concerning the effect of stress on DW motion, Cullity proposed that the effect of micro-stresses on the motion of DWs depends on the type of DW and is related to magnetostriction [Cull. 2009]. When a 90° DW moves, the magnetization direction changes and a distortion in the volume due to magnetostriction arises. This distortion interacts with stress distribution. On the other hand, when a 180° DW moves, the magnetization direction will not change, and

therefore no magnetostriction occurs. Only local stresses change the DW energy by adding a stress anisotropy term ( $K_{\sigma}=3/2\lambda\sigma$ ) to the crystal anisotropy.

Karjalainen et al. were one of the first researchers to have published the effect of stress on MBN in low-carbon steel (LCS) with a yield strength of 280 N/mm<sup>2</sup> [Karj. 1979b]. They tested the MBN response of a sample during a tensile test at a low strain rate ( $\sim 10^{-5}$  s<sup>-1</sup>) in order to measure the MBN continuously up to the yield point. They presented the results of MBN behaviour during interrupted loading-unloading to show the effect of stress when the load is beyond the elastic limit (Figure 3.3).

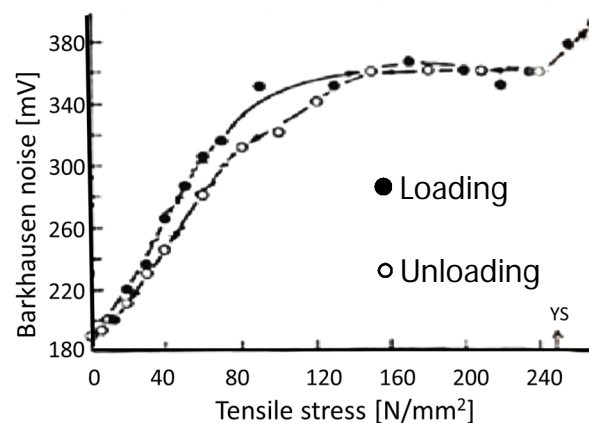


**Figure 3.3: Experimental MBN behaviour during loading and unloading up to the yield point [Karj. 1979b].**

As can be seen, the effect of elastic stress on the MBN up to 80 MPa is linear before it saturates. It was also mentioned that, in some cases, the MBN even decreased. For the linear part, it is proposed that DWs reorient during elastic stress, which induces domains parallel to the loading direction (LD). Therefore, the number of 180° DWs increases, which consequently causes the MBN to increase. For the saturation part of the MBN response, only a short explanation is presented. The authors mention the phenomenon to reflect the changes in magnetostriction under increasing tensile elastic stresses. They also mentioned that the increase in MBN beyond the yield point is due to the creation of a Lüders band zone.

Finally, they summarized that the sensitivity of MBN in relation to plastic deformation is much higher than for elastic deformation, while loading beyond the yield stress causes a permanent decrease in MBN after removal of the load.

Theiner et al. also investigated the stress and micro-structure dependency of MBN [Thei. 1979, Thei. 1983]. They showed that a maximum amplitude of Barkhausen noise increases while coercivity at the maximum of Barkhausen noise decreases with increasing stress.

Jagadish et al. were some of the first researchers to present the behaviour of MBN under tensile and compressive stress [Jaga. 1990]. They studied a steel pipeline and measured the dependency of the root mean square (rms) of the MBN signal and of the total number of induced voltage pulses under a uniaxial applied stress (Figure 3.4).

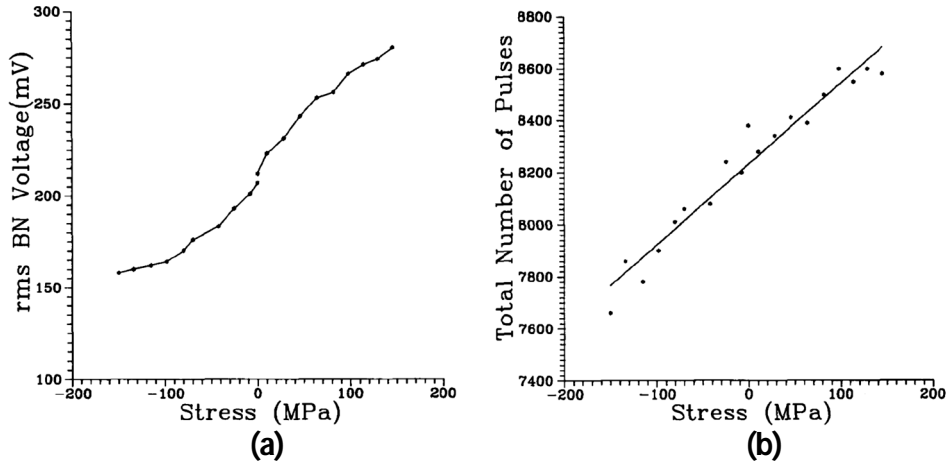


Figure 3.4: a) rms and b) total number of MBN voltage pulses as a function of applied stress [Jaga. 1990].

In this publication, tensile stresses increased the rms MBN voltage (maximum of the MBN signal) and vice versa for compressive stresses. Applied stresses also affect the number of MBN pulses which result from DW jumps. Therefore, the total number of pulses increases with an increasing tensile applied stress and vice versa for compressive stress. The authors explained that the MBN behaviour under applied stress reflects the magnetostriction changes in the sample. They also mentioned that tensile applied stress in positive-magnetostriction materials encourages DWs to arrange in such a way that the magnetization direction aligns with the applied stress. This happens the other way around when applying compressive stress.

In another comprehensive study published by Stefanita et al. [Stef. 2000], the differentiation of the effect of elastic and plastic deformation on MBN was explored. To this end, the authors measured linear and angular MBN in mild steels subjected to different degrees of uniaxial elastic and plastic deformation. They defined a parameter called  $MBN_{energy}$ , and described the effect of stress on this parameter,

$$MBN_{energy} = \alpha \cos^2(\theta - \varphi) + \beta$$

Equation 3.1

where  $\theta$  is the angle of the applied magnetic field with respect to the reference (rolling) direction,  $\alpha$  is associated with the angular-dependent variation of the MBN signal and  $\beta$  with the angular independent signal (isotropic background), and  $\varphi$  is the direction of the magnetic easy

axis with respect to the reference direction.  $\alpha$  and  $\beta$  can be calculated from a linear fit of  $MBN_{energy}$  vs.  $\cos^2(\theta - \varphi)$ . The authors found that the elastic strain affects the magnetic anisotropy ( $\alpha$ ) significantly, while the changes in the isotropic signal ( $\beta$ ) were small. In contrast, plastic deformation has a smaller effect on  $\alpha$  and  $\beta$  in such a way that it changes  $\beta$  but has little effect on  $\alpha$ . Figure 3.5 shows the effect of elastic and plastic deformation on  $MBN_{energy}$  in different directions relative to the applied stress. It also shows that elastic stress affects  $MBN_{energy}$  at a higher rate than plastic deformation. This becomes more evident from Figure 3.6a and b:  $\alpha$ , which is associated with magnetic anisotropy, increases during the deformation process while  $\beta$ , which reflects the isotropic background of the MBN, stays more or less constant. To describe these results, two mechanisms were proposed. The first one implies that  $180^\circ$  DWs reorient in the easy axis direction (100). The second one involves an increase in the  $180^\circ$  DW population. A combination of both mechanisms illustrates that tensile stress creates more DWs in the direction of the applied stress.

On the other hand, Figure 3.7 shows the effect of plastic strain on  $\alpha$  and  $\beta$ . The mechanism of the effect of plastic deformation could be different in comparison with that of elastic deformation. During plastic deformation, which occurs during the slip processes of dislocations, some changes happen in the material which could alter the MBN behaviour. Stefanita et al. propose that three possibilities should be kept in mind when investigating the effect of plastic deformation on MBN: 1) the number of dislocations and their configuration work as pinning sites of DW motion, 2) that plastic deformation may alter the magnetic easy axis because of the development of a crystallographic texture, and 3) that due to the work-hardening process, minor local elastic zones are created in plastic regions. Finally, Stefanita et al. have summarized their study such that MBN is much more dependent on elastic strain than on plastic deformation. This conclusion is completely in contrast with that of Karjalainen et al. [Karj. 1979a].

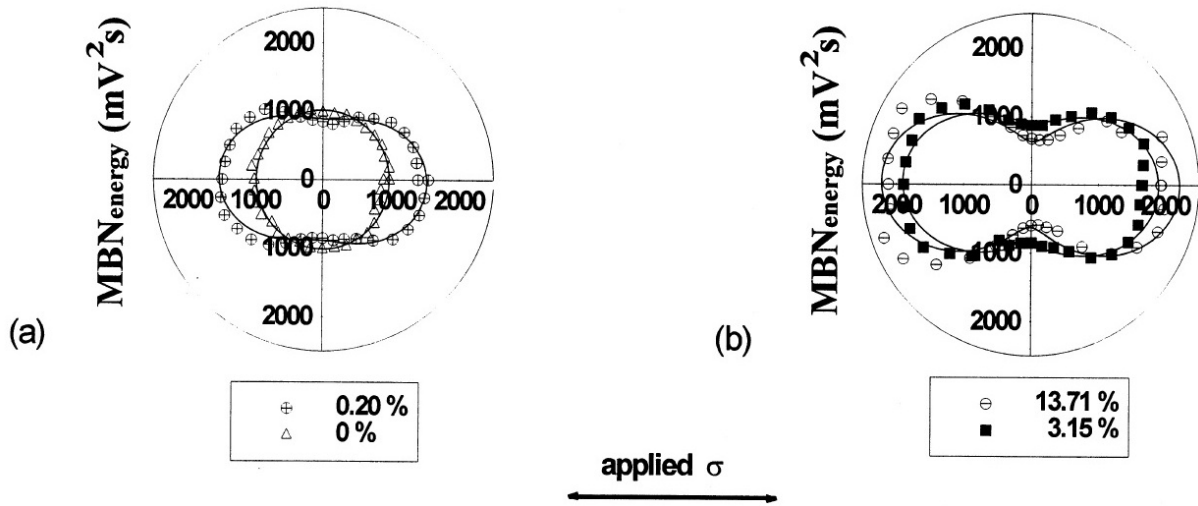


Figure 3.5: Angular MBN<sub>energy</sub> presenting: a) non-deformed and elastic deformed strain states, and b) plastically deformed samples. The solid lines show the best fit based on Equation 3.1 [Stef. 2000].

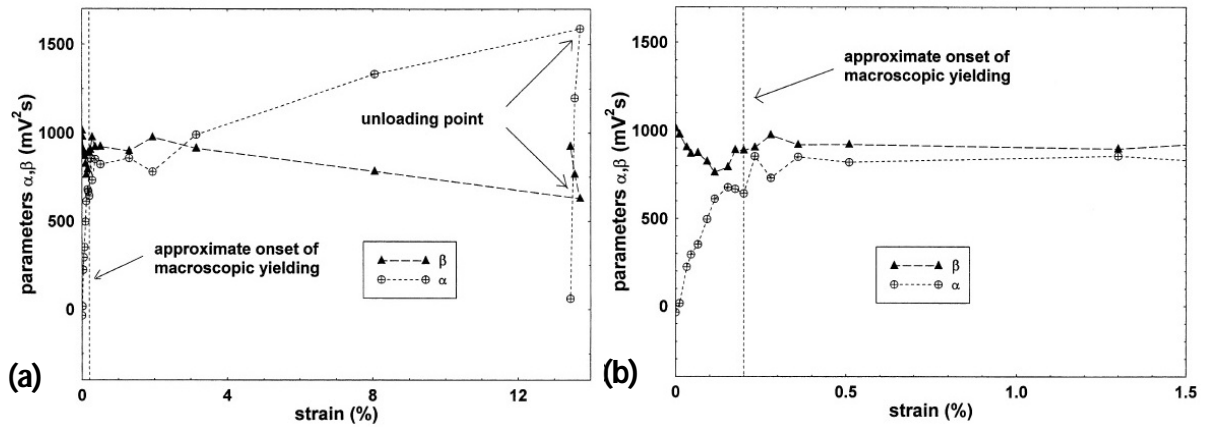


Figure 3.6: Variation of  $\alpha$  and  $\beta$  from Equation 3.1: a) general behaviour over the whole deformation cycle, and b) magnified view on the strain range up to 2% [Stef. 2000].

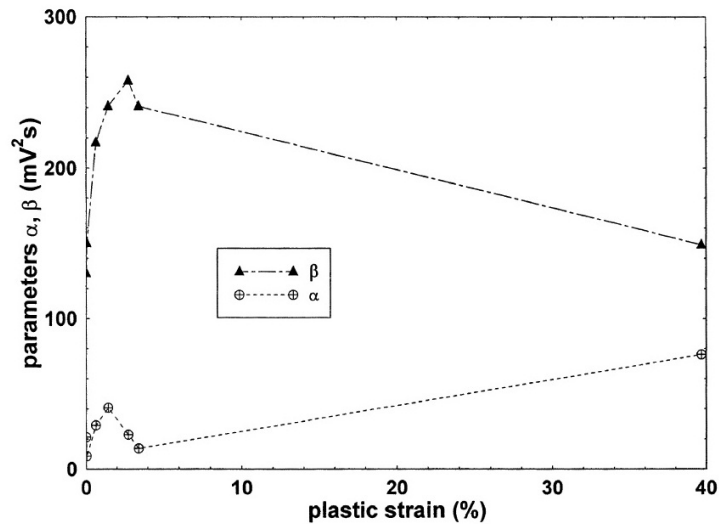


Figure 3.7: Behaviour of  $\alpha$  and  $\beta$  from Equation 3.1 across the plastic strain range [Stef. 2000].

Lindgren et al. have studied and published in a series of publications the effect of the stress and fatigue processes on MBN [Lind. 2001, Lind. 2003a, Lind. 2003b, Lind. 2004]. In [Lind. 2001] they report on the effect of pre-straining on MBN. For this purpose, they pre-strained mild steel specimens at different strains and then unloaded those again (Figure 3.8). Later on, they tested pre-strained samples under applied load in the loading and transverse directions.

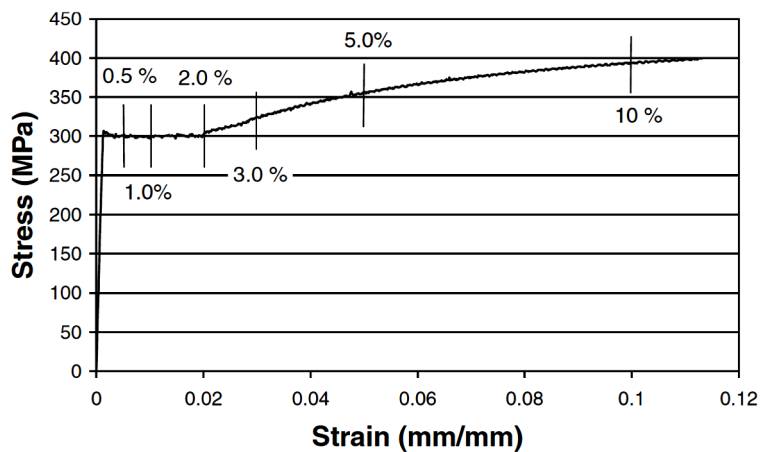


Figure 3.8: Pre-straining levels with respect to the stress-strain curve of mild steel [Lind. 2001].

Figure 3.9 shows the variation in MBN in different pre-strained samples where the angle of measurement related to the LD has been varied. Obviously, the MBN decreases in the LD and increases in the transverse direction (TD). However, this does not agree with the residual stress measurements reported in Figure 3.10, which indicate that pre-straining up to 3% in the LD generates tensile micro-residual stresses after unloading while the MBN increases for those samples. Lindgren et al. also mention that compressive residual stress will be generated after

pre-straining in the plastically deformed area, but in this case and based on the results presented in Figure 3.10, tensile stress has been detected.

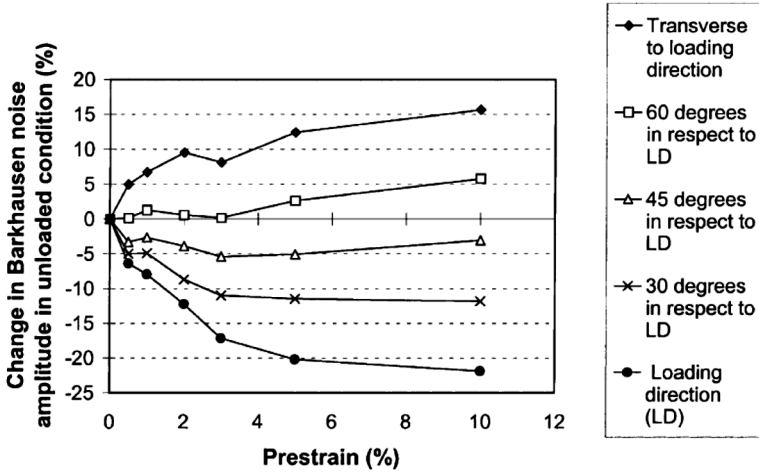


Figure 3.9: MBN behaviour after unloading at different angles with regard to the LD for different pre-strained samples [Lind. 2001].

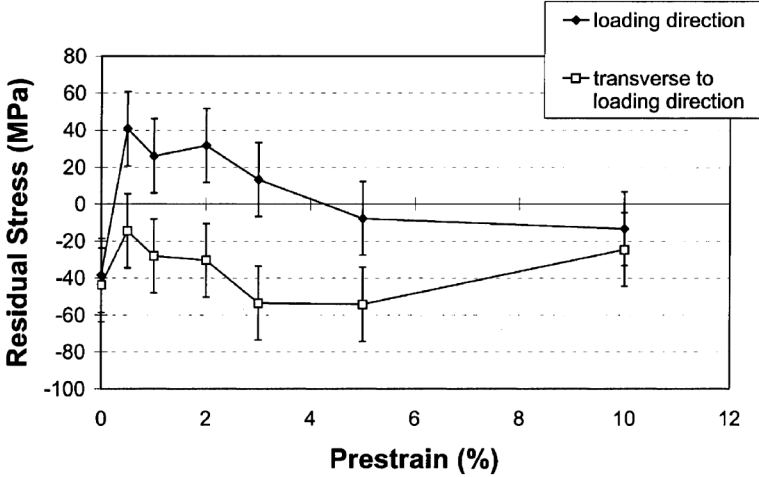


Figure 3.10: Residual stresses measured with XRD in the LD and TD for different pre-strained samples [Lind. 2001].

Lindgren et al. studied the relation between residual stress and applied stresses in duplex steel in two different publications [Lind. 2003b, Lind. 2004]. In the first, they investigated the residual stresses generated by local heating [Lind. 2003b]. Duplex steel, which contains austenite and ferrite phases, inherently has residual stresses because of the different thermal expansion coefficients of those phases. They generate local stresses with local heating. Next, Lindgren et al. performed a line scan over the heated zone with the MBN and XRD in two directions. The result illustrates the good agreement between the MBN and XRD values in the heated zone.

In the second paper [Lind. 2004], Lindgren et al. subjected duplex steel to elastic and plastic strains to investigate the effect of applied and residual stresses on MBN. They generated residual stresses using plastic deformation considering the fact that ferrite and austenite have different elastic moduli and thermal expansions. Therefore, pre-straining generates tensile and compressive micro-stresses in ferrite and austenite material respectively. XRD results show that pre-strained samples have fewer compressive micro-stresses than non-deformed samples. The reason for this, as presented by Lindgren et al., comes from the different behaviour of ferrite and austenite after pre-straining. In any case, pre-strained samples have fewer compressive micro-stresses, which is expected, and should exhibit more MBN, which is in agreement with the authors' results. In a subsequent step, Lindgren et al. subjected the samples to stress within the elastic range after non- and pre-deformation of the samples. Figure 3.11 and Figure 3.12 show the results.

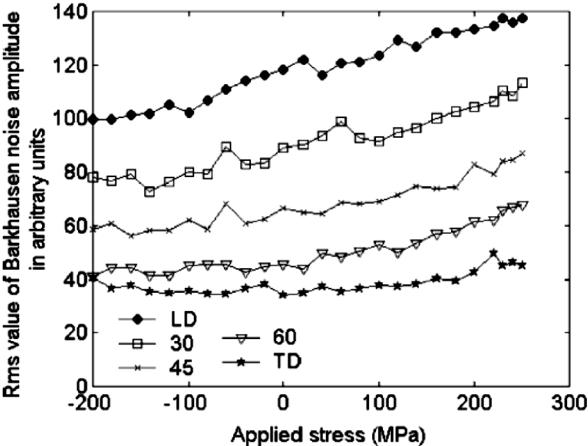


Figure 3.11: MBN results under applied stress in different directions regarding the applied load [Lind. 2004].

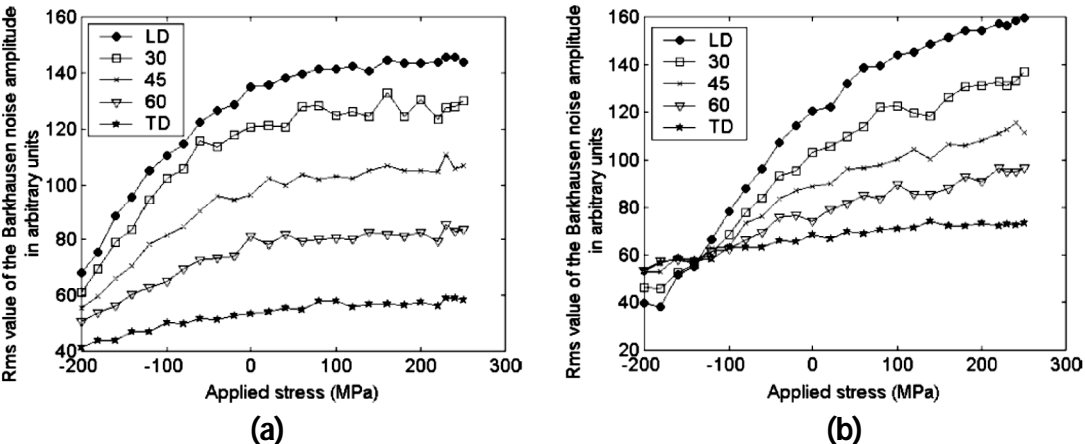


Figure 3.12: MBN behaviour under applied stress for a) 1% and b) 3% pre-deformed samples [Lind. 2004].

As a reason for this, Lindgren et al. described how the mean-free path of the domain motions (average distance of DW motions) is much higher in the LD than in the TD because of the alignment of ferrite grains in the LD and because of how these grains have numerous low-angle grain boundaries in the LD. Lindgren et al. [Lind. 2004] mentioned that the effect of elastic applied strain on MBN is an increase in MBN under tensile stresses with the reorientation of 180° DWs. Although saturation is visible in the results, this has not been discussed.

Anglada-Rivera et al. also investigated the effect of grain size and applied stresses on MBN for commercial carbon steel [Angl. 2001]. They performed different heat treatments to generate different grain sizes. Next, they subjected samples under applied stress up to less than the yield strength. As can be seen in Figure 3.13, all the samples exhibit a maximum in the MBN( $\sigma$ ) curve.

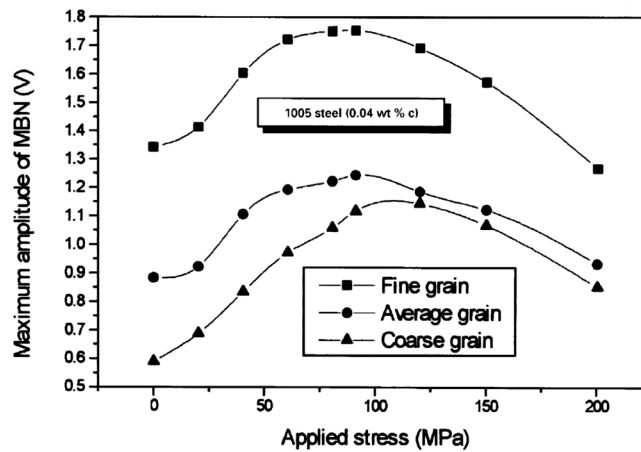


Figure 3.13: MBN behaviour under applied stress on 1005 steel grade with different grain sizes [Angl. 2001].

To describe this behaviour, Anglada-Rivera et al. used Sablik's model [Sabl. 1993a, Sabl. 1993b], which is described below. According to this model, the effective magnetic field ( $H_{eff}$ ) (Equation 3.2) plays the main role for the DW motion,

$$H_{eff} = H + \alpha M + \frac{3\sigma}{2\mu_0} \left( \frac{d\lambda}{dM} \right)$$

Equation 3.2

where  $\alpha$  is an effective field constant,  $\lambda$  is the magnetostriction,  $H$  is the magnetic field strength,  $M$  is the magnetization,  $\sigma$  is the applied stress and  $\mu_0$  is the permeability in the vacuum, respectively. The third term in Equation 3.2 is the effective field contribution due to stress. Anglada-Rivera et al. mentioned that the differential magnetostriction  $d\lambda/dM$  and the applied stress  $\sigma$  are positive for applied stresses up to the maximum of the MBN( $\sigma$ ) curve, which causes

the applied field as well as the effective field  $H_{eff}$  to increase with the domains, thereby moving more easily. Anglada-Rivera et al. explained that for applied stresses larger than those corresponding to the maximum MBN, Equation 3.2 cannot be further applied. They concluded that, in this region, other terms will affect the system which have themselves been related to the stress anisotropy.

Kleber et al. published an interesting paper on the influence of residual stresses and dislocations on MBN in Armco iron (AI) and LCS [Kleb. 2004]. They reported that AI and LCS exhibit different MBN signals, especially under plastic deformations higher than 1%. They illustrated the MBN response under elastic stresses, which increases the MBN with stresses up to a certain point and then allows it to decrease again (Figure 3.14). Kleber et al. also reported that, beyond the maximum of the MBN, apparently, a new mechanism occurs. Kleber et al. explained that, due to the stress-induced anisotropy, magnetization will increase in the [111] direction, which is not a magnetic easy axis for steel. Accordingly, the activity of  $180^\circ$  DWs decreases, and consequently the MBN decreases as well.

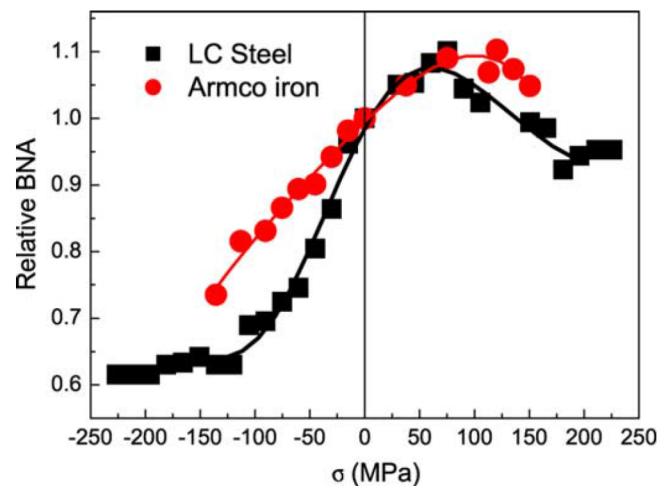


**Figure 3.14: MBN behaviour of AI and LCS under applied stress [Kleb. 2004].**

Figure 3.15 shows the MBN response after plastic deformation. Kleber et al. mention that AI and LCS exhibit relatively similar behaviour for plastic deformations less than 1%, although a small decrease or increase in the MBN of around 1% deformation in the AI and LCS, respectively, is visible, which can be neglected. Actually, the MBN exhibits the opposite behaviour in AI and LCS samples with plastic deformation of more than 1%. Kleber et al. mentioned that the effect of tensile and compressive residual stresses on MBN is in the opposite direction, while the effect of dislocations on MBN is not dependent on the signs of plastic strain. Therefore, based on this fact and the MBN response shown in Figure 3.15 for more than 1%, Kleber et al. concluded that residual stresses control MBN behaviour in LCS, while in AI

dislocations have the dominant effect. Kleber et al. also mentioned that LCS has more residual stress and more dislocations than AI for the same plastic strain.

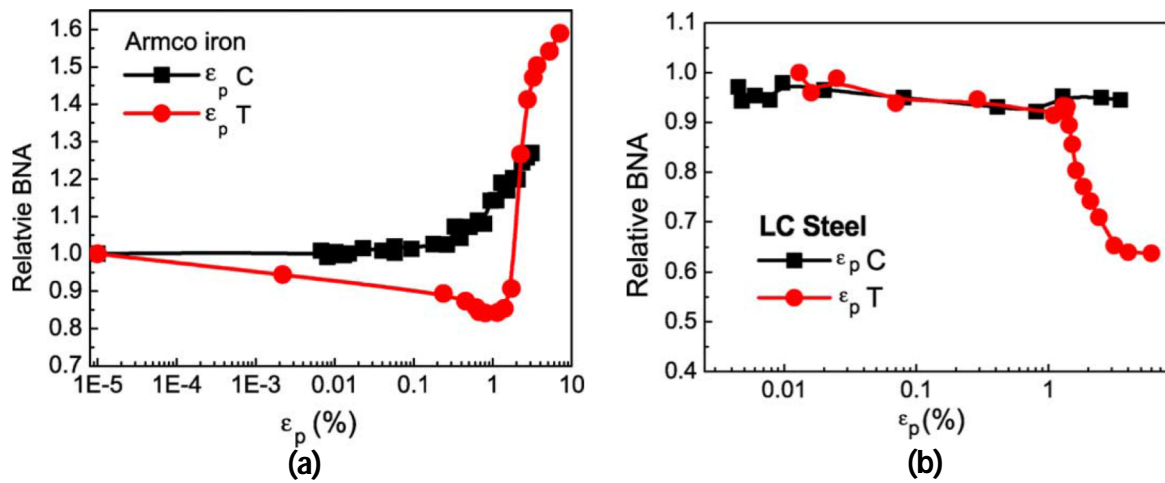


Figure 3.15: MBN behaviour at a) AI and b) LCS after tensile (T) and compressive (C) plastic deformations [Kleb. 2004].

Sorsa et al. proposed a statistical procedure to predict residual stress in case-hardened steel using MBN [Sors. 2012, Sors. 2013]. They divided their approach into the following steps: signal pre-processing, feature selection, model identification and model validation. They used XRD and hardness testing results as reference data for calibration. Finally, they showed the results as presented in Figure 3.16.

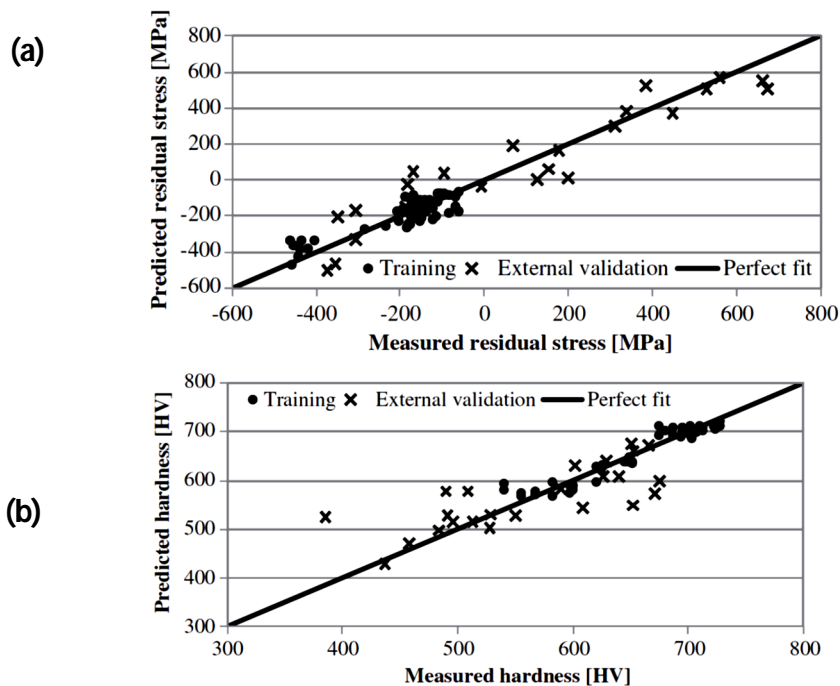
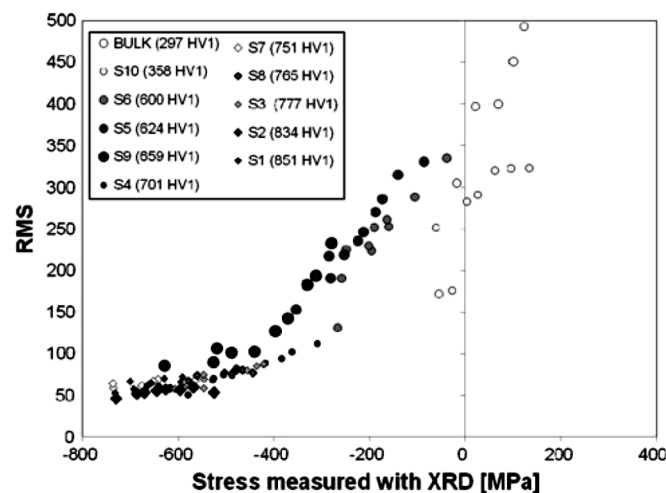


Figure 3.16: Measured and predicted values of a) residual stresses and b) hardness using the MBN method after calibration [Sors. 2012].

Although Sorsa et al. proposed a systematic procedure to measure the residual stress and hardness of the material analysed, their method has been widely used, for example, by Fraunhofer IZFP [Altp. 2002, Altp. 2009, Rabu. 2014, Cosa. 2014, Dobm. 1998, Dobm. 2007, Höll. 1987, Thei. 1987]. In fact, Sorsa et al. proposed a reliable, well-known process to calibrate an MBN device for measuring residual stresses by means of XRD results.

The influence of elastic bending and tensile compressive stress on MBN was studied by Santa-Aho et al. [Sant. 2012a]. Similarly with the other publications, Santa-Aho et al. also compare the MBN results with XRD and show the sensitivity of stress to MBN (Figure 3.17).



**Figure 3.17: MBN measurements vs. XRD stress values for different samples [Sant. 2012a].**

Santa-Aho et al. also investigated the sensitivity of stress to MBN and other metallurgical modifications, like case hardening [Sant. 2012b, Sant. 2012c, Sant. 2012d].

Altpeter et al. [Altp. 2000, 2001, 2009, Thei. 1983] and recently Rabung et al. [Rabu. 2014] extracted new data from MBN behaviour under elastic applied strains to measure micro-residual stresses in ferrite/pearlite carbon steel (1.2 wt.-% C). This steel has inherently micro-residual stress of the second and third types due to the micro-structure of this steel, which contains precipitates with different crystal structures in the base material. The second type comes from the different thermal expansion coefficients of the phases, while the third type results from the different lattice parameters of the phases. After different heat treatments that allowed different distributions and sizes of secondary phases to be generated (in this case, Cu precipitates), Altpeter et al. and Rabung et al. subjected the samples to applied elastic stresses and measured the maximum amplitude of MBN ( $M_{MAX}$ ) to obtain the so-called  $M_{MAX}(\sigma)$ -curve. Their results show the typical MBN behaviour under applied stress (Figure 3.18a), in which  $M_{MAX}$  increases with applied stress and decreases after reaching a critical value. To find the reason for this, they

performed magnetostriction measurements under applied stress. They found that the magnetostriction curve will turn negative exactly at the stress applied when the MBN reaches a maximum (Figure 3.18b). They concluded that when the magnetostriction is negative, the MBN decreases under applied tensile stress. Therefore, Altpeter et al. and Rabung et al. note that a change in magnetostriction is the main reason for the MBN's behaviour under applied stress.

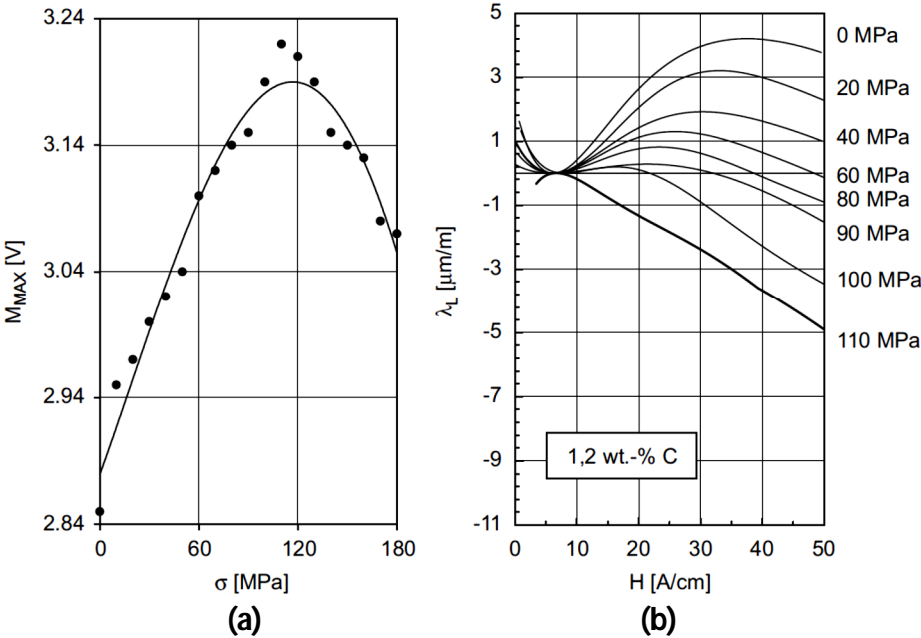


Figure 3.18: a)  $M_{MAX}$  behaviour and b) magnetostriction changes under applied stress [Altp. 2009].

They also found that the position of the maximum of the  $M_{MAX}(\sigma)$  curve depends on the micro-residual stresses in the sample considered. Altpeter et al. and Rabung et al. showed that tensile micro-residual stresses shift the maximum of the  $M_{MAX}(\sigma)$  curve to lower stress values while compressive micro-residual stresses shift the curve to higher stress values (Figure 3.19).

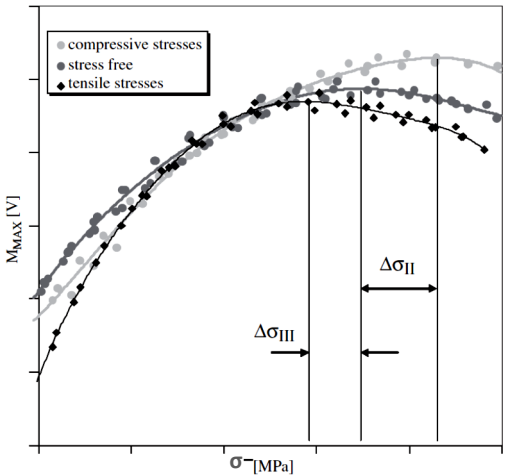
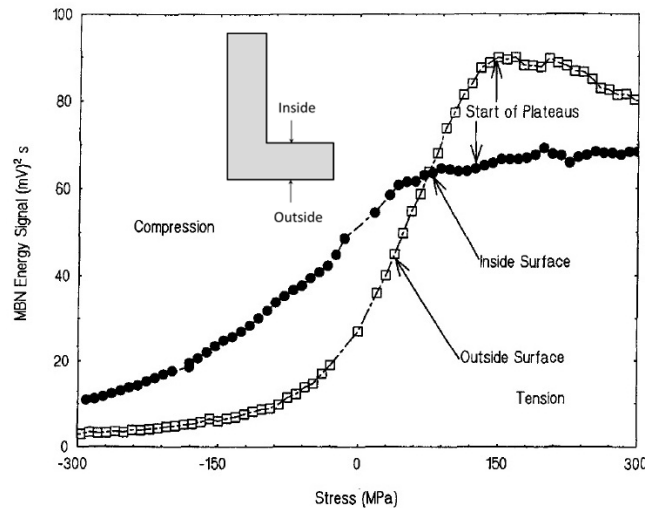


Figure 3.19: Sample representation of a so-called  $M_{MAX}(\sigma)$  shift resulting from different residual stresses of samples [Altp. 2009].

Gauthier et al. calculated the MBN of the energy from Equation 3.1 for an L-shaped steel beam under applied stress [Gaut. 1998]. They performed measurements on both surfaces (inside and outside) and used them for the calibration of the MBN system with respect to stress measurement. Figure 3.20 shows the relationship between the MBN energy and the applied stress for the inner and outer surfaces of the sample.



**Figure 3.20: MBN energy of an L-shaped beam on the inside and outside of the beam under applied load [Gaut. 1998].**

Gauthier et al. used the data in Figure 3.20 as a calibration curve. Next, they estimated the surface stresses at different positions on the sample based on the calibration curves in Figure 3.20 (whereby Figure 3.21 illustrates the estimated stress). As can be seen, there are two plateau areas which originate from the non-linear behaviour of the MBN energy at applied high stresses and which cause the errors for the estimated stress. It is worth noting that Gauthier et al. did not mention any reason for this behaviour. However, it should also be noted that Gauthier et al. mentioned that residual stresses can cause the magnetic easy axis of a sample to change. To this end, Gauthier et al. calculated the MBN energy at different angles relative to the rolling direction on the inside and outside of the sample. The results presented in Figure 3.22 illustrate the magnetic anisotropy changes due to the presence of residual stresses. Finally, Gauthier et al. concluded that residual stresses shift the magnetic easy axis towards angles away from the rolling direction, with the assumption that the rolling direction is the easy axis in the absence of residual stresses.

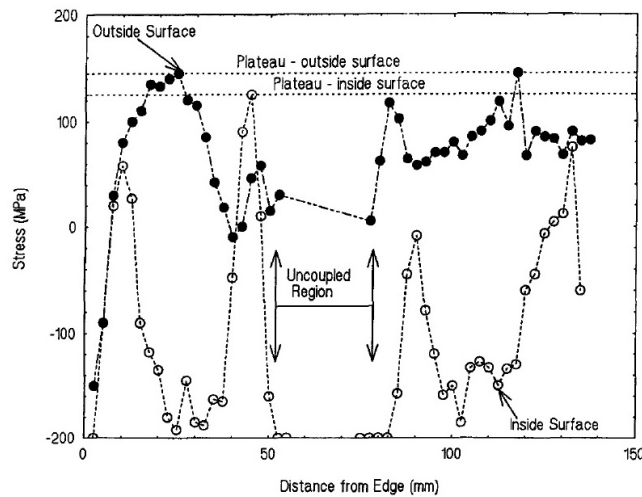


**Figure 3.21: Residual stresses estimated on the inside and outside of an L-shaped beam [Gaut. 1998].**

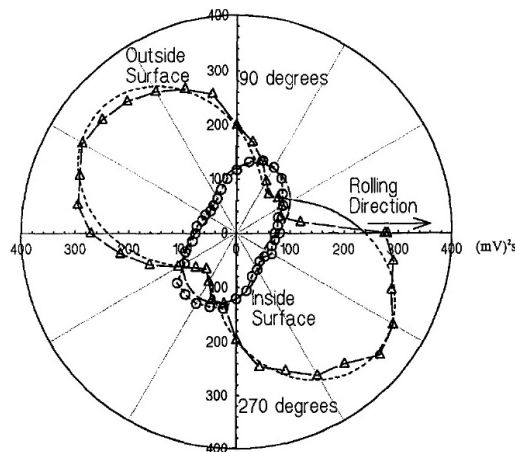


**Figure 3.22: Scan of the MBN energy of the inside and outside of an L-shaped beam at different angles with regard to the rolling direction [Gaut. 1998].**

Yelbay et al. used a similar principle to estimate residual stresses in welded samples in the heat affected zone (HAZ) and the base material [Yelb. 2010]. They measured the changes in MBN and strain under applied stress of two samples cut from the base material and the HAZ. Furthermore, they calculated the stress from the measured strain and the elastic modulus of the samples. Finally, they achieved the result shown in Figure 3.23, which they used as a calibration curve. It is worth noting that Yelbay et al. proposed an extrapolation method to estimate residual stresses from MBN values outside of the calibration curve. Finally, Yelbay et al. estimated the residual stresses of the welded samples by means of an MBN scan over the welded zone. Yelbay et al. also measured the residual stresses of the base material and the HAZ using the hole-drilling method to compare the results with the residual stresses estimated with the MBN method (Figure 3.24).

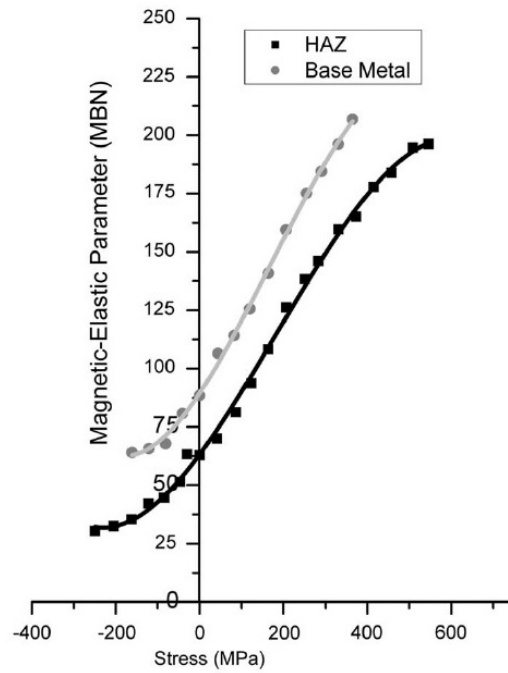


**Figure 3.23: MBN behaviour under applied stress for samples cut from base material and the HAZ [Yelb. 2010].**

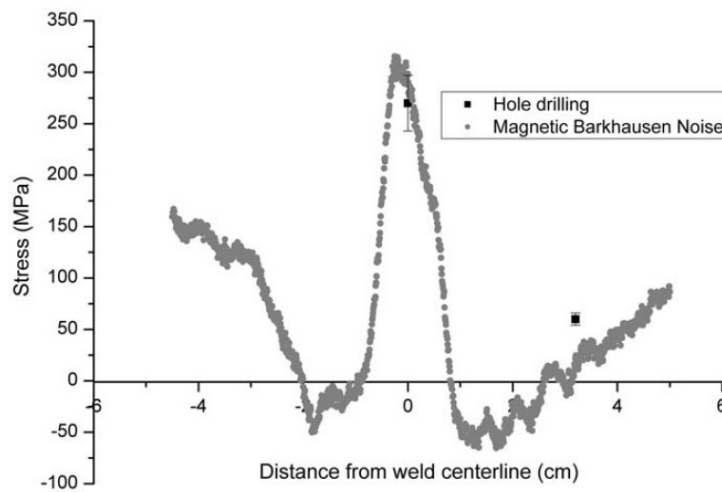


**Figure 3.24: Residual stresses measured with MBN and its verification with the hole-drilling method [Yelb. 2010].**

Ju et al. also used the method mentioned above to estimate stresses in welded samples [Ju. 2003], leading to similar results.

Kasai et al. investigated the effect of elastic stress and the micro-structure on MBN for LCS [Kasa. 2013]. They used three samples, two of which were heat treated at 450° for 1.5 h, and one at 700° for 10 h, and then cooled to room temperature. The MBN was measured under tensile applied stress. Figure 3.25 shows the results.

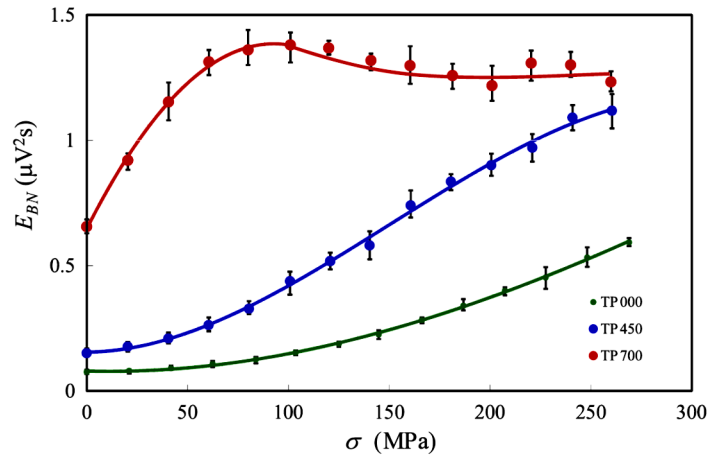


**Figure 3.25: Relationship between MBN energy and elastic applied strains for non-heat treated (TP000) and heat treated samples (TP450 and TP700) [Kasa. 2013].**

Kasai et al. measured the dislocation densities, grain sizes and grain orientations with TEM and electron backscatter diffraction (EBSD) analysis, respectively. The grain size and grain orientation stayed constant in the samples after heat treatments, but the dislocation density (measured based on the Keh method) changed (Table 3.2, Figure 3.26). Based on the Keh method [Kasa. 2013], the dislocation density  $\rho$  is measured according to the following Equation 3.3,

$$\rho = \left( \frac{n1}{L_1} + \frac{n2}{L_2} \right) / t$$

**Equation 3.3**

where  $n1$  is the number of intersection points between the vertical lines and the dislocation lines,  $n2$  is the number of intersection points between the horizontal lines and the dislocation lines,  $L_1$  is the total length of the vertical grid lines in a TEM image,  $L_2$  is the total length of horizontal grid lines in a TEM image, and  $t$  is the test-piece thickness.

It actually makes sense that the heat treatments mentioned above cannot change the micro-structure of steel because the heat treatment temperatures are lower than the A1 line in the iron-carbon phase diagram. Therefore, only the dislocation densities will be affected by the heat treatments. Kasai et al. concluded that different slopes of the MBN( $\sigma$ ) curve originate from different dislocation densities in the samples.

**Table 3.2: Dislocation densities of samples estimated by the Keh method [Kasa. 2013].**

	Thickness of test piece (nm)	Dislocation density $\times 10^{13}$ (m/m <sup>3</sup> )	Average dislocation density $\times 10^{13}$ (m/m <sup>3</sup> )
TP000	70	5.0	4.8
		3.1	
		6.3	
TP450	70	2.8	3.5
		3.4	
		4.2	
TP700	70	2.6	2.8
		2.2	
		3.5	

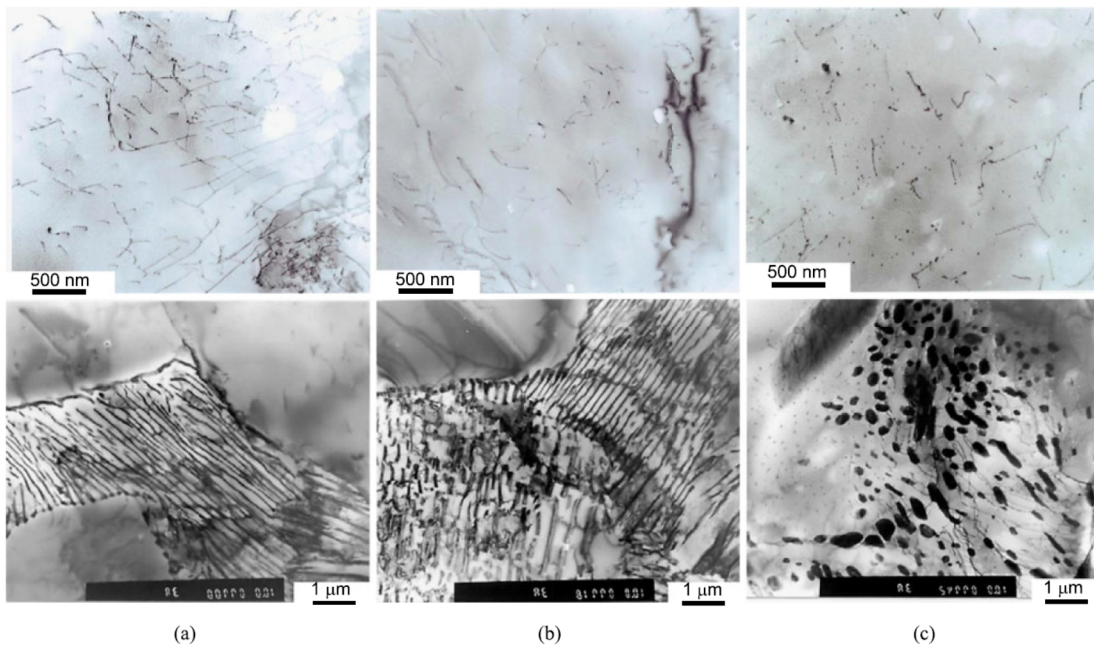


**Figure 3.26: TEM micrographs of a) TP000, b) TP450 and c) TP700 samples [Kasa. 2013].**

Xin et al. proposed a new possibility for measuring the stress distribution in a steel plate using a combination of MBN and metal magnetic memory (MMM) [Xin. 2012]. MMM is a relative new non-destructive method which has been presented by Doubov [Dubo. 1997]. MMM is based on the magneto-elasticity and magneto-mechanical effects. When a ferromagnetic material is mechanically loaded, the magnetic domains dislocate and irreversibly reorient. A magnetic leakage field appears which is related to the dislocation concentration and micro-defects, stress and local uniformity is generated. This magnetic leakage field is scanned on a specimen's surface using a fluxgate probe to find the stress concentration region. Then estimating the residual stress level is performed using MBN at the stress concentration region. MBN was again calibrated with XRD results.

Stewart et al. presented MBN under tensile and compressive applied stresses [Stew. 2004]. Based on Figure 3.27, they illustrate that compressive stress has more of an effect on MBN than on tensile stress.

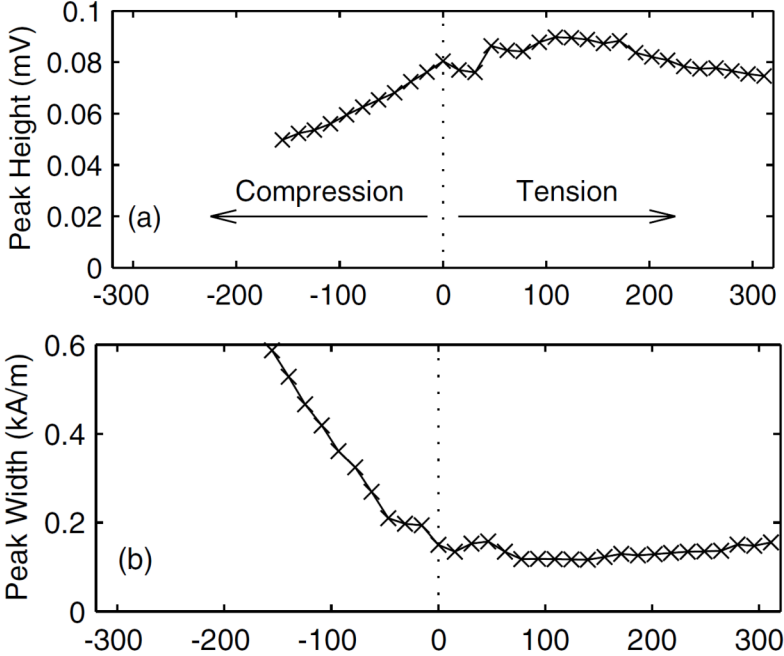


**Figure 3.27: Variation of MBN parameters as a function of applied stress: a) peak height of MBN, and b) full width at half-maximum of peak [Stew. 2004].**

Stewart et al. mentioned that the Villari effect is the main reason for MBN’s behaviour under tensile applied stress. Stewart et al. also describe how the reaction of DWs under applied stress has two steps. First, domains align in the nearest and easiest axis. This alignment of the DWs increases the magnetization ( $M$ ) and magnetostriction ( $\lambda$ ). Next, the domains turn exactly towards the stress direction, which leads to a further increase of  $M$  and a decrease of  $\lambda$ . When the sample is subjected to tensile stress, the first step is dominant up to a maximum, and afterwards the second step plays the main role. The stress component of the effective magnetic field ( $H_{eff}$ ) is proportional to  $d\lambda/dM$ , which changes its sign at stresses higher than the maximum in Figure 3.27. Therefore, MBN decreases with decreasing  $H_{eff}$ . In addition, Stewart et al. investigated the welded sample with MBN. The results show that MBN can represent the residual stress differences between the welded zone and the base material.

Jiles also presents the effect of applied stress on MBN [Jile. 1989]. He measured MBN and magnetization parameters under applied stress for two different types of steels (AISI 4130 and AISI 4140). Table 3.3 shows the results.

**Table 3.3: Variation of MBN and magnetization parameters under tensile applied stress for a) AISI 4130 and b) AISI 4140 steels [Jile. 1989].**

(a)

Stress MPa	Barkhausen			Magnetization	
	Peak Amplitude 10 <sup>3</sup> cps	Hp (Oe)	Total Counts (10 <sup>3</sup> )	μ'max (Gs/Oe)	He (Oe)
0	37.7	12	1015	850	12
17	38.9	11	1106	870	11.7
34	38.2	9	1125	945	11.5
51	38.3	9	1142	1023	11.2
68	38.5	10	1186	1036	11
85	36.8	8	1153	1134	10.8

(b)

Stress MPa	Barkhausen			Magnetization	
	Peak Amplitude 10 <sup>3</sup> cps	Hp (Oe)	Total Counts (10 <sup>3</sup> )	μ'max (Gs/Oe)	He (Oe)
0	15.8	20	207	704	17
17	16.4	20	202	768	16
34	16.4	19.5	191	784	16
51	17.4	18.5	239	844	15
68	16.7	18	197	880	14
85	17.1	17	195	975	14

As can be seen, the peak amplitude of MBN in AISI 4130 increases up to 68 MPa and then decreases again, while in AISI 4140 it increases (small increases and decreases have been noted as an error). He linked the effect of stress on MBN with the maximum differential susceptibility  $\chi'_{\text{Max}}$  and the magnetostriction coefficient, but he did not describe anything more.

Some research groups have focused on the modelling of MBN behaviour and the related effect of stress. Sablik et al. proposed a model for calculating MBN as a function of the applied magnetic field and stress [Sabl. 1993a]. He derived a formula to calculate the MBN power based on the Langevin description of DW motion and some algorithms published by Alessandro et al. [Ales. 1990a, Ales. 1990b]. He showed that the MBN power (J) is given by Equation 3.4,

$$\begin{aligned}
 \mathcal{J} &= \frac{1}{2\pi} \int_0^{\infty} F(\omega) d\omega = \frac{1}{2\pi\tau_c} \int_0^{\infty} F(x) dx = \left( \frac{\xi^2}{\gamma\tau\tau_c} \right) \{1/[1 + (\tau_c/\tau)]\} \\
 &= \left( \frac{A\xi}{(G/\rho)^2} \right) \frac{(\mu/\mu_0)(\mu - \mu_0)\dot{H}}{(\mu/\mu_0)(\mu - \mu_0)\dot{H} + [\xi/(S^2G/\rho)]}
 \end{aligned}$$

**Equation 3.4**

where  $G$  is a dimensionless coefficient ( $G=0.1356$  if  $S \gg d^2$  with  $d$  being the thickness of the sample and  $S$  being the cross-section),  $\omega$  is the angular frequency,  $A$  is a parameter that describes the spatial fluctuations of short-range DW coercive field interactions [Ales. 1990a, Ales. 1990b],  $\tau_c$  and  $\tau$  are time constants which are calculated by  $G S \mu / \rho$  and  $\xi / S \dot{M}$ , respectively,  $\xi$  is the corresponding correlation length, and  $\dot{M}$  is time rate of magnetization change, given as

$$\dot{M} = \chi \dot{H} = (\mu - \mu_0) \dot{H} / \mu_0$$

**Equation 3.5**

where  $\chi$  is the differential magnetic susceptibility  $dM/dH$ ,  $\dot{H}$  is the time rate of the change of the external field,  $\mu$  is the differential permeability  $dB/dH$  and  $\gamma$  is defined as  $\gamma = S \dot{M} (G/\rho)^2 / A \tau$ . Sablik et al. mentioned that for calculating the effect of stress  $\sigma$  on  $J$ , instead of using  $\mu$  and  $\dot{M}$  one should use  $\mu_{irr}$  and  $\dot{M}_{irr}$ , respectively, which are given as

$$\mu_{irr} = \mu_0 \left( 1 + \frac{dM_{irr}}{dH} \right)$$

**Equation 3.6**

$$\mu_{irr} = \mu_0 \left( 1 + \frac{(M_a - M_{irr})}{(k\delta/\mu_0) - [\alpha + (3/2)(\sigma/\mu_0)(\partial^2 \lambda / \partial M^2)_{M=M_a}]} (M_a - M_{irr}) \right)$$

**Equation 3.7**

where  $k$  is the pinning constant (proportional to the DW pinning site density),  $\delta = \pm 1$ ,  $\alpha$  is the inter-domain coupling parameter,  $\sigma$  is the external mechanical stress,  $M_a$  is the anhysteretic magnetization and  $(\partial^2 \lambda / \partial M^2)_{M=M_a}$  is the second derivation of magnetostriction as the total magnetization when  $M=M_a$ . The anhysteretic magnetization is calculated as:

$$M_a = M_s \mathcal{L}(H_e/a)$$

**Equation 3.8**

Here,  $M_s$  is the saturation magnetization,  $\mathcal{L}(x) = \coth x - (1/x)$  is the Langevin function, and  $a$  is a constant proportional to the pinning site density in a demagnetizing state. The effective magnetic field  $H_e$  is calculated as

$$H_e = H + \alpha M_a + \frac{3\sigma}{2\mu_0} \left( \frac{d\lambda}{dM} \right)_{M=M_a}$$

**Equation 3.9**

and the magnetostriction is

$$\frac{3}{2}\lambda = -\left(\frac{2b(1+\nu)}{3Y}\right)\left\{\left[1 + \left(\frac{9Y}{2b^2(1+\nu)^2}\right)\frac{1}{2}\mu_0\alpha M_s^2\right]^{1/2} - \left[1 + \left(\frac{9Y}{2b^2(1+\nu)^2}\right)\frac{1}{2}\mu_0\alpha(M_s^2 - M_a^2)\right]^{1/2}\right\}$$

**Equation 3.10**

where  $Y$  is Young's modulus,  $\nu$  is Poisson's ratio and  $b$  is the magnetoelastic coupling constant.

Sablík et al. solved the equations for simple carbon steel, as shown in Figure 3.28.

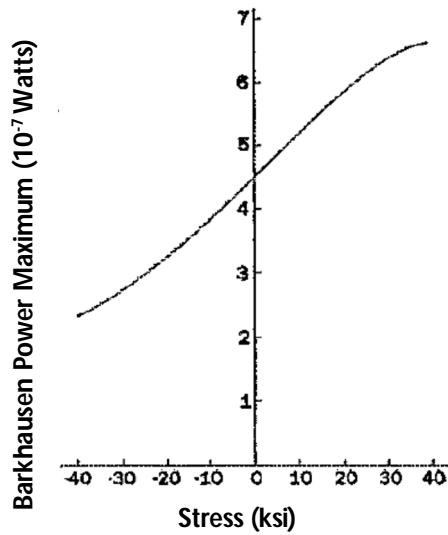


**Figure 3.28** Calculated maximum power of MBN as a function of applied stress [Sabl. 1993a].

More details of this model have been presented by Sablík et al. [Sabl. 1993b] and Ramesh et al. [Rame. 1996]. These two publications help to understand the basics and physics behind the Sablík model.

Szewczyk et al. simulated the effect of stress on the hysteresis loop based on the Jiles-Atherton-Sablík model of amorphous alloys. This model is an energy-based model which describes the magnetization process in the presence of external stress [Szew. 2004]. After solving the equations for the specific conditions, Szewczyk et al. presented Figure 3.29 as an output of the model.

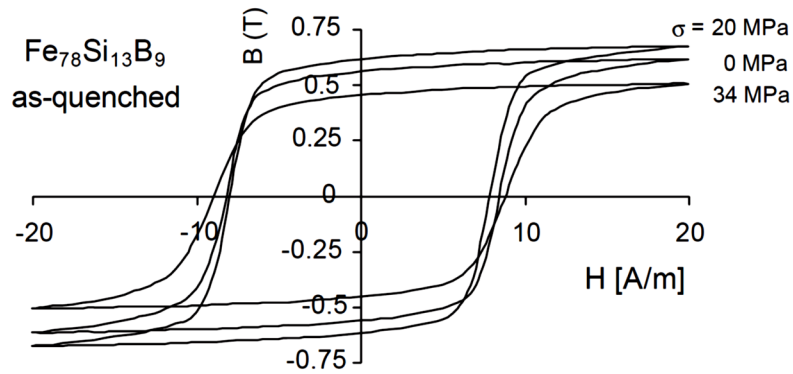


**Figure 3.29: The influence of stress on the shape of the hysteresis loop for the Fe78Si13B9 amorphous alloy [Szew. 2004].**

Obviously, the B-H hysteresis loop tends to be thinner and then thicker again at different stresses. Szewczyk et al. related this behaviour to the Villari effect, which describes the magnetization process changes due to external stress. Moreover, Szewczyk et al. showed the trend of the stress dependency of the model parameters on external stress. Figure 3.30 shows the effect of stress on the Jiles-Atherton-Sablik model parameters  $a$ ,  $k$ ,  $c$ ,  $\tilde{\alpha}$ ,  $K_{an}$  and  $t$ . The parameters  $a$  and  $c$  describe the slope and reversibility of the hysteresis loop, respectively.  $K$  is the average energy required to break the pinning site and  $\tilde{\alpha}$  quantifies the domain interactions while  $K_{an}$  and  $t$  relate to the anisotropy of the material.

As can be seen,  $a$  and  $c$  increase with stress and then decrease, while  $k$  and  $\tilde{\alpha}$  exhibit the opposite behaviour.  $K_{an}$  and  $t$  behave the same as  $a$  and  $c$ . Szewczyk et al. did not describe any further their method of calculation or the physical meaning of each parameter. However, it seems that their results could be extrapolated for MBN's behaviour under stress. Based on the behaviour of  $K$  and  $\tilde{\alpha}$ , the energy required to break pinning sites and DW interactions decreases up to a certain point and then increases again. This is in good agreement with the MBN( $\sigma$ ) curve. An increase in the domain interactions and the energy required for DW motion causes MBN to decrease after a certain amount of stress. Anisotropy changes could also affect DW motion and MBN.

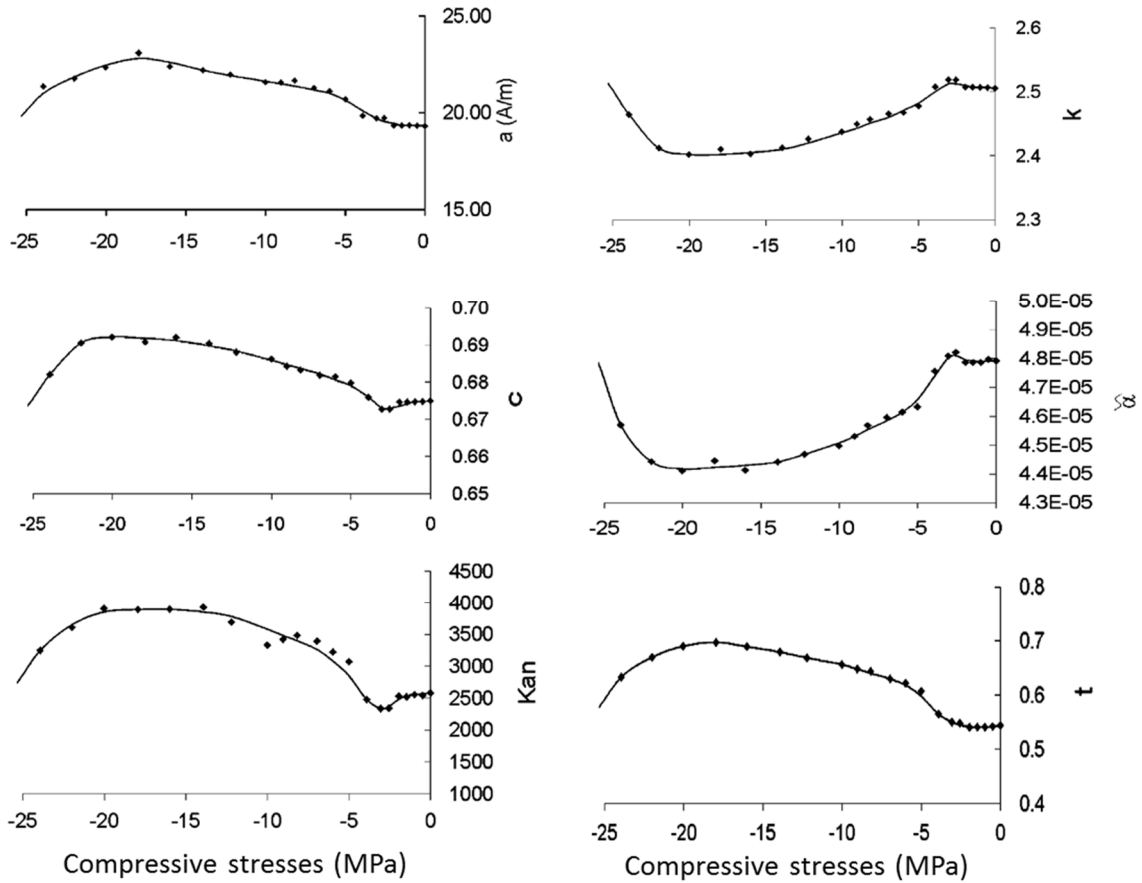


Figure 3.30: Behaviour of the Jiles-Atherton-Sablik model of applied stress [Szew. 2004].

Perevertov studied in depth the influence of residual stress on the magnetization process by measuring B-H curves [Pere. 2007]. He measured B-H curves in different magnetization directions as well. Figure 3.31 shows the results ( $\phi$  is the angle between the applied stress and the measurement direction). The normalized classic magnetic parameters are shown in Figure 3.32. It is noteworthy that Perevertov calculated the anisotropy energy ( $E_a$ ) from simulated anhysteretic curves. Therefore, Perevertov concluded that a uniaxial anisotropy induced in a material causes the magnetization process and the B-H loop to alter. Moreover, Perevertov mentions that, by using the effective magnetic field concept, the effect of stress on magnetization and the B-H curve could be modelled.

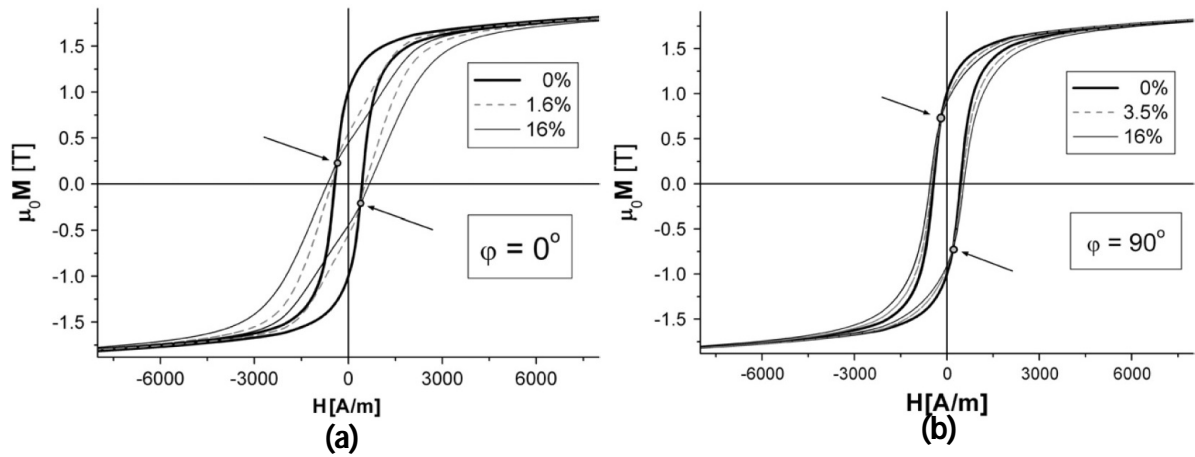


Figure 3.31: Hysteresis loops measured in: a) the applied stress direction, and b) perpendicular to the applied stress [Pere. 2007].

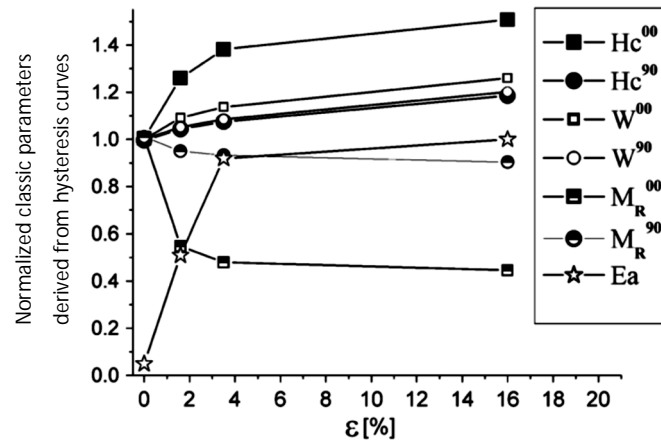


Figure 3.32: Normalized classic parameters (coercivity  $H_c$ , losses  $W$ , remanence  $M_R$  and the anisotropy energy  $E_a$ ) derived from hysteresis curves measured in parallel and perpendicular to the applied stress [Pere. 2007].

Perevertov et al. also studied the influence of stress on the B-H curves and domain structures in Fe-3Si steel using Kerr microscopy [Pere. 2012]. They applied compressive stresses on samples, measured B-H curves and performed Kerr microscopy images at the same time. Figure 3.33 shows the B-H curves at different stress levels.

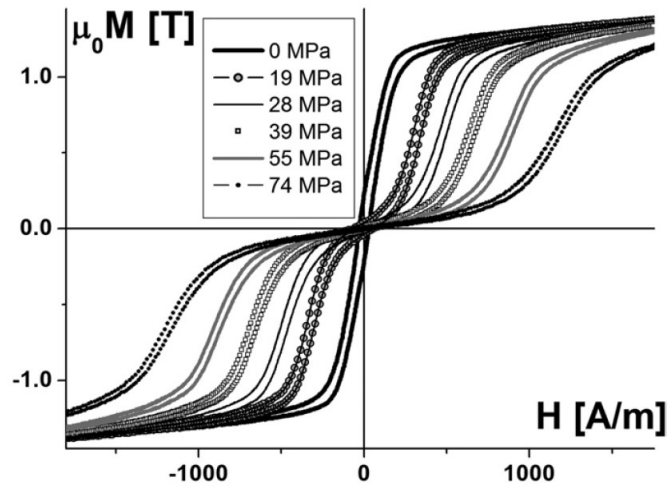


Figure 3.33: Hysteresis loops for an Fe-3Si sample at different applied stresses [Pere. 2012].

Perevertov et al. used an effective magnetic field model to describe the phenomena described in Figure 3.31 and Figure 3.33, respectively. Perevertov et al. mentioned that coincident points (shown by arrows in Figure 3.31) in the B-H curves of the samples under stress could be calculated where  $\Delta H/\Delta\sigma=0$ . In addition, Perevertov et al. investigated the domain structures in situ under applied stress to monitor the micro-magnetic behaviour of the samples (Figure 3.34 - Figure 3.36).

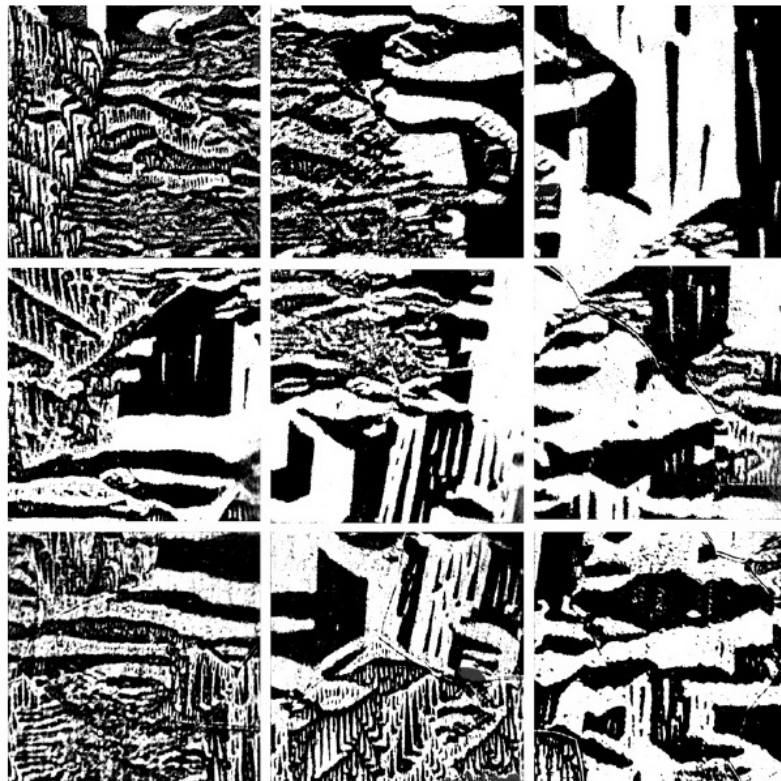


Figure 3.34: Magnetic domain structures in nine neighbouring areas for zero applied stress [Pere. 2012].



Figure 3.35: Magnetic domain structures in nine neighbouring areas under -35 MPa applied stress [Pere. 2012].

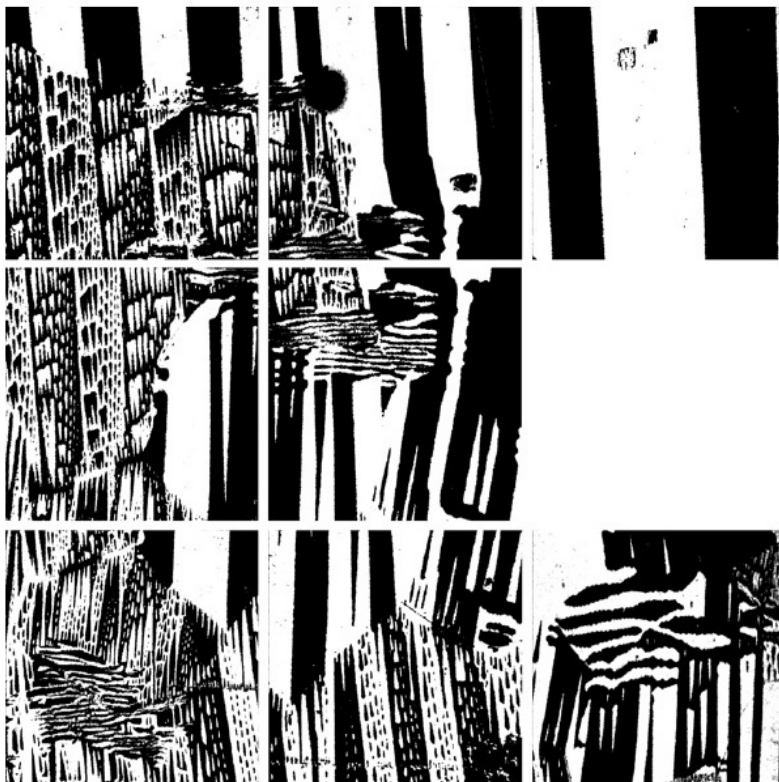


Figure 3.36: Magnetic domain structures in nine neighbouring areas under -70 MPa applied stress [Pere. 2012].

To describe these results, Perevertov et al. mentioned that the role of stress on magnetic domain structures is to activate one or more of the easy crystal axes depending on the sign of the stress and its alignment relative to the crystal's orientation. Perevertov et al. showed that the energy difference between [001] and [010] (or [100]) directions is minimum at some critical magnetic field and stress levels using the minimization of total magnetic energy under the stress. Therefore, some new magnetic easy axes are favourable, which consequently causes the domain structure pattern to change. It is of note that compressive stress increases this energy difference between the axes. Finally, Perevertov et al. presented how the magnetization process has a delay with compressive stress, which is due to the effect of the stress on the energy differences between the magnetic easy directions and the change in the domain structure.

The influence of stress on the B-H loop and magnetization process has also been studied by Bulte et al. [Bult. 2002]. They also presented how stress causes an intersection between the B-H curves. As a reason for this, they mentioned that stress causes the angles between the easy axes in materials to change (which are [100], [010] and [001]), thereby causing a new anisotropy. Therefore, any non-easy aligned domains will be affected by this distortion due to the dependency of the domain energy on the domain angles relative to the crystallographic directions. Hence, the exchange energy of the system is also changed, which causes the domains to turn to a new favourable axis.

### **3.2. Effect of the micro-structure on magnetic Barkhausen noise**

Investigating the effect of the micro-structure on MBN has been the subject of much research for many years. For instance, Moorthy et al. successfully characterized different zones of welded steel using MBN [Moor. 1997a]. They also investigated the effect of the tempering temperature on the micro-structure with MBN [Moor. 2009]. In another example, Dobmann et al. presented the ability of MBN to differentiate between different types of cast iron with different graphite shapes in a casted car engine [Dobm. 2007]. In addition, Bükki-Deme et al. showed the effect of the rolling direction on the grain orientation and MBN results [Bükk. 2010]. Moreover, Ktena et al. used MBN as a tool for the characterization of electrical steels with different grain sizes [Kten. 2014]. These examples and many other papers illustrate the ability and sensitivity of MBN in relation to different micro-structures. Since the subject of this work is the relation between stress and MBN, most of the literature reviews are focused on the effect of stress on MBN.

### **3.3. Summary**

As is reported in Section 3.1, many researchers have published a number articles regarding the effect of stress on MBN. In a word, they state that the MBN signal increases with tensile strain

and decreases with compressive strain; however, they reported different reasons, specifically when they described the maximum of an MBN( $\sigma$ ) curve. For instance, Altpeter et al. [Altp. 2001, Altp. 2009] mentioned that magnetostriction is the main reason for the MBN( $\sigma$ ) behaviour, while Anglada-Rivera et al. [Angl. 2001] noted the changing of the effective magnetic field ( $H_{eff}$ ) and Stewart et al. [Stew. 2004] mentioned the Villari effect as the reasons for the MBN( $\sigma$ ) behaviour. In addition, Sablik et al. [Sabl. 1993a] proposed an analytical model to calculate the MBN( $\sigma$ ) curve; however, they did not discuss the reason. On the other hand, Perevertov et al. [Pere. 2007, Pere. 2012] studied the magnetization process under applying stress by means of measuring the B(H) curve and monitoring the domain structure. Although Perevertov et al. showed the effect of stress on the magnetization process, they did not mention the link between MBN and magnetization.

It is noteworthy that different material types and measuring conditions could involve the results [Seeg. 1966]. Therefore, although the authors of the publications reported in Section 3.1 had a similar goal, their results and discussions are somehow different to each other.

Furthermore, several researchers used XRD results to calibrate an MBN device for estimating residual stresses [Sors. 2012, Sors. 2013, Altp. 2002, Altp. 2009, Rabu. 2014, Cosa. 2014, Dobm. 2007, Höll. 1987, Thei. 1987, Sant. 2012a,b,c,d].

In summary of the last two sections, it should be mentioned that:

- The capability and sensitivity of MBN in relation to stress (MBN( $\sigma$ )) has been presented in a lot of research.
- There has been no comprehensive or deep explanation of MBN( $\sigma$ ) proposed thus far.
- A calibration process using XRD as the reference has been the standard method proposed for the estimation of residual stresses in almost all of the work published to date.

Therefore, the present work focuses on filling the gap observed between the results provided in the literature and the MBN( $\sigma$ ) relationship, which will be further discussed in the next chapters.

## 4. Statement and approach

As presented in Chapter 3, numerous researchers have investigated the effect of stress (applied and residual) on MBN. A variety of results and trends regarding the relationship between MBN and stress have been published showing that MBN reacts to stresses and stress changes. Based on these results, there is little doubt that MBN represents an alternative to those application cases where conventional stress measurement methods cannot be applied. It worth noting that almost all the results discussed in the various publications referenced above do not present any method to directly measure residual stresses. In other words, the different authors have only presented the trend for MBN at different levels of stress, and they then validated this trend with conventional stress measurement methods such as XRD. Several of them used XRD data to calibrate the MBN for stress measurements. It should be mentioned that such calibration processes are time consuming and expensive. None of the publications discussed or proposed any method based on MBN to measure stresses without any reference data. Therefore, an easy and quick non-destructive, high-resolution method for mapping and measuring micro-residual stress distributions is needed.

Recently, as presented in Chapter 3, a few researchers have proposed some possibilities for stress measurement based solely on the MBN response. Such opportunities arose from the behaviour of MBN parameters under applied stress. The MBN exhibited unique behaviour under applied stress whereby it increases with increasing applied stress and then decreases again. Altpeter and Rabung [Altp. 2009, Rabu. 2004] have shown that the position of the maximum in the MBN( $\sigma$ ) curve is directly related to the micro-residual stresses in the samples. In addition, Yelbay [Yelb. 2010] proposed a method based on the linear part of the MBN( $\sigma$ ) curve to measure the residual stresses of welded steel. Among the different publications addressing residual stress measurements, these two approaches developed the idea that residual stresses

can be measured by means of the stress dependency of the MBN without any need for reference data, such as that obtained from XRD measurements.

The work presented in this thesis has focused on developing an NDT method to characterize micro-residual stress distributions quantitatively, requiring minimal calibration effort. For this purpose, the MBN behaviour under applied stress (the MBN( $\sigma$ ) curve) was investigated to find a proper method for measuring micro-residual stresses. To this end, first of all, the behaviour of MBN under elastic and plastic strains has been investigated for different ferromagnetic (soft and hard magnetic) steels. Next, the MBN( $\sigma$ ) curve in the elastic range has been determined to find a proper physical reason behind the trend presented in MBN( $\sigma$ ). Therefore, the RESTMAB is presented. The RESTMAB includes the analysis of the behaviour of MBN signals under applied and residual stresses (MBN( $\sigma$ ) curves), proposes a method to calculate micro-residual stresses using MBN ( $\sigma$ ) curves, and performs a calibration method involving less effort since it does not require reference data for calibrating the MBN device, such as a BEMI device.

It should be noted that, although a lot of research has focused on the effect of stress on MBN, there is no exact or explicit clarification about the MBN( $\sigma$ ) curve. Most of the publications either do not present any reason or else just mention a short description. However, among the publications one can find some ideas as to what the reasons for the shape of the MBN( $\sigma$ ) curve might be. The investigation of magnetic hysteresis loops under applied stress is one of these aspects which could help in understanding the phenomenon [Bult. 2002, Pere. 2007, Pere. 2012]. Therefore, studying the effect of stress on the B-H loop can be of help in understanding the MBN( $\sigma$ ) curve. In other words, the interpretation of the method presented for mapping micro-residual stresses can be explained according to a model based on a crystal structure and its behaviour under stresses. Hence, besides proposing a method for mapping residual stress using MBN results, a model is postulated to calculate the micro-residual stress from MBN results. The model is based on the magnetic behaviour of a single crystal of ferromagnetic material under applied stress. Since a polycrystalline material consists of several single crystals which are oriented randomly, the model can be extended to polycrystalline materials. This model simplifies the effect of stress (micro-residual and applied stresses) on micro-magnetic properties for a better understanding. The model is proposed as follows:

- Static magnetization study:
  1. Assume a 2D single crystal of a ferromagnetic material which exhibits magnetostrictive behaviour.
  2. Calculate the magnetostriction and, consequently, the induced stresses at completely fixed boundaries (magnetostriction effect) (Figure 4.1a). The stresses generated due to

magnetostriction are the maximum micro-residual stresses ( $\epsilon_R$ ), which can be generated in a crystal structure at completely fixed boundaries.

3. Apply  $\epsilon_R$  to the model and calculate the induced magnetization (M) (the Villari effect) due to the residual stresses (Figure 4.1b).

- Dynamic magnetization study

1. Calculate the magnetostriction and magnetization of the crystal under a varying magnetic field. This gives the  $\epsilon_R(H)$  and  $M(H)$  of a sample at completely fixed boundaries.
2. Apply the calculated  $\epsilon_R$  to the model and measure the  $M(H)$  curve at completely free boundaries. Furthermore, calculate the  $M(H)$  curve for a sample without any residual stresses at completely free boundaries.
3. Compare the  $M(H)$  measured from Steps 1 and 2 mentioned above. The difference between the  $M(H)$  curves between samples with and without residual stresses shows the effect of the minimum residual stresses ( $\epsilon_R$ ) on the magnetization curve. Using this result, the MBN behaviour of a sample with residual stresses can be explained since the MBN response reflects the magnetization process of the sample.
4. Calculate the  $M(H)$  curves at different magnetic field angles related to the model according to Steps 1 and 2 above. This will show the behaviour of a single crystal under different magnetizing directions.
5. Calculate the  $M(H)$  curve under applied stress for the situation mentioned under Step 2. This presents the effect of the applied stress on the  $M(H)$  curve of a single crystal.
6. Calculate the  $M(H)$  curve under applied stress at different angles related to the magnetization angle.
7. Apply the non-linear elastic-plastic stress-strain behaviour to the model and calculate the  $M(H)$  curves.
8. Calculate the  $M(H)$  curve for a single crystal with a different crystal structure (BCC, HCP). This gives the effect of the micro-structure on the magnetization process of the model.
9. After performing all the above steps, a polycrystalline model can be made. Now, the magnetization behaviour of a polycrystalline sample can be calculated and explained.

All these calculations can be performed either with finite element modelling (FEM) software, such as COMSOL, or with analytical methods using, for example, MATLAB. For the validation of the model, measurement of the magnetostriction and hysteresis curves under stress is required. Moreover, monitoring the behaviour of the domain structures under stress eases the understanding of the material's behaviour under stress.

Figure 4.2 shows all the steps of the model presented and Figure 4.3 presents a schematic overview of the various steps and tests which are performed to achieve the goals of this work.

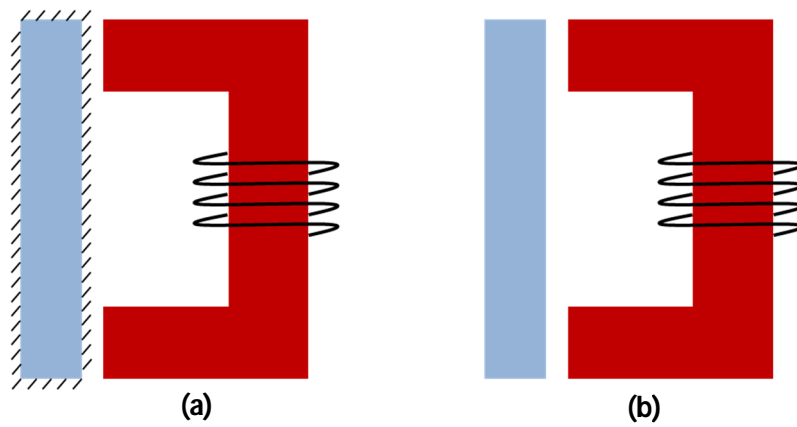


Figure 4.1: Schematic design of the model's setup for a single crystal on a) fixed-boundary and b) free-boundary conditions.



Figure 4.2: Process flow diagram of the model presented.

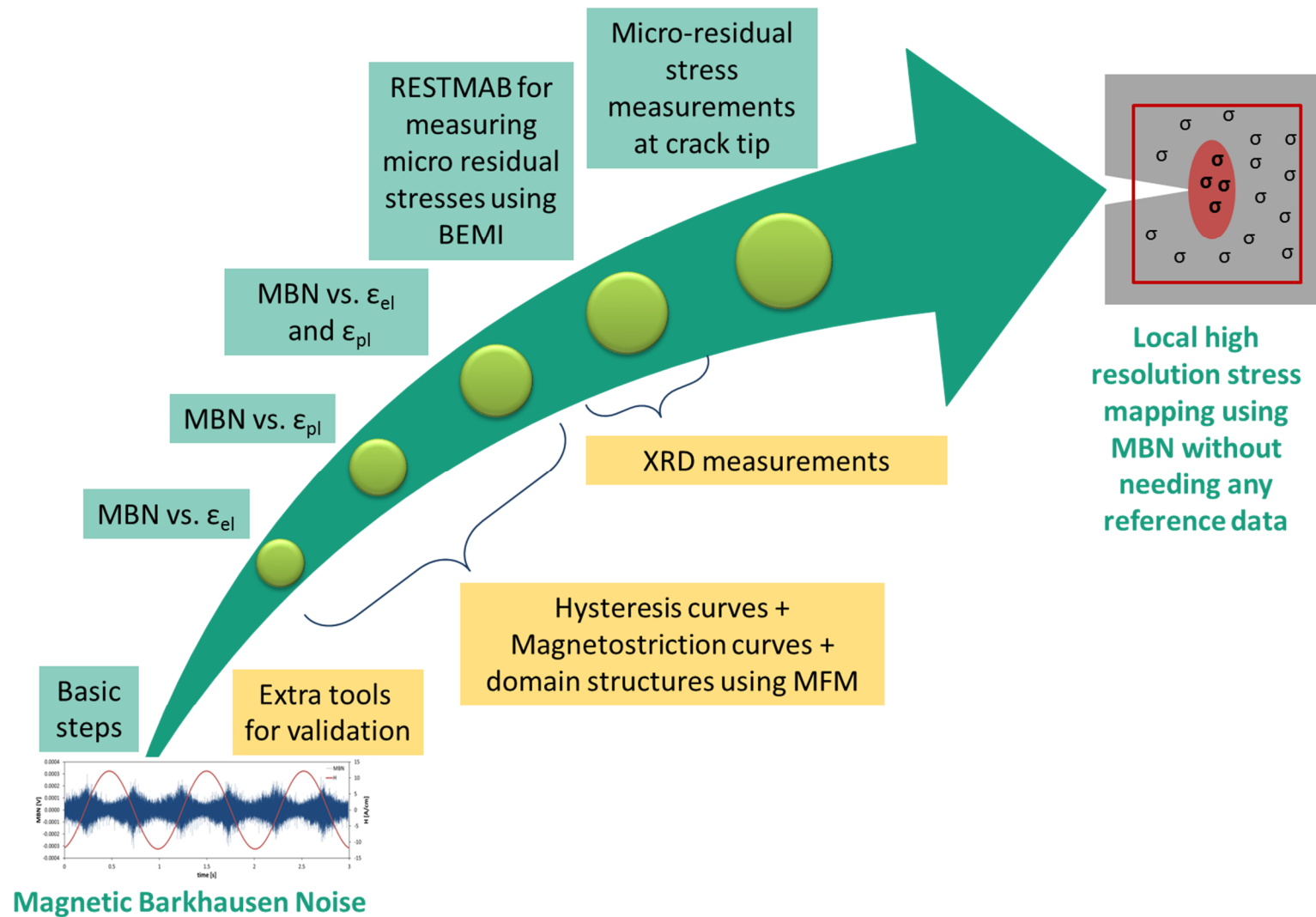


Figure 4.3: Schematic overview of work presented and its steps. The green blocks show the basic steps and the yellow blocks present the extra techniques or measurements which have been performed for validation and the better understanding of the results.

## 5. Materials, experimental methods and devices

In this chapter, first of all, the preparation of the sample is described. Next, the experimental micro-magnetic methods are briefly explained. In the next section, the devices which have been used in this work are introduced. In the last section, the experimental setups which are used to achieve the goals of this work are described step by step.

### 5.1. Sample preparation

Two different ferromagnetic steels with different micro-structures and micro-magnetic properties were used in this research: Fe-Si steel, as a ferritic steel, and a pipeline steel as a martensitic steel. Table 5.1 shows the chemical composition of these two steel grades.

**Table 5.1: Chemical composition of the steel grades used.**

Fe-Si		Pipeline	
element	Percentage (%)	element	Percentage (%)
C	0.003	C	0.16
Si	2.7	Si	0.31
Mn	0.15	Mn	0.92
P	0.01	Cr	0.51
Si	0.001	Mo	0.53
Fe	Rest	Ni	0.54
		Fe	Rest

Figure 5.1a shows the micro-structure of the Fe-Si sample, which has been obtained through light microscopy. The pipeline steel used is a commercial steel which was received from a steel company. Figure 5.1b shows the micro-structure of the pipeline steel as received, where the images have been taken with a scanning electron microscope (SEM). The grain sizes of the samples were measured using the electron backscatter diffraction (EBSD) technique and were found to be 50  $\mu\text{m}$  and 10  $\mu\text{m}$  for the Fe-Si and pipeline steels, respectively.

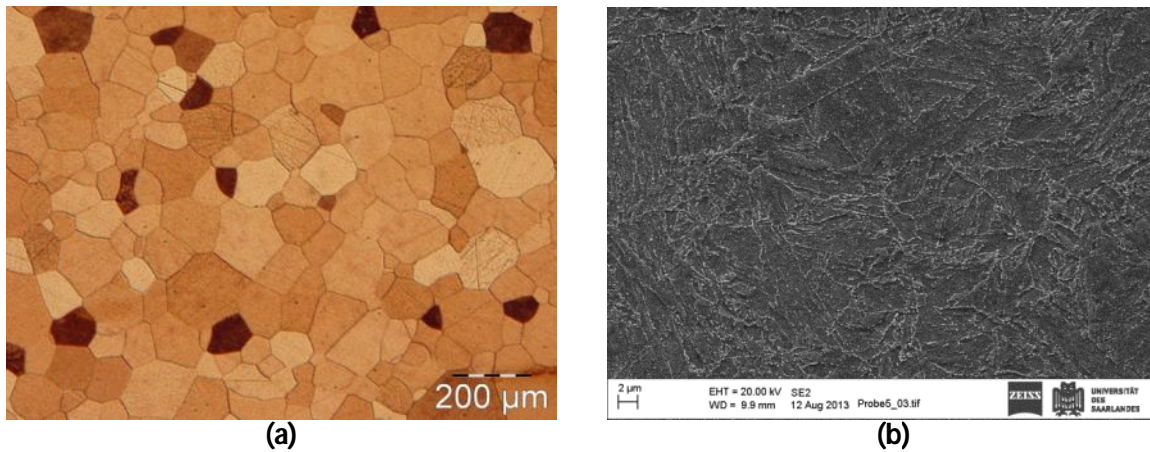


**Figure 5.1: a) Micro-structure of Fe-Si steel taken with light microscopy, and b) micro-structure of pipeline steel taken with scanning electron microscopy.**

First, small tensile test specimens (thickness 1 mm, gauge length 20 mm, width 4 mm) were cut (Figure 5.2a). Next, a tensile test was performed on each sample type using an Instron servo hydraulic tensile tester 8511.20 controlled by an MTS 6342F extensometer to determine the yield stress (Figure 5.2b). As expected, the Fe-Si steel has a yield point of 326 MPa and the pipeline steel a yield point of 1,100 MPa, due to the fact that Fe-Si has large grains and a ferritic micro-structure while the pipeline steel has a fine martensitic micro-structure. These micro-structures also affect the micro-magnetic properties of the samples in such a way that the Fe-Si steel is magnetically soft and the pipeline steel is magnetically hard. Moreover, no work hardening in the stress-strain curve of the pipeline steel was observed, while the Fe-Si steel shows work hardening. This information reveals that the dislocation density in the pipeline steel stays constant while it changes in the Fe-Si steel during plastic deformation. Therefore, the changes in dislocation densities are negligible in the pipeline steel but in the Fe-Si steel they are not. On the other hand, the investigation of the effect of crystallographic direction on the magnetic parameters is easier for the Fe-Si samples when compared to the samples made from the pipeline steel since the Fe-Si steel has a larger grain size in comparison to the pipeline steel sample. In other words, the two steel grades are two different materials which exhibit differing magnetic properties and behaviour. Therefore, these two model materials were chosen for this research.

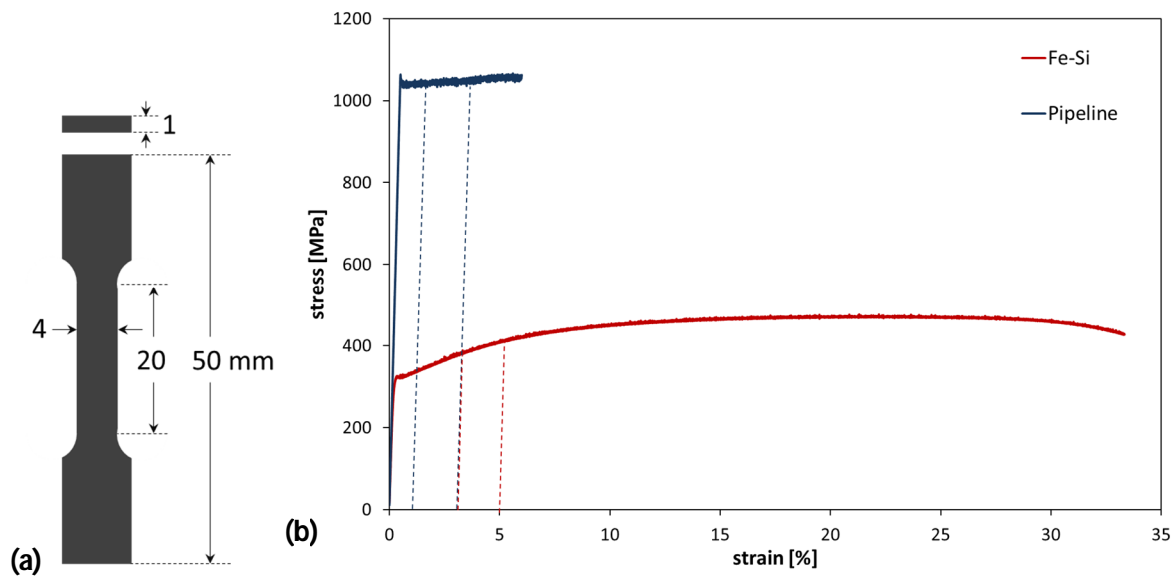


Figure 5.2: a) Sample shape and dimensions, and b) engineering stress-strain curve of the pipeline and Fe-Si steels.

## 5.2. Devices

This section focuses on the devices which were used for the research presented here. A short theoretical background of each device is discussed to give an overview of how each of them operates.

### 5.2.1. The micro-magnetic, multi-parameter, micro-structure and stress analysis device

The **micro-magnetic multi-parameter micro-structure and stress analysis (3MA)** system is a combination of four non-destructive electromagnetic testing methods in a testing device. It was developed at the Fraunhofer Institute for Non-destructive Testing (IZFP) and allows one to determine magnetic materials' properties quantitatively [Altp. 2002, Altp. 2009, Rabu. 2014, Cosa. 2014, Dobm. 2007, Höll. 1987, Thei. 1987].

The harmonic analysis (HA) of a tangential magnetic field, MBN, incremental permeability (IP) and multi-frequency eddy current (EC) testing comprise four different methods which are combined in the 3MA system. Four electromagnetic testing methods described below are performed in the 3MA system, one after another. The 3MA system has the option whereby each method relating to the measuring parameters, such as the magnetizing field strength, filtering, gains, etc., can be set separately. Any of the four methods can be enabled or disabled.

Figure 5.3 shows a 3MA system consisting of the 3MA hardware, the 3MA sensor and a laptop computer for controlling the whole system. The 3MA hardware contains the necessary electronic

parts for the four testing methods. The sensor includes a magnetizing device, various magnetic inductive pickup coils, a Hall sensor and preamplifier electronics.



**Figure 5.3: The 3MA device and a standard sensor (picture © Bellhäuser).**

The 3MA system includes the following electromagnetic non-destructive testing methods:

- HA of the tangential magnetic field strength;
- MBN analysis;
- IP analysis;
- Multi-frequency EC impedance analysis.

A short description of each method and the parameters which can be measured using the 3MA equipment has been provided in Section 5.3. Since, in most materials, the separation of the different parameters affecting magnetic properties such as micro-structure and stress is difficult, different electromagnetic methods (being differently sensitive to micro-structure and stress) are required such that, when using the appropriate combination of the test methods, the different properties of the material such as the micro-structure, stress, texture and temperature can be separated. The differentiation in terms of penetration depth of individual methods is an additional advantage of the 3MA system. The multi-frequency EC analysis can be performed at four different excitation frequencies, obtaining different information from different depths of the specimen. As well as multi-frequency EC analysis, the sensitivity of the IP also depends on the excitation frequency of the high-frequency alternating field. Similarly, the MBN analysis can also present the different levels of information through the selection of different analysis frequencies. In contrast, the HA of the tangential magnetic field only depends on the magnetization frequency. This ensures that the 3MA system presents information from different

depths of a specimen. In addition, the 3MA system allows for sweep measurements in an arbitrary frequency range. Therefore, there are many variations for combinations of measurement parameters which are used for the computation of the results. In total, there are 41 testing parameters used for the calibration of the 3MA system. The calibration is achieved through a mathematical correlation between the target - such as the micro-structure and mechanical properties of the sample - and the testing parameters being measured with the 3MA system.

**5.2.1.1. The standard sensor of the micro-magnetic, multi-parameter, micro-structure and stress analysis system**

The principle design of the 3MA sensor is shown in Figure 5.4. Since the 3MA system periodically magnetizes the sample, an electromagnet is integrated inside the sensor. A U-shaped electromagnet (also called the “yoke”) has a core made from a steel transformer and a coil wound around it. This electromagnet magnetizes the sample periodically. To this end, an alternating voltage is applied to the coil whereby the frequency and amplitude depend on the magnetization frequency and the amplitude. The magnetic field is nearly homogenous in the middle of the pole shoes; therefore, the sensing elements consisting of at least one Hall probe and an inductive pick-up coil are located at this position. The Hall probe is used as a measuring element of the tangential magnetic field on the surface of the material. The measurement of the tangential magnetic field is used, on the one hand, to control the magnetic field strength, and on the other hand for calculating the parameters measured. The MBN, EC and IP are all measured and/or generated by the inductive pick-up coils. Figure 5.5 shows a standard sensor used for the 3MA system.

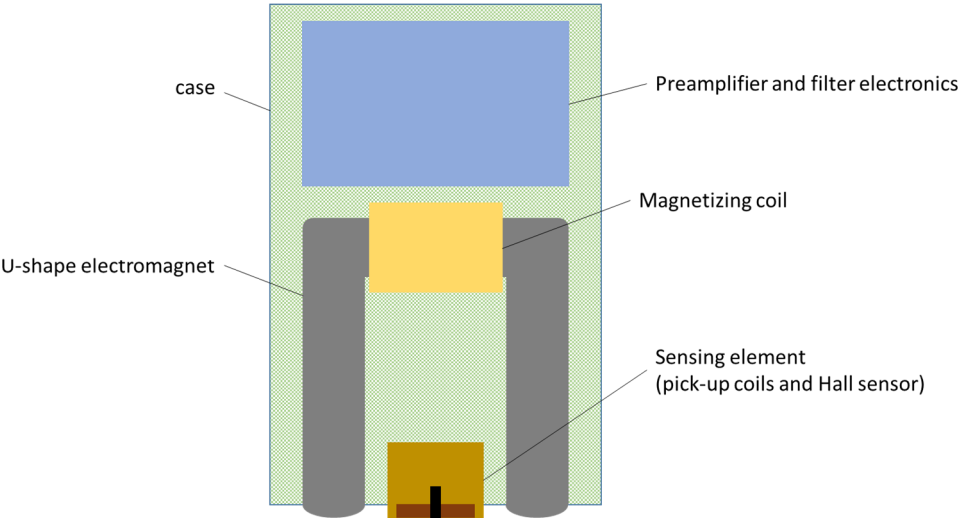


Figure 5.4: Schematic sketch of a standard 3MA sensor.



Figure 5.5: A standard 3MA sensor.

### 5.2.2. Barkhausen noise and eddy current microscopy

The BEMI is a scanning probe microscope for the non-destructive testing of electromagnetic materials (Figure 5.6) [Altp. 1992a, Altp. 1992b, Bend. 1997]. The BEMI is also a 3MA system, using a miniature probe for scanning the surface of a material to measure its micro-magnetic properties. The probe, which is a modified video cassette recorder head, consists of a miniaturized ferrite core with two parts just separated by an air gap of 300 nm at the head of the probe. Two coils are wound around each part of the ferrite cores, which act as sender and receiver coils respectively (Figure 5.7).

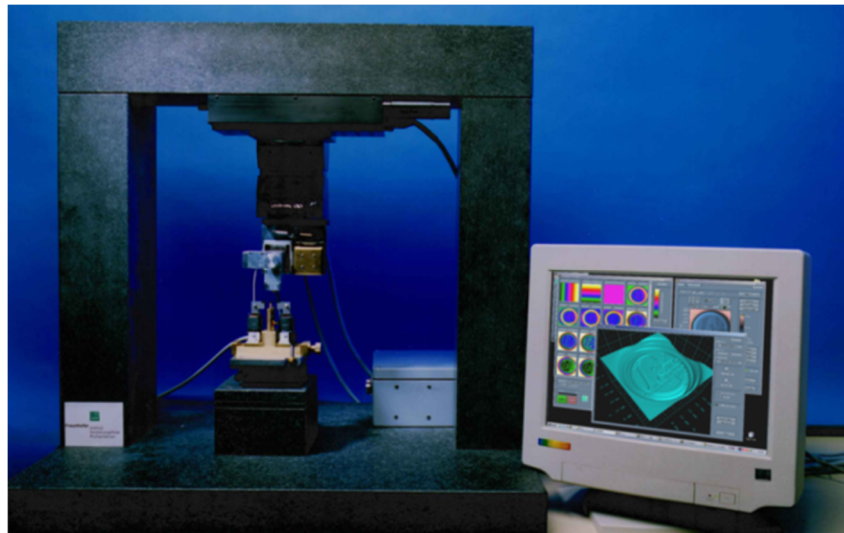
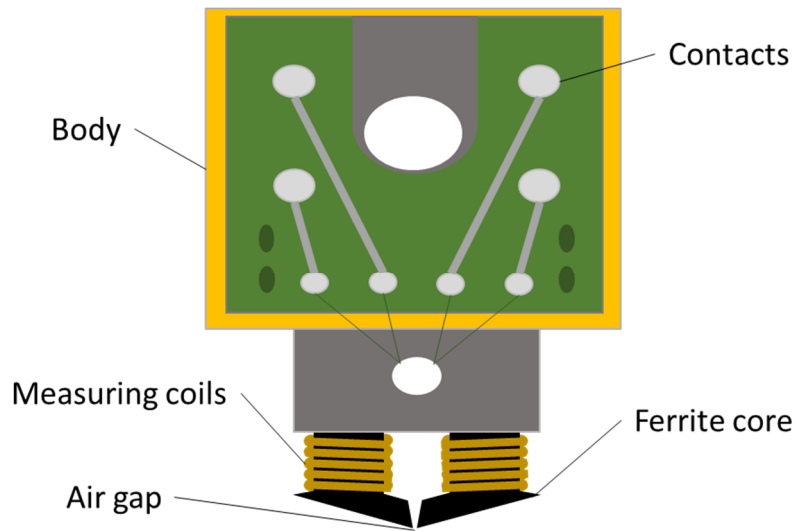


Figure 5.6: The BEMI.



**Figure 5.7: Schematic sketch of the BEMI sensor.**

Using a precision manipulator, the probe moves over the sample surface such that the air gap of the core is bridged by the sample. Therefore, the impedance of the coil will thus change due to the permeability and conductivity of the sample at the contact point in the gap. This property is useful for EC testing and IP testing. The EC and IP testing can be performed at four testing frequencies at the same time within a range of 10 kHz to 4 MHz. For Barkhausen noise testing, the sample is additionally magnetized using an electromagnet at a magnetic field frequency of 10 Hz to 1 kHz and magnetic field amplitudes of 5-100 A/cm. DW jumps induce electrical voltage pulses in the coils of the probe. The HA is carried out globally using a stationary measurement of the magnetic field strength with a Hall sensor. It is worth mentioning that all four methods are performed with active magnetization as for the 3MA system.

The device achieves a measurement speed of up to five points per second and can scan a maximum area of 30×15 mm in the X and Y directions at a maximum spatial resolution of 10 μm. Figure 5.8 shows a microscopic image and a scan image of a ferritic steel with notches from 20 μm up to 1 μm which are filled with a non-conductive polymer. As can be seen, the BEMI is able to easily detect the notches up to 10 μm.

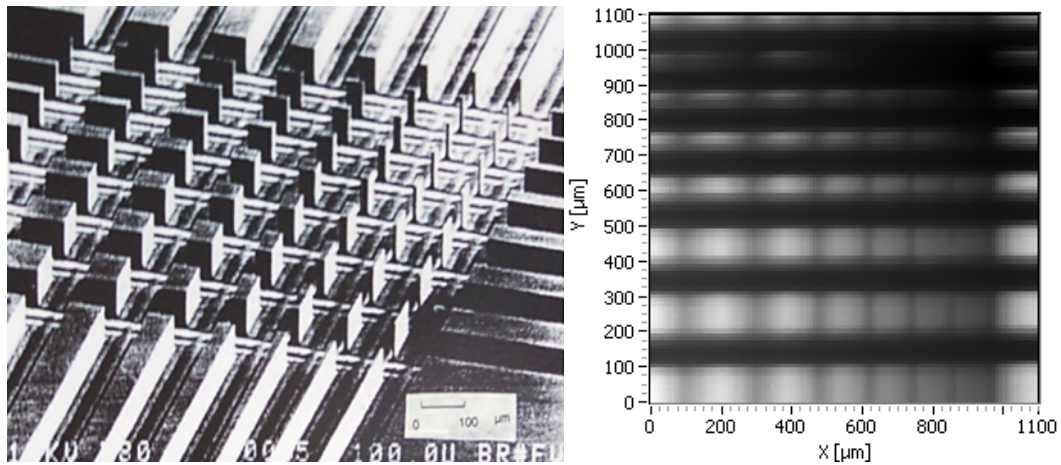


Figure 5.8: a) Image of a ferritic steel with notches filled with a non-conducting polymer using a light microscope, and b) a BEMI scan of the same sample which shows the lateral resolution of the BEMI.

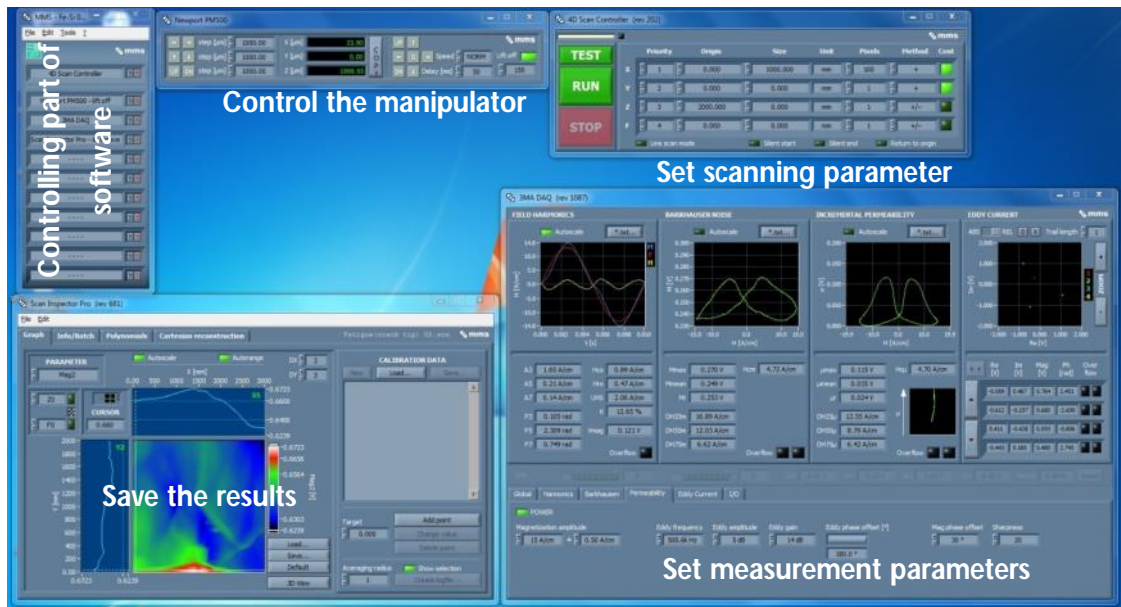


Figure 5.9: Screenshot of the software needed to control the BEMI as well as for saving and analysing the scan data.

A comprehensive software package is used to control the mechanical and electronic components as well as for evaluating and documenting the measurement results. Figure 5.9 shows a screenshot of all the modules included in the BEMI device. The output of the software, as a result, is a 2D colour-coded image for each measurement parameter, although a representation of the results as a 3D image is possible too. The software also has the option to calibrate a combination of measurement data with reference values (residual stress, film thickness, hardness, etc.). This can be done using multi-parameter regression analysis and/or pattern recognition.

### 5.3. Micro-magnetic methods

#### 5.3.1. Harmonic analysis of the tangential magnetic field strength

The sample has been magnetized using a yoke, which generated an alternating magnetic field following a sinusoidal excitation. The time signal of the tangential magnetic field has been measured by a Hall sensor, which was mounted halfway between the pole shoes of the yoke. Figure 5.10 shows the applied and measured field signal. A distortion in the curve shape of the measured signal is clearly visible, especially around a zero magnetic field strength. The non-linear behaviour of the ferromagnetic hysteresis is the reason for this distortion. Using fast Fourier transformation (FFT), the harmonic parts - which contain information about the ferromagnetic properties of the sample tested - are numerically determined. Table 5.2 lists the parameters which are the output of the HA.

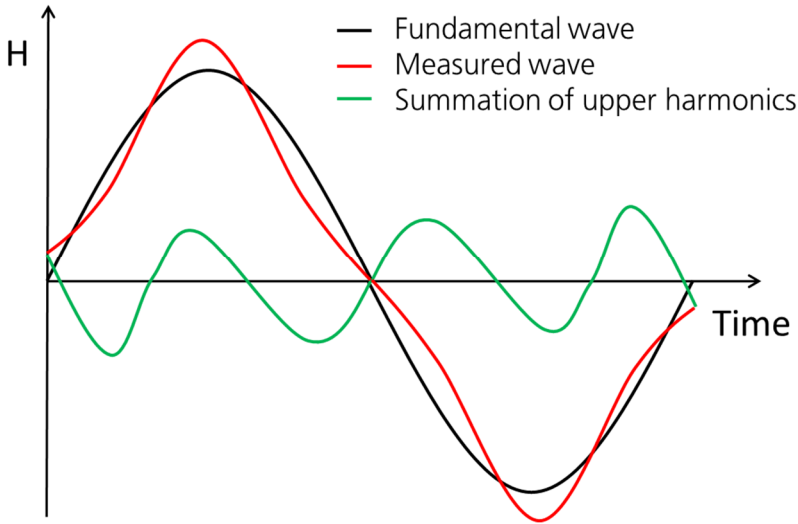


Figure 5.10: Output of the HA method using the 3MA system.

Table 5.2: Parameters obtained from the HA method.

Test Variable	Description
A3, A5, A7	Amplitudes of the third, fifth and seventh harmonics of $H_t$
P3, P5, P7	Phase shifts of the third, fifth and seventh harmonics compared to summation of all harmonics amplitudes
UHS	harmonic distortion factor
K	coercive field strength derived from the HA
Hco	summation of upper harmonics of $H_t$ at zero crossing
Hro	

#### 5.3.2. Magnetic Barkhausen noise

The basics of MBN have been described in detail in Chapter 2. As mentioned previously, the Barkhausen effect is a series of sudden changes in the size and orientation of the domains

which occur during a continuous magnetization or demagnetization process. These sudden changes induce high-frequency pulses in an air coil which is mounted between the pole shoes of the yoke. Figure 5.11 shows the output of the 3MA system for MBN, showing the envelope of the MBN versus the applied magnetic field strength. From the MBN envelope shown in Figure 5.11, seven parameters are derived which are listed in Table 5.3.

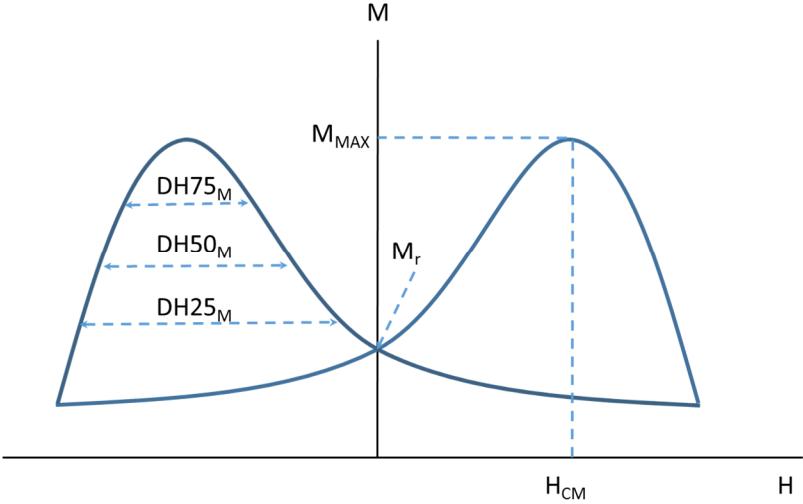


Figure 5.11: Schematic output of the 3MA system for MBN measurements.

Table 5.3: Parameters derived from MBN method using the 3MA system.

Test Variable	Description
$M_{MAX}$	Maximum of the M(H) curve during one cycle
$M_{Mean}$	Average of the M(H) curve during one cycle
$M_r$	Noise amplitude at the remanence point
$H_{CM}$	Field strength at the maximum of the M(H) curve
$DH25_M$	Width of the M(H) curve at 25% curve amplitude
$DH50_M$	Width of the M(H) curve at 50% curve amplitude
$DH75_M$	Width of the M(H) curve at 75% curve amplitude

### 5.3.3. Multi-frequency eddy current

EC testing is a classic non-destructive testing method used to characterize the effect of the conductivity and permeability of materials on a coil's impedance. ECs which are caused by an alternating magnetic field in a conductive material generate a magnetic field in the opposite direction to the excitation field. The impedance of the measuring coil is dependent on the conductivity and permeability as well as the lift-off and surface roughness. Using the multi-frequency EC method allows for inspection down to different depths of a sample, depending on the testing frequency, the electrical resistance and the magnetic permeability of the sample. With a 3MA system, up to four different frequencies can be applied in a time-multiplexed way.

Figure 5.12 presents an impedance plane showing the real and imaginary parts of the impedance. In Table 5.4, a description of 16 parameters is provided which can be measured with the EC testing method.

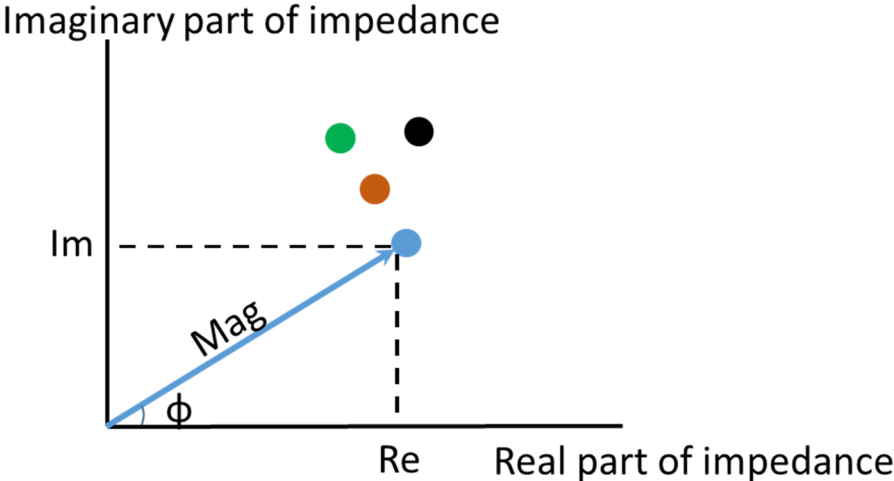


Figure 5.12: Schematic impedance plane output from an EC test using the 3MA system.

Table 5.4: Parameters derived from EC testing using the 3MA system.

Test Variable	Description
Re1, Re2, Re3, Re4	Real part of the EC signal at frequency Nos. 1, 2, 3, 4
Im1, Im2, Im3, Im4	Imaginary part of the EC signal at frequency Nos. 1, 2, 3, 4
Mag1, Mag2, Mag3, Mag4	Magnitude of the EC signal at frequency Nos. 1, 2, 3, 4
Ph1, Ph2, Ph3, Ph4	Phase of the EC signal at frequency Nos. 1, 2, 3, 4

**5.3.4. Incremental permeability**

The IP technique is based on the reversible portion of the temporary magnetization variation. The low-frequency dynamic magnetization with the exciter frequency  $f_E$  and the magnetic field rejection  $H_E$  is superimposed by an EC with a substantially higher frequency at a significantly lower modulation ( $f_D \gg f_E, H_D \ll H_E$ ). The superimposed alternating field causes small internal hysteresis loops, of which the slope of the loop produces the IP data ( $\Delta\mu \sim \Delta B/\Delta H$ ). If the IP is drawn versus the magnetic field strength, then a curve similar to the Barkhausen noise signal envelope is generated, called the  $\mu(H)$  curve (Figure 5.13). Table 5.5 shows the parameters which have been derived from Figure 5.13.

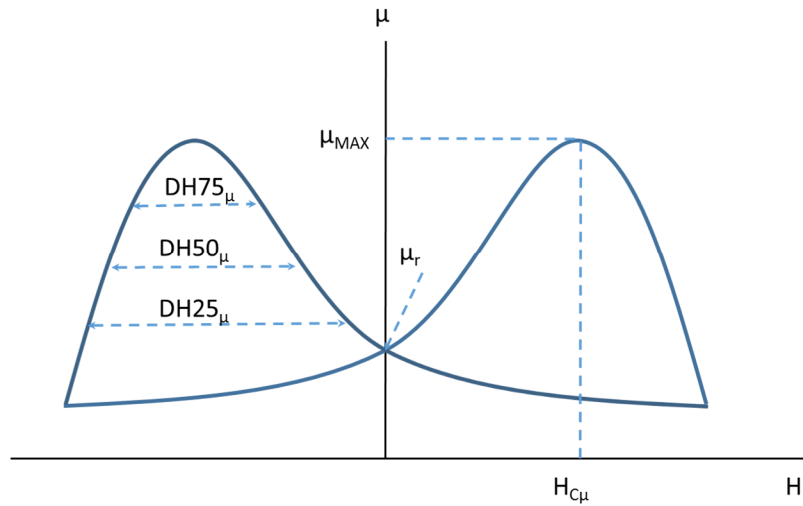


Figure 5.13: Schematic output of the 3MA system for IP measurements.

Table 5.5: Derived parameters from the IP method using the methods provided by the 3MA system.

Test Variable	Description
$\mu_{MAX}$	Maximum of the $\mu(H)$ curve during one cycle
$\mu_{MEAN}$	Average time period of the $\mu(H)$ curve during one period
$\mu_r$	Noise amplitude at the remanence point
$H_{C\mu}$	Coercive field strength at the maximum of the U(H) curve
DH25 $_{\mu}$	Expansion of the $\mu(H)$ curve at 25% curve amplitude
DH50 $_{\mu}$	Expansion of the $\mu(H)$ curve at 50% curve amplitude
DH75 $_{\mu}$	Expansion of the $\mu(H)$ curve at 75% curve amplitude

### 5.3.5. Hysteresis measurement

The hysteresis loop is obtained by measuring the magnetic flux of a ferromagnetic material as a function of the magnetic field strength in an alternating field. To apply the magnetic field, an electromagnet is needed. In experiments performed here, a small yoke was used to magnetize the sample from below. In Section 5.4.1.2, the design of the yoke is described in detail. A function generator (TTi 40 MHz DDS model TG4001) was used to generate a sinusoidal wave. The output of the function generator was connected to the KEPCO bipolar operational power amplifier model BOP 72-6m, which allowed the output signal of the function generator to be amplified. The power amplifier was connected to the yoke. A Hall sensor was used to measure the magnetic field strength (H) at the surface of the material. An indirect method was used for measuring the magnetic flux density (B) using a small coil with 100 turns wound around the sample (Figure 5.14a). The voltage induced in the coil is proportional to the flux change ( $d\varphi$ ) within the sample. Therefore,  $\varphi$  was calculated using the integration of  $d\varphi$  over time. Since the

flux density ( $B$ ) is the product of the flux ( $\phi$ ) and the cross-section ( $A$ ) of the sample ( $B = \phi.A$ ). Figure 5.14b shows a B-H loop and Table 5.6 shows the parameters which can be derived from the curve.

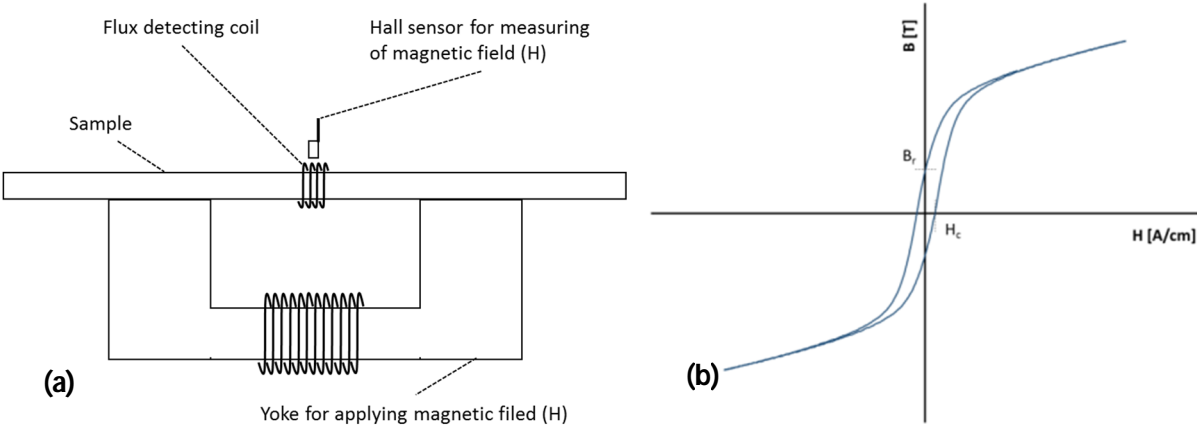


Figure 5.14: (a) Schematic setup for measuring the B-H curve, and (b) a B-H curve measured on a sample.

Table 5.6: Parameters derived from a B-H curve.

Test variable	Description
$H_c$	Coercive field strength
$B_{max}$	Maximum magnetic flux density in a period
$B_r$	Remanence point
$Ah$	Hysteresis loss
$\mu_{rc}$	Relative permeability at the coercive field
$\mu_{rr}$	Relative permeability at the remanence point

### 5.3.6. Magnetostriction measurement

Dimension changes of a sample when subjected to a magnetic field are called magnetostriction. Therefore, dimension and magnetic field measurements are necessary for magnetostriction measurement. A magnetic field has been applied using the same coil as for the other measurements and a Hall sensor was used to monitor the magnetic field strength. A strain gauge model HBM 3/120LY41A was attached to the surface of the sample. Since the dimension change obtained from magnetostriction is very small (~10 μm/m), a high amplification of the strain gauge output signal is required. Therefore, the strain gauge was connected to a special strain gauge amplifier, which allowed for a connection to a data acquisition device. Figure 5.15 a shows a schematic setup for magnetostriction measurement. If the output of the strain gauge is drawn against the output of the Hall sensor, a magnetostriction curve is obtained. Table 5.7 explains the parameters derived from the magnetostriction curve.

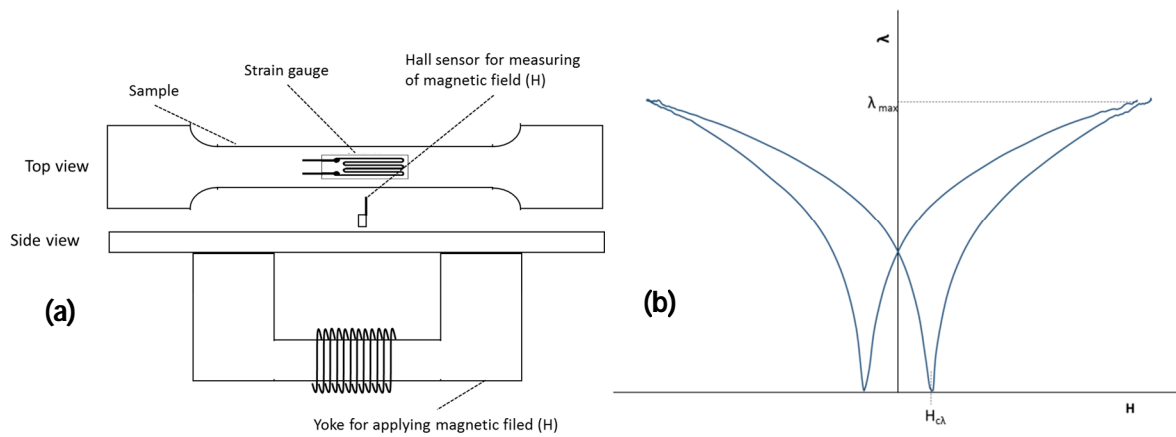


Figure 5.15: (a) Schematic setup for the measurement of magnetostriction, and (b) a magnetostriction curve measured from a sample.

Table 5.7: Parameters derived from a magnetostriction curve.

Test Variable	Description
$H_{C\lambda}$	Coercive field strength at the minimum of the $\lambda(H)$ curve
$\lambda_{MAX}$	Maximum magnetostriction in a period

## 5.4. Experimental setups

In this section, the experimental setups which have been used for this thesis are explained. First, the behaviour of non-deformed samples of unloaded and elastically loaded samples is investigated. Secondly, the behaviour of plastically pre-deformed samples for unloaded and elastically loaded samples is analysed. Next, the micro-magnetic and domain structure of non- and pre-deformed samples is studied, and then the novel RESTMAB used for stress measurements is proposed. In the last step, two applications of the RESTMAB are explained.

### 5.4.1. Micro-magnetic characterization of non-deformed samples

#### 5.4.1.1. Investigation of the micro-magnetic properties of non-deformed samples in an unloaded state

In the first step, the micro-magnetic properties of the Fe-Si and pipeline steels were tested using a BEMI, hysteresis and magnetostriction measurements to determine the effect of the micro-structure on the samples' micro-magnetic properties. The test setups and devices have been described in Sections 5.2 and 5.3.

**5.4.1.2. Investigation of the micro-magnetic properties of non-deformed samples in an elastically loaded state**

Investigating the effect of tensile stress on the samples' micro-magnetic properties was the next step. To this end, a small tensile testing machine (Kamarath & Weiss GmbH) was used which was small enough to be integrated within the BEMI. The same tensile testing machine was used for the other experiments in this work as well.

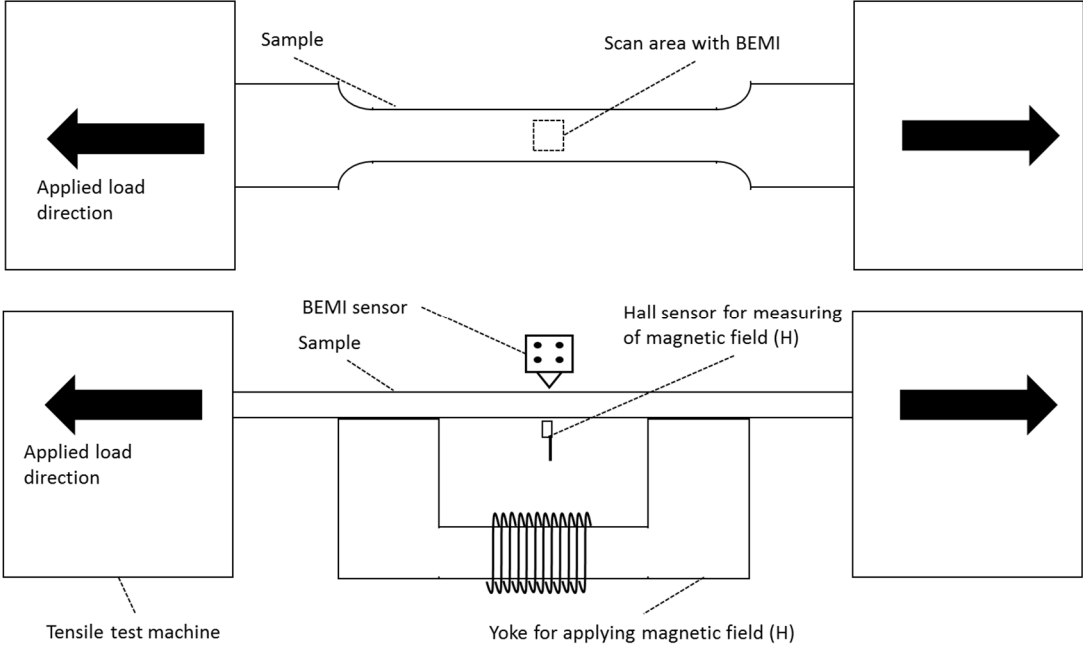


Figure 5.16: Schematic setup for in situ MBN measurement under applied stress.

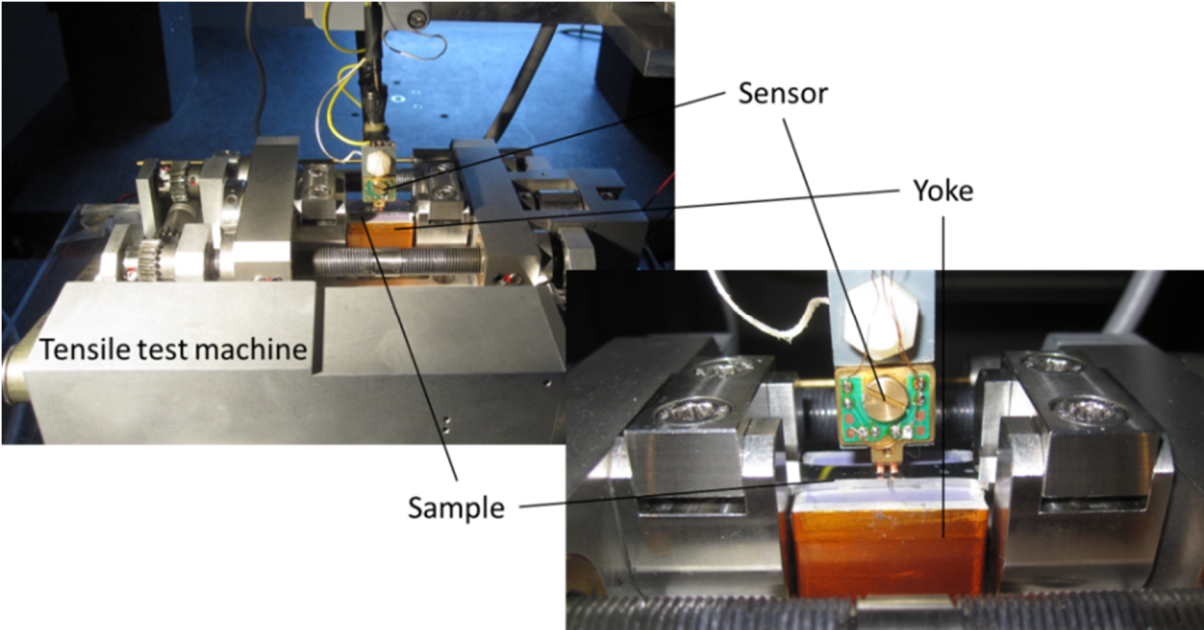
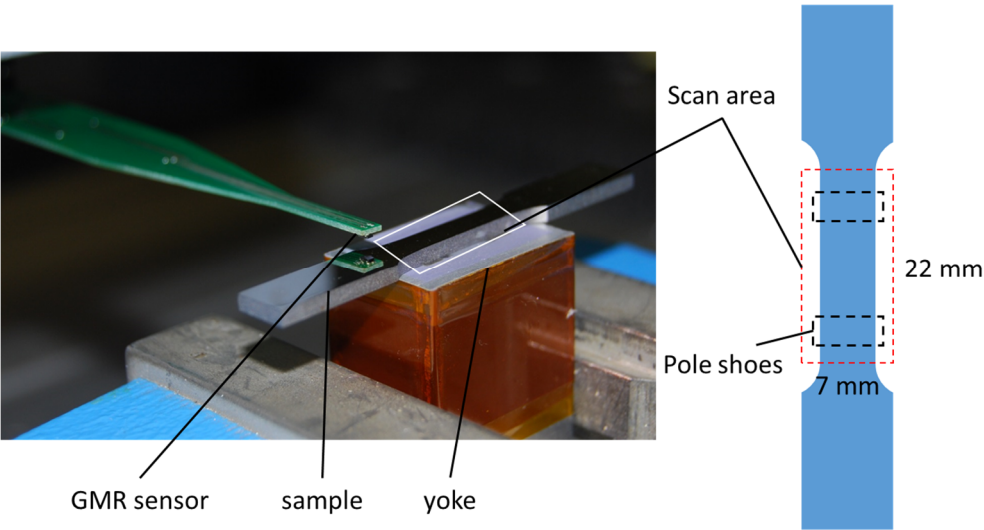


Figure 5.17: Actual setup for in situ MBN measurement under applied stress.

The measurement setup for the in situ measurement of micro-magnetic parameters under applied stress is illustrated in Figure 5.16 and Figure 5.17. It is worth noting that some modifications were made to the BEMI, hysteresis and magnetostriction measurement setups. First of all, an electromagnet (a yoke) was designed to fit inside the tensile testing machine between the sample clamps (Figure 5.17 and Figure 5.18). U-shaped transformer steel plates were used as a core of the yoke and a Hall sensor was mounted halfway between the two pole shoes. Since the yoke was used for magnetizing the sample from below while the pick-up coil was placed on top of the sample, it was important to know in which area the magnetic field could be assumed to be homogenous. Thus, the tangential magnetic field close to the surface was measured using a very small GMR sensor (Sensitec GF705). For this purpose, an area over the sample was scanned at different active magnetization amplitudes. Figure 5.18 and Figure 5.19 show the setup and results obtained from the test mentioned above. As can be seen in Figure 5.19 and Figure 5.20, the magnetic field is nearly homogenous for all different magnetization amplitudes in a small area of 1.5×1.5 mm in the middle of the sample. Later on, all the measurements were performed in this area. A BEMI measurement was performed as well by scanning a surface of 1×1 mm with a lateral resolution of 10 μm using the BEMI sensor. It of note that the magnetic field strength (H) was measured using the Hall sensor in the middle of the yoke and that the MBN signals were picked up with one of the two coils in the BEMI sensor.



**Figure 5.18: Measurement of a tangential magnetic field using a GMR sensor.**

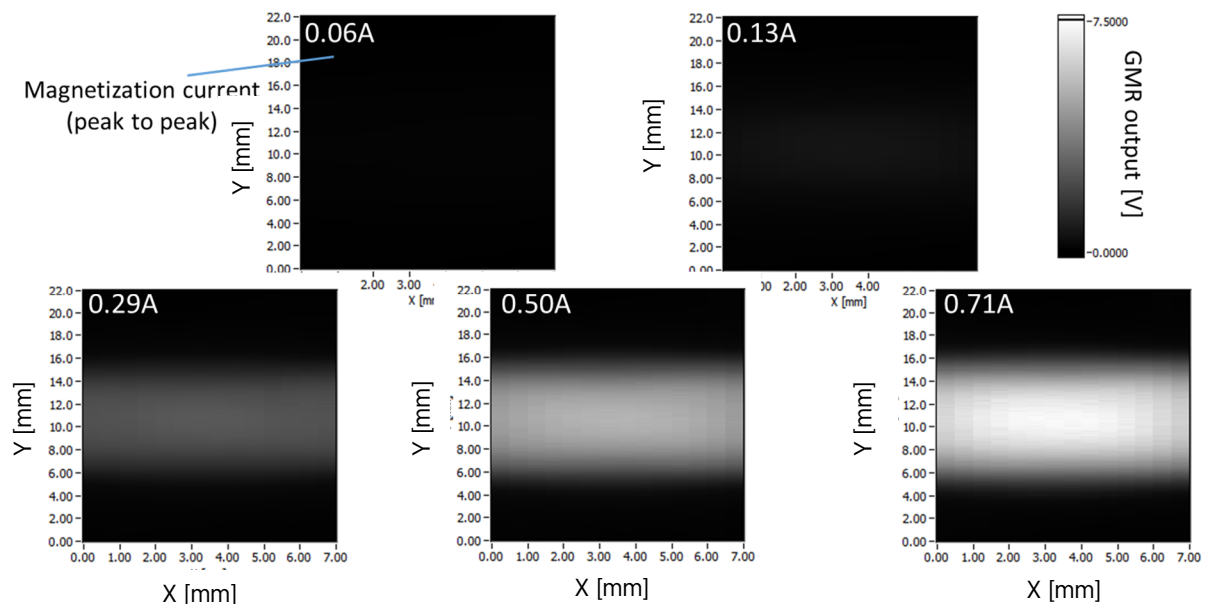


Figure 5.19: The GMR output related to the strength of the magnetic field at different magnetization currents.

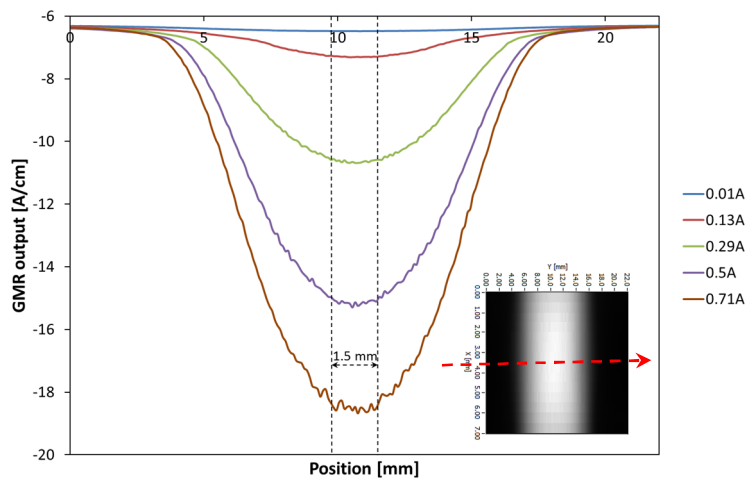
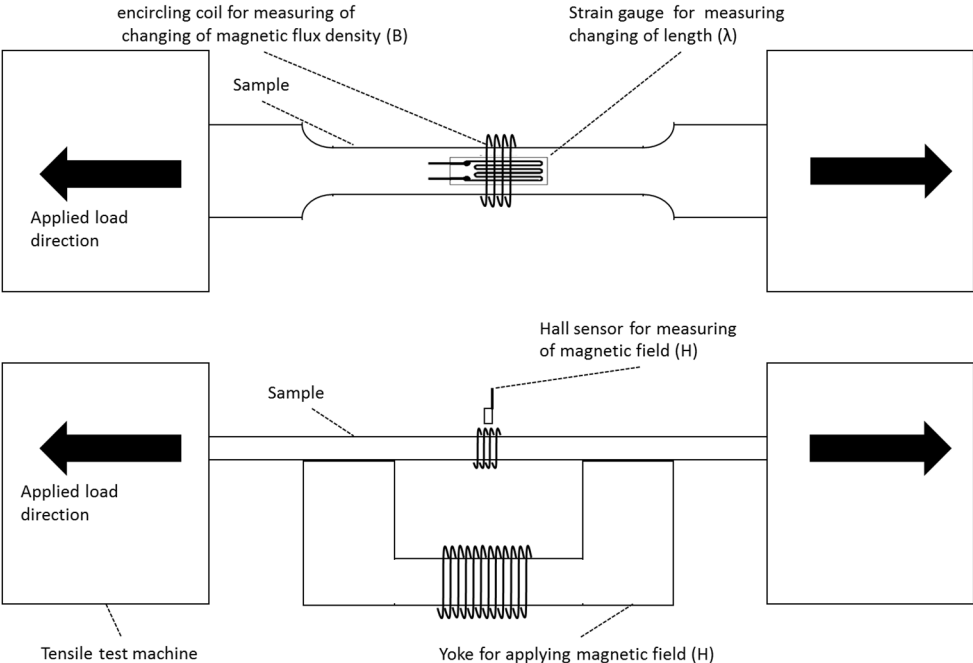


Figure 5.20: Linear data analysis of GMR scans over a sample magnetized at different magnetic field strengths.

Figure 5.21 shows the measurement setups for measuring the B-H curve and the magnetostriction of the materials under applied stress. For the hysteresis measurements, a coil wound around the sample was used to pick up the magnetic flux density (B) by integrating the induced voltage and a Hall sensor to measure the magnetic field strength (H). In order to measure the magnetostriction of the samples, a strain gauge was attached to the surface of the sample to measure the length changes ( $\lambda$ ) resulting from the variation of the magnetic field (H) (Figure 5.21). Note that the magnetizing frequency and amplitude were different for each measurement. Samples were magnetized at 100 Hz and 15 A/cm for the MBN measurement, at 1 Hz for the hysteresis curves and at 0.05 Hz for the magnetostriction measurement, while magnetization amplitude was 40 A/cm for both measurements mentioned above. The device's

limitations were the reason for choosing different frequencies for different measurements. Although the tests were performed at different frequencies and amplitudes, the results of the different methods are comparable [Pits. 1990]. Pitsch has presented that the frequency and the amplitude have a direct effect on the value of a measured parameter (such as  $M_{MAX}$ ), the penetration depth and the phase, yet the trend of the MBN, magnetostriction and B(H) curves under stress are not affected by the magnetization frequency or amplitude [Pits. 1990]. Therefore, the effects of stress on the MBN, hysteresis and magnetostriction resulting from different methods are comparable.

It should be noted that the effect of tensile stress was investigated under gradually increasing applied stress until half of the yield stress was reached. Micro-local plastic deformation happens when the applied stress exceeds half of the yield strength even though the macro-plastic deformation still has not been reached. It is noteworthy that, for Fe-Si steel, magnetic measurement tests were performed at each 10 MPa step, while for the pipeline steel those steps were at 50 MPa each.



**Figure 5.21: Schematic measurement setup for measuring the B-H curve and magnetostriction of the samples.**

## 5.4.2. Micro-magnetic characterization of plastically pre-deformed samples

### 5.4.2.1. Investigation of the micro-magnetic properties of pre-deformed samples in an unloaded state

After investigating the elastic strain, the effect of plastic deformation on the samples' magnetic properties was examined. To this end, some samples from both steel types were plastically deformed up to the necking strain with an Instron servo hydraulic tensile tester 8511.20 controlled by an MTS 6342F extensometer. The Fe-Si steel samples were plastically deformed for 3% and 5% plastic strain, while the pipeline steel was deformed for 1% and 3% plastic deformation (Figure 5.22). Thereafter, the micro-magnetic properties of the samples were determined with the BEMI, hysteresis and magnetostriction measurements. The measurement setups were the same as for the testing setups mentioned before, except that this time the samples were tested in the absence of applied stress such that the effect of the plastic deformation could be determined by itself.

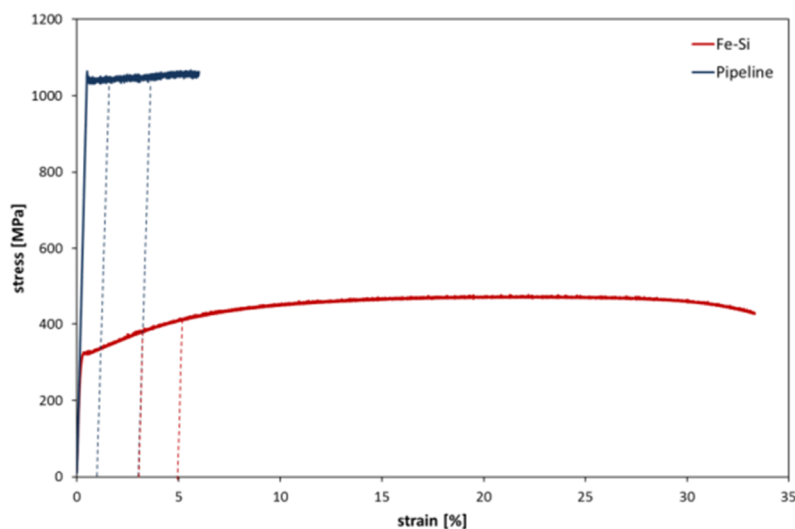


Figure 5.22: Stress-strain curves for Fe-Si and pipeline steels. The dashed lines show the different levels of plastic deformation.

### 5.4.2.2. Investigation of the micro-magnetic properties of pre-deformed samples in an elastically loaded state

This step includes two subsections. First, the micro-magnetic parameters of the non-deformed samples of the Fe-Si and pipeline steels were analysed in situ within the range from the elastic to the plastic regimes (yield point) while gradually increasing the applied stress. The setups and devices were the same as before. As with the previous step, it is of note for the Fe-Si steel that the tests were performed in increments of 10 MPa each while for the pipeline steel they were 50

MPa. The effect of compressive elastic applied stresses was also tested up to -20 MPa for the Fe-Si steel in order to prevent the bending of the samples under compression.

Secondly, the effect of applied elastic strain was investigated on non- and pre-plastically deformed samples. The results include very considerable information which is the basis of the RESTMAB. The setups and test stages were the same as for the tests under applied elastic strain.

#### **5.4.3. Study of the domain structure of non- and pre-deformed samples in un- and elastically loaded states**

To better understand the effect of elastic and plastic strains on the samples' micro-magnetic properties, micro-structure investigations were performed with the SEM model Zeiss Sigma VP. In addition, the grain orientation in the samples was determined using EBSD. Besides this, and in order to better understand the behaviour of MBN under applied stress, the domain structures under applied stress were analysed in an in situ test using the Digital Instruments magnetic force microscope (MFM) DI3000. To be sure that the measurements were always performed at the same location in the sample, a region was marked in the middle of the sample where the stress field in the tensile test was supposed to be homogeneous. To minimize any topography effects, the samples were then polished using a 0.25  $\mu\text{m}$  diamond suspension. It is worth noting that it has been reported in a study that grinding with a sandpaper with a grid size smaller than 600 has no effect on the MBN signal [Clap. 1991, Stef. 2000]. After polishing, the topography of the sample was measured using an atomic force microscope (AFM). The surface roughness was less than 5 nm.

#### **5.4.4. Analysis of magnetic Barkhausen noise behaviour to find a new stress measurement method**

The analysis of all the results from the tests mentioned above - including their reasons - leads to the conclusion that MBN exhibits unique behaviour under applied elastic deformation which is directly related to the micro-residual stresses of the samples. In this step, the so called  $\text{MBN}(\sigma)$  curve has been analysed in detail from the point of view that the micro-residual stresses of the samples can be determined using the  $\text{MBN}(\sigma)$  relationship only, except for any conventional stress measurement methods such as XRD. It is found that two different aspects of the  $\text{MBN}(\sigma)$  relationship are closely correlated with micro-residual stresses. One of them is the position of the maximum of  $\text{MBN}(\sigma)$  curve and the other is the linear behaviour before the maximum. Finally, based on these aspects, two methods are proposed based on  $\text{MBN}(\sigma)$  for the micro-residual stresses, called the "peak shift method" and the "slope method". Once these relationships had been determined, the BEMI was calibrated using a multi-parameter linear regression analysis based on these methods for estimating the micro-residual stresses of the samples. The

calibration process was carried out using the results of the tests performed under elastic applied strain on non- and pre-plastically deformed samples of 3% and 5% for the Fe-Si steel and 1% and 3% for the pipeline steel samples. It should be mentioned that all the samples analysed were tested with XRD methods - in the specific case here - in order to measure the residual stresses for reference purposes. The results of XRD were, however, not the input of the regression analysis for determining a calibration formula, but rather the benchmark for state-of-the-art technology. Different parameters and methods have been tested and the estimated stresses obtained with the calibration formula were compared with the data obtained from the XRD measurements, allowing the optimum method and parameters for the calibration process to be found.

#### **5.4.5. Simulation of the magnetization changes due to residual stresses for a soft magnetic material and a hard magnetic material**

As mentioned in Chapter 4, a model has been proposed for the better understanding of the effect of stress on MBN. This model is based on calculating the  $M(H)$  curve for soft and hard magnetic samples with minimum residual stresses. The minimum residual stresses could be generated due to magnetostriction phenomena in ferromagnetic materials. To verify this assumption, a simplified model was designed and solved using COMSOL Multiphysics. As can be seen in Figure 5.23, a ferromagnetic sample was placed near an electromagnet. A soft iron without losses was defined for the material of the electromagnet. The material of the sample was defined as a ferromagnetic iron. Two  $B(H)$  curves were imported for the hard and soft magnetic materials as the reference for determining the sample's material properties. It should be noted that the magnetic field was generated on an electromagnet and, consequently, on the sample to be analysed using the external current density as an option in the magnetic field module. The effect of stress on the magnetization curve - and vice versa - was modelled with a combination of the "structural mechanics" and "magnetic field" modules.

The study was performed in two steps. First, the maximum residual stresses generated by magnetostriction at the saturation of the magnetic field were calculated for completely fixed (clamped) boundary conditions for the soft and hard magnetic materials. Secondly, the  $M(H)$  curves were calculated for samples subjected to the residual stresses measured from the previous step. It is of note that both studies were carried out for a stationary state and only a sweep module was used for the second step for the varying magnetic field ( $H$ ). Figure 5.24 shows a screenshot of the COMSOL program.

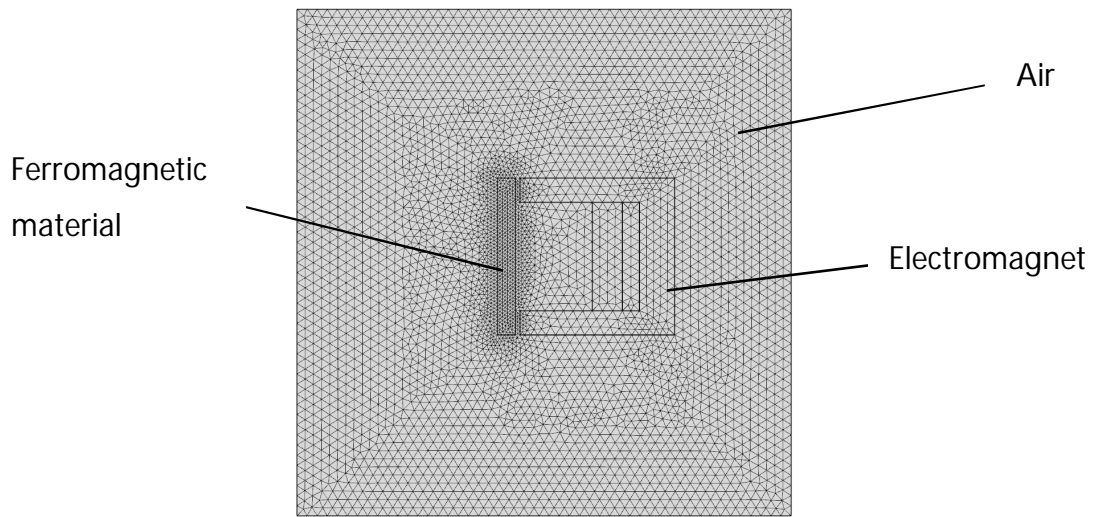


Figure 5.23: The model designed using COMSOL, including an electromagnet, a ferromagnetic material and air.

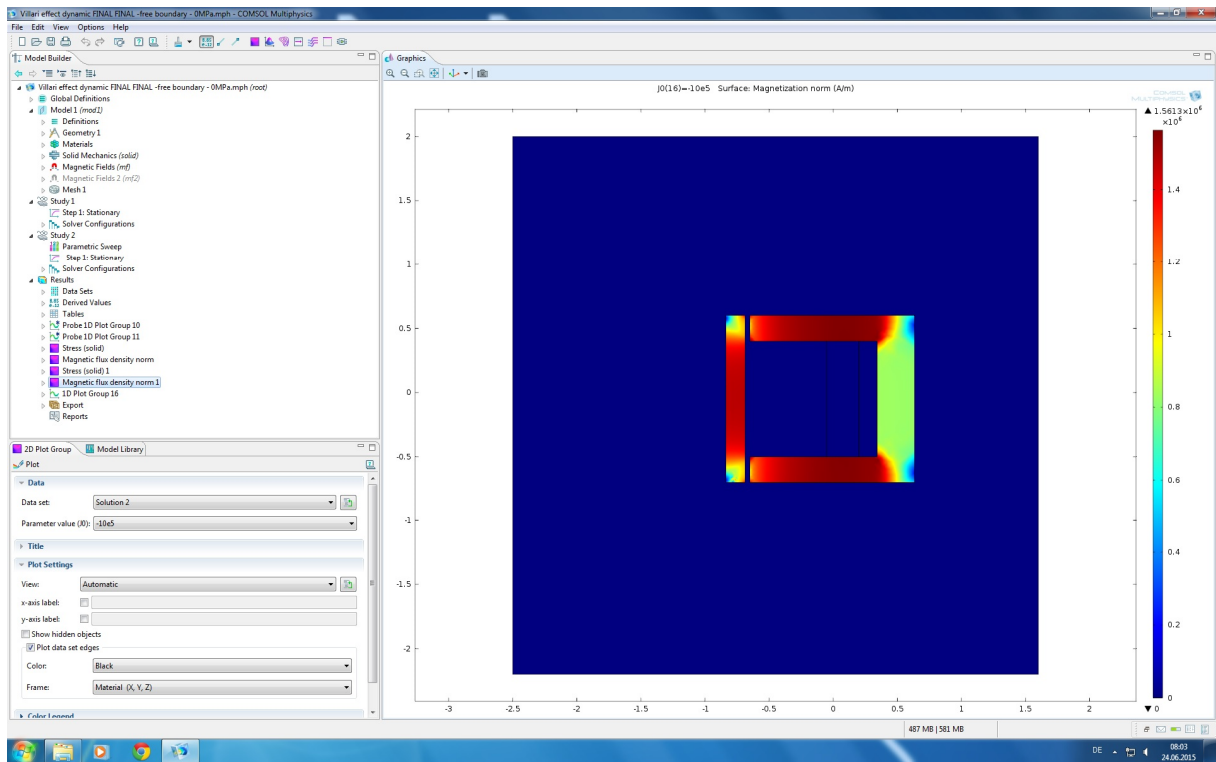


Figure 5.24: Screenshot of the COMSOL Multiphysics software for modelling the effect of stress on the magnetization of soft and hard ferromagnetic materials.

## 6. Results

The results obtained are presented in this chapter. The appropriate discussions are given in the next chapter.

### 6.1. Micro-magnetic characterization of non-deformed samples

#### 6.1.1. Investigation of the micro-magnetic properties of non-deformed samples in an unloaded condition

As presented in the previous chapter, the Fe-Si steel has a ferritic micro-structure while the pipeline sample has a martensitic one. The micro-structure is one of the most important parameters, affecting micro-magnetic properties such as MBN [Moor. 1997a, Moor. 1997b]. Figure 6.1 - Figure 6.3 also imply that the micro-structure directly affects micro-magnetic properties.

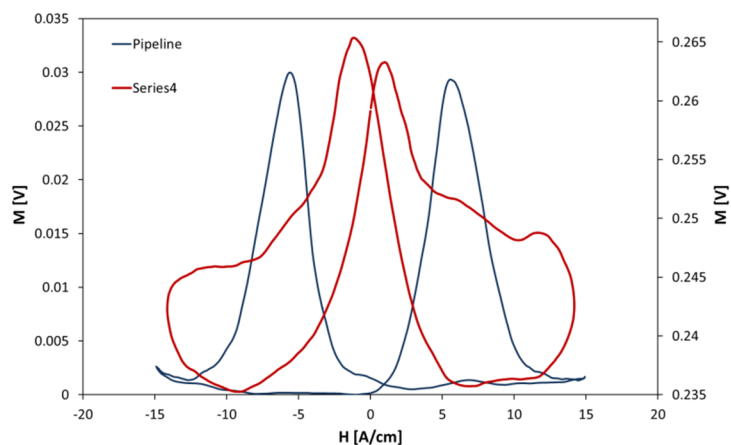


Figure 6.1: MBN curves of Fe-Si and pipeline steels.

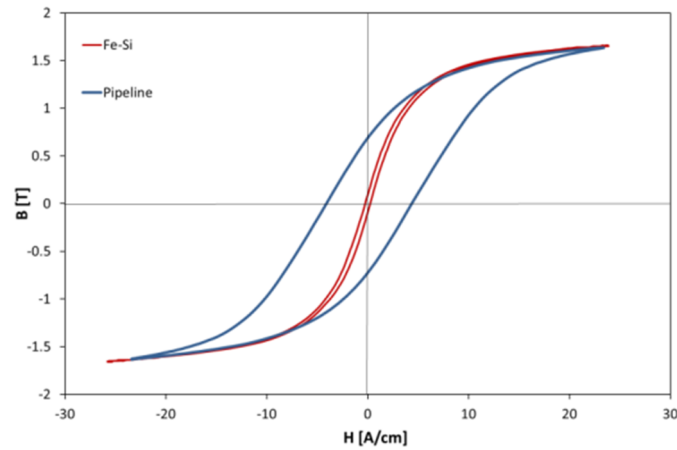


Figure 6.2: Hysteresis loops of Fe-Si and pipeline steels.

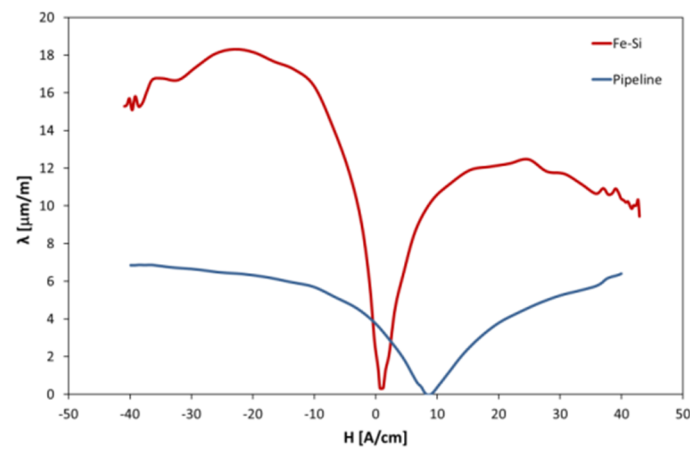


Figure 6.3: Magnetostriction curves (one half-wave) of Fe-Si and pipeline steels.

### 6.1.2. Investigation of the micro-magnetic properties of non-deformed samples in an elastically loaded condition

In order to find out the influence of elastic tensile stress on the micro-magnetic measurement quantities without the influence of plastic deformation, the non-deformed samples of the two steels were investigated under increasing applied tensile stress up to half of the yield strength. Figure 6.4 and Figure 6.5 show the relationship between applied stress and MBN parameters for the non-deformed condition of the pipeline and Fe-Si steel samples, respectively. As can be seen,  $M_{MAX}$ , and  $M_{mean}$  increase with increasing applied stress up to a certain point and then decrease again, while  $H_{CM}$ ,  $DH25_m$ ,  $DH50_m$  and  $DH75_m$  decrease with increasing applied stress and then increase again.

It should be mentioned that MBN occurs during the magnetization process; therefore, measuring the  $B(H)$  curve - which represents the magnetization process of the samples - helps in understanding the behaviour of  $MBN(\sigma)$ . As can be seen in Figure 6.6a and Figure 6.7a, the

shape of the B(H) curves changes slightly with increasing applied tensile stress. This is more visible for the pipeline steel. Zooming into the coercivity and remanence points can help to illustrate the effect of stress on the B(H) curves. Figure 6.8a-b - presenting the coercivity ( $H_c$ ) and remanence ( $B_r$ ) behaviour under applied stress - exhibit behaviour similar to the MBN parameters, since  $B_r$  and  $H_c$  are in the same sense to  $M_{MAX}$  and  $H_{CM}$  respectively.

To calculate the stress anisotropy, the magnetostriction under applied stress was measured. Figure 6.9 shows half of the magnetostriction curves for different applied stresses. As can be seen, the maximum magnetostriction  $\lambda_{MAX}$  decreases with increasing applied stress. Changes in the DW structures under applied stress are the reason for decreasing magnetostriction with increasing applied stress, because the tensile applied stress on steel which generates positive magnetostriction increases the ratio of  $180^\circ$  to  $90^\circ$  DWs. Since  $90^\circ$  DWs are responsible for magnetostriction, the magnetostriction decreases with an increase in applied stress.

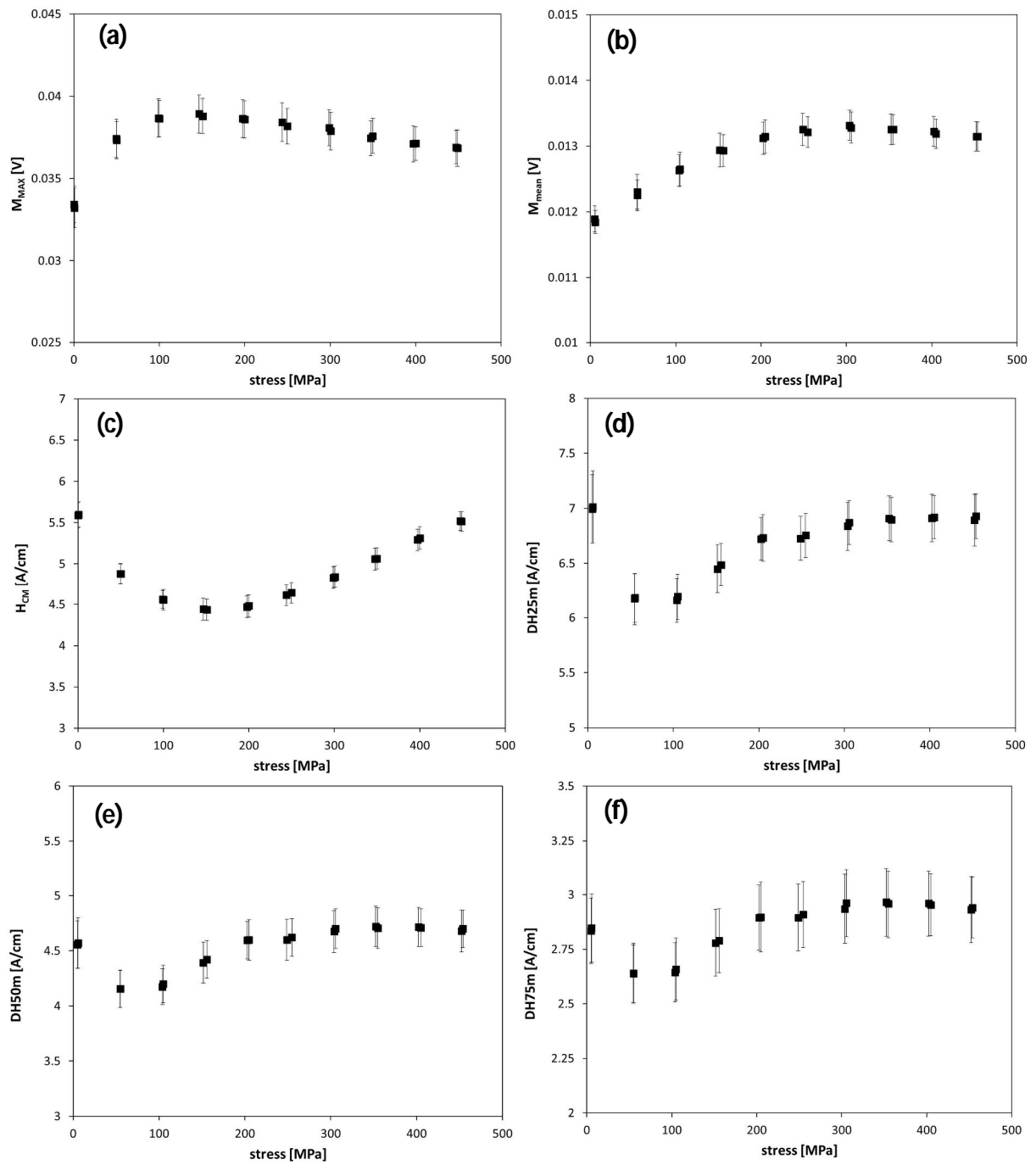
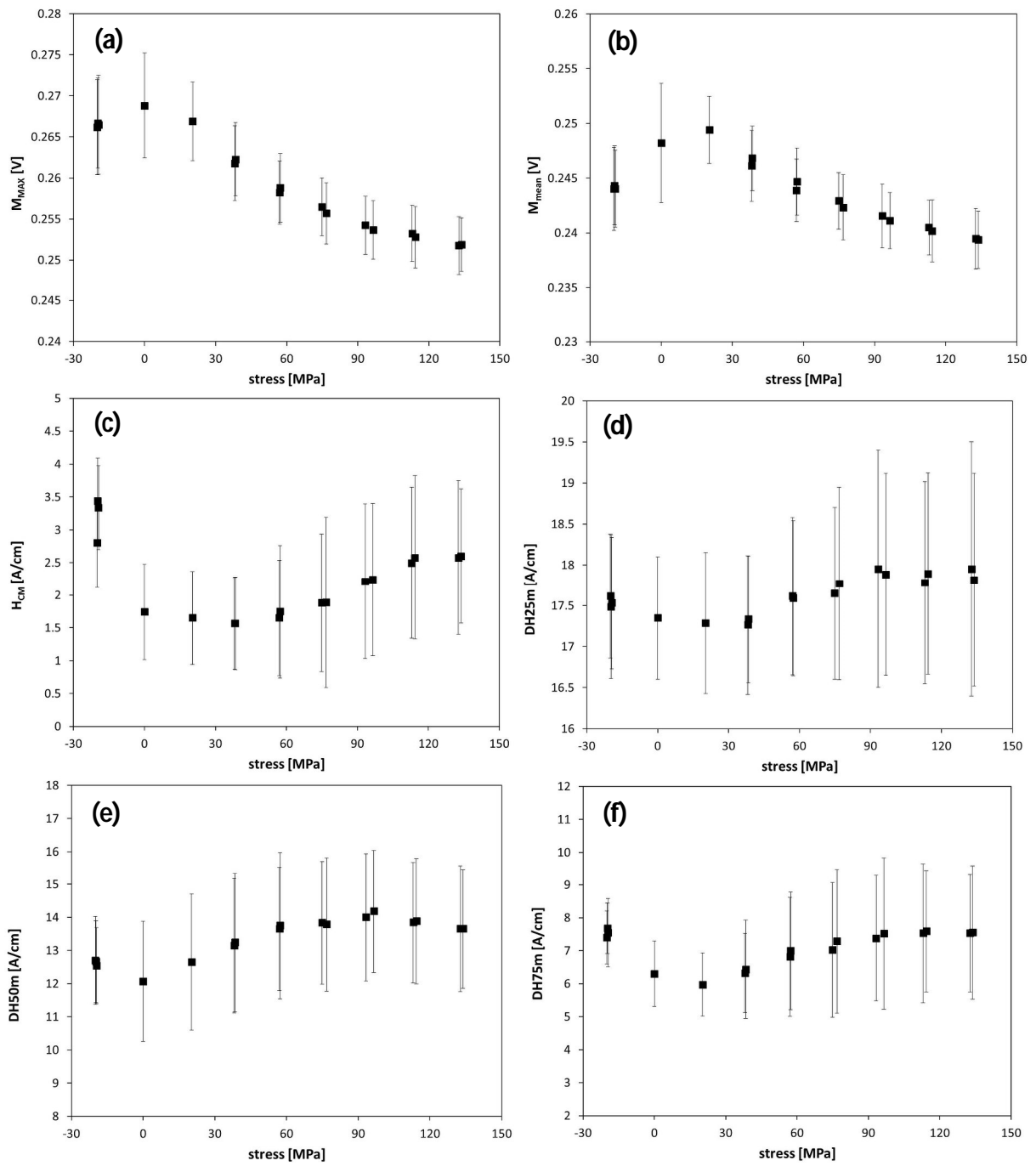
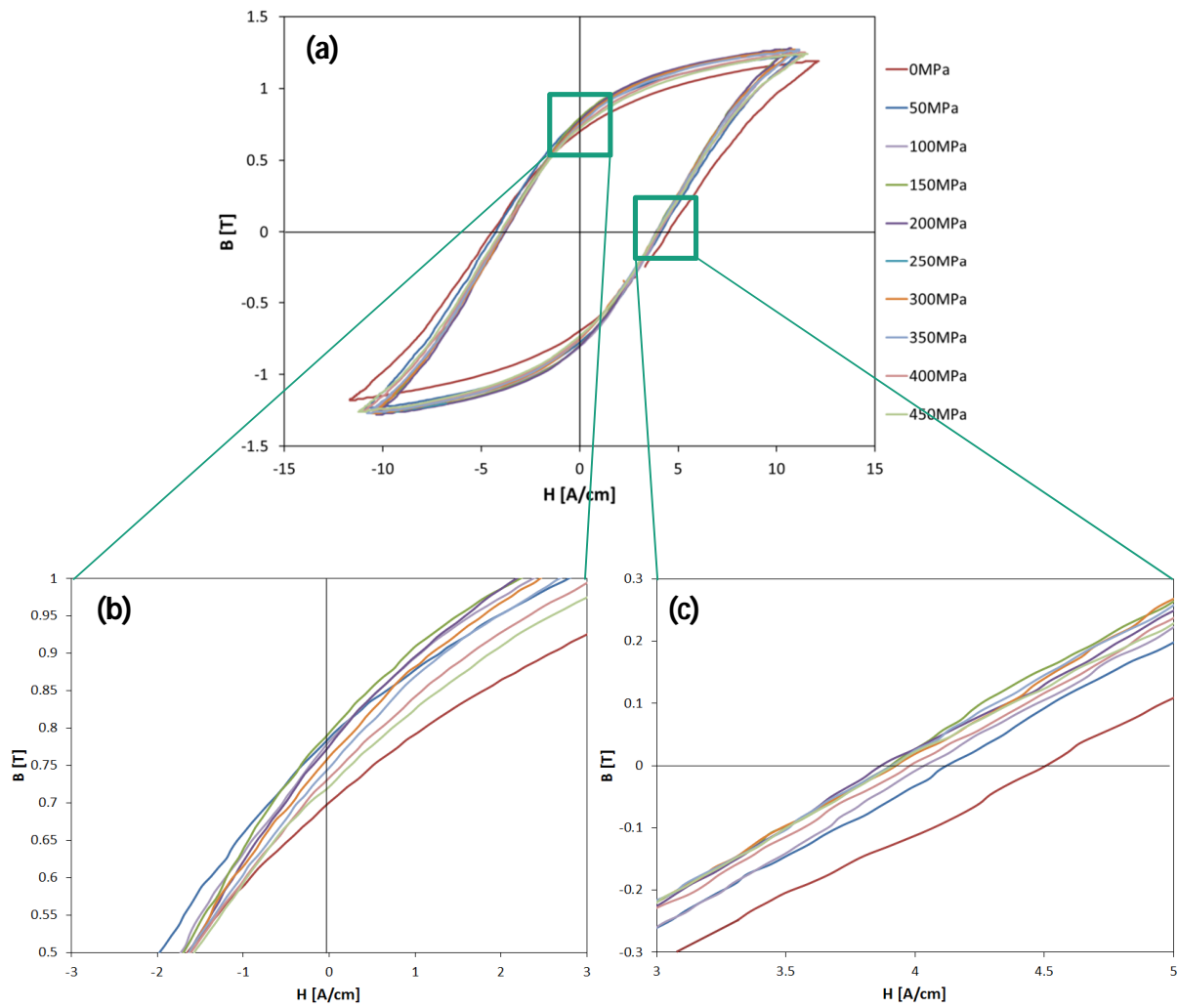


Figure 6.4: Behaviour of the MBN parameters under tensile elastic applied stress in pipeline steel. The black dots show the mean value of 100 measurements each and the error bar represents the standard deviation of a single measurement.



**Figure 6.5: Behaviour of the MBN parameters under tensile elastic applied stress in Fe-Si steel. The black dots show the mean value of 100 measurements and the error bar represents the standard deviation of a single measurement.**



**Figure 6.6: a) General hysteresis behaviour of pipeline steel under applied elastic strain at the same magnetizing voltage amplitude, b) behaviour of the remnant point ( $B_r$ ), and c) coercivity ( $H_c$ ) under applied stress.**

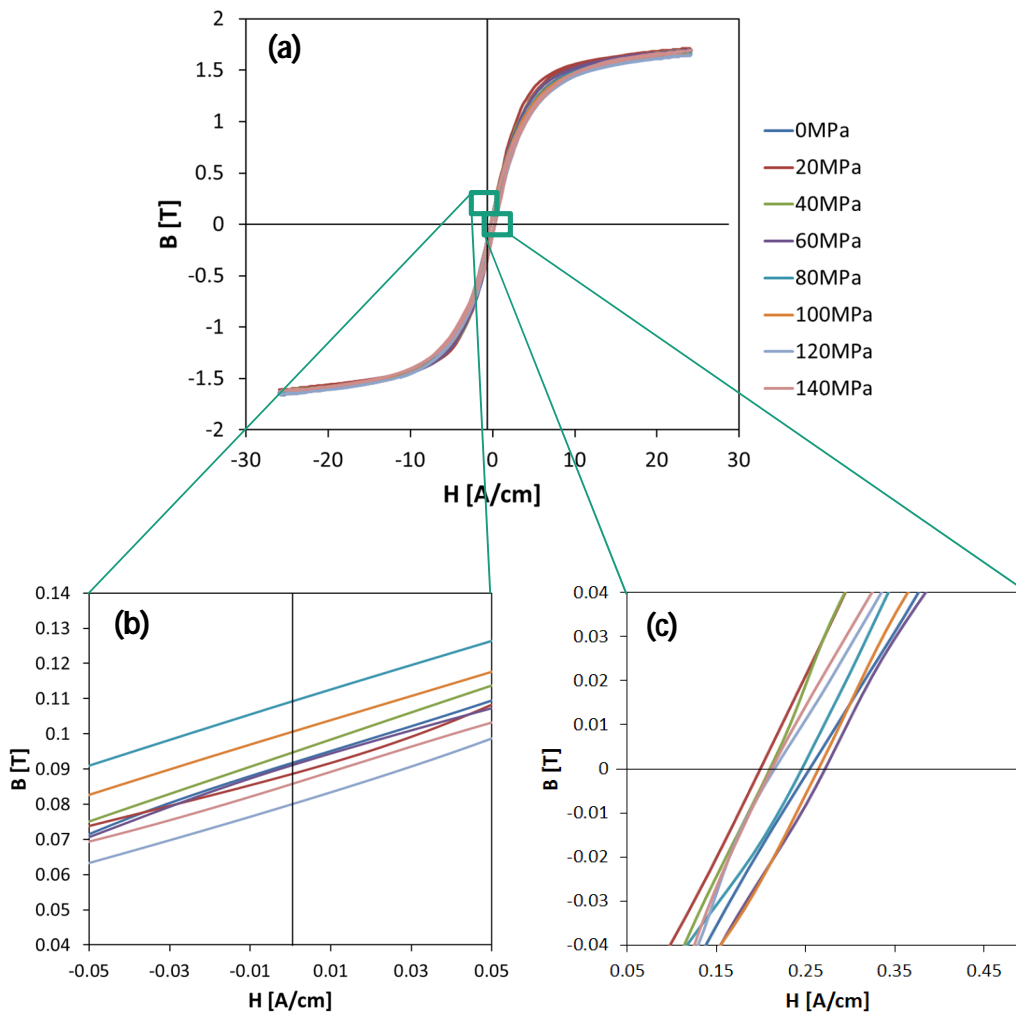


Figure 6.7: a) General hysteresis behaviour of Fe-Si steel under applied elastic stress at the same magnetizing voltage amplitude, b) behaviour of the remnant point ( $B_r$ ), and c) coercivity ( $H_c$ ) under applied stress.

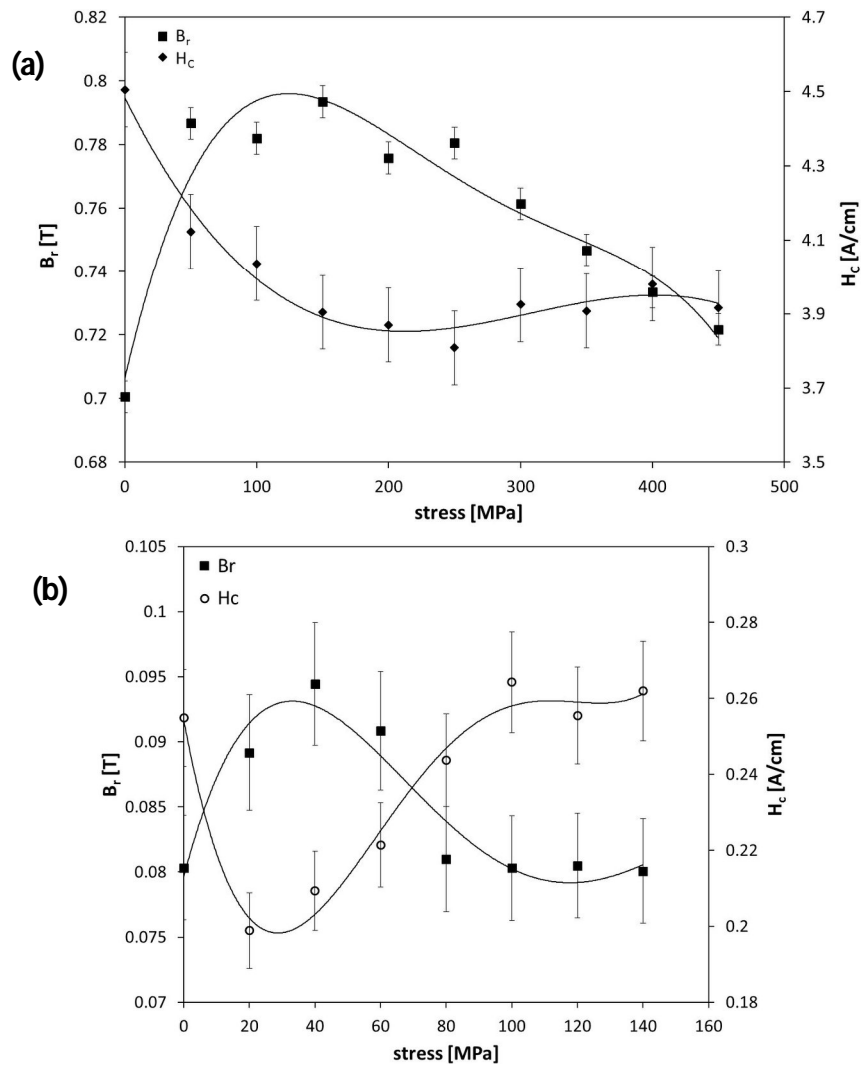


Figure 6.8: Relation between the remanence ( $B_r$ ) and coercivity of a magnetic field ( $H_c$ ) derived from hysteresis curves with applied stress in a) pipeline steel and b) Fe-Si steel.

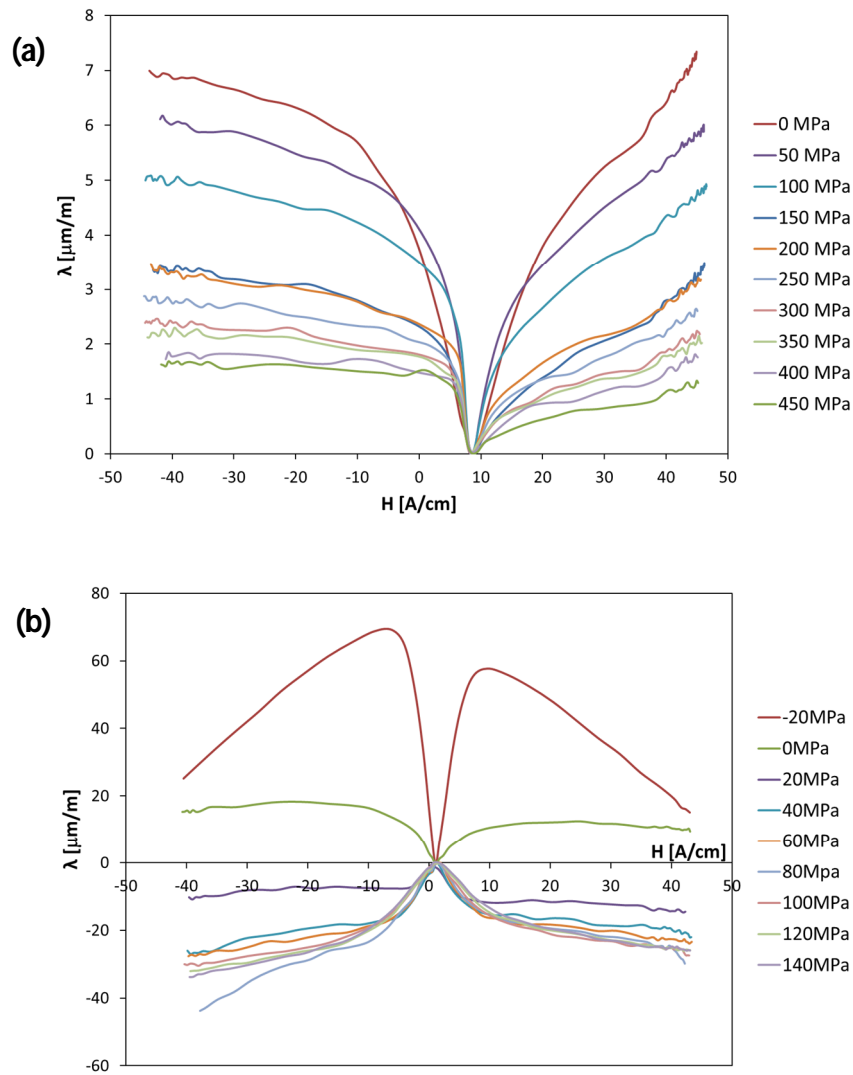


Figure 6.9: Magnetostriction changes of a non-deformed sample under applied stress for a) pipeline steel and b) Fe-Si steel.

### 6.1.3. Study of the domain structure of non-deformed samples in elastically loaded conditions

Figure 6.10 shows the EBSD image of the pipeline and Fe-Si steels. As can be seen, the pipeline steel has a complex micro-structure in which the grains are oriented in different directions, while the Fe-Si steel has a simpler micro-structure. As apparent in Figure 6.10, a large portion of the EBSD image in the pipeline steel is oriented in the (111) direction, especially in the lower-left side of the picture, while the scanned area in the Fe-Si steel is oriented between (001) and (111).

Figure 6.11 and Figure 6.12 show the domain structures at different applied stresses for the pipeline steel and Fe-Si steel samples, respectively.

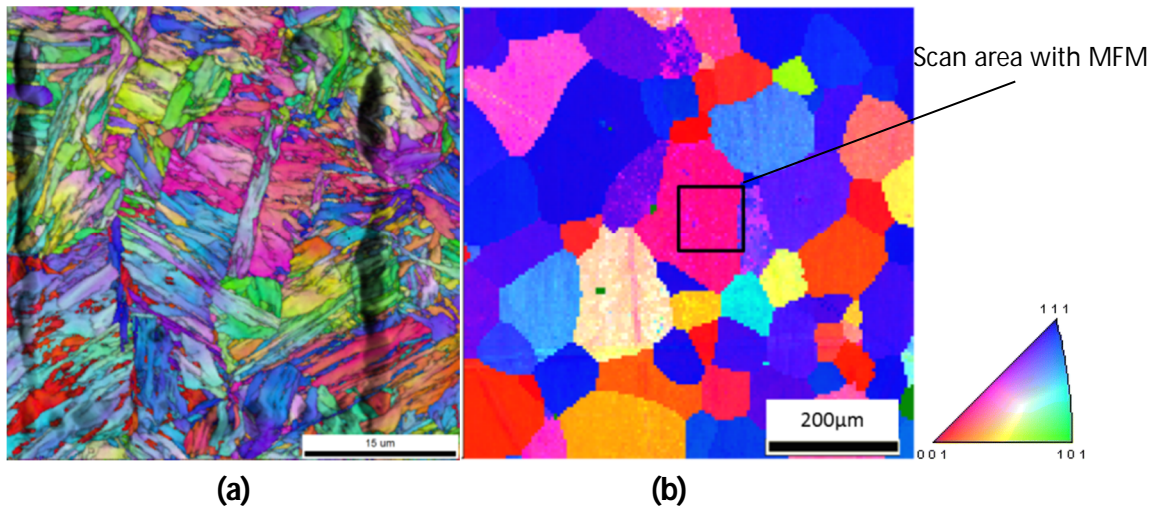


Figure 6.10: EBSD image of the marked area of which MFM scans have been performed in a) pipeline steel and b) Fe-Si steel.

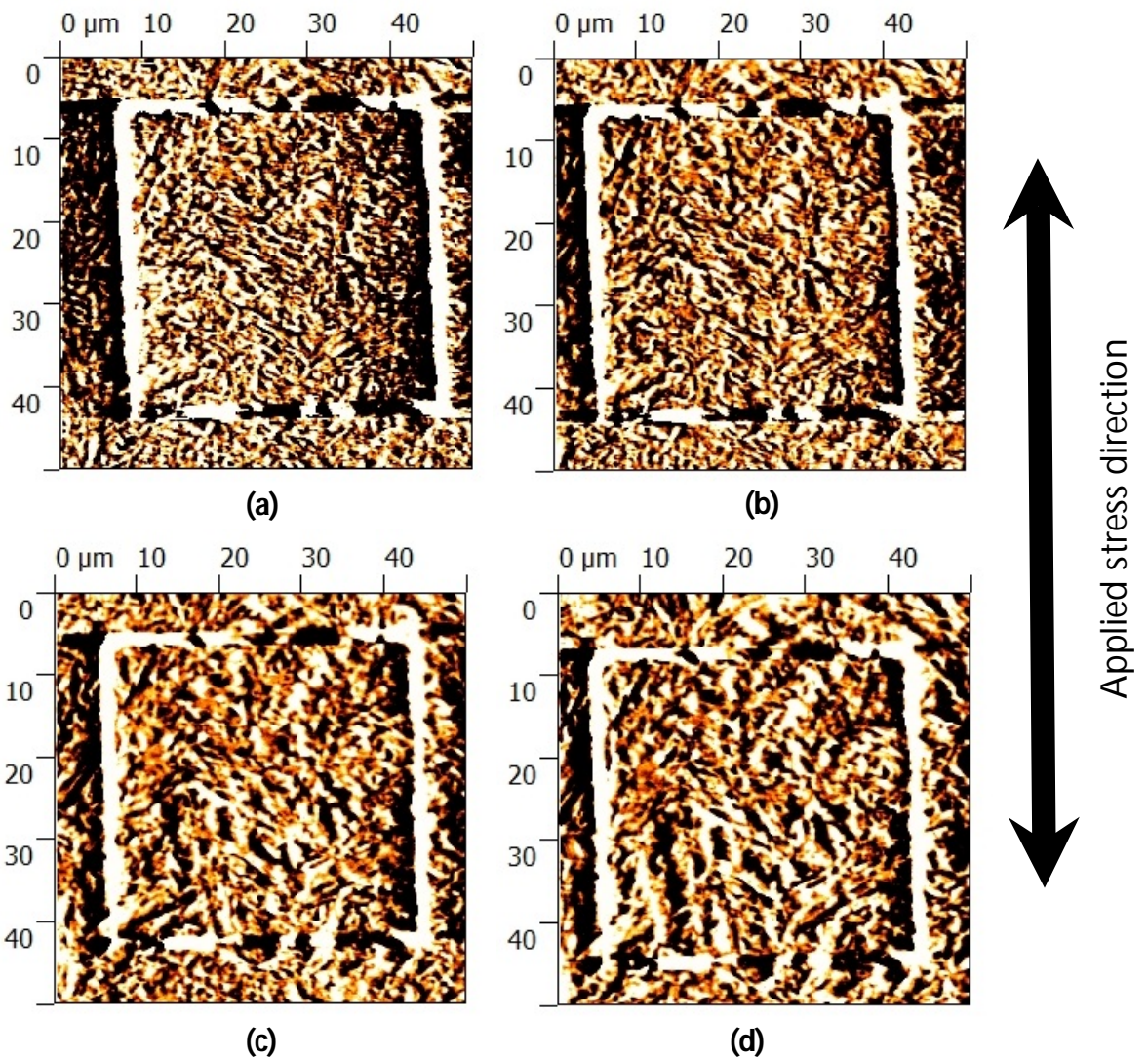


Figure 6.11: Domain structures of pipeline steel under applied stress using MFM: a) 0 MPa, b) 100 MPa, c) 200 MPa, and d) 300 MPa (the white square shows the marked area and it is not a domain).

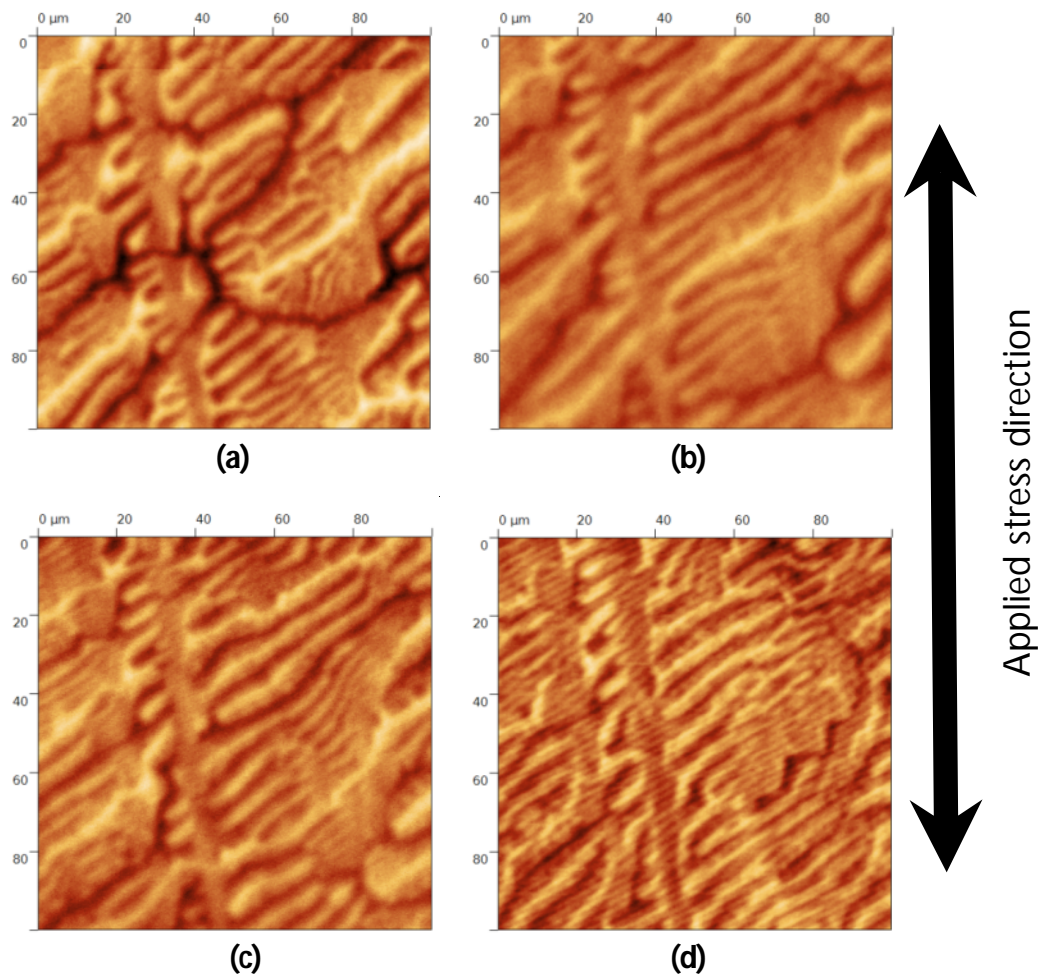


Figure 6.12: Domain structures of Fe-Si steel under applied stress using MFM: a) -20 MPa, b) 0 MPa, c) 20 MPa, and d) 60 MPa.

## 6.2. Micro-magnetic characterization of plastically pre-deformed samples

### 6.2.1. Investigation of the micro-magnetic properties of pre-deformed samples in an unloaded condition

Figure 6.13 - Figure 6.15 show the MBN, hysteresis and magnetostriction curves for non- and pre-deformed samples of the pipeline and Fe-Si steel samples.

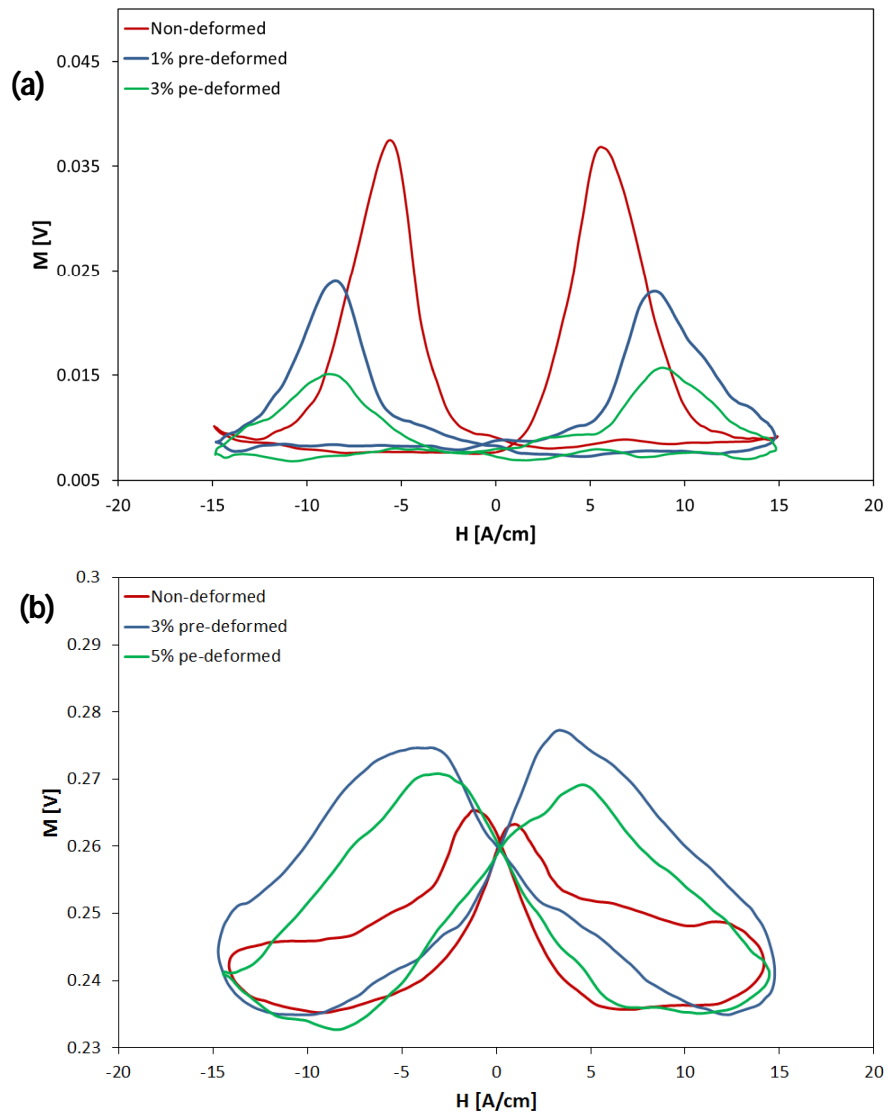


Figure 6.13: Barkhausen noise signal for non- and pre-deformed samples of a) pipeline and b) Fe-Si steels.

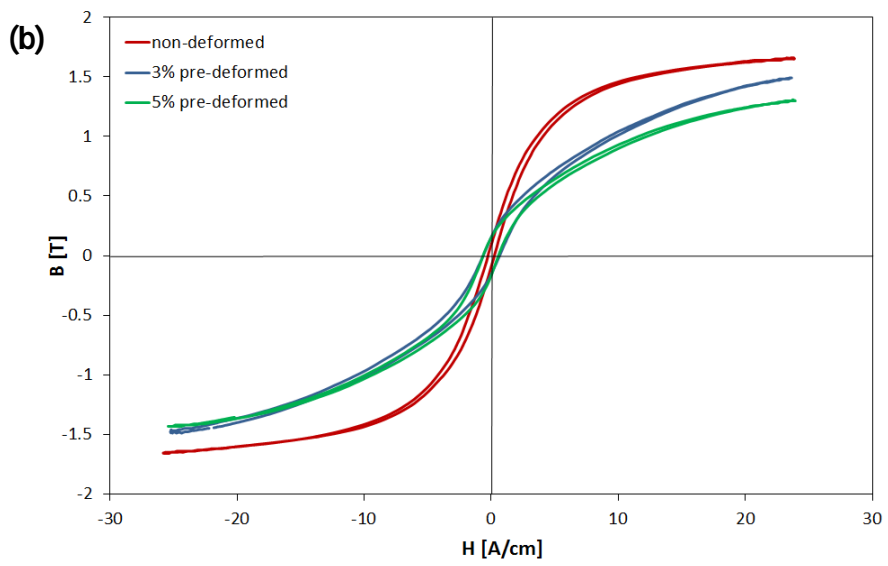
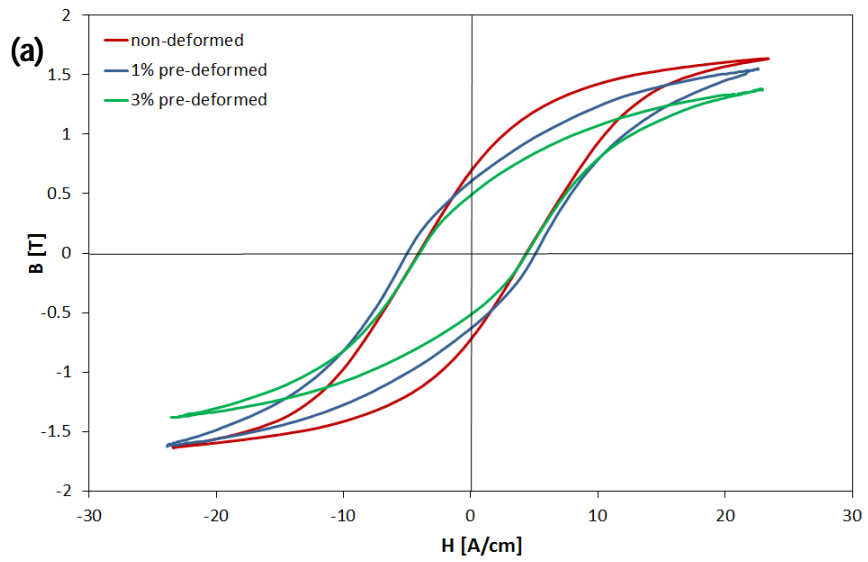


Figure 6.14: Hysteresis curves for non- and pre-deformed samples of a) pipeline and b) Fe-Si steels.

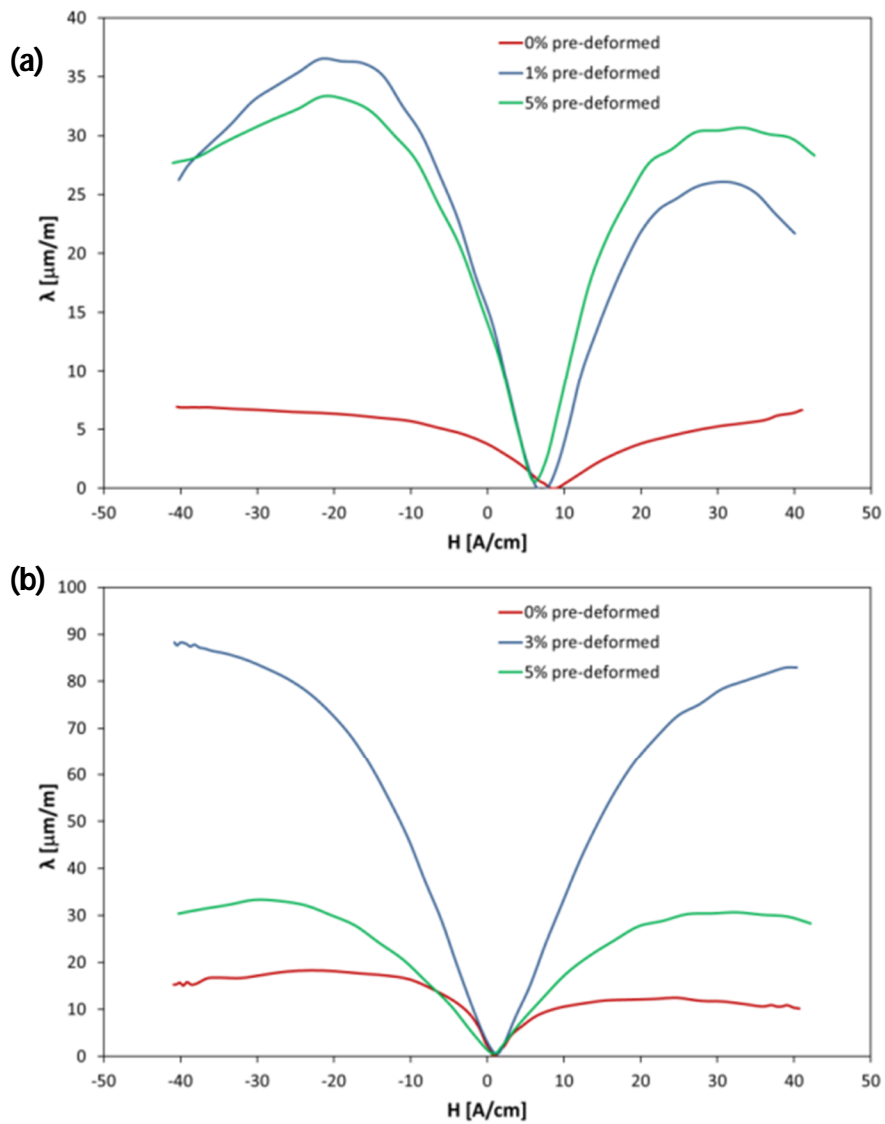


Figure 6.15: Magnetostriction for non- and pre-deformed samples in a) pipeline and b) Fe-Si steels.

The effect of plastic deformation on the parameters derived from MBN is presented in Figure 6.16. As can be seen, parameters such as  $M_{MAX}$  and  $M_{mean}$  decrease with increasing plastic deformation and compressive micro-residual stresses, while  $H_{CM}$ ,  $DH_{25_m}$ ,  $DH_{50_m}$  and  $DH_{75_m}$  increase with increasing plastic deformation in the pipeline steel.

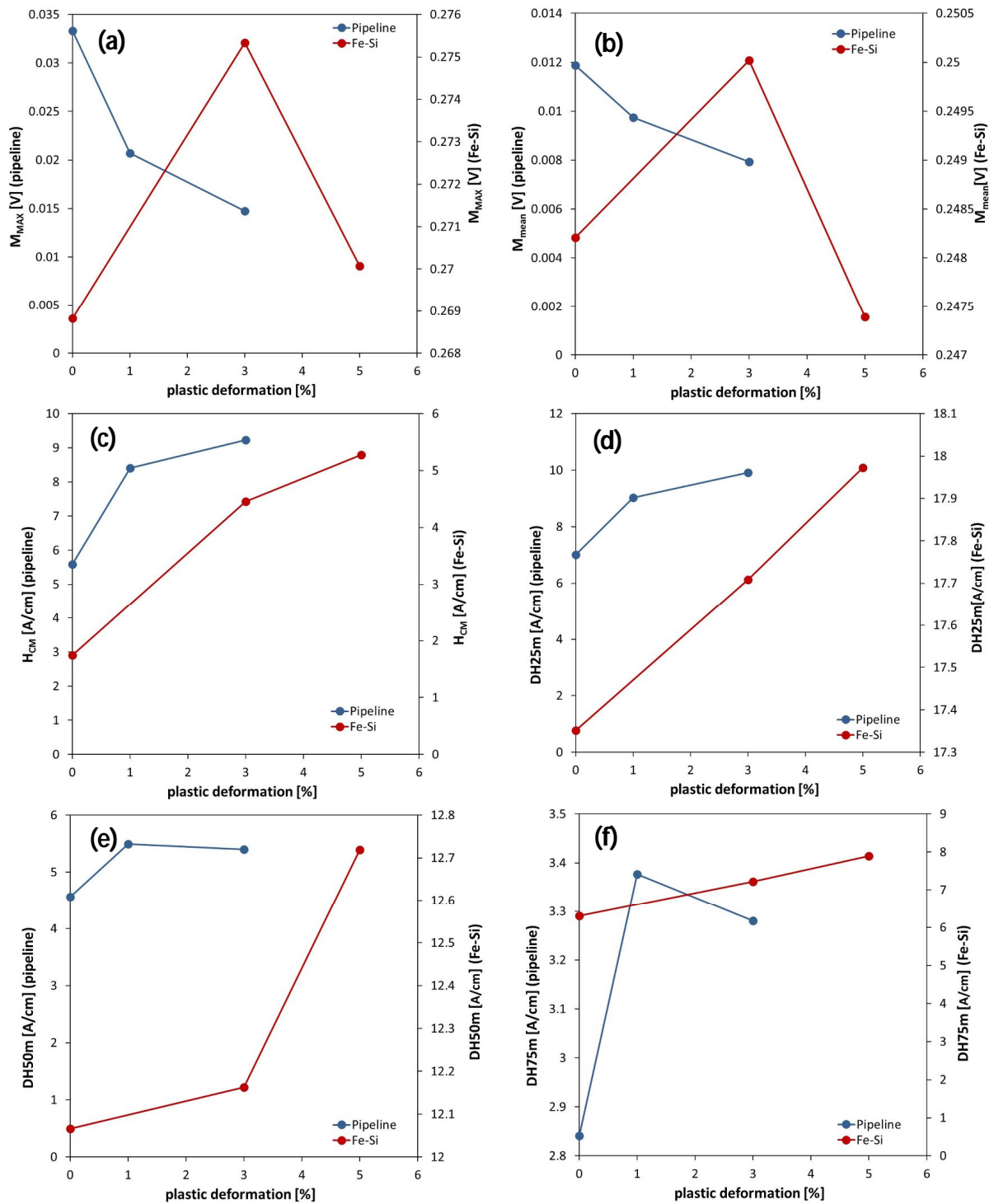


Figure 6.16: Behaviour of MBN parameters for samples with different plastic deformations for pipeline and Fe-Si steels.

## 6.2.2. Investigation of the micro-magnetic properties of pre-deformed samples in an elastically loaded condition

Figure 6.17 and Figure 6.18 show the relationship between the applied stress and MBN parameters for non- and pre-deformed samples in pipeline and Fe-Si steels, respectively.

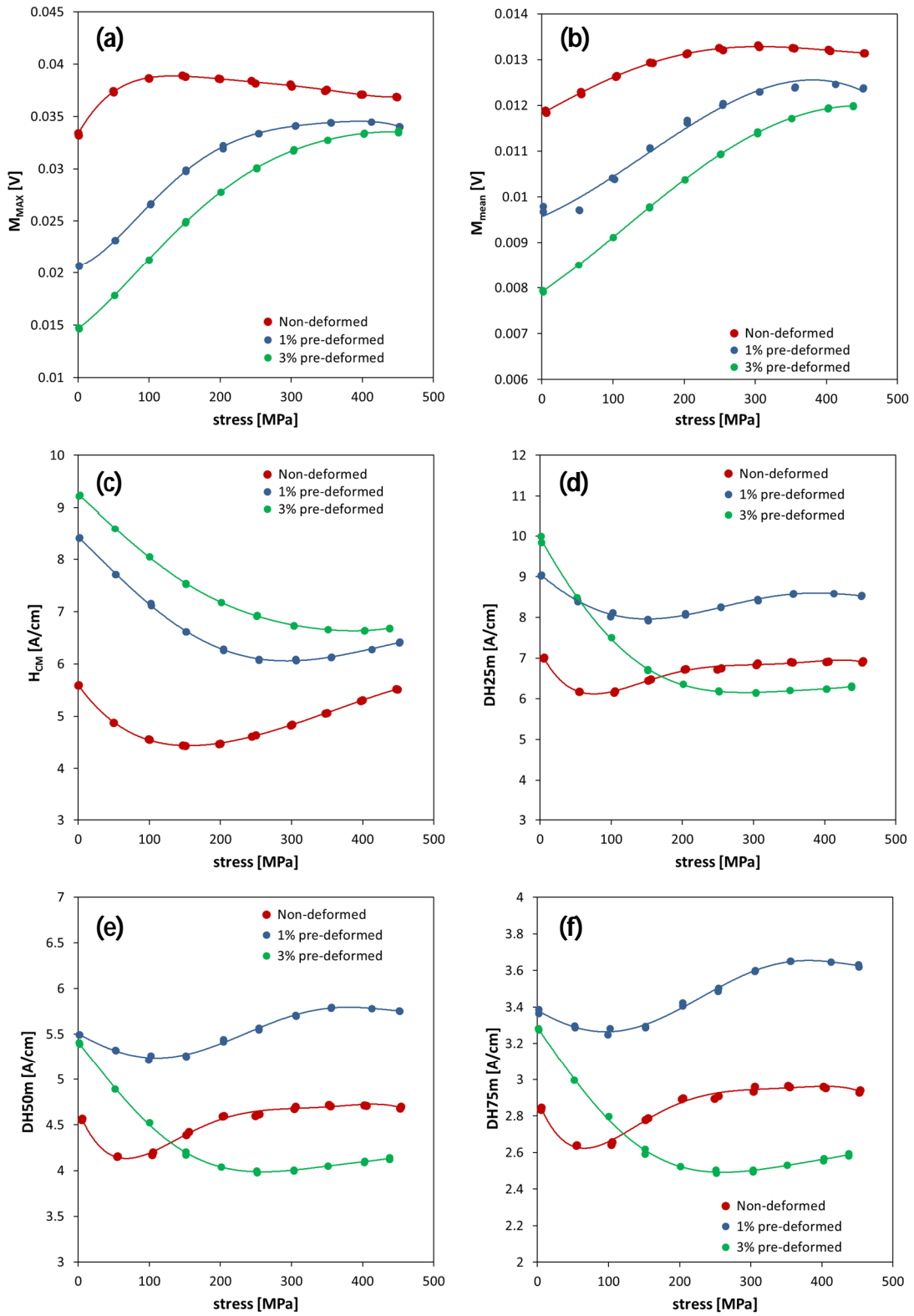


Figure 6.17: The relationships between the MBN and applied stress parameters for non- and pre-deformed samples of pipeline steel. The points show the mean value of 100 measurements.

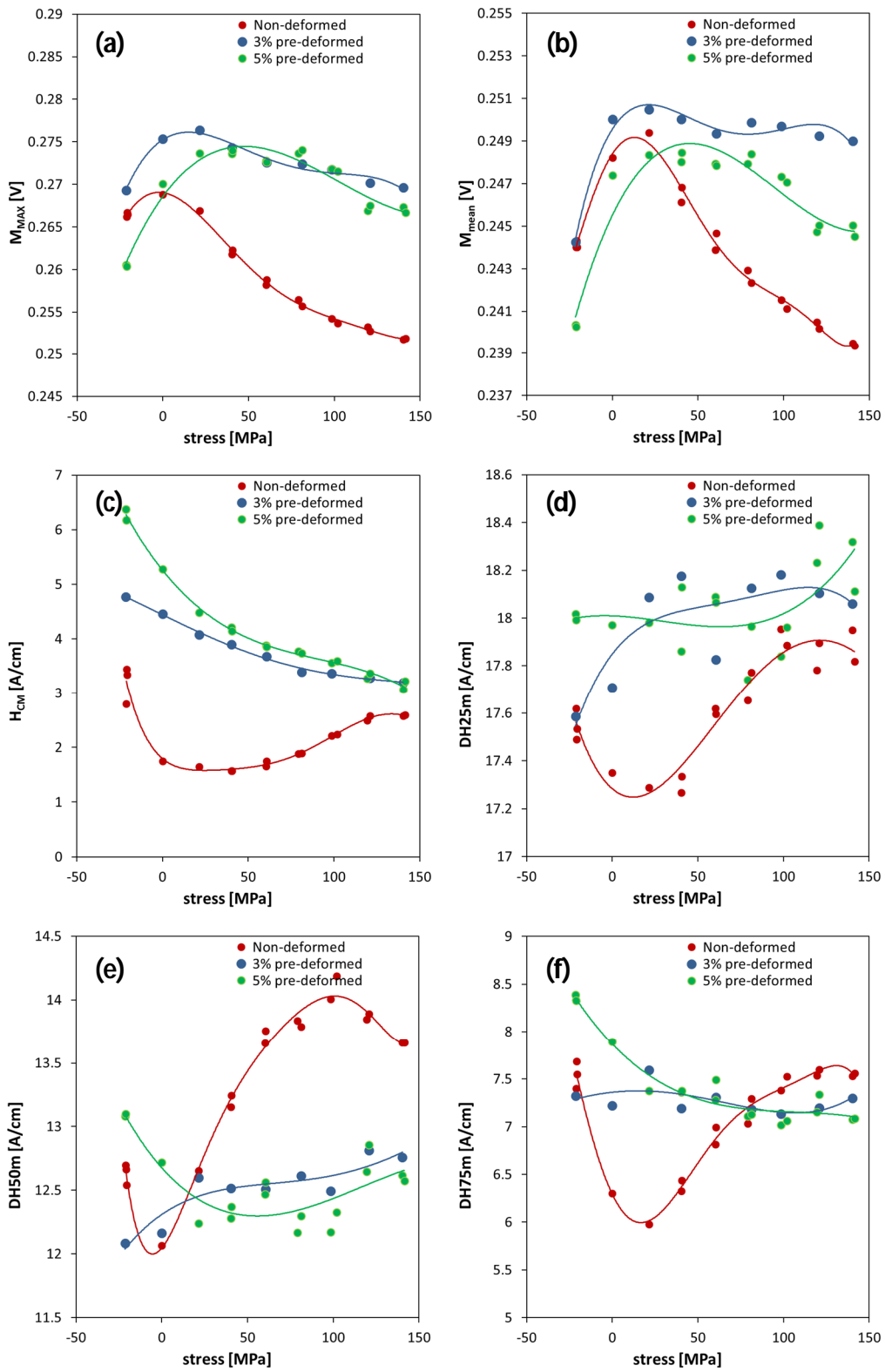
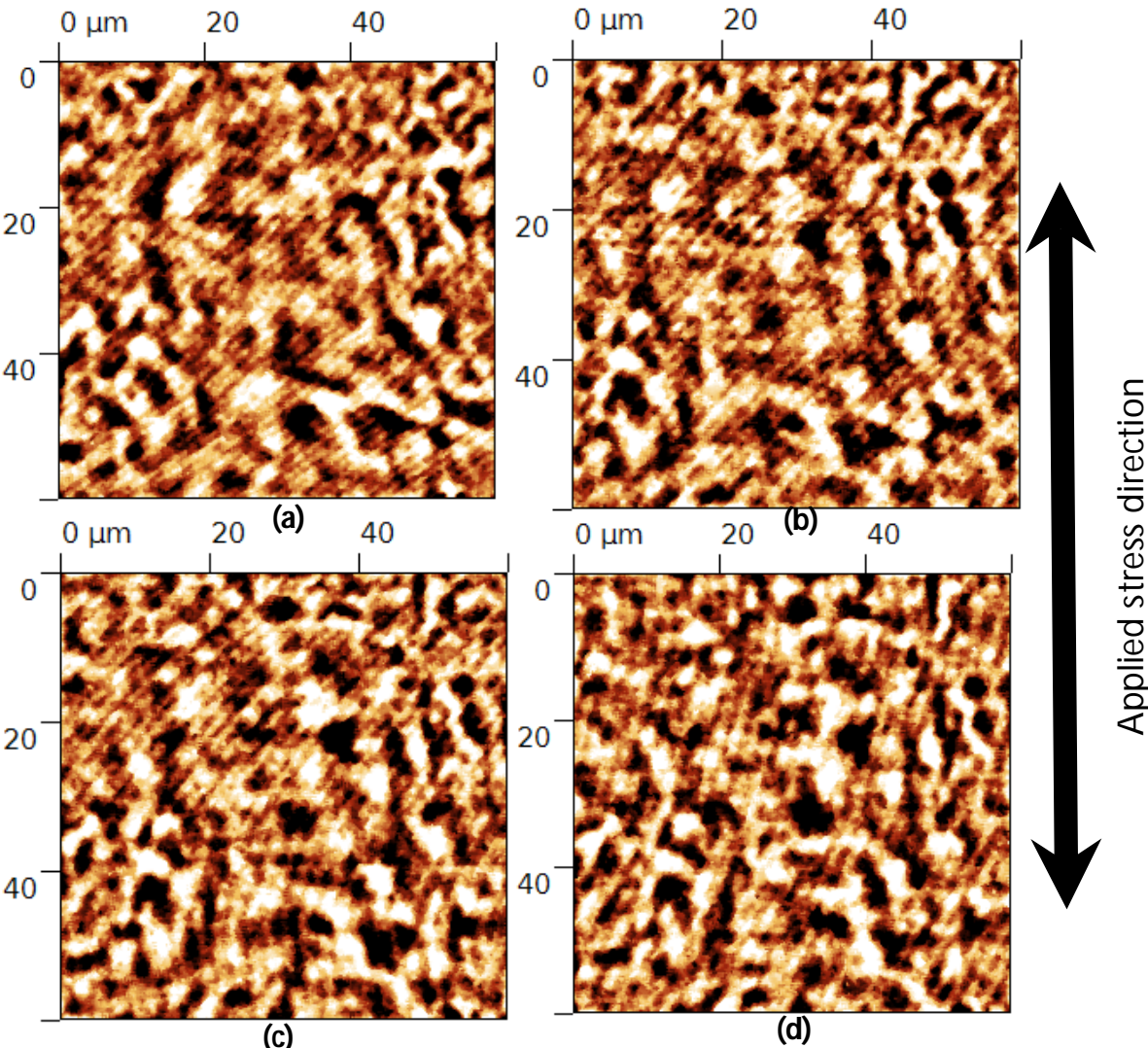


Figure 6.18: Relationships between the MBN and applied stress parameters for non- and pre-deformed samples in Fe-Si steel. The points show the mean value of 100 measurements.

**6.2.3. Study of the domain structure of plastically pre-deformed samples in elastically loaded conditions**

Figure 6.19 through to Figure 6.23 comprise the in situ MFM pictures under applied stress for the pre-deformed pipeline and Fe-Si steels.



**Figure 6.19: Domain structures of 1% pre-deformed pipeline steel under applied stress using MFM: a) 0 MPa, b) 300 MPa, c) 400 MPa, and d) 500 MPa.**

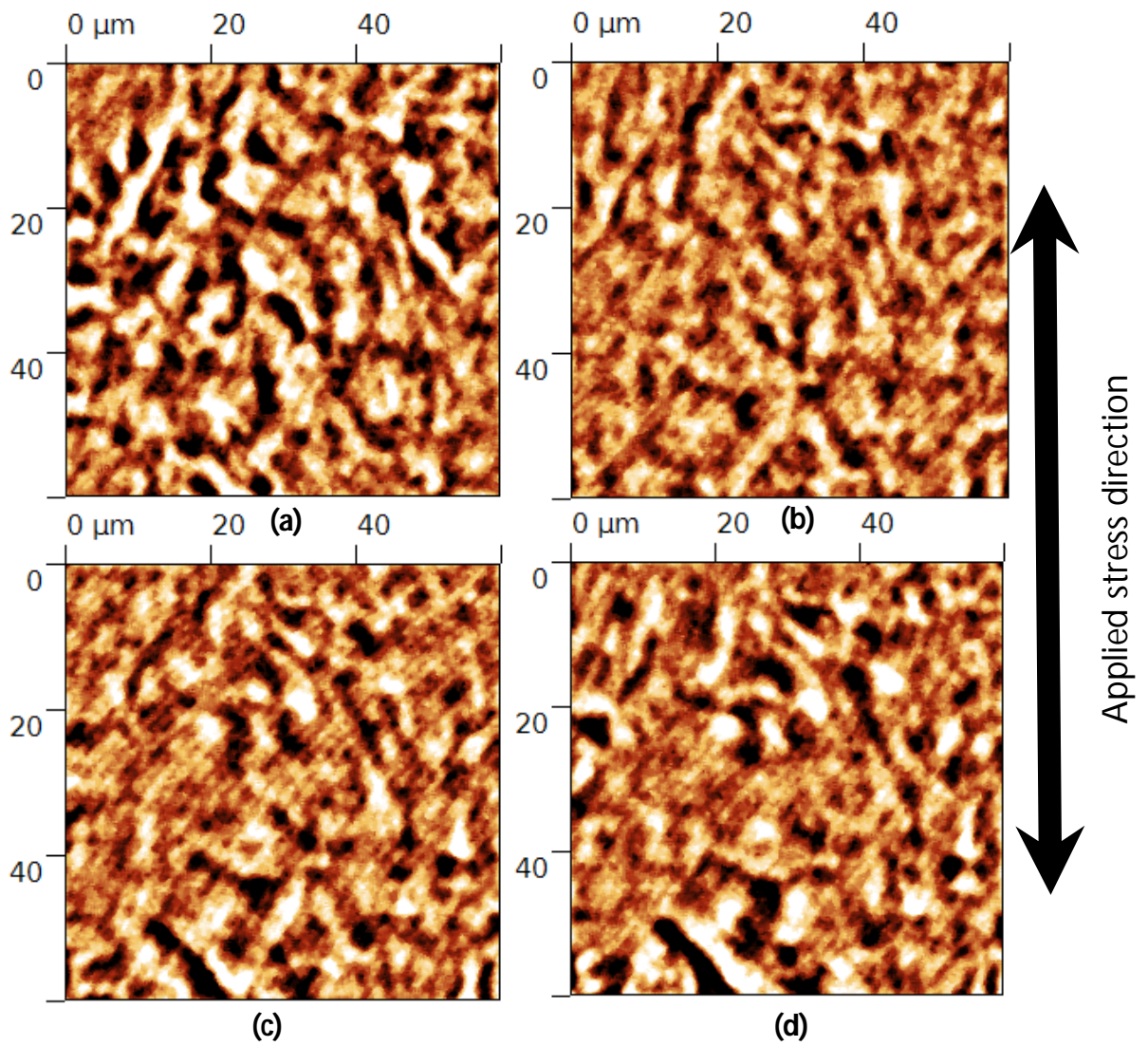


Figure 6.20: Domain structures of 3% pre-deformed pipeline steel under applied stress using MFM: a) 0 MPa, b) 300 MPa, c) 400 MPa, and d) 500 MPa.

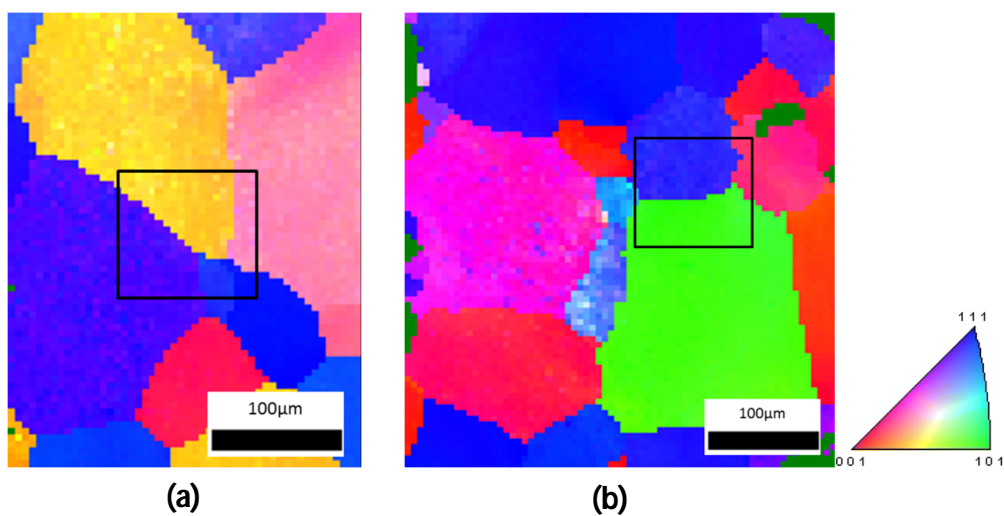


Figure 6.21: EBSD image of the marked area in which MFM scans have been performed for a) 3% and b) 5% pre-deformed Fe-Si steel.

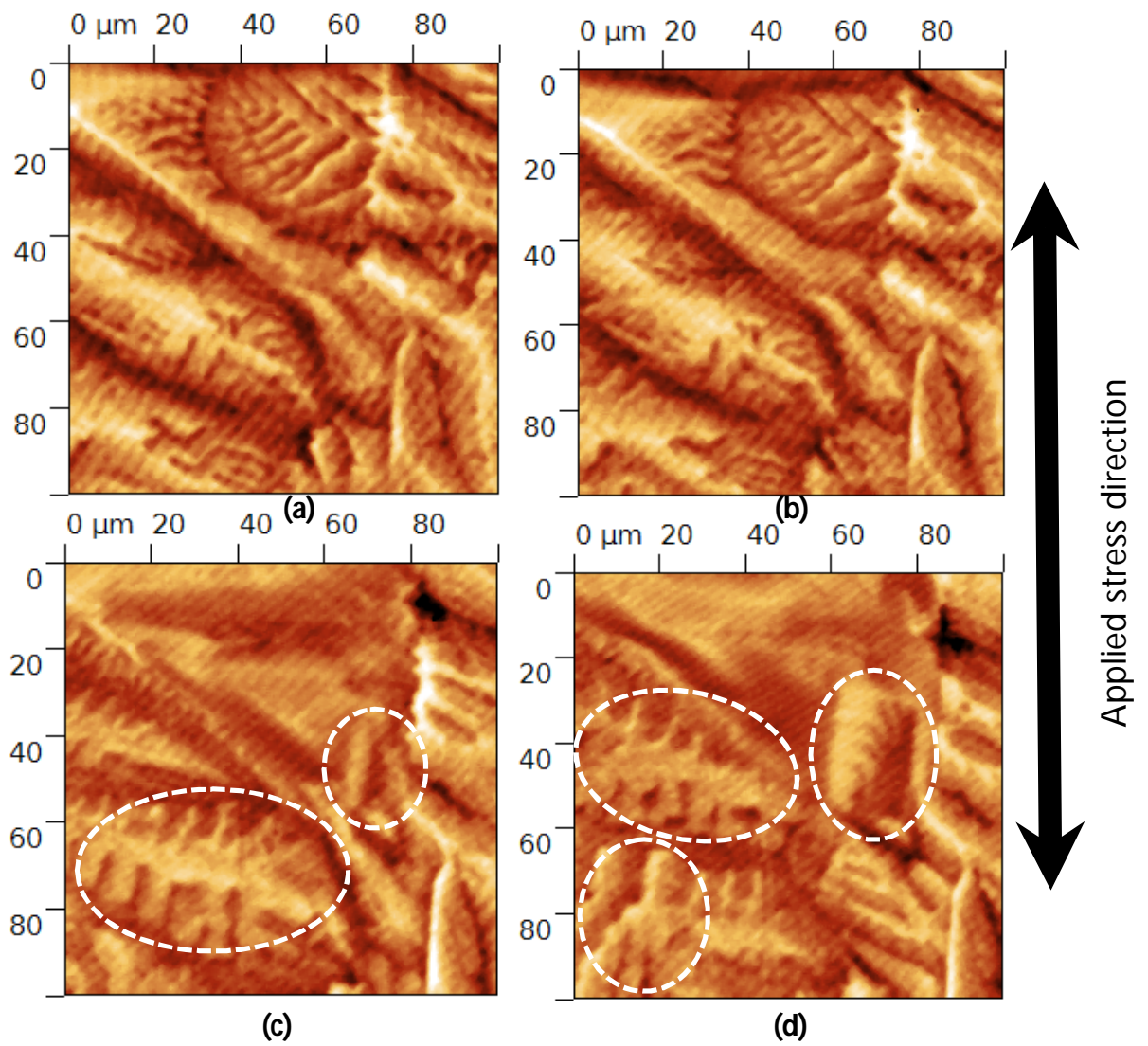


Figure 6.22: Domain structures of 3% pre-deformed Fe-Si steel under applied stress using MFM: a) -20 MPa, b) 0 MPa, c) 60 MPa, and d) 100 MPa. The dashed lines represent the spike domains created under applied stress.

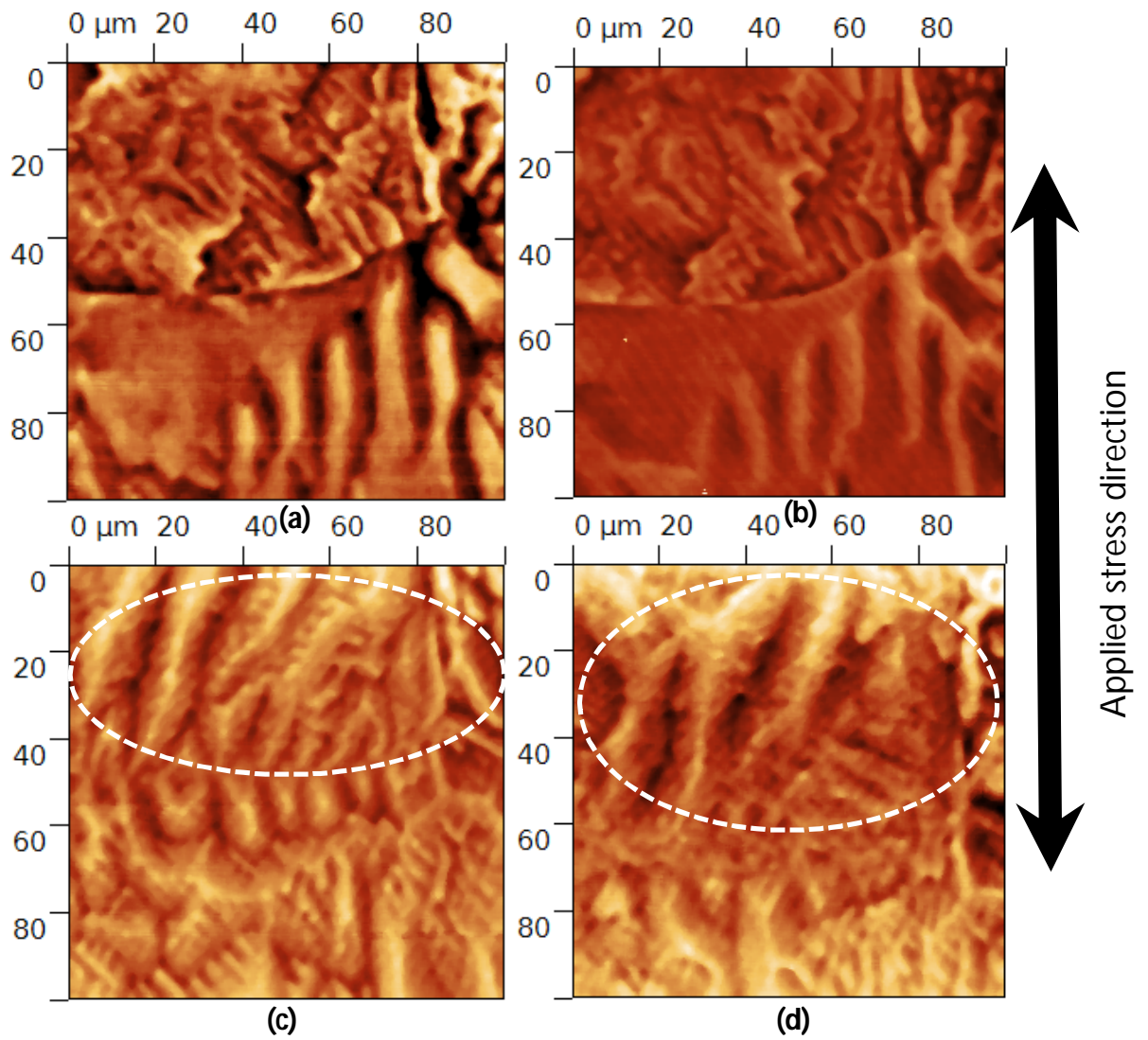


Figure 6.23: Domain structures of 5% pre-deformed Fe-Si steel under applied stress using MFM: a) -20 MPa, b) 0 MPa, c) 60 MPa, and d) 100 MPa. The dashed lines represent the domains created under applied stress.

### 6.3. Modelling of the magnetization process under the effect of stress

As mentioned in Chapter 4, a soft and a hard magnetic material model have been simulated using COMSOL Multiphysics for better understanding the effect of stress on the magnetization process and, consequently, on MBN. In the first step, the micro-residual stresses which are generated by magnetostriction have been calculated. Figure 6.24 shows the von Mises stresses generated in samples due to magnetostriction. The maximums of the calculated micro-residual stresses are -18 MPa and -55 MPa for the soft and the hard magnetic samples, respectively. It is noteworthy that the soft magnetic material has a narrow, long hysteresis curve (high  $B_r$ , low  $H_c$ ), while the hard magnetic material shows a wide, short hysteresis curve (low  $B_r$ , high  $H_c$ ). In the second step, the magnetization changes were measured for two situations for each sample. The first situation was without any residual stresses while the second was with micro-residual stresses, which were calculated in the last step. It should be noted that there were no boundary restrictions or constraints for the model in order to prevent further micro-strains due to magnetostriction.

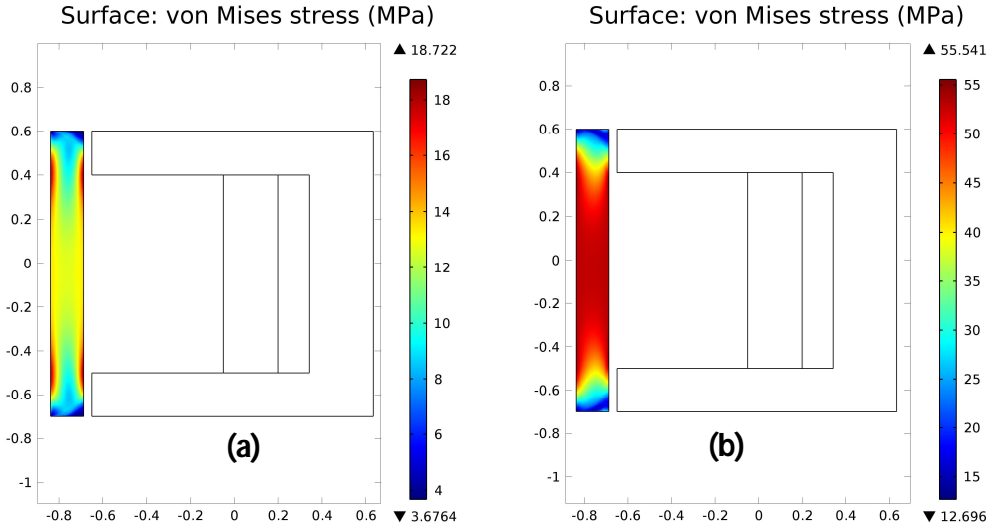
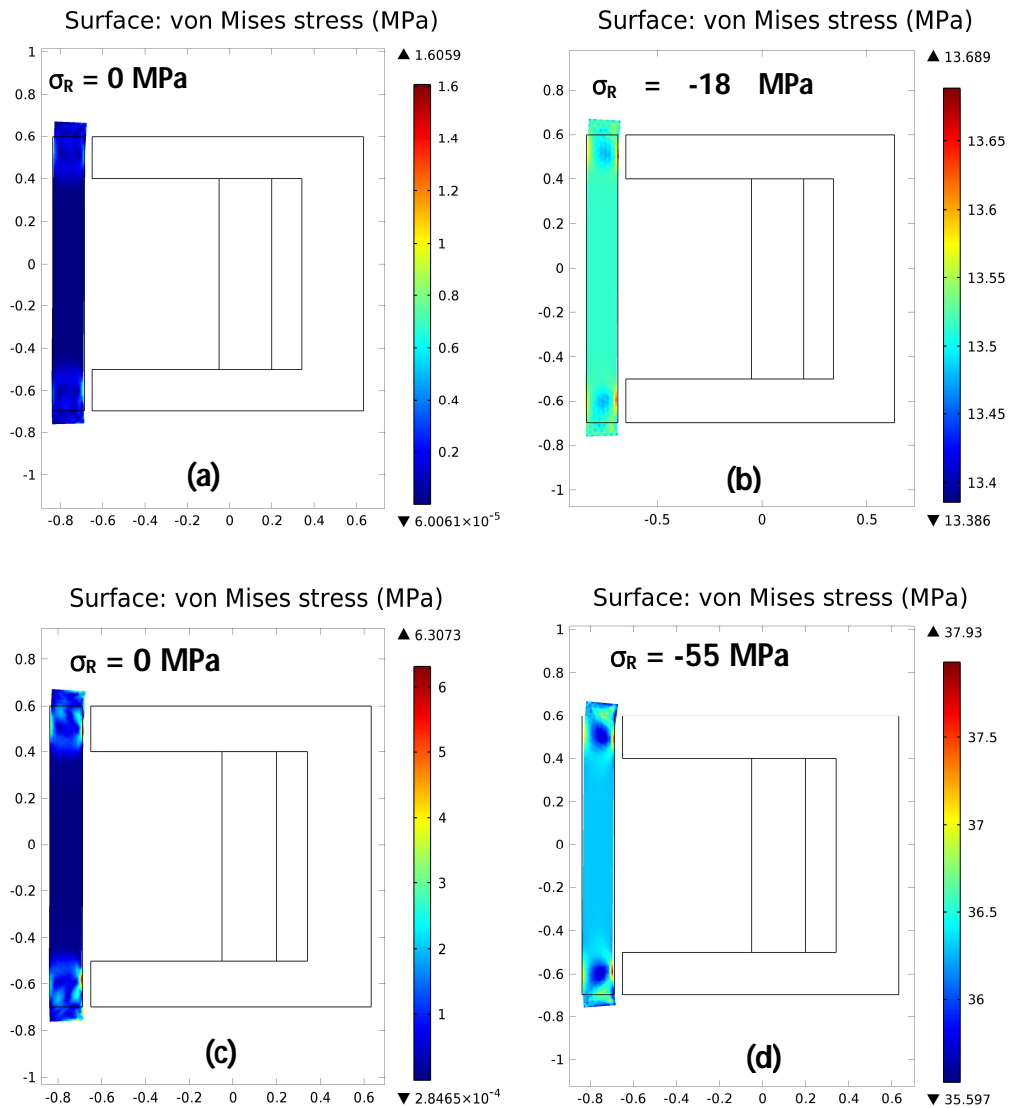


Figure 6.24: Von Mises stresses generated by magnetostriction for a) soft and b) hard magnetic samples.



**Figure 6.25: Von Mises stresses for samples with and without residual stresses on a,b) soft and c,d) hard samples.**

Figure 6.25 shows the von Mises stresses and Figure 6.26 presents the total displacement for samples with and without residual stresses. As can be seen, the von Mises stresses for samples with open boundaries are negligible. In the next step, the samples were magnetized up to saturation and the magnetization changes were calculated for samples with and without residual stresses. Figure 6.27 and Figure 6.28 demonstrate the magnetization changes with an increasing magnetic field  $M(H)$  and the effect of residual stresses on the magnetization of the soft and hard samples.

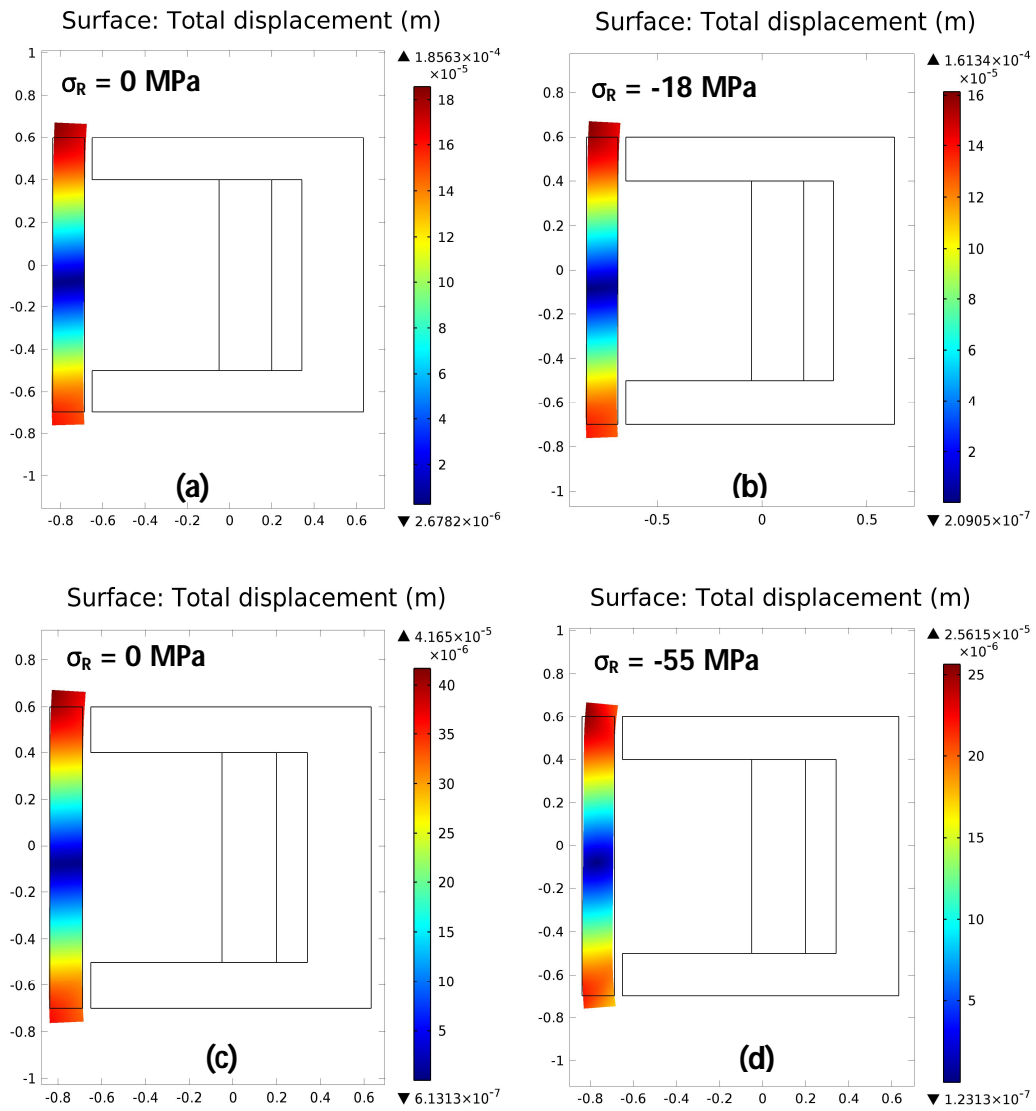


Figure 6.26: Total displacement of samples with and without residual stresses on a,b) soft and c,d) hard samples.

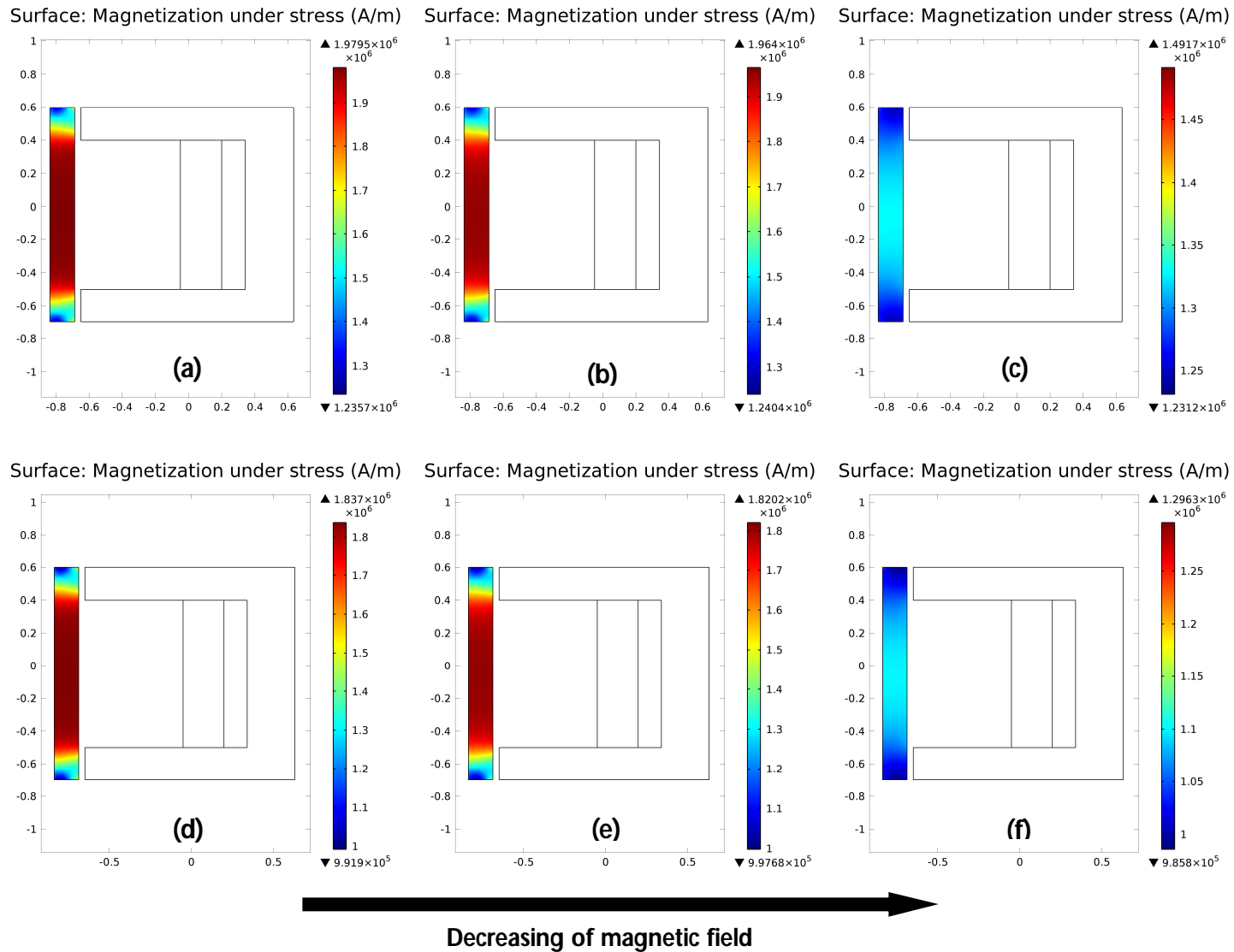


Figure 6.27: Magnetization (M) changes of different magnetic fields (H) for soft magnetic samples under a,b,c) no residual stresses and d,e,f) residual stresses of -18 MPa.

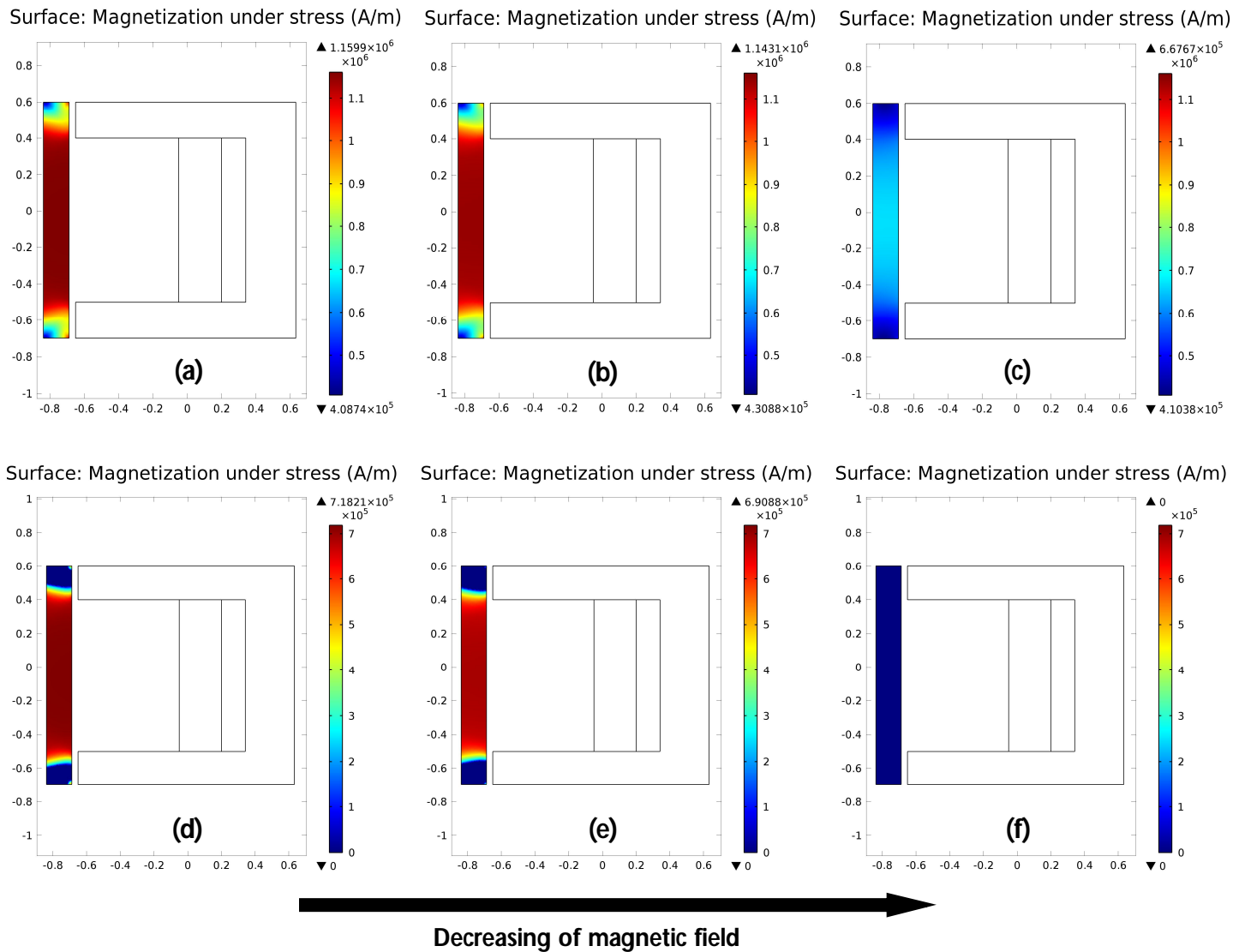


Figure 6.28: Magnetization (M) changes of different magnetic fields (H) for hard magnetic samples under a,b,c) no residual stresses and d,e,f) residual stresses of -55 MPa.

## 7. Discussion

### 7.1. Micro-magnetic characterization of non-deformed samples

#### 7.1.1. Investigation of the micro-magnetic properties of non-deformed samples in an unloaded condition

Figure 6.1 showed the effect of ferritic (Fe-Si steel) and martensitic (pipeline steel) micro-structures on MBN. It should be mentioned that the MBN response was normalized for the Fe-Si and pipeline samples, which helps for better comparison. As can be seen, ferritic steel has a narrow, tall MBN signal, while martensitic steel has a wide, low MBN signal. These represent typical behaviour of MBN, presenting the effect of the micro-structure on MBN [Moor. 1997a, Moor. 1997b]. Ferrite has a body-centred cubic (BCC) crystal structure with an easy axis of (100) while martensite has a body-centred tetragonal (BCT) crystal structure with the same easy axis as ferrite (100) [Cull. 2009, Bozo. 1993]. It is worth noting that an easy axis is an energetically favourable direction in a crystal unit which all domains prefer to align with. Martensitic transformation consists of a shear strain with a magnitude of about 22% which determines the shape of the plates of the martensite [Bhad. 2001]. This internal strain causes the magnetoelastic energy in martensite to increase [Cull. 2009]. Furthermore, the fine martensite plates, which are laid down in fine grains, cause a barrier for DW movement. In contrast, there is no additional barrier for DW motion in the BCC crystal structure of ferrite. Therefore, the MBN signal in the pipeline steel is smaller and wider than that for Fe-Si steel. This phenomenon has an impact on the B-H curves, which can be easily recognized (Figure 6.2). The Fe-Si sample has a narrow B-H curve which is caused by a soft magnetic material, but the pipeline steel presents a wide B-H curve which comes from a hard magnetic material. Magnetostriction also proves that Fe-Si is a soft magnetic material while the pipeline steel sample is a comparatively hard one (Figure 6.3). Since magnetostriction comes from changes in domain directions and is due to the easy movement of the domains on a soft sample (Fe-Si), magnetostriction shows greater

changes in soft samples in comparison to hard magnetic samples. In other words, in the Fe-Si sample, many domains can freely orient in the direction of magnetization, which consequently causes higher magnetostriction, while in the pipeline steel a large number of domains are fixed in their positions and cannot reorient easily in the direction of magnetization, consequently leading to lower magnetostriction.

### **7.1.2. Investigation of the micro-magnetic properties of non-deformed samples in an elastically loaded condition**

Two different possibilities could cause the behaviour observed in Figure 6.4 and Figure 6.5.

1) A change of micro-structure and of the micro-residual stress level of the samples was the first possibility considered. This idea of a change in the micro-structure and/or micro-residual stresses causes the unique behaviour of the MBN presented in Figure 6.4 and Figure 6.5, and indeed originates from the fact that the MBN parameters are indirectly affected by the micro-structure and micro-residual stresses. MBN measurements under applied stress were repeated several times to investigate the micro-structure and micro-residual stress changes of the samples. The point is, if there are any micro-structure or micro-residual stress changes, such as local micro-plastic deformation in the samples, the  $MBN(\sigma)$  curve should exhibit different behaviour in relation to the loading and the unloading curve because the micro-structural changes are irreversible after unloading. However, with the  $MBN(\sigma)$  curves shown here, the curves for loading and unloading behave the same. This result agrees with other published results, which indicates that local micro-plastic deformation happens immediately above half of the yield strength of the sample [Karj. 1979a, Altp. 2009].

2) The second possibility, which could explain the reason for the  $MBN(\sigma)$  curve's behaviour under applied stress, might be presumed to result from the micro-structure and must thus be measurable from the micro-magnetic parameters under applied stress. In other words, although the micro-structure and micro-residual stresses do not change under tensile applied stress until half of the yield point, the micro-magnetic parameters should be affected by applied stress [Altp. 2009, Rabu. 2014].

In order to better understand the observations made in Figure 6.4 and Figure 6.5, hysteresis measurements were carried out. The behaviour of the  $B(H)$  curves - presented in Figure 6.6a and Figure 6.7a - under applied stress can be described by means of the Villari effect [Pere. 2007, Pere. 2012, Szew. 2004, Maka. 2000]. According to the Villari effect, mechanical stress changes magnetic susceptibility, which is directly related to the magnetization of the material [Vill. 1865, Bozo. 1993]. Since MBN is also directly related to the magnetization process, the unique behaviour of MBN under applied stress must therefore be associated with the change in the

magnetization of the sample. This is in agreement with the results from the model presented in Section 6.3. It is noteworthy that some studies suggest that the different shapes of the hysteresis loops resulting from applied stress originate from the different sensitivities of 90° and 180° DWs [Bozo. 1993, Maka. 2000], while others refer the effect to stress-induced anisotropy as the main reason for this behaviour [Pere. 2007, Angl. 2001]. The second suggestion is in agreement with the observations made above and will be explained in what follows. Therefore, further examinations and tests were performed to find more evidence to prove the idea. To this end, the effect of stress on the energy equilibrium for the formation of stable domain structures was investigated, which is presented below.

Equation 7.1, obtained from [Cull. 2009], shows the energy as a function of the crystal and stress anisotropy

$$E = K_1(\alpha_1^2\alpha_2^2 + \alpha_2^2\alpha_3^2 + \alpha_3^2\alpha_1^2) - \frac{3}{2}\lambda_{100}\sigma(\alpha_1^2\gamma_1^2 + \alpha_2^2\gamma_2^2 + \alpha_3^2\gamma_3^2) - \frac{3}{2}\lambda_{111}\sigma(\alpha_1\alpha_2\gamma_1\gamma_2 + \alpha_2\alpha_3\gamma_2\gamma_3 + \alpha_3\alpha_1\gamma_3\gamma_1)$$

**Equation 7.1**

where  $E$ ,  $K_1$ ,  $\lambda$  and  $\sigma$  are the energy, crystal anisotropy, saturation magnetostriction in a certain direction and applied stress, respectively, while  $\alpha$  and  $\gamma$  are the direction cosines of saturation magnetization ( $M_s$ ) and stress ( $\sigma$ ), respectively. The first term of Equation 7.1 describes the crystal anisotropy energy and the next two terms denote magnetoelastic energies. Therefore, the equilibrium direction of  $M_s$  is that which makes  $E$  a minimum and which is largely influenced by the crystal anisotropy ( $K_1$ ) and the stress anisotropy ( $K_\sigma$ ). The stress anisotropy can be calculated using Equation 7.2 [Cull. 2009],

$$K_\sigma = \frac{3}{2}\lambda_s\sigma$$

**Equation 7.2**

where  $\lambda_s$  is the saturation magnetostriction.

Using Equation 7.1 and Equation 7.2, the behaviour of the MBN( $\sigma$ ) curve can be described. It should be mentioned that the descriptions are all discussed on the basis of the  $M_{MAX}$  behaviour, since the results could be transformed into the other MBN parameters, such as  $H_{CM}$ .

The crystal anisotropy ( $K_1$ ) is a constant parameter of the material, but the stress anisotropy ( $K_\sigma$ ) depends on the stress applied and the saturation magnetostriction (Equation 7.2). Using the results shown in Figure 6.9 and Equation 7.2,  $K_\sigma$  was calculated. Figure 7.1 shows the effect of

applied stress on  $\lambda_{MAX}$  and  $K_\sigma$ , where the values have been taken from Figure 6.9 and calculated according to Equation 7.2, respectively. Although  $\lambda_{MAX}$  decreases with increasing applied stress in the pipeline steel,  $K_\sigma$  increases. In other words, the applied stress has a higher effect on  $K_\sigma$  than that of  $\lambda_{MAX}$ . The results obtained with the Fe-Si steel samples are similar to the results for the pipeline steel if the absolute value of  $K_\sigma$  is taken into account.

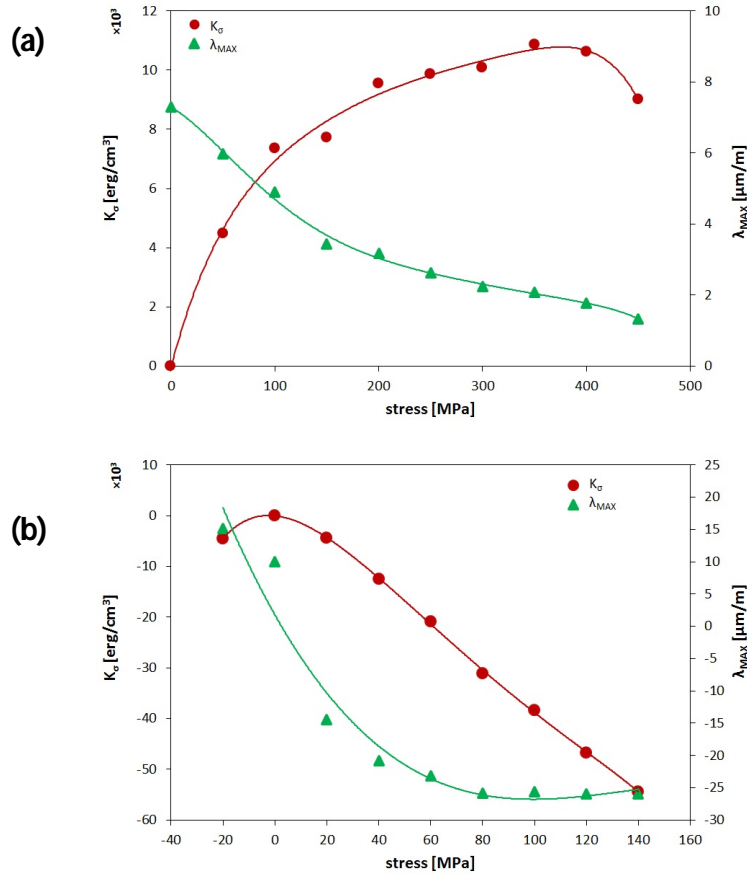


**Figure 7.1: Effect of applied stress on the maximum magnetostriction ( $\lambda_{MAX}$ ) and stress anisotropy ( $K_\sigma$ ) in a) pipeline steel and b) Fe-Si steel.**

The crystal anisotropy constant  $K_1$  for iron and mild steels has been reported in different publications [Bozo. 1993, Cull. 2009, Jile. 1998]. Since the methods of measurement were different in the different publications, different values have also been reported for  $K_1$ . If we assume a value of  $K_1$  reported in the publications as a reference,  $K_1$  turns out to be  $480 \times 10^3$  erg/cm<sup>3</sup> [Cull. 2009]. Comparing  $K_1$  (reported in the publications) to  $K_\sigma$  (presented in Figure 7.1), it is obvious that  $K_1$  is much larger than  $K_\sigma$  [Cull. 2009]. Therefore, the magnetization direction is still controlled by the crystal anisotropy, even under applied stress, up to half a yield.

However, if the magnetization direction does not change with applied stress, then the result obtained as shown in Figure 6.4 and Figure 6.5 can be explained. The energy equilibrium of the

domain structures changes when a sample is subjected to an applied external stress, resulting in an increase in magnetoelastic energy. This is the key point in describing the increase and subsequent decrease in  $M_{BN}(\sigma)$ . In other words, this happens because of a superimposed anisotropy (induced-stress anisotropy) that is additional to the system.

In general, each anisotropy is controlled by the anisotropy energy and has a corresponding anisotropy field ( $H_k$ ), which acts like an external magnetic field to magnetize the sample by aligning the domains in the direction of their easy axes. Therefore, each anisotropy creates a preferable direction (along the easy axis) to orient the domains close to that easy axis direction.

As a consequence, applied stress activates some new easy axes which are controlled by stress anisotropy due to increasing induced-stress anisotropy under applied stress. Under loading conditions, one can, therefore, observe two active easy directions in the system, one of which is defined by the crystal anisotropy and the other by the stress anisotropy. It is of note that most domains prefer to align in the direction of the easy axis defined by the crystal anisotropy, but, from an energy point of view, some of the domains prefer to align along the easy axis direction defined by the stress anisotropy, of which the proportion increases with increasing stress. In other words, the system finds a new equilibrium point as a consequence of the minimum of the crystal and stress anisotropy energy. Consequently there is a competition between two anisotropies, determining the magnetization easy axis under applied stress. With low applied stress, crystal anisotropy ( $K_l$ ) is dominant, while at higher stresses, stress anisotropy ( $K_\sigma$ ) also plays a role in the magnetization process.

This means that in the case of the samples investigated for applied stress values lower than the applied stress at the maximum of the  $M_{MAX}(\sigma)$  curve, the easy axis is controlled by the crystal anisotropy. Hence, the domains turn in the direction of the crystal easy axis, with which the magnetization increases as well. Therefore,  $M_{MAX}$  increases with any increase of the applied stress up to a maximum value.

On the other hand, at higher applied stresses (higher than the applied stresses at the maximum of the  $M_{MAX}(\sigma)$  curve) the stress anisotropy activates an extra magnetization easy axis. The direction of the new activated easy axes is the same as that of the applied tensile stress for a material with positive magnetostriction, and is perpendicular to the stress direction for a material with negative magnetostriction. Therefore, domains where the magnetization direction is aligned close to the new easy axes are preferred in order to turn in the direction of the new easy axis controlled by the stress [Pere. 2012, Noto. 2004]. In summary, the magnetization of a sample decreases when there are different active magnetizing directions, which is a

consequence of the different orientations of the domains. Thus, the stress anisotropy acts as a new obstacle for domain movements, which ultimately causes the MBN to decrease.

A change of energy equilibrium during DW motion can be described by Equation 7.1 when a sample is subjected to stress. It was shown that the stress anisotropy  $K_\sigma$  increases with increasing applied stress (Figure 7.1). Increasing  $K_\sigma$  imposes extra energy on the system. Therefore, the domain structure prefers to reorient for a decrease in the energy equilibrium [Cull. 2009, Noto. 2004]. It is noteworthy that the rearrangement of domains is in the direction of an activated easy direction. Therefore, the stress anisotropy acts as a factor affecting directly the domain structure and - consequently - the magnetization process in such a way that the magnetization will be harder. The MBN will also decrease since it has a direct relation to the magnetization process of the sample.

### **7.1.3. Study of the domain structure of non-deformed samples in an elastically loaded condition**

In order to confirm the explanations mentioned above on a microscopic scale, and since the macroscopic behaviour of a material is directly related to its microscopic behaviour at the scale of a grain, an MFM was used to monitor the magnetic domains at different applied stresses.

It is of note that in Figure 6.11 and Figure 6.12 the higher contrasts come from the domains with opposite directions - which are perpendicularly aligned with the surface - while domains which are aligned parallel to the surface have lower contrast [Bati. 2014]. For the pipeline steel samples, the growth of the domains under applied stress is visible in Figure 6.11a-d. Frequency analysis using 2D-FFT was done in Figure 6.11a and Figure 6.11d to prove quantitatively the growth of the domain structure under applied stress. The 2D-FFT was performed on the MFM image using the LabVIEW programming software. To this end, the FFT analysis was carried out in two axial directions and the amplitude of each frequency was plotted in Figure 7.2. It is noteworthy that the frequency in this case is  $1/\mu\text{m}$ , since the calculation of the FFT is based on the size of the image and the number of pixels in each direction. Based on Figure 7.2, it can be seen that Figure 6.11a has a higher frequency component than Figure 6.11d. Since the higher frequency component results from a finer structure - and vice versa for lower frequency ones - Figure 6.11a has a finer domain structure when compared with Figure 6.11d.

As can be seen in Figure 6.11a-b, the domain structures stay constant with regard to their orientation and domains and only grow with increasing applied stress, while Figure 6.11c-d shows that the domain structure changes gradually and some domains - such as the lower left side of the picture being oriented in the (111) direction according to Figure 6.10a - grow in the direction of the applied stress. This means that the domain structure at higher applied stresses -

higher than 150 MPa in the case considered here - is different and tends to grow in the applied stress direction. Therefore, changes in the domain structures beyond 150 MPa in the applied stress cause the magnetization process to alter gradually, which consequently affects the MBN.

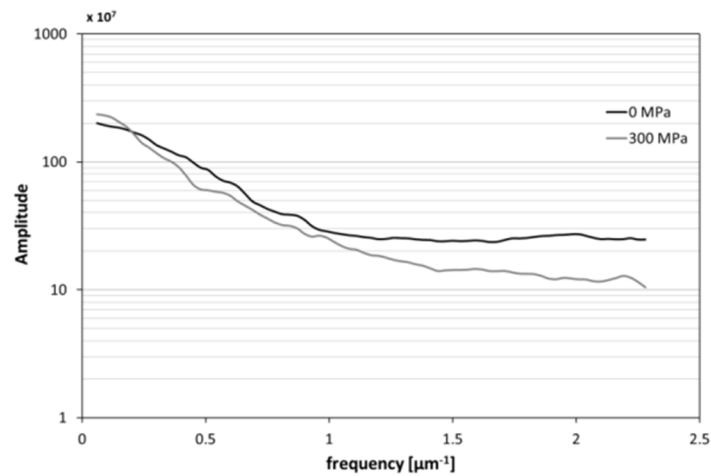


**Figure 7.2: 2D-FFT based on data measured and presented in Figure 6.11a and d.**

The same process happens with the Fe-Si steel (Figure 6.12). The MBN behaviour under applied stress shows a maximum for the  $M_{\text{MAX}}$  parameter around 0 MPa of applied stress. The domain structure, therefore, changes, which comes from the stress anisotropy and should be observed around 0 MPa, which is also visible in Figure 6.12a and b. As can be seen from Figure 6.12a, captured at -20 MPa, the domain structure is different when compared to the higher stresses applied (Figure 6.12b-d). It is also clearly visible that a large domain in the stress direction is created in the middle of the scanned area, which also shows the role of stress anisotropy in a domain structure under applied stress. Therefore, the hypothesis of the competition of anisotropies to control easy axes is also valid for Fe-Si steel.

As a brief conclusion, Figure 7.3 shows schematically the DW motions under applied elastic stresses in a crystal. First, the DWs move in the direction of the easy axis, which is defined by the crystal anisotropy. The black arrow shows the direction of the assumptive easy direction. With increasing stress after a certain level, some DWs move in the new easy axis, for which it is easier for them to move. The green, bold arrow shows the DW motion direction under applied stress. Figure 7.4 and Figure 7.5 also present a conclusion of the MFM results and the schematic DW motion on the MBN( $\sigma$ ) curve.

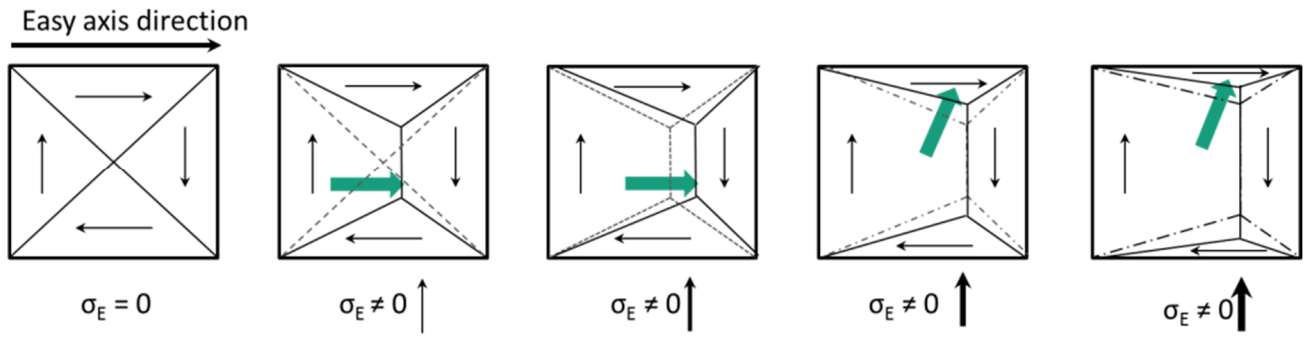


Figure 7.3: Schematic DW motion under elastic applied stress  $\sigma_E$ . The green arrow shows the motion of the DW. Dashed lines show the previous position of the DW.

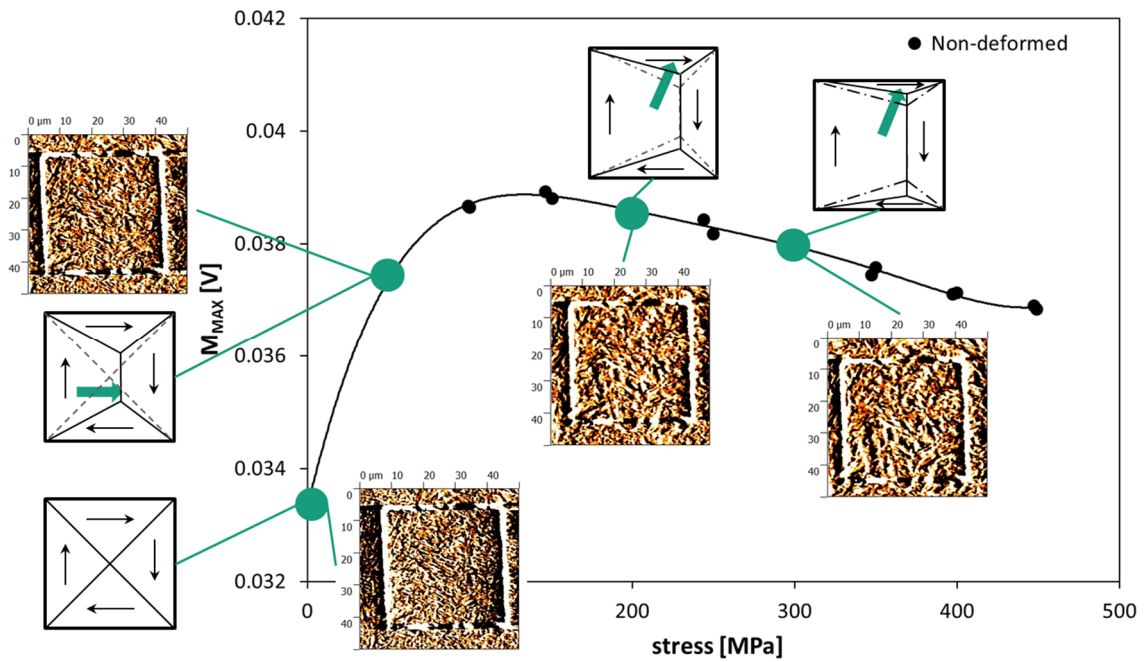


Figure 7.4: Correlation between changes in the domain structures (schematic and MFM results) and the  $M_{MAX}(\sigma)$  curve of the pipeline steel sample.

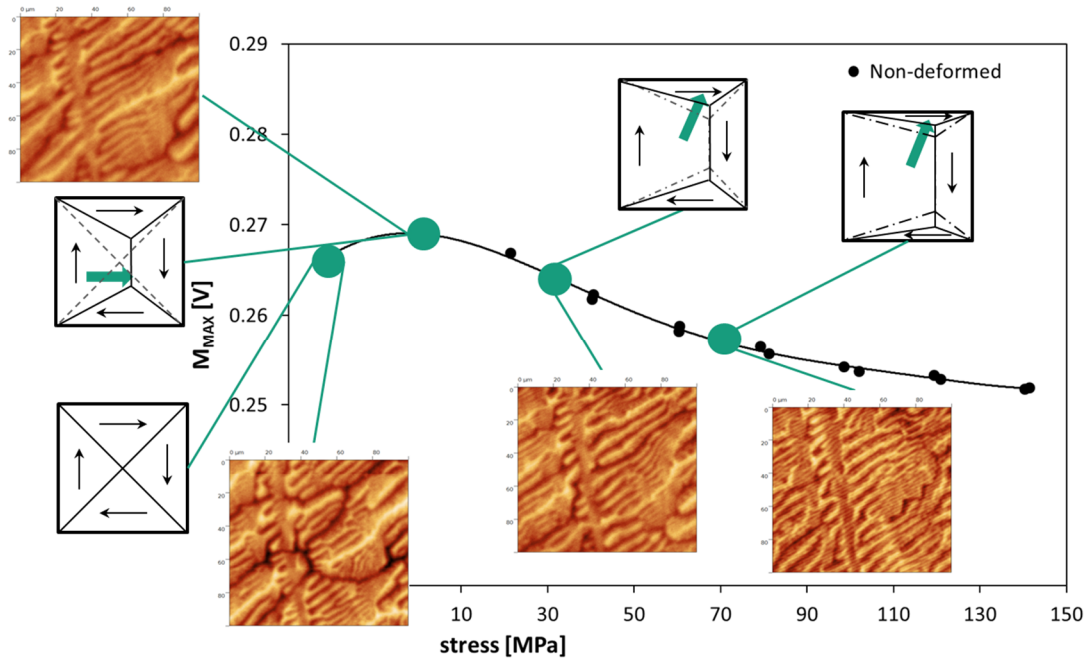


Figure 7.5: Correlation between changes in the domain structures (schematic and MFM results) and the  $M_{MAX}(\sigma)$  curve of the Fe-Si steel sample.

## 7.2. Micro-magnetic characterization of plastically pre-deformed samples

### 7.2.1. Investigation of the micro-magnetic properties of pre-deformed samples in an unloaded condition

The results in Figure 6.13-Figure 6.15 can be described based on the fact that tensile plastic deformation generates micro-compressive residual stresses after unloading. At first glance,  $M_{MAX}$  decreases and the magnetic field at the maximum amplitude of the Barkhausen noise ( $H_{CM}$ ) increases with the generation of compressive micro-residual stresses [Cull. 2009, Hauk. 1997, Jaga. 1990, Thei. 1979, Thei. 1983]. The reason for this behaviour is related to the activity of the  $90^\circ$  and  $180^\circ$  DWs in the presence of residual stress. Tensile residual stresses extend the  $180^\circ$  DWs while compressive residual stresses extend the  $90^\circ$  DWs [Bozo. 1993, Cull. 2009]. Due to their elastic volume distortion, the motion of the  $90^\circ$  DWs requires higher magnetic fields when compared with the  $180^\circ$  ones, which is the reason why they are also known as the barely movable DWs. Since the MBN occurrence is directly related to the motion of the DWs,  $M_{MAX}$  decreases with increasing compressive micro-residual stresses.

Hysteresis curves also confirm the features of the MBN curves. As shown in Figure 6.14, the  $B(H)$  curve is widened with increasing plastic deformation. In other words, compressive residual stress

increases the coercivity field ( $H_c$ ) and decreases the remnant flux density ( $B_r$ ) [Bozo. 1993, Cull. 2009]. The effects of the  $90^\circ$  DWs are also visible in Figure 6.15. The  $90^\circ$  DWs are responsible for the magnetostriction changes [Cull. 2009]. Since compressive residual stresses increase the number of  $90^\circ$  DWs, the magnetostriction increases in the pre-deformed samples. This is the main reason for the difference in magnetostriction of the non- and pre-deformed samples.

The effect of plastic deformation on the micro-magnetic parameters could be explained by the schematic domain structures presented in Figure 7.6. This figure shows that plastic deformation changes the domain structure drastically and irreversibly because of micro-structural changes, in such a way that even after unloading the domain structure is totally different from the domain structure before plastic deformation.

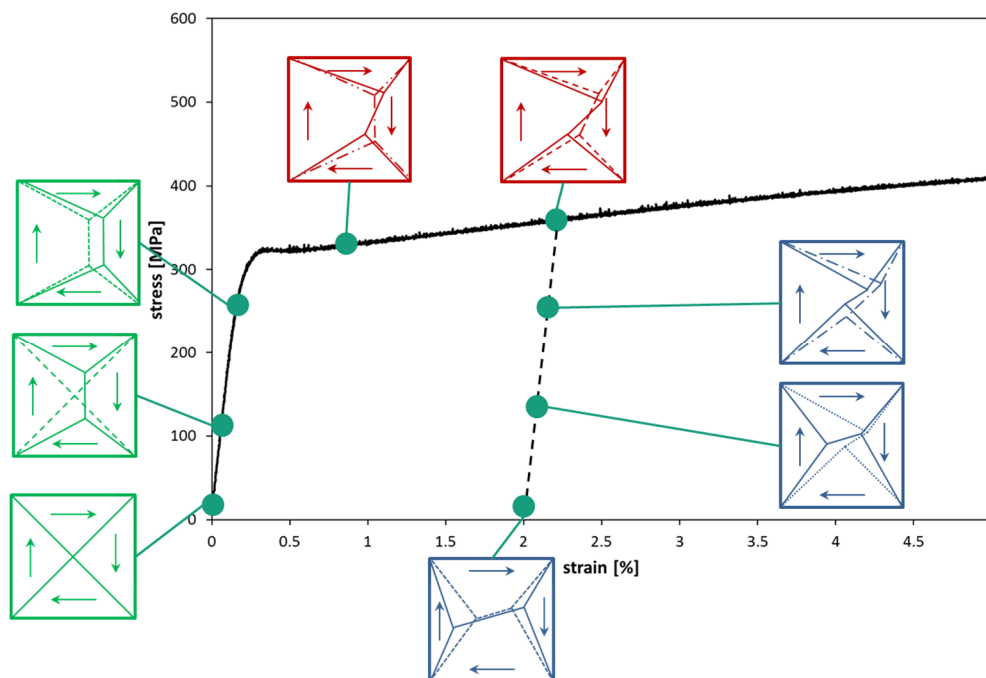


**Figure 7.6: Schematic domain changes from elastic to plastic deformation and back to zero applied stress. Green shows the domains before the yield point, red after the yield point, and blue shows the domain changes at unloading to zero stress. The dashed lines show the previous position of the DWs.**

Regarding the results presented in Figure 6.16, it is of note that the  $M_{MAX}$  and  $M_{mean}$  parameters exhibit different behaviour in Fe-Si steel when compared with the pipeline steel. The  $M_{MAX}$  and  $M_{mean}$  parameters first increase with increasing plastic deformation and then decrease again in the Fe-Si steel samples, while a continuous decrease is observed for the pipeline steel samples. The reasons for this can be seen in the change in the micro-residual stresses and dislocation densities with plastic deformation and their effects on the MBN [Kleb. 2004]. The pipeline and Fe-Si steel samples were, therefore, analysed with the kernel average misorientation method

using an SEM device and the EBSD technique [Taka. 2005, Wrig. 2011]. This method is based on measuring the average misorientation between each neighbouring pair of measurement points within a kernel in the EBSD image (which has been taken at very high resolution). A kernel is a set of points with a predetermined size surrounding a selected scan point. Since the misorientation at the grain boundaries and dislocations is more than that inside a grain or a non-deformed area, this method can therefore qualitatively show the dislocation density differences between non- and pre-deformed samples. Hence, EBSD scans were performed on the non- and pre-deformed pipeline and Fe-Si steel samples. Figure 7.7 and Figure 7.8 show the results obtained by the kernel average misorientation method. The red-scale colour shows a high misorientation and green shows a low misorientation.

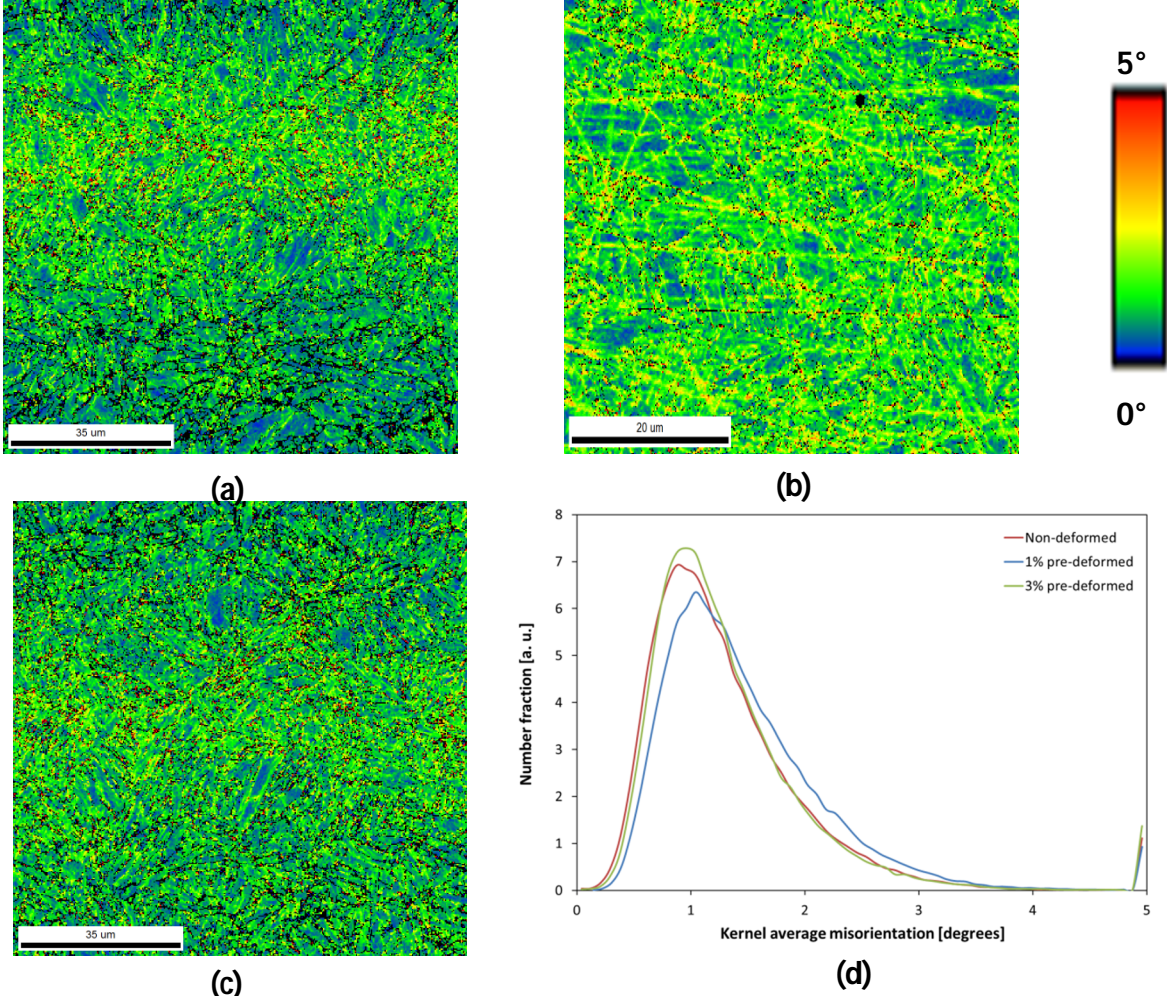


**Figure 7.7: Kernel average misorientation maps of a) non-, b) 1% pre-, and c) 3% pre-deformed pipeline samples. d) Distribution of the Kernel average misorientation for non- and pre-deformed pipeline steel samples.**

The pipeline samples do not show a substantial difference between the non- and pre-deformation samples. In other words, during plastic deformation of the pipeline steel, the dislocation density stays constant. However, the results of the Fe-Si steel samples show a significant difference in the Kernel average misorientation maps between the non- and pre-

deformed samples. This means that the dislocation densities during the plastic deformation of the Fe-Si steel were drastically changed. Furthermore, it is obvious that most changes in the 3% pre-deformed Fe-Si steel samples happen at the grain boundaries. The concentration of dislocations at the grain boundaries imposes elastic strain, which consequently changes the energy equilibrium of the DW in such a way that the number of DWs increases [Cull. 2009]. An increase in the DW causes the MBN signal to increase. However, dislocation densities are spread inside the grains within the 5% pre-deformed Fe-Si steel sample. This causes dislocation tangles to be created, known as DW hindrances [Cull. 2009]. Therefore, the MBN decreases with the occurrence of dislocation tangles in the sample.

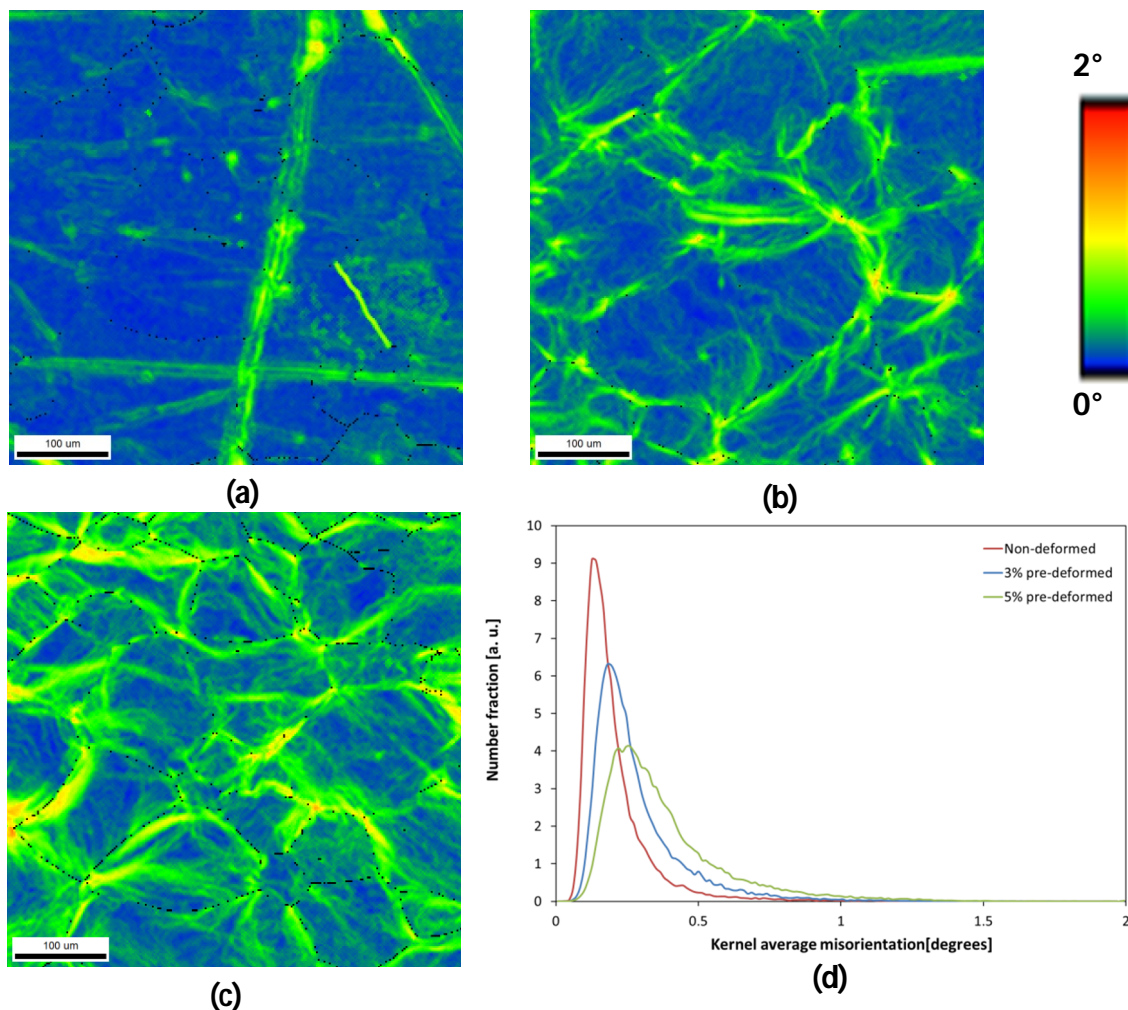


**Figure 7.8: Kernel average misorientation maps of a) non-, b) 3% pre-, and c) 5% pre-deformed Fe-Si steel samples. d) Distribution of the Kernel average misorientation for non- and pre-deformed Fe-Si steel samples.**

### 7.2.2. Investigation of the micro-magnetic properties of pre-deformed samples in an elastically loaded condition

According to Figure 5.23 and Figure 5.24, in general the MBN( $\sigma$ ) curve reaches a peak at higher applied stresses in the pre-deformed samples compared to the non-deformed samples. This means that the stress anisotropy can affect the MBN at a higher applied stress in competition to

determine the magnetic easy axis because of the effect of micro-compressive residual stresses, which causes a hard magnetization axis in the direction of the applied stress [Szew. 2004]. In other words, three different anisotropies are active here: the crystal anisotropy ( $K_1$ ), the stress anisotropy caused by the micro-compressive residual stress ( $K_\sigma$ ), and the stress anisotropy caused by the applied tensile stress ( $K_{\sigma+}$ ). Insofar as the last two stress anisotropies are acting in opposite directions, the applied tensile stress has to overcome a higher anisotropy in the pre-deformed sample for the activation of the new magnetic easy axes. Thus, the extremum of MBN( $\sigma$ ) is detected at higher stresses in the case of the pre-deformed samples.

### **7.2.3. Analysis of the domain structure of plastically pre-deformed samples under elastically loaded conditions**

Figure 6.19-Figure 6.20 present the domain structures of the pipeline steel under applied stress, whereby the changes in the domains can barely be distinguished. The complexity of the micro-structure of the pipeline steel and the effect of compressive micro-residual stresses on stabilizing the domain structures are the reasons why the domain changes are so small.

On the other hand, Figure 6.22 and Figure 6.23, which illustrate the effect of applied stress on the domain structures in Fe-Si steel, show drastic domain structure changes under applied stress. Figure 6.22 and Figure 6.23 could be explained by the EBSD images (Figure 6.21). As can be seen in Figure 6.21a, which shows that the area scanned with MFM, the 3% pre-deformed sample contains two grains, one of which is oriented in the (111) direction (blue) and the other of which is oriented between the (001) and (101) directions (yellow) respectively. When comparing the results in Figure 6.22 and Figure 6.21a, it becomes clear that the spike domains (the marked area in Figure 6.22 c-d) are created in the directions of the applied stress in grains oriented towards the (111) direction [Noto. 2004]; however, in the other grain all the domains lie down in the direction (001) (the crystal easy axis) [Bati. 2014]. These explanations are also valid for the 5% pre-deformed sample. In Figure 6.23, the upper grain is oriented in the (111) direction (Figure 6.21b) and, therefore, the domains tend to turn and grow in the direction of the applied stress. In the lower grain, the changes in the domain structure are complex, since the grain is oriented in the (101) direction. As illustrated, the formation of the spike-shaped domains is visible in Figure 6.22 and Figure 6.23, with an increase in applied stress. It has been reported that a spike-shaped domain causes the magnetostatic energy of the system to decrease, but due to the stress anisotropy, the formation of these types of domains causes the break-up of the 180° domain into the other type of DW (e.g., 90°) [Noto. 2004], which leads the fraction of 180°/90° domains to decrease [Noto. 2004]. Therefore, the magnetization

decreases after the formation of the spike-shaped domains, which consequently causes the MBN signal to decrease as well.

### **7.3. Modelling of the magnetization process under the effect of stress**

As discussed in Sections 7.1 and 7.2 above, the investigation of micro-magnetic behaviour at the grain-level is necessary for the proper understanding of MBN behaviour under stress. The understanding of MBN behaviour will be easier when the effect of stress on MBN is simplified down to a model based on the behaviour of the unit cell of the ferromagnetic material under stress [Catt. 1995]. Furthermore, magnetization changes under stress simplify the MBN response. Therefore, a model has been proposed (Chapter 4) and some initial calculations have already been performed using the COMSOL Multiphysics software.

According to the results presented in Figure 6.24, magnetostriction can generate micro-residual stresses for completely fixed boundary conditions. Since magnetostriction originates from the orientation of magnetic dipoles [Cull. 2009], the generated micro-residual stresses must be of Type III.

Figure 6.27 and Figure 6.28 present how the magnetic field strength, material type and residual stresses have a direct effect on the magnetization of the samples. As can be seen, the magnetization  $M$  decreased with a decreasing magnetic field as well as with increasing compressive residual stresses. The  $M(H)$  curves derived from the calculations presented in Figure 6.27 and Figure 6.28 can deliver valuable information about the magnetization of the samples. The  $M(H)$  curves for the soft and hard magnetic samples are shown in Figure 7.9. Two points can be made deriving from Figure 7.9: 1) The  $M(H)$  curve for the hard sample is under the  $M(H)$  curve of the soft sample. This shows that the magnetization process of the soft sample is easier than that of the hard sample. 2) Micro-residual stresses decrease the magnetization ( $M$ ). This is in agreement with the results published by Jiles and Cullity et al. [Jile. 1989, Jile 1998, Cull. 2009]. Based on Figure 7.9, it was shown that even minimum residual stresses have a direct effect on the magnetization process.

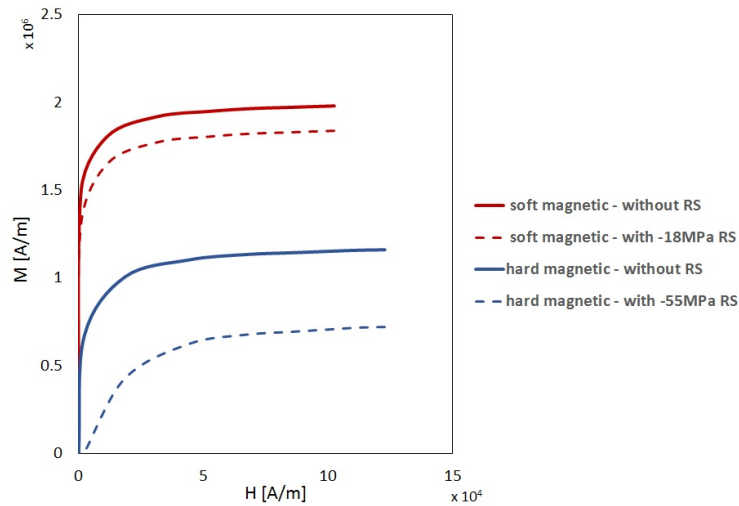


**Figure 7.9: Effect of residual stress on the magnetization curve  $M(H)$  for soft and hard magnetic samples.**

Although the results presented in Figure 7.9 are in good agreement with the experimental data presented in Sections 7.1 and 7.2, it is significant that the calculation of the  $B(H)$  curve requires the analytical simulation that it is based on, for example the Jiles-Atherton-Sablik model [Jile. 1998, Sabl. 1993, Rame. 1998]. This can be done either with COMSOL or MATLAB or else a linked combination of both. Furthermore, the model can be extended to a polycrystalline materials system based on the steps mentioned in Chapter 4. Since the subject of the work presented here is the experimental measurement and validation of micro-residual stresses, the results and validations have been used as reference data for the validation of the model.

## 7.4. The micro-residual stress mapping method based on magnetic Barkhausen noise

The novel **RESTMAB** is proposed in this section. The aim of the RESTMAB is the non-destructive estimation of the micro-residual stresses of materials **without** any help from conventional stress measurement methods based on XRD. The XRD measurements presented here have, therefore, only been performed for the purpose of validation.

The RESTMAB is based on the MBN behaviour of non- and pre-deformed samples under elastic applied strain, or more simply based on the MBN( $\sigma$ ) curve. As described in Sections 7.1 and 7.2, the  $M_{MAX}$  obtained from the MBN measurements exhibits unique behaviour. The MBN parameters increase or decrease (depending on the parameter) with an increase in the applied stress and then decrease or increase again, respectively. This behaviour has been observed for non- and pre-deformed samples (Section 6.2.2). Moreover, the MBN behaviour before the maximum in the non- and pre-deformed samples shows a peculiar parallel linear behaviour, especially in the pipeline steel samples analysed. These two elements of information - which are

the basis of the RESTMAB - led to the idea of measuring micro-residual stresses based only on the MBN( $\sigma$ ) curve. The corresponding process is described in what follows.

Two independent approaches are proposed here, one of which is based on the shifting of the MBN( $\sigma$ ) curve and the other on the linearity of MBN under applied stress for non- and pre-deformed samples (called the "peak shift method" and the "slope method" respectively).

#### **7.4.1. The peak shift method**

Figure 6.17 and Figure 6.18 present the effect of elastic applied strain on micro-magnetic properties, which has been discussed in detail in Sections 7.1 and 7.2. Since the behaviour of all the parameters provides similar information, we will first of all concentrate on discussing the  $M_{MAX}$  behaviour here.

Altpeter and Rabung [Altp. 2001, Altp. 2009, Rabu. 2014] have shown that the position of the maximum of the  $M_{MAX}(\sigma)$  curve is proportional to the micro-residual stresses of the samples. In other words, the peak shift of  $M_{MAX}(\sigma)$  of a known sample related to the reference sample is equal to the micro-residual stress of the unknown sample. Therefore, two things are very important in obtaining reliable results:

1. Since a sample must be compared with a reference sample, a reference non-deformed sample in a stress-free state is required;
2. The position of the maximum of the  $M_{MAX}(\sigma)$  curve must be precisely determined.

To satisfy the first point, the residual stress of the non-deformed sample has to be known. However, in this case, the micro-residual stresses of the non-deformed sample can be assumed to be equal to zero if there was no surface treatment of the samples. Nonetheless, in some cases - such as within a martensitic micro-structure - a micro-residual stress of Type III could be observed due to the displacive transformation from a FCC to a BCT crystal unit. Such micro-residual stresses of Type III will be relaxed, partially, with the plastic deformation of the transformed grain [With. 2001]. However, the micro-residual stresses of Type II will be zero in a polycrystalline sample because of the different orientations of grains. Therefore, any micro-residual stresses can be considered negligible. Hence, a non-deformed sample can be considered to be the reference sample.

The  $M_{MAX}(\sigma)$  curve was fitted by a polynomial equation. The program was written using the National Instruments LabVIEW software and a peak detector algorithm was used to improve the precision of the calculation. Figure 7.10 shows the position of the maximum of the  $M_{MAX}(\sigma)$  curve for non- and pre-deformed samples calculated with the software. Since it was assumed for the non-deformed sample that the residual stress was 0 MPa, the difference between the

maximum of the non-deformed and pre-deformed samples indicates the micro-residual stress of the pre-deformed sample. The indication of micro-residual stresses was defined with the position of the maximum of the  $M_{MAX}(\sigma)$  curve of the pre-deformed sample related to the  $M_{MAX}(\sigma)$  curve of the non-deformed sample. If the maximum of the  $M_{MAX}(\sigma)$  curve of the pre-deformed sample locates at the left-hand side of the maximum of the  $M_{MAX}(\sigma)$  curve of the non-deformed sample, then the pre-deformed sample has a tensile micro-residual stress ( $\sigma^+$ ). It has a compressive micro-residual stress ( $\sigma$ ) when the maximum locates at the right-hand side in relation to the non-deformed sample [Altp. 2009, Rabu. 2014]. More simply, the micro-residual stress of the pre-deformed sample is calculated using Equation 7.3,

$$\sigma_R = \sigma_{crit.(n)} - \sigma_{crit.(p)}$$

**Equation 7.3**

where  $\sigma_R$  is the residual stress, and  $\sigma_{crit.(n)}$  and  $\sigma_{crit.(p)}$  are the applied stresses at the maximum of the  $M_{MAX}(\sigma)$  curve for the non- and pre-deformed samples, respectively.

Table 7.1 shows the micro-residual stresses of the non- and pre-deformed samples calculated with the peak shift method as well as the residual stresses measured with XRD. Since tensile plastic deformation generates compressive micro-residual stresses after unloading, the indication of calculated and measured residual stress can be described. Moreover, the difference between the calculated and measured residual stress values is within an acceptable range for the 0% and 1% pre-strained samples compared with the large difference between the calculated (peak shift method) and measured values of the residual stress for the 3% pre-deformed sample. The 1% pre-deformed sample shows -11 MPa residual stress, which is caused by the martensitic micro-structure [Bhad. 2001]. Martensite induces slight compressive residual stress because of the nature of martensitic transformation [Bhad. 2001, Port. 1992]. Martensitic transformation is a massive and diffusionless transformation from austenite with an FCC crystal structure to martensite with a BCT crystal structure, which happens in a fraction of a second in such a way that Fe and C atoms do not have enough time to rearrange in the BCC system. Therefore, the BCT system, which is a deformed form of a BCC system, creates some compressive micro-residual stresses [Bhad. 2001, Port. 1992]. These compressive micro-residual stresses were detected in XRD measurements for the non-deformed sample.

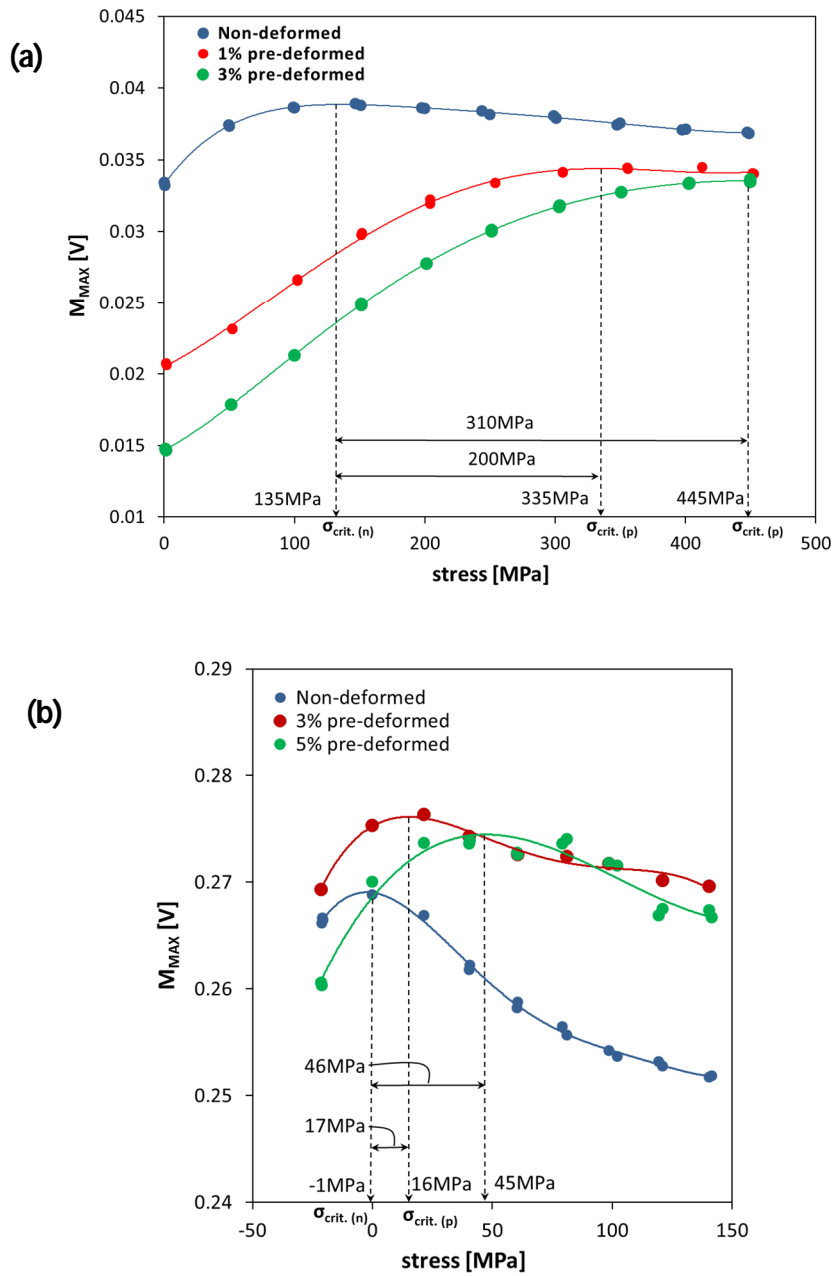


Figure 7.10: Difference between the maximum of the  $M_{MAX}(\sigma)$  curve of non-deformed (reference) samples as well as pre-deformed samples of a) pipeline and b) Fe-Si steels.

Table 7.1: Micro-residual stress values of pipeline steels measured with the peak shift method and XRD.

Samples	Residual stress	
	Peak shift method [MPa]	XRD [MPa]
Non-deformed	0	-11.5
1% pre-deformed	-200.18	-208.4
3% pre-deformed	-310.87	-185.3

Another case which needs to be explained is the reason why the samples with 1% and 3% pre-deformation exhibit roughly the same compressive residual stress in the XRD results while the peak shift method shows a significant difference! To address this issue, we need to consider the nature of each method. The XRD method for measuring macro-residual stress is based on the change in the position of the peak of the lattice parameter-intensity curve, while for micro-residual stresses it is based on the change in the width of the peak at half the maximum of the lattice parameter-intensity curve [Hauk. 1997]. In this work, the method mentioned first was used, since no change in the width of the peak at half the maximum of the lattice parameter-intensity curve was observed. Therefore, the XRD values indicate the macro-residual stresses of the samples while the peak shift method shows the macro- and micro-residual stresses. In other words, with a plastic deformation of more than 1%, only the local micro-residual stresses increase due to an increase in the number of dislocation tangles [Kleb. 2004]. Since the micro-residual stresses caused by dislocations are Type III residual stresses, it is difficult for XRD to detect it. In contrast, the peak shift method is capable of measuring residual stresses of Type II and Type III. Furthermore, the penetration depth of the XRD technique is much less than that of MBN. This is also a source of error for the XRD measurements.

Table 7.2 presents the micro-residual stress values of Fe-Si steel samples estimated with the peak shift method and measured with XRD. As can be seen, the residual stresses estimated with the peak shift method are in very good agreement with the values measured by XRD.

**Table 7.2: Micro-residual stress values of Fe-Si steels measured with the peak shift method and XRD.**

Samples	Residual stress	
	Peak shift method [MPa]	XRD [MPa]
Non-deformed	0	0
3% pre-deformed	-17	-9.4
5% pre-deformed	-46	-48.4

#### 7.4.2. The slope method

The slope method is also based on the MBN( $\sigma$ ) curve, but it is only in the linear range before the maximum. The basis for this method comes from an observation of the MBN( $\sigma$ ) curve of all the non- and pre-deformed samples, which generally exhibit linear and parallel behaviour before the maximum [Yelb. 2010, Ju. 2003]. The slope method uses this linearity of the MBN behaviour under applied stress to measure the micro-residual stress of the samples. It of note that a reference non-deformed sample is also required for this method. As with the peak shift method, it is assumed that the non-deformed sample is free from any residual stresses. For this method,

in general, the equation of the linear part of the MBN( $\sigma$ ) curve of the reference sample should be measured and then the interception point of the calculated equation for the reference sample should be modified with the MBN response of the pre-deformed samples at zero applied stress. The first question, which comes to mind is: "Is the MBN behaviour really linear until the maximum?" To prove the linearity of the MBN( $\sigma$ ) function, the MBN was measured for two compressive applied stresses.

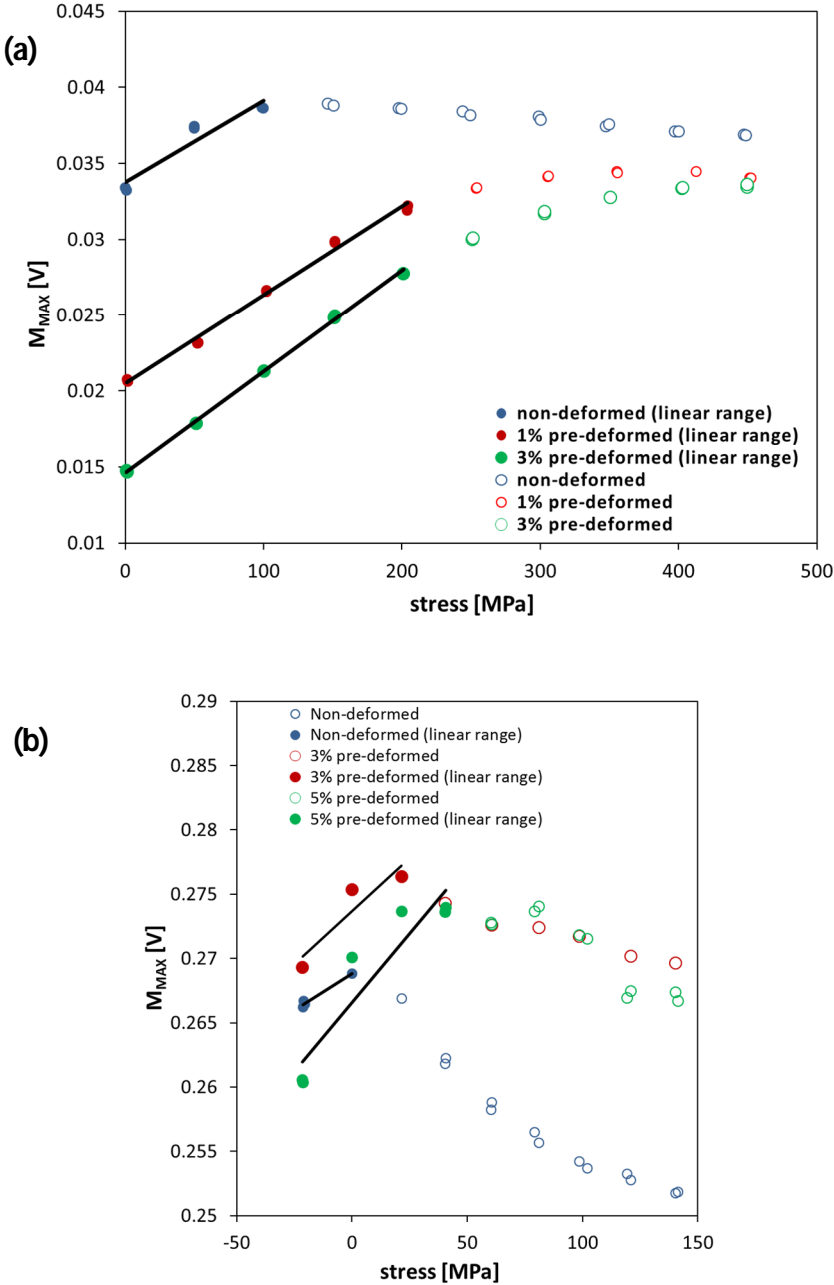


**Figure 7.11: The slope method, which shows the linearity of the  $M_{MAX}(\sigma)$  curve before the maximum for a) pipeline and b) Fe-Si steels.**

As Figure 7.11 shows, the MBN behaves linearly until it reaches the maximum (except for the non-deformed Fe-Si sample). The latter problem arises from there being too few points before

the maximum. Therefore, the linearity of the behaviour cannot be presented properly for the non-deformed Fe-Si samples. It should be mentioned that, due to technical limitations such as the bending of the sample under compressive applied stress, the MBN( $\sigma$ ) curve was only measured up to -20 MPa for the Fe-Si samples.

For the estimation of the micro-residual stresses of an unknown sample, the following steps were performed. The linear equation between stress and MBN (here  $M_{MAX}$ ) is symbolically represented in Equation 7.4,

$$\sigma = A \times M_{MAX} + B$$

**Equation 7.4**

where  $\sigma$ ,  $M_{MAX}$ , A and B denote the stress, the  $M_{MAX}$  signal, the slope of MBN( $\sigma$ ) and the interception of the MBN( $\sigma$ ) curve, respectively.

As mentioned, the reference sample is stress-free ( $\sigma=0$ ); therefore, the interception of Equation 7.4 can be calculated as follows:

$$\sigma = A \times M_{MAX} (\text{reference sample}) + B = 0 \Rightarrow B = -A \times M_{MAX} (\text{reference sample})$$

**Equation 7.5**

With the substitution of Equation 7.5 into Equation 7.4, a general formula is derived for the calculation of the residual stress of an unknown sample:

$$\begin{aligned} \sigma &= (A \times M_{MAX}) + (-A \times M_{MAX} (\text{reference sample})) \Rightarrow \\ \sigma &= A \times (M_{MAX} - M_{MAX} (\text{reference sample})) \end{aligned}$$

**Equation 7.6**

Using Equation 7.6, the micro-residual stresses of any sample can be measured using a simple MBN measurement.

Based on Figure 7.11 and the calculations presented above, linear equations of the non- and pre-deformed samples were calculated. Table 7.3a shows the micro-residual stresses estimated by the slope method and measured by the XRD method. As can be seen, the micro-residual stress values measured with the slope method are similar to the peak shift method values and are in good agreement with the XRD values. The reason for the differences has been discussed in the previous section.

**Table 7.3: Micro-residual stress values of a) pipeline and b) Fe-Si steel measured with the peak shift method and XRD.**

(a)	Samples	Residual stress	
		Slope method [MPa]	XRD [MPa]
	Non-deformed	0	-11.5
	1% pre-deformed	-212.73	-208.4
	3% pre-deformed	-313.15	-185.3

(b)	Samples	Residual stress	
		Slope method [MPa]	XRD [MPa]
	Non-deformed	0	0
	3% pre-deformed	+31.32	-9.4
	5% pre-deformed	+5.22	-48.4

Table 7.3b shows the residual stress measured with the slope method and XRD in Fe-Si samples. In contrast to the pipeline steel samples, the residual stresses measured with the slope method in Fe-Si steel do not properly agree with the values obtained from the XRD measurements. To understand this difference, a relationship needs to be established to demonstrate some of the reasons which could cause the difference between the slope method and XRD measurement values in Fe-Si steel. First, the slope of the linear range for the non-deformed Fe-Si steel samples is different from the slope of the pre-deformed samples. Second, the plastic deformation in Fe-Si sample is non-uniform according to Figure 7.8, which causes tensile and compressive residual stresses depending on the grain orientation. In other words, when considering MBN measurements to be local, the results obtained are actually dependent on the position of the measurement. This means that the result depends on the position of the MBN sensor being on either low or high plastically deformed grains.

In conclusion, it should be mentioned that the slope method is useful and efficient only for materials with a uniform plastic deformation in different grains, such as pipeline steel. In the case of samples like Fe-Si - with a non-uniform deformation - the peak shift method is to be preferred since it represents good agreement in terms of both uniform and non-uniform plastic deformation.

### 7.4.3. The calibration process of the Barkhausen noise and eddy current microscope for measuring micro-residual stresses

Before describing the calibration method of the BEMI using the RESTMAB, one needs to address why a calibration process is principally required. For this, it is necessary to describe the basics of the method proposed in Section 7.4.1 and 7.4.2. As can be seen in Figure 7.10 and Figure 7.11, the measurement of the micro-residual stresses of each sample requires the MBN( $\sigma$ ) curves to be available for reference for the non-deformed and pre-deformed samples. In other words, to have one value for the micro-residual stress of an unknown sample, in situ measurement of the MBN( $\sigma$ ) curve is required. This measurement essentially requires a sample preparation. Furthermore, the in situ measurement of the MBN( $\sigma$ ) curve is time consuming. Therefore, a general calibration curve which allows for micro-residual stresses to be estimated easily is a necessity. This calibration process - which is presented in the following - uses a regression analysis to find a general formula for measuring micro-residual stresses. It also describes which parameters are used, why they are used and how they improve the regression analysis results.

The calibration process is a statistical method for finding a relationship between two measurements from two different devices and methods. Therefore, each calibration needs at least two parameters which, in this case, are residual stress ( $\sigma$ ) and a micro-magnetic parameter, such as  $M_{MAX}$ . Based on the number and types of parameters to be used in the calibration process, the calibration results may differ. In addition to the input parameters, the calibration method and calibration conditions also affect the results. Assuming all of these parameters as a variant makes the calibration process very sophisticated, but also time-consuming. Therefore, the method and conditions of calibration were kept the same for all processes and only the input parameters were different. Linear multi-parameter regression analysis was defined as a calibration method. The basic idea of this analysis is to find a linear relationship between one dependent variable  $y$  (which in this case is  $\sigma$ ) and the multiple explanatory variable  $x$  (which in this case denotes MBN parameters, like  $M_{MAX}$ ). Therefore, the output of analysis is an equation like Equation 7.7, which shows the relationship between the dependent and explanatory parameters:

$$Y = \alpha_0 + \alpha_1 X_1 + \alpha_2 X_2 + \alpha_3 X_3 + \dots + \alpha_n X_n$$

**Equation 7.7**

As previously mentioned, the residual stress and micro-magnetic parameters (here, the MBN parameters) are the inputs of the regression analysis. First of all, the residual stresses will be discussed. It is important to recall that the MBN( $\sigma$ ) curve presented in Figure 7.10 and Figure 7.11 provides the input parameters of the regression analysis, although some

modifications were carried out. In other words, the  $M_{MAX}(\sigma)$  curves of the pre-deformed samples were moved to the  $M_{MAX}(\sigma)$  curve of the non-deformed sample in such a way that all the maxima were aligned under the maximum of the  $M_{MAX}(\sigma)$  curve of the non-deformed sample. The modification comes from the fact that the MBN response is affected by the summation of the applied and residual stresses. In other words, the MBN output shows the effect of the residual stress and the applied stress at the same time. Therefore, the Y-axis (such as  $M_{MAX}$ ) in Figure 7.10 and Figure 7.11, is affected by the residual and the applied stresses, while the X-axis just presents the applied stresses. Since the separation of the effect of the residual and the applied stress for MBN is not possible, the X-axis was modified to show the summation of the applied and residual stresses. The residual stress of each sample was measured based on the peak shift method. It is worth mentioning again that the non-deformed sample has no residual stresses. Using Equation 7.8, the new X-axis values were measured,

$$\sigma_{tot.} = \sigma_{app.} + \sigma_R$$

**Equation 7.8**

where  $\sigma_{tot.}$ ,  $\sigma_{app.}$  and  $\sigma_R$  are total, applied and residual stresses, respectively. It should be noted that  $\sigma_R$  was measured using the peak shift method.

After modifying the X-axis and driving the MBN( $\sigma$ ) curves over the modified X-axis, Figure 7.12 was obtained. Here, the X-axis represents the summation of the applied and residual stresses and the Y-axis represents the effect of the summation of the applied and the residual stresses on the MBN parameters. Therefore, Figure 7.12 shows the physical relation between the X-axis (here, the stress) and the Y-axis (here, the MBN parameter). As can be seen in Figure 7.12, the positions of the maximum of the MBN( $\sigma$ ) curve for all the graphs are the same. This represents an interesting effect whereby all the samples exhibit the maximum of the MBN( $\sigma$ ) curve at the same stress level. In other words, Figure 7.12 illustrates that the stress anisotropy - which needs to activate a new magnetization direction - is almost the same for different samples and that it is independent of the crystal anisotropy.

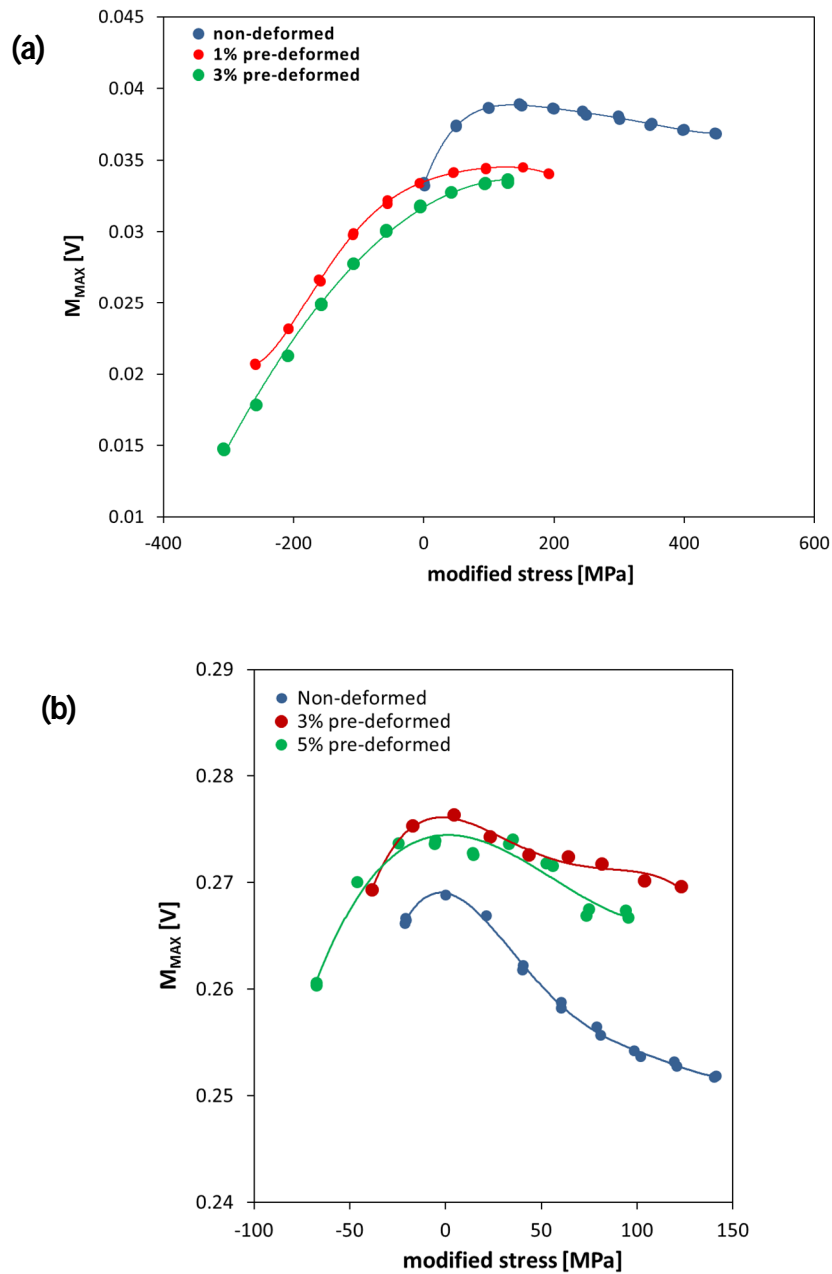


**Figure 7.12: Modified  $M_{MAX}$ -( $\sigma$ ) curves for the calibration process: a) pipeline steel, and b) Fe-Si steel.**

After modification of the X-axis (stress), the modified X-axis values are used as input for the regression analysis as a target. The second input comprised the MBN parameters, such as  $M_{MAX}$ . As previously described in Section 5.3.2, seven parameters were derived from the MBN curve (Table 5.3). To choose the optimum parameters, it is necessary to answer three questions: 1) What is the physical reason for the behaviour of each parameter? 2) How can we choose a useful parameter? 3) How can a useful parameter help to improve the output of a regression analysis?

The investigation of the physical reasons for the MBN parameters has been presented in several publications [Altp. 2009, Sant. 2012c, Sors. 2012, Sors. 2013]. In addition, the sensitivity of the

MBN parameters has been investigated and published in numerous publications [Altp. 1996, Dobm. 1998]. In summary, the MBN parameters presented in this work have a direct relation with the micro-residual stresses of the materials. Therefore, in principle, all of them can be used for the calibration process. Now a question arises as to the behaviour of these parameters in the present study. In other words, how can we find useful parameters? To answer this question, it should be noted that parameters should be chosen which represent sensitivity to micro-residual stresses and which have a specific trend. A specific trend here means that the MBN( $\sigma$ ) curves should be described with the results of other publications, such as [Altp. 2001, Altp. 2009]. If a trend cannot be described with such results, then the repeatability of the trend should be tested as to whether the result is due to a measurement error or a coincidence. Furthermore, one should seek a proper reason for the trend observed. As can be seen in Figure 7.12, all the MBN( $\sigma$ ) curves exhibit unique behaviour. In Sections 7.1 and 7.2, the reason for the behaviour observed in Figure 7.12 has been described in detail. One now has to determine how a parameter can improve the output of the regression analysis. To this end, the effect of gradually including each parameter in a calibration of the coefficient of determination ( $R^2$ ) was calculated. It should be noted that  $M_{MAX}$  was chosen as the basic input parameter.

Since finding a relationship between parameters through a multi-parameter linear regression analysis can be very time consuming and complicated, a computer program based on LabVIEW was used for the calibration process. The formula with the highest  $R^2$  value derived from the regression analysis was chosen as the general formula for measuring the residual stresses. Using the formula allows the residual stresses of a sample to be directly estimated from a simple MBN measurement.

Figure 7.13 shows the relationship between the measured residual stress with the RESTMAB and the estimated residual stresses using the formula derived from the regression analysis. Obviously, the estimated residual stresses show a very good trend with the measured residual stresses obtained with the RESTMAB. Therefore, using the RESTMAB and the BEMI device, the estimation of the local micro-residual stresses of the materials in general as well as in the front of a crack tip is readily possible. The next section will describe the applications of the proposed method using the BEMI for measuring the micro-residual stress distributions at the front of a crack tip in a sample.

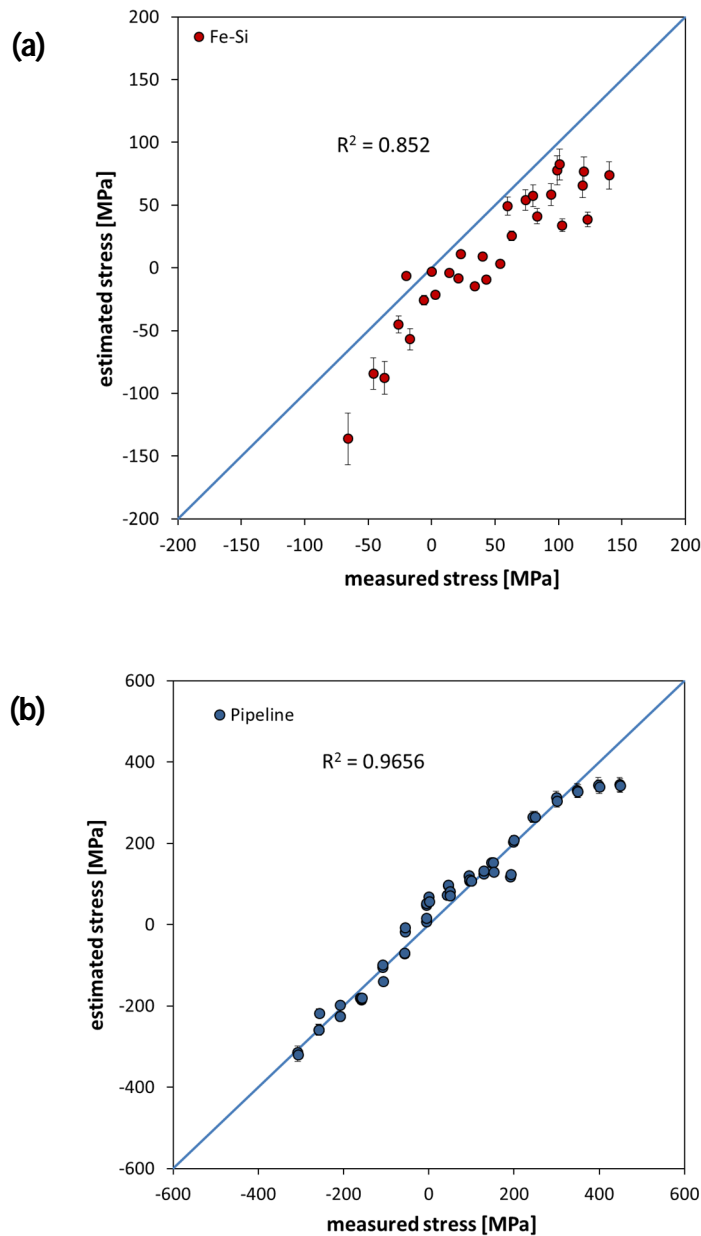


Figure 7.13: Relationship between the measured residual stress with the RESTMAB and the estimated residual stress using the formula derived from the regression analysis.

## 7.5. Applications of the calibrated Barkhausen noise and eddy current microscope using the micro-residual stress mapping method based on magnetic Barkhausen noise

### 7.5.1. High-resolution determination of micro-residual stress distributions

A simple and very useful application of the RESTMAB in combination with the BEMI is the residual stress distribution in an arbitrary area with a lateral resolution of 10  $\mu\text{m}$ . To this end, 1×1 mm areas of non- and pre-deformed samples were scanned with the BEMI. Next, using the RESTMAB, the stress distributions of the samples were determined. In addition, the changes in

micro-residual stresses were performed for different grains using a linear data extraction from the scanned data.

After calibration of the BEMI using the RESTMAB, surface scans were performed to monitor the micro-residual stress distributions. Figure 7.14 illustrates the BEMI scans of non- and pre-deformed samples of the pipeline steel.

As can be seen, a small stress variation between the grains resulting from the micro-residual stresses of the second-order can be detected with the BEMI. These small variations result from the fact that the plastic deformation in different grains with different orientations is not the same [Hert. 1996]. Grains with slip planes oriented in the direction of the applied stress deform more easily and more than grains with slip planes not oriented in the direction of an applied stress. Therefore, there is always some degree of micro-residual stress inhomogeneity in materials. This fact is more evident in Figure 7.15, which shows the micro-stress gradient of non- and pre-deformed samples and which was taken from the linear traces of the BEMI scans presented in Figure 7.14. As can be seen, when using the BEMI micro-residual stresses at any point, the macro-residual stresses can be determined. Therefore, the BEMI scans always have a grainy appearance due to the local micro-residual stresses.

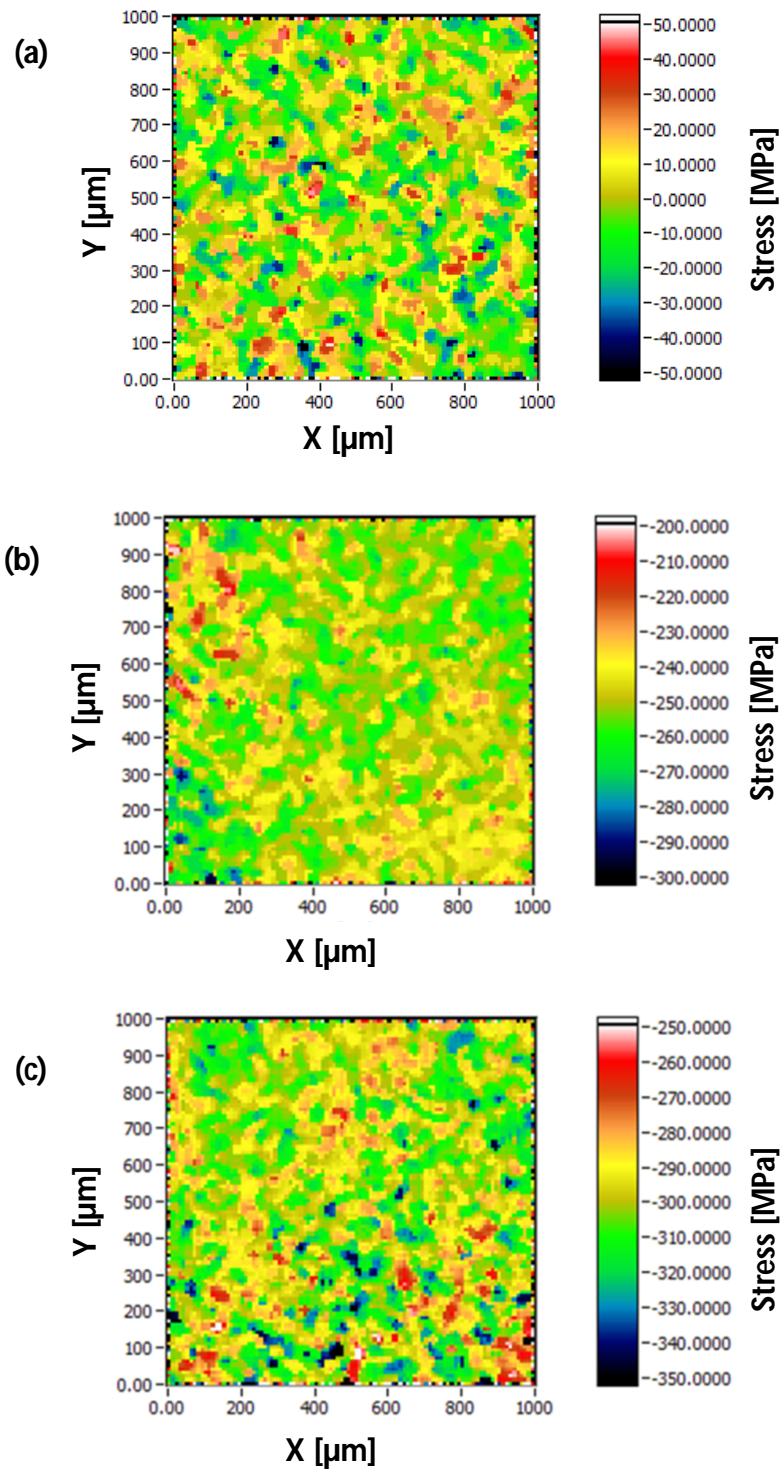


Figure 7.14: Micro-residual stress distributions measured with the calibrated BEMI using the RESTMAB for a) non- and b,c) pre-deformed samples.

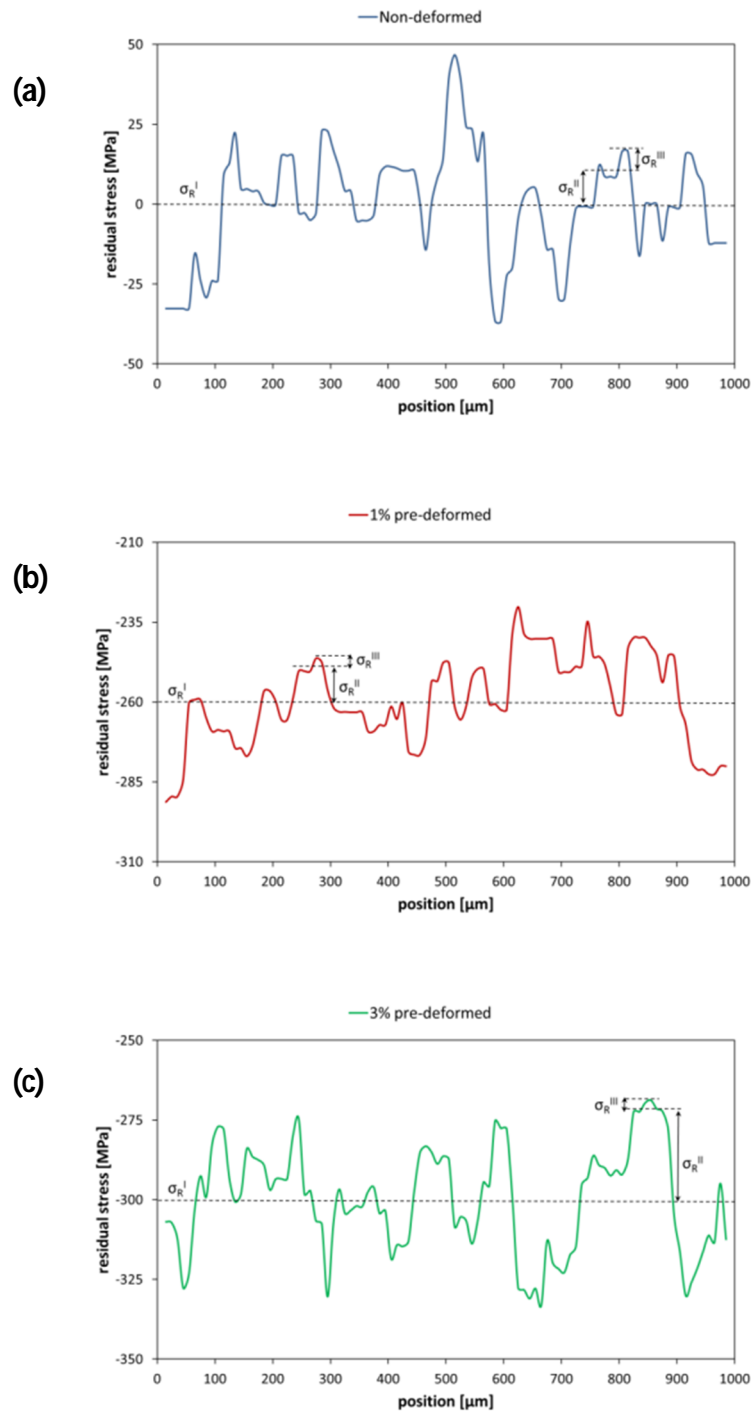
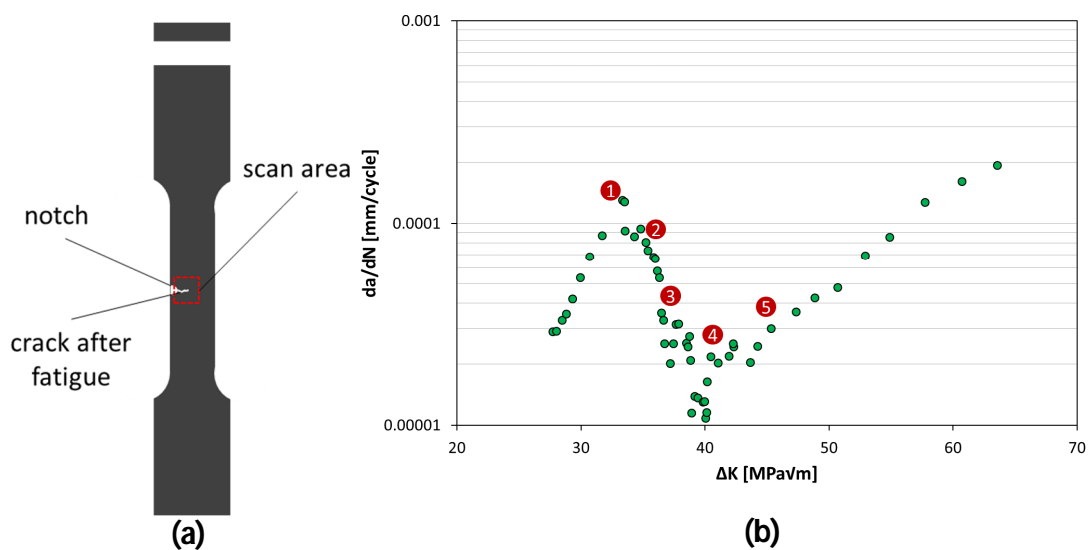


Figure 7.15: Different orders of residual stresses measured with the RESTMAB with the calibrated BEMI for a) non- and b,c) pre-deformed samples.

### 7.5.2. Measurement of the residual stress and size of the plastic zone in front of a crack tip

After calibration of the BEMI and having presented the ability of the BEMI with respect to the mapping of the micro-residual stress distributions, another application of the BEMI using the RESTMAB is the determination of the micro-residual stress distributions in front of a crack tip. To

this end, a series of experiments were carried out to detect the size of the plastic zone and the residual stresses' distribution around the crack tip for different crack lengths. A non-deformed pipeline sample was cut up to 1 mm in the middle of the sample with an electric discharge machine (EDM). Next, a notch was created using a sharp scalpel as a crack initiator, following which the sample was fatigue-loaded with a maximum amplitude of 250 MPa to create a fatigue crack in front of the notch (Figure 7.16a). The sample was then loaded up to 575 MPa to generate local micro-residual stresses at the front of the crack tip. After this, the sample was again fatigue-loaded with a maximum stress of 250 MPa. The crack growth rate ( $da/dN$ ) was measured using a replica method during the test process (Figure 7.16b). After each 100  $\mu\text{m}$  of crack propagation, the fatigue test was interrupted to measure the size of the plastic zone and the stress distribution of the crack tip. The size of the plastic zone was measured using digital image correlation (DIC) and light microscopy according to the Normarski contrast method, analytical calculation based on the Irwin method, and the BEM. It is of note that all the measurements mentioned above were performed at the department of material science and methods (MWW) at Saarland University. As can be seen in Figure 7.16b, the crack-opening rate increases linearly before it reaches an overload position (Position 1). After the overload, the crack-opening rate ( $da/dN$ ) decreases although the range in stress intensity ( $\Delta K$ ) increases. The generation of compressive micro-residual stresses at the front of the crack tip is the reason for a decreasing  $da/dN$  crack propagation rate. In other words, the micro-residual stresses at the front of the crack tip compress the crack and prevent it from growing. This trend continues up to Position 4, where  $da/dN$  then increases again parallel to the linear trend, and hence with the same slope as that before the overload (Position 1). Figure 7.17 shows the SEM picture of the crack at Positions 1 and 3 in Figure 7.16.



**Figure 7.16: a) Schematic sketch of a sample with a notch and crack initiated after fatigue-loading. b) Change in the crack propagation rate ( $da/dN$ ) related to the range of stress intensity factor. The fatigue process was interrupted for further investigation at the points marked.**

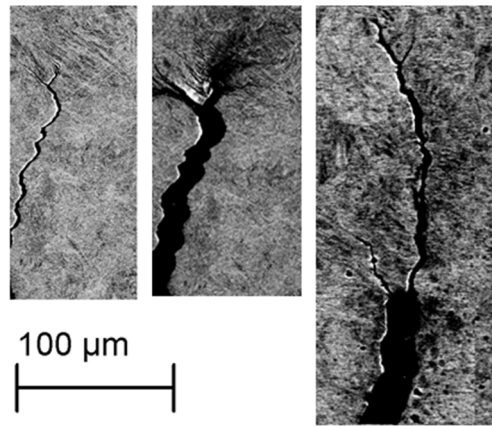


**Figure 7.17: SEM pictures of the crack at different positions.**

As reported in [Lee. 2011], the local residual stresses are the reason for the behaviour observed in Figure 7.16, where the stress and strain distribution in the sample was measured at the front of the crack tip using DIC [Kamm. 2013], while the BEMI was used to find a reason for the trend observed in Figure 7.16. The DIC method works on the basis of a comparison between the pixels of an image of a sample with and without residual stresses. Therefore, first of all, an image was taken of the crack tip without any stress applied, and then stress was applied and a second picture was taken. The comparison between the two images reveals the strain field distribution at the front of the crack. The strain field was measured at different positions, which are shown in Figure 7.16. Figure 7.18 shows the result of the DIC measurements. As can be seen, the size of the plastic zone in the front of the crack tip can be easily measured, but it cannot present quantifiable stress values. Furthermore, for the DIC measurements, a reference image is always required, which is totally dependent on the device and the situation of the DIC. Therefore, an area in the front of the crack tip was scanned in 10 μm lateral resolution using the RESTMAB-calibrated BEMI.

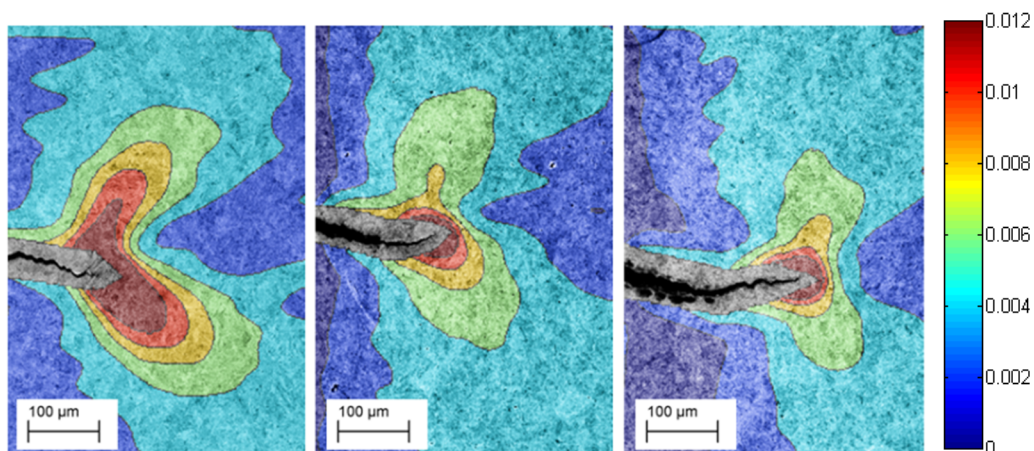


**Figure 7.18: Strain distribution around the crack tip using the DIC method at different points in Figure 7.16.**

Figure 7.19 shows the BEMI results, which illustrate the stress distribution as well as the plastic zone at the front of the crack. There are similar scans from a BEMI of a crack tip reported by Altpeter et al. [Altp. 1998]. In particular, Altpeter et al. calibrated the BEMI using XRD data.

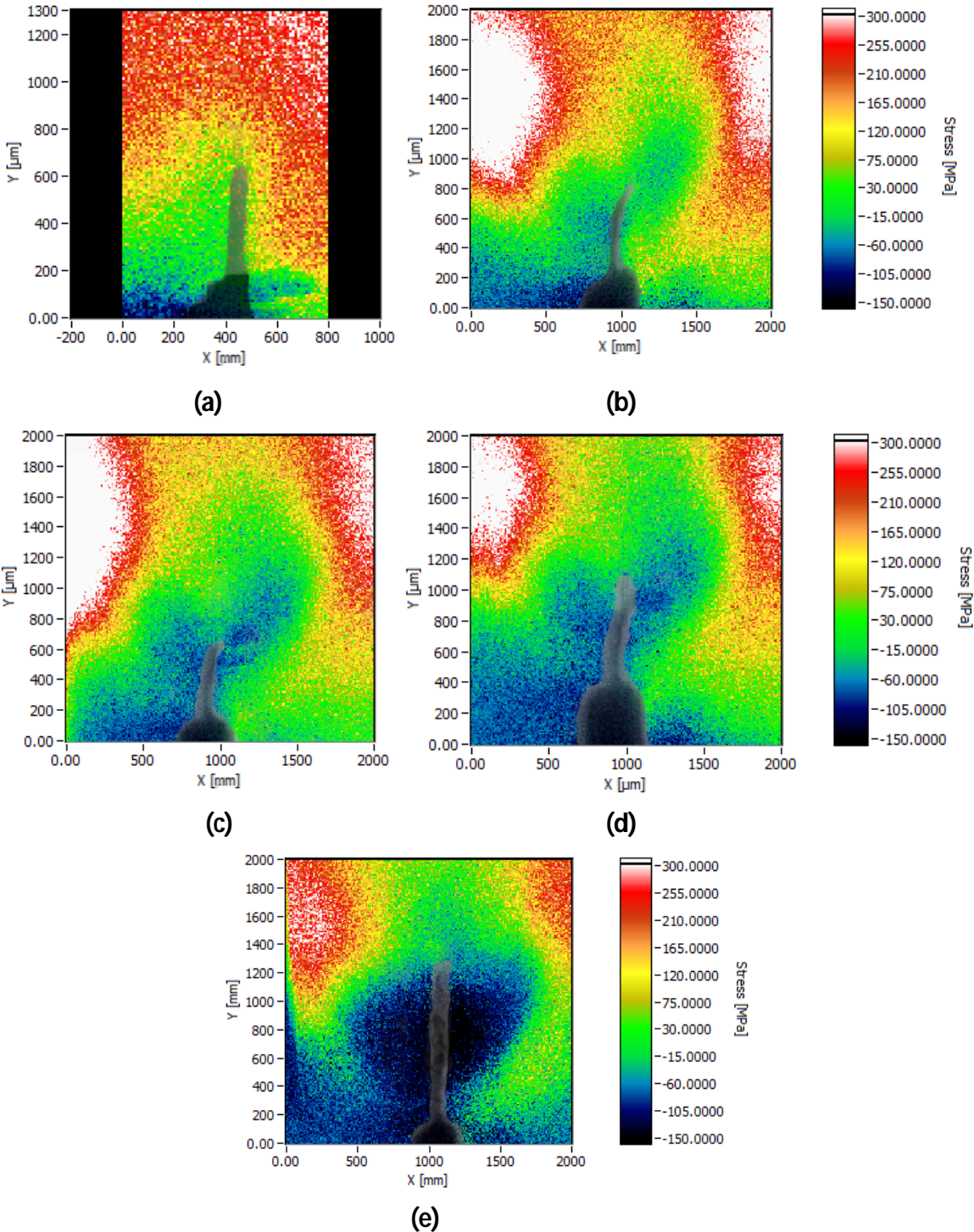


**Figure 7.19: BEMI scans for different positions of a crack propagation curve (Figure 7.16): a) Position 1 (before overload), b) Position 2 (after overload), c) Position 3, d) Position 4, and e) Position 5 (crack passes the compressive residual stresses area). The dark grey sketch shows the notch and crack.**

As can be seen in Figure 7.19a, there is no visible plastic zone around the crack tip before overloading of the sample, but after overloading Figure 7.19b shows a significant change in the

stress distribution around the front of the crack tip. Using the BEMI scans, the size of a plastic zone and the resulting stress distribution around a crack can be measured.

Figure 7.20 shows the steps for measuring the size of the plastic zone around a crack tip using the BEMI. These steps are:

1. Find the position of the crack tip: locate the Y trace line aligned to the crack (Position 1). Look at the stress gradient. Locate the X trace line at Position 2 where the residual stresses change to positive values;
2. Find the length of the plastic zone (L): move the X trace line in the Y direction and look at the stress gradient of the X trace line. Position 3 is where the stress gradient at the X trace line turns positive;
3. Find the width of the plastic zone (W): move the Y trace line in the X direction and look at the stress gradient along the Y trace line. Position 4 is where the stress gradient along the Y trace line turns positive;
4. Calculate the size of the plastic zone of the crack tip using the length and the width of the plastic zones, measured according to the previous steps.

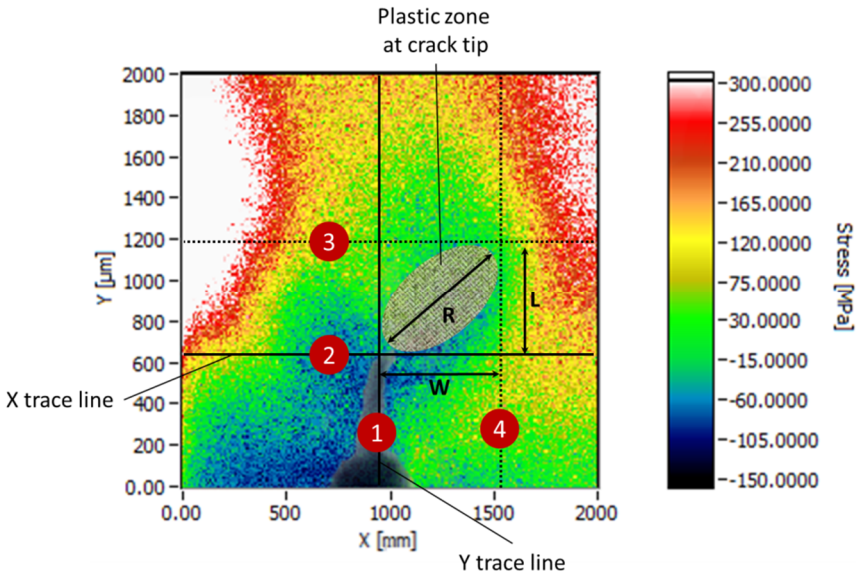


Figure 7.20: Schematic presentation for measuring the size of the plastic zone of the crack tip.

The size of the plastic zone was also measured with DIC, light microscopy with the Normarski contrast method, and then determined through analytical calculation based on the Irwin method. Table 7.4 shows the results which illustrate that the BEMI results are in good agreement with the results obtained through other approaches. There is only a difference between the sizes of the plastic zone measured with DIC and the other methods.

**Table 7.4: Size of the plastic zone in front of a crack tip after overload measured with different methods.**

Method	DIC	N-DIC	Irwin	BEMI
Pl. Zone [ $\mu\text{m}$ ]	675	838	828	840

Furthermore, the BEMI scans show that a big compressive residual stress zone has built up at the front of the crack after overload. This is the reason why the crack opening rate decreases after overload. The maximum measured compressive residual stress is -150 MPa in the plastic zone. It is noteworthy that this compressive stress zone at the front of the crack tip was balanced with tensile stresses, which are visible in the BEMI scans as well.

According to the results mentioned above, it has been shown that the decrease in the crack propagation rate after overload comes from the compressive residual stresses at the front of the crack. Therefore,  $da/dN$  should increase when the crack passes the end of the plastic zone. In other words, an increase in  $da/dN$  after Position 4 in Figure 7.16 happens when the crack passes the end of the compressive plastic zone, and the crack will grow at the same rate as before the occurrence of overload. Figure 7.21 shows the changes of  $da/dN$  (the replica method) and the residual stresses (the BEMI scan) versus the crack length and the stress intensity factor. As can be seen, the trend for the residual stresses and  $da/dN$  are very similar. In other words, in Position 4 the crack growth rate  $da/dN$  increases again after the crack tip has left the compressive plastic zone. Specifically, with regard to the experiment considered, the residual stress trend measured by the BEMI also reveals that the compressive plastic zone passes after 300  $\mu\text{m}$  of crack growth.

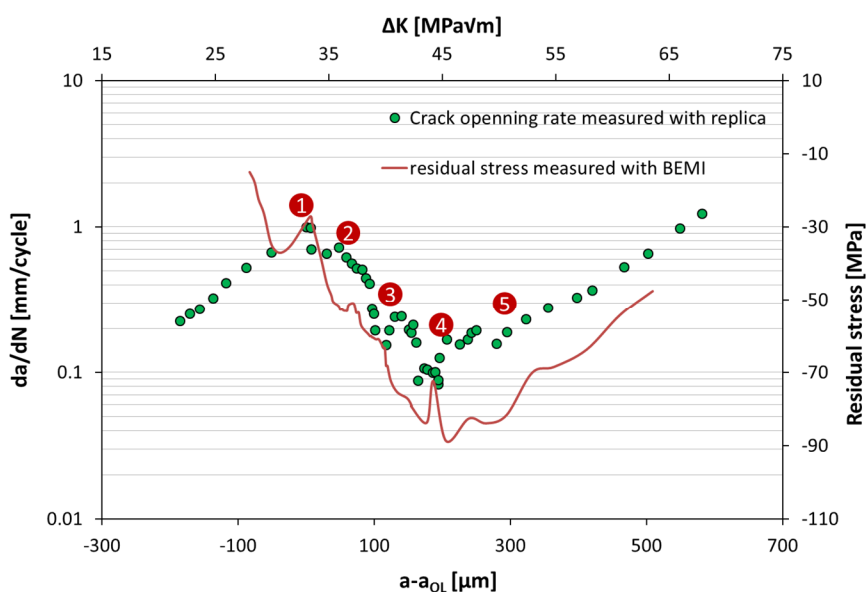


**Figure 7.21: Changes in the crack propagation rate ( $da/dN$ ) and micro-residual stresses versus the position of the crack tip and the stress intensity factor.**

As a short conclusion, it can be noted that the BEMI calibrated with the RESTMAB can successfully detect stress distributions at the front of a crack tip with a high lateral resolution. The BEMI scan, which is quick and has a high resolution, is useful to investigate the crack opening process during fatigue.

## 8. Summary and future work

### 8.1. Summary

In this work, a RESTMAB has been presented. In other words, micro-residual stresses can be estimated using the RESTMAB according to the following steps:

- a) Specify the reference sample and its material conditions. The micro-structure, mechanical properties and residual stresses should be known. The micro-structure could be specified using either light or an SEM. The stress-strain curve of the sample is needed, which could be measured by a tensile test. It is recommended to have a non-deformed sample. Therefore, the micro-residual stresses can be assumed to be zero.
- b) Set up the optimal MBN parameters (such as the magnetization amplitude) of the investigated sample. It is recommended to define the magnetizing frequency and the amplitude, the yoke shape and the direction of measurement.
- c) Measure the MBN( $\sigma$ ) curve for the reference sample up to half of the yield stress.
- d) Calculate the slope as well as the maximum of the MBN( $\sigma$ ) curve (which are needed for the definition of the slope and the peak shift methods, respectively).
- e) Measure the MBN( $\sigma$ ) curve on at least one pre-deformed sample with the same conditions as the reference sample.
- f) Calibrate the BEMI using the MBN( $\sigma$ ) curves measured from the reference and pre-deformed samples.
- g) Measure the micro-residual stresses using the RESTMAB on the same type as the reference sample.

Using the steps mentioned above, the RESTMAB can help to deliver the micro-residual stress mapping of the surface of an unknown sample using a simple scan of the BEMI. On the other hand, the RESTMAB will simplify the mapping of the residual stresses for a series of unknown samples. It is of note that RESTMAB can even be applied to different batches - and as such, different components - as long as they belong to the same material type.

Besides proposing the RESTMAB, the physical reasons for the MBN( $\sigma$ ) curves have been analysed in detail. The outcome of this work to be highlighted include:

- The behaviour of the MBN parameters under applied elastic strain showed a maximum or a minimum in the MBN( $\sigma$ ) curve for both steels considered.
- A model based on the micro-structure of the material was proposed for the interpretation and better understanding of the effect of stress on MBN. The initial results from the model simulated with the finite element method (COMSOL Multiphysics) are in good agreement with the experimental results.
- The behaviour of the MBN( $\sigma$ ) curve was widely studied to find the physical meaning behind its unique trend. To this end, the B(H) curves of samples under applied stress were measured and a similar trend was observed in the B(H) and MBN curves. It was concluded that the Villari effect is the reason for the MBN behaviour.
- To explain the results observed at a macroscopic scale, the magnetostriction changes of samples under applied stress were measured. Based on the results and the energy equilibrium of the domain, it was then shown that the stress anisotropy activates one or more magnetic easy axes for domain motion.
- The domain structure was monitored in situ under applied elastic strain to explain the results observed at a microscopic scale. The results proved that the domain structure tends to grow in the direction of the applied stress when the applied stress goes beyond the extremum of MBN( $\sigma$ ). Therefore, the stress anisotropy plays the major role with regard to the domain structures and - consequently - the MBN behaviour.
- Based on the MBN( $\sigma$ ) curve under applied elastic strain conditions, a method has been proposed to measure micro-residual stresses (i.e., RESTMAB). This method arose from two characteristics of the MBN( $\sigma$ ) curve, namely the "peak shift" and the "slope".
- It has been confirmed that the peak shift between non- and pre-deformed samples in the MBN( $\sigma$ ) curve presents the micro-residual stress differences between the samples (the peak shift method).
- It has been found that the linear part of the MBN( $\sigma$ ) curve has a direct relation to micro-residual stresses. In other words, the slope of the MBN( $\sigma$ ) curve can be assumed to be the same for non- and pre-deformed samples.
- Using the BEMI device together with the RESTMAB, the micro-residual stress distribution at the front of a crack tip can be measured with a lateral resolution of 10  $\mu\text{m}$ .
- As a final result, with the combination of the proposed novel stress measurement method based on the BEMI, a new non-destructive, precise and quick alternative has been presented for the local measurement of micro-residual stress distributions.

## 8.2. Future work

As mentioned above, this work has presented several original results about micro-residual stress measurements using MBN. However, it also opens many new doors for further work which could assist in investigating additional features of this work. Some of the most important are suggested here:

- The analytical modelling of the MBN( $\sigma$ ) curve for pipeline and Fe-Si samples using the Jiles-Atherton-Sablik model. Coupling the analytical model with the proposed model in COMSOL software to develop an analytical method for estimating micro-residual stresses.
- Investigate the "slope method" for different ferromagnetic materials with different micro-magnetic and mechanical properties to find a general pattern of behaviour.
- Study the MBN behaviour of a single crystal under applied stress. In situ monitoring of domain structures using MFM are also suggested.
- Study the effect of fatigue parameters on the MBN( $\sigma$ ) curve to find a method for monitoring the fatigue process non-destructively.
- Investigate the micro-residual stress distributions between different phases of ferromagnetic alloys using the BEMI device and the RESTMAB.
- Investigate the behaviour of other micro-magnetic methods, like EC and IP, for measuring residual stresses.

## References

- [Ales. 1990a] Alessandro B., Beatrice C., Bertotti G. and Montorsi A., "Domainwall dynamics and Barkhausen effect in metallic ferromagnetic materials. I.Theory." *Journal of Applied Physics*, 68 (1990) 2901-2907.
- [Ales. 1990b] Alessandro B., Beatrice C., Bertotti G. and Montorsi A., "Domain wall dynamics and Barkhausen effect in metallic ferromagnetic materials. II. Experiments." *Journal of Applied Physics*, 68 (1990) 2908-2915.
- [Altp. 1992a] Altpeter I. and Theiner W., "Vorrichtung zum ortsaufgelösten, zerstörungsfreien Untersuchen des magnetischen Barkhausenrauschens." Patent No. DE4235387 C1 (1992).
- [Altp. 1992b] Altpeter I., Gessner M. and Theiner W., "Vorrichtung zum ortsaufgelösten, zerstörungsfreien Untersuchen von magnetischen Kenngrößen." Patent No. EP0595117 B1 (1992).
- [Altp. 1996] Altpeter I., "Nondestructive evaluation of cementite content in steel and white cast iron using inductive Barkhausen noise." *Journal of Nondestructive Evaluation*, 15 (1996) 45-60.
- [Altp. 1998] Altpeter I., Dobmann G., Meyendorf N., Blumenauer H., Horn D. and Krempe M., "Residual stress measurements in front of a crack tip with high spatial resolution by using Barkhausen microscopy." *Nondestructive Characterization of Materials VIII*, (1998) 659-663.
- [Altp. 2000] Altpeter I. and Dobmann G., "Detection of copper precipitates in 15NiCuMoNb (WB 36) steel by using micro-magnetic NDE techniques." *International Symposium on the Relationship between Magnetic and Structural Properties*, 2000, Hanamaki, Japan.

- [Altp. 2001] Altpeter I., Dobmann G., Katerbau K. H., Schick M., Binkele P., Kizler P. and Schmauder S., "Copper precipitates in 15 NiCuMoNb 5 (WB 36) steel: material properties and microstructure, atomistic simulation, and micro-magnetic NDE techniques." *Nuclear Engineering and Design*, 206 (2001) 337–350.
- [Altp. 2002] Altpeter I., Becker R., Dobmann G. and Kern R., "Robust solutions of inverse problems in electromagnetic non-destructive evaluation." *Inverse Problems*, 18 (2002) 1907-1921.
- [Altp. 2009] Altpeter I., Dobmann G., Kröning M., Rabung M. and Szielasko K., "Micro-magnetic evaluation of microresidual stresses of the II<sub>nd</sub> and III<sub>rd</sub> order." *NDT&E International*, 42 (2009) 283-290.
- [Angl. 2001] Anglada-Rivera J., Radovese L. R. and Capo-Sanchez J., "Magnetic Barkhausen noise and hysteresis loop in commercial carbon steel: influence of applied tensile stress and grain size." *Journal of Magnetism and Magnetic Materials*, 231 (2001) 299-306.
- [Bark. 1919] Barkhausen. H., "Zwei mit Hilfe der neuen Verstärker entdeckte Erscheinungen." *Physik Zeitschrift*. XX, (1919) 401-403.
- [Bati. 2014] Batista L., Rabe U., Altpeter I., Hirsekorn S. and Dobmann G., "On the mechanism of nondestructive evaluation of cementite content in steels using a combination of magnetic Barkhausen noise and magnetic force microscopy techniques." *Journal of Magnetism and Magnetic Materials*, 354 (2014) 248–256.
- [Bend. 1997] Bender J., "Barkhausen noise and eddy current microscopy (BEMI): microscope configuration, probes and imaging characteristics." *Review of Progress in Quantitative Evaluation*, 16 (1997) 2121-2128.
- [Bert. 1998] Bertotti G., "Hysteresis in magnetism." Academic Press, 1998, London, UK.
- [Bhad. 2001] Bhadeshia H. K. D. H., "Worked examples in the Geometry of Crystals." The Institute of Materials, 2001, London, UK.
- [Bozo. 1993] Bozorth R. M., "Ferromagnetism." IEEE Press, 1993, New York, NY.

- [Bükk. 2010] Bükki-Deme A., Szabo I. A. and Cserhati C., "Effect of anisotropic microstructure on magnetic Barkhausen noise in cold rolled low carbon steel." *Journal of Magnetism and Magnetic Materials*, 322 (2010) 1748–1751.
- [Bult. 2002] Bultea D. P. and Langman R. A., "Origins of the magnetomechanical effect." *Journal of Magnetism and Magnetic Materials*, 251 (2002) 229–243.
- [Catt. 1995] Catty J., "Etude des relations entre la microstructure, l'état de contrainte d'une part, les propriétés magnétiques & magnétostrictives d'autre part, dans du fer pur & des alliages à bas carbone." PhD dissertation, 1995.
- [Cosa. 2014] Cosarinsky G., Kopp M., Rabung M., Seiler G., Petragalli A., Vega D., Sheikh Amiri M., Ruch M. and Boller C., "Non-destructive characterization of laser hardened steels." *Insight*, 56 (2014) 553-559.
- [Cull. 2009] Cullity B. D. and Graham C. D., "Introduction to magnetic materials." John Wiley Press, 2009, Hoboken, NJ.
- [Clap. 1991] Clapham L., Jagadish C. and Atherton D. L., "The influence of pearlite on Barkhausen noise generation in plain carbon steels." 39 (1991) 1555-1562.
- [Dobm. 1998] Dobmann G., Altpeter I., Becker R., Kern R., Laub U. and Theiner W., "Barkhausen noise measurements and related measurements in ferromagnetic materials." *Topics on Non-destructive Evaluation*, 1 (1998) 233-251.
- [Dobm. 2007] Dobmann G., Altpeter I., Wolter B. and Kern R., "Industrial applications of 3MA – micromagnetic multiparameter microstructure and stress analysis." 5th Int. Conference Structural Integrity of Welded Structures (ISCS2007), 2007, Timisoara, Romania.
- [Dubo. 1997] Dubov, A. A., "A study of metal properties using metal magnetic memory method." *Metal Science Heat Treatment*, 39 (1997) 401–405.
- [Gaut. 1998] Gauthier J., Krause T. W. and Atherton D. L., "Measurement of residual stress in steel using the magnetic Barkhausen noise technique." *NDT&E International*, 31 (1998) 23-31.
- [Hauk. 1997] Hauk V., "Structural and residual stress analysis by nondestructive methods." Elsevier, 1997, Amsterdam, The Netherlands.

- [Hert. 1996] Hertzberg R. W., "Deformation and fracture mechanics of engineering materials", John Wiley & Sons, 1996.
- [Höll. 1987] Höller P., "Nondestructive analysis of structure and stresses by ultrasonic and micro-magnetic methods." *Nondestructive Analysis of Structure and Stresses by Ultrasonic and Micromagnetic Methods*, 1986, Montreal, QC.
- [Jaga. 1990] Jagadish C., Clapham L. and Atherton D. L., "Influence of uniaxial elastic stress on power spectrum and pulse height distribution of surface Barkhausen noise in pipeline steel." *IEEE Transactions on Magnetics*, 26 (1990) 1160-1163.
- [Jile. 1989] Jiles D. C., "The effect of stress on magnetic Barkhausen activity in ferromagnetic steels." *IEEE Transactions on Magnetics*, 25 (1989) 3455-3457.
- [Jile. 1998] Jiles D. C., "Introduction to magnetism and magnetic materials." Chapman & Hill, 1998.
- [Ju. 2003] Ju J. B., Lee J. S., Jang J. I., Kim W. S. and Kwon D., "Determination of welding residual stress distribution in API X65 pipeline using a modified magnetic Barkhausen noise method." *International Journal of Pressure Vessels and Piping*, 80 (2003) 641-646.
- [Kamm. 2013] Kammers A. D. and Daly S., "Digital image correlation under scanning electron microscopy: methodology and validation." *Experimental Mechanics*, 53 (2013) 1743-1761.
- [Karj. 1979a] Karjalainen L. P. and Moilanen M., "Detection of plastic deformation during fatigue of mild steel by the measurement of Barkhausen noise." *NDT&E International*, 12 (1979) 51-55.
- [Karj. 1979b] Karjalainen L. P., Moilanen M. and Rautioaho M., "Influence of tensile and cyclic loading upon Barkhausen noise in a mild steel." 37 (1979) 45-51.
- [Kasa. 2013] Kasai N., Koshino H., Sekine K., Kihira H. and Takahashi M., "Study on the effect of elastic stress and microstructure of low carbon steels on Barkhausen noise." *Journal of Nondestructive Evaluation*, DOI 10.1007/s10921-013-0180-1.
- [Kleb. 2004] Kleber X. and Vincent A., "On the role of residual internal stresses and dislocations in Barkhausen noise in plastically deformed steel." *NDT&E International*, 37 (2004) 439-445.

- [Knel. 1962] Kneller E., "Ferromagnetismus." Springer, 1962, Berlin, Germany.
- [Kten. 2014] Ktena A., Hristoforou E., Gerhardt G., Missell F. P., Landgraf F., Rodrigues D. and Alberteris-Campos M., "Barkhausen noise as a microstructure characterization tool." *PhysicaB*, 435 (2014) 109-112.
- [Lind. 2001] Lindgren M. and Lepistö T., "Effect of prestraining on Barkhausen noise vs. stress relation." *NDT&E International*, 34 (2001) 337-344.
- [Lind. 2003a] Lindgren M. and Lepistö T., "Effect of cyclic deformation on Barkhausen noise in a mild steel." *NDT&E International*, 36 (2003) 401-409.
- [Lind. 2003b] Lindgren M. and Lepistö T., "Relation between residual stress and Barkhausen noise in a duplex steel." *NDT&E International*, 36 (2003) 279-288.
- [Lind. 2004] Lindgren M. and Lepistö T., "On the stress vs. Barkhausen noise relation in duplex stainless steel." *NDT&E International*, 37 (2004) 403-410.
- [Maka. 2000] Makar J. M. and Tanner B. K., "The effect of plastic deformation and residual stress on the permeability and magnetostriction of steels." *Journal of Magnetism and Magnetic Materials*, 222 (2000) 291-304.
- [Moor. 1997a] Moorthy V., Vaidyanathan S., Laha K., Jayakumar T., Bhanu Sankara Rao K. and Raj B., "Evaluation of microstructures in 2.25Cr-1Mo and 9Cr-1Mo steel weldments using magnetic Barkhausen noise." *Materials Science and Engineering*, A231 (1997) 98-104.
- [Moor. 1997b] Moorthy V., Vaidyanathan S., Jayakumar T. and Raj B., "Microstructural characterization of quenched and tempered 0.2% carbon steel using magnetic Barkhausen noise analysis." *Journal of Magnetism and Magnetic Materials*, 171 (1997) 179-189.
- [Moor. 1999] Moorthy V., Choudhary B. K., Vaidyanathan S., Jayakumar T., Bhanu Sankara Rao K. and Baldev Raj., "An assessment of low cycle fatigue damage using magnetic Barkhausen emission in 9Cr-1Mo ferritic steel." *International Journal of Fatigue*, 21 (1999) 263-269.
- [Moor. 2005] Moorthy V., Shaw B. A., Mountford P. and Hopkins P., "Magnetic Barkhausen emission technique for evaluation of residual stress alternation by grinding in case-carburised En36 steel." *Acta Materialia*, 53 (2005) 4997-5006.

- [Moor. 2009] Moorthy V., Vaidyanathan S., Jayakumar T. and Raj B., "On the influence of tempered microstructures on magnetic Barkhausen emission in ferritic steels." *Philosophical Magazine A*, 77 (1998) 1499-1514.
- [Noto. 2004] Notoji A., Saito A. and Hayakawa M., "Strain-magnetization properties and domain structures of silicon steel sheets." *Electrical Engineering in Japan*, 149 (2004) 10-17.
- [Noza. 1994] Nozawa T., Mizogami M., Mogi H. and Matsuo Y., "Domain structures and magnetic properties of advanced grain-oriented silicon steel." *Journal of Magnetism and Magnetic Materials*, 133 (1994) 115-122.
- [Nucc. 1997] Nucci J. A., Keller R. R., Field D. P. and Shacham-Diamand Y., "Grain boundary misorientation angles and stress-induced voiding in oxide passivated copper interconnects." *Applied Physics Letter*, 70 (1997) 1242-1244.
- [Palm. 2005] Palma E. S., Mansur T. R., Ferreira Silva Jr. S. and Alvarenga Jr. A., "Fatigue damage assessment in AISI 8620 steel using Barkhausen noise." *International Journal of Fatigue*, 27 (2005) 659-665.
- [Pere. 2007] Perevertov O., "Influence of residual stress on the magnetization process in mild steel." *Journal of Physics D: Applied Physics*, 40 (2007) 949-954.
- [Pere. 2012] Perevertov O. and Schäfer R., "Influence of applied compressive stress on the hysteresis curves and magnetic domain structure of grain-oriented transverse Fe-3%Si steel." *Journal of Physics D: Applied Physics*, 45 (2012) 135001-135012.
- [Piot. 2010] Piotrowski L., Augustyniak B., Chmielewski M., Hristoforou E. V. and Kosmas K., "Evaluation of Barkhausen noise and magnetoacoustic emission signals properties for plastically deformed Armco iron." *IEEE Transactions on Magnetics*, 46 (2010) 239-242.
- [Pits. 1990] Pitsch. H., *Die Entwicklung und Erprobung der Oberwellenanalyse im Zeitsignal der magnetischen Tangentialstärke als neues Modul des 3MA-Ansatzes.* PhD Thesis, Saarland University, 1990.
- [Prev. 1986] Prevey P. S., "X-ray diffraction residual stress techniques, *Metals Handbook*. 10." ASM International, 1986.

- [Port. 1992] Porter D. A. and Easterling K. E., "Phase transformations in metals and alloys." CRC press, 1992.
- [Rab. 2010] Rabung M., Altpeter I., Dobmann G. and Szielasko K., "Micro-magnetic evaluation of residual stresses of 2<sup>nd</sup> and 3<sup>rd</sup> order." Electromagnetic Nondestructive Evaluation (XIII), IOS press (2010) 71-78.
- [Rab. 2014] Rabung M., Altpeter I., Boller C., Dobmann G. and Herrmann H. G., " Non-destructive evaluation of the microresidual stresses of 3<sup>rd</sup> order by using micro magnetic methods." NDT&E International, 63 (2014) 7-10.
- [Rame. 1996] Ramesh A., Jiles D. C. and Roderick J. M., "A model of anisotropy anhyseretic magnetization." IEEE Transactions on Magnetics, 32 (1996) 4234-4236.
- [Ranj. 1987] Ranjan R., Jiles D. C. and Pastogi P. K., Magnetic properties of decarburized I steels: an investigation of the effects of grain size and carbon content." IEEE Transactions on Magnetics, 23 (1987) 1869-1876.
- [Ross. 2012] Rossini N. S., Dassisti M., Benyounis K. Y. and Olabi A. G., "Methods of measuring residual stresses in components." Materials and Design, 35 (2012) 572-588.
- [Sabl. 1993a] Sablik M. J., "A model for the Barkhausen noise power as a function of applied magnetic field and stress." Journal of Applied Physics, 74 (1993) 5898-5900.
- [Sabl. 1993b] Sablik M. J. and Jiles D. C., "Coupled magnetoelastic theory of magnetic and magnetostrictive hysteresis." IEEE Transactions on Magnetics, 29 (1993) 2113-2123.
- [Sant. 2012a] Santa-aho S., Vippola M., Saarinen T., Isakov M., Sorsa A., Lindgren M., Leiviska K. and Lepistö T., "Barkhausen noise characterisation during elastic bending and tensile compression loading of case-hardened and tempered samples." Journal of Material Science, 47 (2012) 6420-6428.
- [Sant. 2012b] Santa-aho S., Vippola M., Sorsa A., Latokartano J., Lindgren M., Leiviska K. and Lepistö T., "Development of Barkhausen noise calibration blocks for reliable grinding burn detection." Journal of Materials Processing Technology, 212 (2012) 408-416.

- [Sant. 2012c] Santa-aho S., Vippola M., Sorsa A., Lindgren M., Latokartano J., Leiviska K. and Lepistö T., "Optimized laser processing of calibration blocks for grinding burn detection with Barkhausen noise." *Journal of Materials Processing Technology*, 212 (2012) 2282-2293.
- [Sant. 2012d] Santa-aho S., Vippola M., Sorsa A., Leiviskä K., Lindgren M. and Lepistö T., "Utilization of Barkhausen noise magnetizing sweeps for case-depth detection from hardened steel." *NDT&E International*, 52 (2012) 95-102.
- [Seeg. 1966] Seeger, A. "Moderne Probleme der Metallphysik." Springer, 1966, Berlin, Germany.
- [Sors. 2012] Sorsa A., Leiviskä K., Santa-aho S. and Lepistö T., "Quantitative prediction of residual stress and hardness in case-hardened steel based on the Barkhausen noise measurement." *NDT&E International*, 46 (2012) 100-106.
- [Sors. 2013] Sorsa A., Leiviskä K., Santa-aho S., Vippola M. and Lepistö T., "An efficient procedure for identifying the prediction model between residual stress and Barkhausen noise." *Journal of Nondestructive Evaluation*, 32 (2013) 341–349.
- [Stef. 2000] Stefanita C. G., Atherton D. L. and Clapham L., "Plastic versus elastic deformation effects on magnetic Barkhausen noise in steel." *Acta Materialia*, 48 (2000) 3545-3551.
- [Stef. 2008] Stefanita. C. G., "From bulk to nano, the many sides of magnetism." Springer, 2008.
- [Stew. 2004] Stewart D. A., Stevens K. J. and Kaiser A. B., "Magnetic Barkhausen noise analysis of stress in steel." *Current Applied Physics*, 4 (2004) 308-311.
- [Szew. 2004] Szewczyk R. and Bienkowski A., "Application of the energy-based model for the magnetoelastic properties of amorphous alloys." *Journal of Magnetism and Magnetic Materials*, 272–276 (2004) 728–730.
- [Taka. 2005] Takayama Y., Szpunar J. A. and Kato H., "Analysis of intragranular misorientation related to deformation in an Al-Mg-Mn alloy." *Materials Science Forum*, 495-497 (2005) 1049-1054.
- [Thei. 1979] Theiner W., Grossmann J. and Repplinger W., "Zerstörungsfreier Nachweis von Spannungen insbesondere Eigenspannungen mit magnetostruktiv angeregten

Ultraschallwellen, Messung der Magnetostriktion mit DMS bzw. mittels des Barkhausenrauschens.“ DGZFP e.V. Inertationales Symposium, Saarbrücken, 1979.

- [Thei. 1983] Theiner W. A. and Altpeter I., “Determination of residual stresses using micromagnetic parameters.“ In: New Procedure in Nondestructive Testing, edited by Höller P., Springer, 1983.
- [Thei. 1987] Theiner W. A. and Deimel P., “Non-destructive testing of welds with the 3MA-analyzer.“ Nuclear Engineering and Design, 102 (1987).
- [Tott. 2002] Totten G., Howes M. and Inoue T., “Handbook of residual stress and deformation of steel.“ ASM International, 2002.
- [Vill. 1865] Villari E., “V. Über die Änderungen des magnetischen Momentes, welche der Zug und das Hindurchleiten eines galvanischen Stroms in einem Stabe von Stahl oder Eisen hervorbringe.“ Monatsbericht. d. Berliner Akad., (1865) 87-122.
- [With. 2001a] Withers P. J. and Bhadeshia H. K. D. H., “Residual stress: part 1 – measurement techniques.“ Materials Science and Technology, 17 (2001) 355-365.
- [With. 2001b] Withers P. J. and Bhadeshia H. K. D. H., “Residual stress: part 2 – nature and origins.“ Materials Science and Technology, 17 (2001) 366-375.
- [With. 2008] Withers P. J., Turski M., Edwards L., Bouchard P. J. and Buttle D.J., “Recent advances in residual stress measurement,“ International Journal of Pressure Vessels and Piping, 85 (2008) 118–127.
- [Wrig. 2011] Wright S. I., Nowell M. M. and Field D. P., “A review of strain analysis using electron backscatter diffraction.“ Microscopy and Microanalysis, 17 (2011) 316-329.
- [Xin. 2012] Xin Q., Shu D., Hui L., Wie W. and Chen J., “Magnetic Barkhausen noise, metal magnetic memory testing and estimation of the ship plate welded structure stress.“ Journal of Nondestructive Evaluation, 31 (2012) 80–89.
- [Yelb. 2010] Yelbay H. I., Cam I. and Gür C. H., “Non-destructive determination of residual stress state in steel weldments by magnetic Barkhausen noise technique.“ NDT&E International, 43 (2010) 29-33.